ORNL/Sub/89-95915/2

DEVELOPMENT OF ADHERENT CERAMIC COATINGS TO REDUCE CONTACT STRESS DAMAGE OF CERAMICS

S. F. Wayne, J. H. Selverian, and D. O'Neil

ORNL/Sub--89-95915/2

DE93 012518

Date Published-November 1992

FINAL REPORT

Prepared by
GTE Laboratories Incorporated
40 Sylvan Road
Waltham, Massachusetts 02254

Funded by
Office of Transportation Materials
Office of Transportation Technologies
the Assistant Secretary for Conservation and Renewable Energy
U.S. Department of Energy
EE 51 01 00 0

for
OAK RIDGE NATIONAL LABORATORY
Oak Ridge, Tennessee 37831
managed by
MARTIN MARIETTA ENERGY SYSTEMS, INC.
for the
U.S. DEPARTMENT OF ENERGY
under Contract DE-AC05-84OR21400

MASTER

Table of Contents

Abstract 1
Introduction 2
Executive Summary 5
Design of Coating Configuration 8
Requirements of the Application 8
Chemical, Physical, and Mechanical Property Considerations 9
Coating Process Development 11
Thermodynamic Analysis of Coating Process 11
High Temperature Coating Deposition Reactor 11
Experimental Coating Process 13
Material Characterization 17
Microstructure of Coating 17
Phase I Coating 17
Phase II Coating 20
Physical Properties of Coating 22
Oxidation-Literature Review 22
Oxygen Diffusion through Al_2O_3 27
Oxidation Testing 28
Coatings on Sapphire Substrates 29
AlN Coated Sapphire Substrates 29
Al_2O_3/AlN Coated Sapphire Substrates 29
Al_2O_3+ZrO_2/AlN Coated Sapphire Substrates 30
Oxidation Kinetics of Uncoated and AlN Coated Substrates 30
Phase Formation During Oxidation of Uncoated and Coated Substrates 33
Contact Stress Testing 34
Friction Coefficient Tests 39
Scratch Tests 44
Measurement of Fracture Stress and Toughness of Coatings on Substrates 51
Computer Modelling of Brittle Coatings 52
Computer Simulation of Residual Stress 52
Simple Beam Theory 54

Table of Contents

Composite Plate Theory 56
Comparison to Finite Element Results 59
Si_3N_4 Substrate 60
SiC Substrate 61
Computer Simulation of Coating Fracture 63
Single Layer with Interface - Initial Vertical Flaw 63
Geometry 63
Boundary Conditions 64
Material Properties 65
Crack Propagation Studies 65
Multilayer Analysis - Initial Vertical Flaw 73
Geometry 73
Material Properties 73
Crack Propagation Studies 74
Multilayer Analysis - Initial Horizontal Flaw 75
Conclusions 85
Acknowledgments 87
Publications 88
Presentations 89
Patents 90
References 91
Appendix A - Oxidation Results 95
Appendix B - Method to Measure Fracture Stress and Fracture Toughness of Coatings on Substrates 111
Summary 111
Introduction 111
Stresses in Coatings - Theory 114
Stresses in Uncracked Coatings 114
Stresses in Cracked Coatings 117
Determination of the Weibull Modulus - Theory 119
Determination of Surface Energy - Theory 122
Strain Energy Balance 122
Griffith Energy Balance 126
Experimental Details 126

Table of Contents

Coating Procedure 126
Residual Stress Measurements 127
Results 131
Discussion 136
Coating Properties 136
Limitations on Modeling and Experimental Data 140
Conclusions 143
Appendix C - Curve Fitting of Profilometer Data 144
Background 144
Experiments and Results 144
Conclusions 150
Computer Routines for Curve Fitting of Profilometer Data 150
Appendix D - Simple Composite Plate and Beam Theory 154
Composite Plate Theory 154
Nomenclature 157

List of Tables

Table 1. Properties of the materials used in this study.....10

Table 2. Process conditions for CVD deposition of AlN and Al_2O_3+ZrO_2.....16

Table 3. Summary of oxidation tests for uncoated and AlN coated RBSN, SSC, and HSN substrates. The tests were done in static air at 1200°C and 1275°C in a box furnace.....32

Table 4. Summary of contact testing and post-contact MOR strength testing for CVD coated RBSN.....36

Table 5. Summary of contact testing and post-contact MOR strength testing for CVD coated HSN.....37

Table 6. Summary of contact testing and post-contact MOR strength testing for CVD coated SSC.....38

Table 7. Results from pin-on-disk friction tests of uncoated and Al_2O_3+ZrO_2/AlN coated RBSN, HPSN, and SSC. All tests were done on self-mated samples. Reported values, unless otherwise indicated, are an average of three tests on the same pair of samples.....41

Table 8. Calculated fracture stress, fracture toughness, and Weibull modulus for Al_2O_3 and Al_2O_3+ZrO_2 coatings.....51

Table 9. Material properties used for substrates and coating layers in this part of the study.....59

Table 10. Comparison of 2-D finite element results using special hybrid elements to the composite plate theory described here. Stress values are from reference [SHA88], values in parentheses are results from the composite plate code described here. For both tables ΔT = -1000°C. Note use of Si_3N_4 and SiC substrates.....61

Table A-1. Weight gain as a function of oxidation time for AlN coated sapphire oxidized in static air at 1000°C. The weight gain at a given time was calculated from the original weight and the measured weight after a given oxidation time.....95

Table A-2. Phases identified by X-ray diffraction after oxidation in static air. Samples were sapphire with AlN, Al_2O_3/AlN,

and $Al_2O_3+ZrO_2/AlN$ coating. Phases associated with substrate reflection are not listed....97

Table A-3. Weight gain as a function of oxidation time for Al_2O_3/AlN coated sapphire oxidized in static air at 1100°C, 1200°C, and 1275°C. The weight gain at a given time was calculated from the original weight and the measured weight after a given oxidation time....98

Table A-4. Weight gain as a function of oxidation time for $Al_2O_3+ZrO_2/AlN$ coated sapphire oxidized in static air at 1100°C, 1200°C, and 1275°C. The weight gain at a given time was calculated from the original weight and the measured weight after a given oxidation time....99

Table A-5. Phases identified by X-ray diffraction after 500 hours of oxidation in static air. Samples include uncoated and AlN coated RBSN, SSC, and HSN....100

Table A-6. Phases identified by X-ray diffraction after 500 hour oxidation in static air. Samples had coating of AlN, Al_2O_3/AlN, and $Al_2O_3+ZrO_2/AlN$. Phases associated with substrate reflection are not listed....101

Table B-1. Material elastic constants used in calculations....130

Table B-2. Coating and substrate thicknesses, measured radius of curvature, predicted stress and predicted radius of curvature of samples tested....133

Table B-3. Calculated fracture stress, temperature at the onset of cracking, fracture toughness, Weibull modulus, and surface energy for coatings in this study. All of the reported values are valid at "The Temperature at First Cracking"....134

Table B-4. Fracture toughness, tensile strength, and surface energy of bulk ceramics from the literature....135

List of Figures

Figure 1. Schematic of coating design. 9

Figure 2. Phase II high temperature CVD reactor being used for coating deposition. 12

Figure 3. SEM micrograph of the surface of a Phase I Al_2O_3 coating on SSC. 18

Figure 4. SEM micrograph of a Phase I Al_2O_3+ZrO_2 coating on SSC. a) Back scattered electron image, b) Al X-ray map, c) Zr X-ray map. 19

Figure 5. SEM micrograph of the surface of Phase II Al2O3 coating on SSC. 20

Figure 6. SEM micrograph of a Phase II Al_2O_3+ZrO_2 coating on SSC. a) Back scattered electron image, b) Al X-ray map, c) Zr X-ray map. 21

Figure 7. Plot of silicon nitride oxidation data [BAB83, SIN76a, POR84]. 24

Figure 8. Plot of silicon carbide oxidation data [DUT84, SIN76b]. 25

Figure 9. Plot of AlN oxidation data [LAV83, BOC82]. 27

Figure 10. Schematic of pin-on-disk wear test system. F is the normal force on the pin, d is the pin diameter, D is the disk diameter, R is the wear track radius, and w is the rotation velocity of the disk. 39

Figure 11. Wear tracks on the pins and disks for uncoated HPSN (top), RBSN Si_3N_4 (middle), and SSC (bottom), after a sliding distance of 500 meters at a sliding velocity of 0.01 m/s. 42

Figure 12. Wear tracks on the AlN/Al_2O_3+ZrO_2 coated pins and disks for HPSN (top), RBSN (middle), and sintered SSC (bottom), after a sliding distance of 500 meters at a sliding velocity of 0.01 m/s. 43

Figure 13. Scratch test results of uncoated HSN. The load trace is the solid line (left axis) and the acoustic signal is represented by the spikes (right axis). 45

Figure 14. Scratch test results of coated HSN. The load trace is the solid line (left axis) and the acoustic signal is represented by the spikes (right axis). 46

List of Figures

Figure 15. Scratch test results of uncoated RBSN. The load trace is the solid line (left axis) and the acoustic signal is represented by the spikes (right axis). 47

Figure 16. Scratch test results of coated RBSN. The load trace is the solid line (left axis) and the acoustic signal is represented by the spikes (right axis). 48

Figure 17. Scratch test results of uncoated SSC. The load trace is the solid line (left axis) and the acoustic signal is represented by the spikes (right axis). 49

Figure 18. Scratch test results of coated SSC. The load trace is the solid line (left axis) and the acoustic signal is represented by the spikes (right axis). 50

Figure 19. Thermal expansion coefficients of the various materials present in this system over the temperature range 25°C to 1500°C. 53

Figure 20. At coating thicknesses less than 10% of the substrate thickness most of the stress in the coating is due to the axial component and is therefore independent of the coating and substrate thicknesses. 55

Figure 21. Stress in coating versus ΔT for AlN coatings on SiC and Si_3N_4, and Al_2O_3 coatings on SiC and Si_3N_4 56

Figure 22. Flow chart for computer code implementation of composite plate theory. Layer properties were used to get transformed stiffnesses for each layer, and these were cumulated into a total stiffness matrix for the entire coated system. Unknown mid-plane strains were then solved for, and stresses in each of the layers recovered 57

Figure 23. Schematic of the coated substrate model 58

Figure 24. Numbering scheme for a multicoated system. h is the total coating thickness, and all interface positions are measured relative to the mid-plane at h/2, which the z = 0 plane. Note that layers below this plane have negative interlayer position values 59

List of Figures

Figure 25. Schematic of the finite element mesh relative to microstructural cross section. Direction and positioning of scratch test indenter is shown....66

Figure 26. Schematic of the boundary conditions used in the fracture simulation. Coefficient of friction was 0.5. The value of `p' (the maximum magnitude of the load distribution) was assigned a value such that the stress results are normalized....67

Figure 27. Energy release rate for the interface as a function of mode mixity. A mode-mixity of 0.0 describes pure mode I loading at the crack tip, and a mode-mixity of 90 (degrees) describes pure mode II loading at the crack tip....68

Figure 28. Initial (uncracked) mesh used in the fracture simulation study. The top four elements are the Al_2O_3+ZrO_2 coating material....69

Figure 29. Initial vertical flaw, 0.5 microns long (1/4 coating thickness)....70

Figure 30. Deformed shape and crack growth direction prior to crossing the bimaterial interface....71

Figure 31. Deformed shape and crack path in final increment....72

Figure 32. Energy release rate for both interfaces as a function of mode mixity. A mode-mixity of 0.0 describes pure mode I loading at the crack tip, and a mode-mixity of 90 (degrees) describes pure mode II loading at the crack tip....74

Figure 33. Initial (uncracked) mesh used in the fracture simulation study. The top four elements are the Al_2O_3+ZrO_2 coating material. The next four were the AlN coating material....77

Figure 34. Initial vertical flaw, 0.5 microns long (1/4 coating thickness). Solid lines are deformed geometry (thermal and mechanical loads). Dashed lines are undeformed geometry....78

Figure 35. Deformed shape and crack growth direction as the crack encountered the top bimaterial interface....79

List of Figures

Figure 36. Deformed shape and crack path in final increment. The crack has propagated through both coating layers.....80

Figure 37. Initial horizontal flaw in the second coating layer. The flaw is positioned at the middle of the layer. Solid lines are deformed geometry (thermal and mechanical loads). Dashed lines are undeformed geometry.....81

Figure 38. Deformed shape and crack path in final increment for the case where the initial flaw was in the second (middle) coating layer. The crack has been directed away from the substrate.....82

Figure 39. Initial horizontal flaw in the top coating layer. The flaw is positioned at the middle of the top layer. Solid lines are deformed geometry (thermal and mechanical loads). Dashed lines are undeformed geometry.....83

Figure 40. Deformed shape and crack path in final increment for the initial flaw in the top coating layer. The crack has been directed away from the substrate.....84

Figure A-1. Weight gain versus time for AlN, Al_2O_3/AlN, and Al_2O_3+ZrO_2 /AlN coated sapphire oxidized in static air at 1100°C.....95

Figure A-2. Weight gain versus time for AlN and Al_2O_3+ZrO_2/AlN coated sapphire oxidized in static air at 1200°C.....96

Figure A-3. Weight gain versus time for Al_2O_3/AlN and Al_2O_3+ZrO_2/AlN coated sapphire oxidized in static air at 1275°C.....96

Figure A-4. Weight gain versus time for uncoated and AlN coated RBSN oxidized in static air at 1100°C.....102

Figure A-5. Weight gain versus time for uncoated and AlN coated SSC oxidized in static air at 1100°C.....102

Figure A-6. Weight gain versus time for uncoated and AlN coated HSN oxidized in static air at 1100°C.....103

Figure A-7. Weight gain versus time for uncoated and Al_2O_3/AlN and Al_2O_3+ZrO_2/AlN coated RBSN oxidized in static air at 1100°C.....103

List of Figures

Figure A-8. Weight gain versus time for uncoated and Al_2O_3/AlN and Al_2O_3+ZrO_2/AlN coated SSC oxidized in static air at 1100°C.....104
Figure A-9. Weight gain versus time for uncoated and Al_2O_3/AlN and Al_2O_3+ZrO_2/AlN coated HSN oxidized in static air at 1100°C.....104
Figure A-10. Weight gain versus time for uncoated and AlN coated RBSN oxidized in static air at 1200°C.....105
Figure A-11. Weight gain versus time for uncoated and AlN coated SSC oxidized in static air at 1200°C.....105
Figure A-12. Weight gain versus time for uncoated and AlN coated HSN oxidized in static air at 1200°C.....106
Figure A-13. Weight gain versus time for Al_2O_3/AlN and Al_2O_3+ZrO_2/AlN coated RBSN oxidized in static air at 1200°C.....106
Figure A-14. Weight gain versus time for Al_2O_3/AlN and Al_2O_3+ZrO_2/AlN coated SSC oxidized in static air at 1200°C.....107
Figure A-15. Weight gain versus time for Al_2O_3/AlN and Al_2O_3+ZrO_2/AlN coated HSN oxidized in static air at 1200°C.....107
Figure A-16. Weight gain versus time for uncoated and AlN coated RBSN oxidized in static air at 1275°C.....108
Figure A-17. Weight gain versus time for uncoated and AlN coated SSC oxidized in static air at 1275°C.....108
Figure A-18. Weight gain versus time for uncoated and AlN coated HSN oxidized in static air at 1275°C.....109
Figure A-19. Weight gain versus time for Al_2O_3/AlN and Al_2O_3+ZrO_2/AlN coated RBSN oxidized in static air at 1275°C.....109
Figure A-20. Weight gain versus time for Al_2O_3/AlN and Al_2O_3+ZrO_2/AlN coated SSC oxidized in static air at 1275°C.....110
Figure A-21. Weight gain versus time for Al_2O_3/AlN and Al_2O_3+ZrO_2/AlN coated HSN oxidized in static air at 1275°C.....110
Figure B-1. Scanning electron micrograph of a crack in a coating.....112

List of Figures

Figure B-2. Schematic of stress versus ΔT plot for a cracked ceramic coating on a substrate. ΔT is the deposition temperature minus the instantaneous temperature, σ_p is the predicted stress at T_1 and T_2 (Eq. B-3), sm is the measured stress at T_1 and T_2 (Eq. B-4), and sf is the fracture stress of the coating.....113

Figure B-3. Schematic of coating on substrate with a single crack. The ends are treated as crack faces. The relative size of the coating was greatly exaggerated to show detail.....115

Figure B-4. At coating thicknesses less than 10% of the substrate thickness most of the stress in the coating was due to the axial component and was therefore independent of the coating and substrate thicknesses.....117

Figure B-5. Plot of the stress distribution in a 4.7 microns Al_2O_3 coating on a SiC substrate according to Eq. (B-5) for three different crack spacings (10, 30, and 100 microns). The crack is located at x = 0.....119

Figure B-6. Plot of theoretical stress in coating and measured stress in coating.....120

Figure B-7. Plot of number of cracks (NC) versus the average stress in the coating, for a 2.3 microns Al_2O_3 coating on SiC.....121

Figure B-8. Schematic of bent substrate. NA is the location of the neutral axis, 'b' is the distance from the NA to the uncoated side of the substrate, 'a' is the distance from the coated side to the NA, and 'r' is the radius to any given location in the substrate.....124

Figure B-9. Flow chart of experimental procedure outlining important steps in the force balance used to calculate the fracture strength, fracture toughness, Weibull modulus, and temperature of first cracking of thin coatings on substrates.....128

Figure B-10. Flow chart of experimental procedure outlining important steps in the energy balance used to calculate the surface energy of thin coatings on substrates.....129

Figure B-11. Plot of the coefficients of thermal expansion for materials used in this study [TOU75]. Data for the Al_2O_3+5 v/o ZrO_2 coating is from the volume weighted average of Al_2O_3 and ZrO_2. Data for Si_3N_4 at temperatures below 20°C was extrapolated. 130

Figure B-12. Plot of stress versus ΔT for a 2.34 microns Al_2O_3 coating on SiC. The predicted stress was calculated from Eq. (B-3) and the measured maximum stress (•) was calculated from Eqs. (B-5) and (B-8). 132

Figure B-13. Scanning electron micrograph of the coatings deposited on a SiC substrate at 950°C in a) Al_2O_3 deposited in an Inconel chamber, b) Al_2O_3 deposited in a graphite chamber, and c) Al_2O_3+5 v/o ZrO_2 deposited in a graphite chamber. 137

Figure B-14. Scanning electron micrograph of the coatings deposited on a SiC substrate at 970°C in a) TiN sample # 1, b) TiN sample #2. 141

Figure C-1. Plot of experimental profilometer data. In this example the RMS noise is approximately 0.94 microns and the radius of curvature was calculated to be 7.861 m ±5% using the "GUESS" routine (see end of Appendix), compared to 6.229 m calculated by the Rodenstock software. 145

Figure C-2a. Plot of computer generated data for a radius of curvature of 7.861 m and an RMS noise level of 0.94 microns with a uniform distribution, calculated R = 8.002 m. The calculated radius of curvature value is within 2% of the actual radius of curvature of 7.861 m. 146

Figure C-2b. Plot of computer generated data for a radius of curvature of 7.861 m and an RMS noise level of 0.94 microns with a Gaussian distribution, calculated R = 8.204 m. The calculated radius of curvature value is within 4% of the actual radius of curvature of 7.861 m. 147

Figure C-3. Ratio of the calculated radius of curvature to the actual radius of curvature versus the signal-to-noise ratio for

data sets with 2000 data points. For the Gaussian distribution the critical S/N ratio was 1.8 and for the uniform distribution it was 0.7. Only the results from the Gaussian distribution are shown.....148

Figure C-4. Values of the maximum RMS noise level for which the fitted radius of curvature is within 5% of the true radius of curvature. A critical S/N ratio of 1.8 was used.....149

Figure C-5. Plot of error in the radius of curvature versus S/N.....149

Figure D-1 In-plane residual stresses for a Si_3N_4 substrate coated with alumina-zirconia without an interlayer. Stresses for 1, 4 and 10 microns coating thicknesses are shown. Thickness of the coating layer has negligible effect on residual stress.....158

Figure D-2. In-plane residual stresses for a Si_3N_4 substrate coated with alumina-zirconia with an AlN interlayer. Stresses for 1, 4 and 10 microns interlayer thicknesses are shown. Thickness of the interlayer has negligible effect on residual stress.....159

Figure D-3. In-plane residual stresses for a Si_3N_4 substrate coated with AlN and an alumina-zirconia interlayer (coating order is reversed from the previous figure). Stresses for 1,4 and 10 microns interlayer thicknesses are shown. Comparing to the previous figure, order of the coating layers has negligible effect on residual stress.....160

Figure D-4. In-plane residual stresses for a SiC substrate coated with AlN and alumina-zirconia. Stresses shown are applicable for a wide range of coating thicknesses.....161

ABSTRACT

This report is a summary of results of a study aimed at the development of thin, oxidation-resistant ceramic coatings to reduce contact stress damage of ceramic heat engine components†. Strongly adherent coatings were deposited on reaction bonded Si_3N_4 (RBSN), sintered SiC (SSC), and HIP'ed Si_3N_4 (HSN) and using a newly developed chemical vapor deposition (CVD) process. The performance of the coating was assessed by oxidation, strength and contact stress testing. A new method was developed to experimentally determine the strength and Weibull modulus of thin brittle films on ceramic substrates. A significant portion of the study was devoted to numerical modeling of the coatings in order to understand the contributions of residual stress as different coating materials and thicknesses were combined. Coating designs were further analyzed by simulating the crack growth behavior in multilayer films while accounting for the interface fracture mechanics. This work has shown that the $Al_2O_3+ZrO_2$ composite coating developed in this program can provide resistance to oxidation and contact stress, as determined by laboratory measurements. Commercial application of the composite coating has been successfully demonstrated by use of the $Al_2O_3+ZrO_2$ composite as a protective coating on a Si_3N_4 cutting tool.

---

† Research sponsored by the Advanced Materials Development Program, Office of Transportation Systems, U.S. Department of Energy, under contract DE-AC05-840R21400 with Martin Marietta Energy Systems, Inc.

INTRODUCTION

Heat engine operating efficiencies have been significantly improved by using uncooled ceramics components at temperatures above those attainable with superalloys. A large number of studies have used Si_3N_4-based and SiC based materials, and these have shown considerable potential for use as heat engine components. However, due to their brittle nature, high surface stresses in contact regions cannot redistribute as in metals. This can result in localized stresses which may exceed the baseline strength, thus damaging the surface of the component and reducing its strength. This susceptibility to contact stress damage has led to projections of premature failure of ceramic heat engine components that undergo sliding contact.

It has been suggested that surface damage and strength loss under these conditions can be substantially reduced by applying a thin ceramics coating [LAC84]. Exploratory studies using plasma sprayed oxide coatings [GTE81] demonstrated improvements in the contact stress damage resistance of both Si_3N_4 and SiC ceramics, but the adherence of these coatings was inadequate. Yttria-stabilized zirconia coatings deposited by electron beam physical vapor deposition were also studied [SCH87], but adherence was still poor. The poor adherence precluded performance testing of coated components.

A new coating designed specifically for heat engine applications was proposed for this work. This coating is unique in that it consists of two layers, each of which is compositionally graded so that there are not sharp interfaces. The outer layer is oxidation resistant and should provide toughness and a low coefficient of friction, while the intermediate layer serves primarily as a bonding layer. A composite of Al_2O_3 and ZrO_2 was selected for the outer layer, and AlN was selected for the intermediate layer. Figure 1 is a schematic of the proposed coating configuration.

Unlike previous studies, one coating configuration was used for all substrates in this program. However, coating properties (e.g., composition, thickness, microstructure) could in principle be varied to achieve compatibility with each substrate by modifying the coating deposition conditions. Chemical vapor deposition (CVD) was proposed as the coating

application technique. CVD is preferred for this application because with this technique, adhesion can be enhanced via chemical bonding or solid solution formation between coating and substrate, interdiffusion at the interface, or formation of new phases at the interface due to reaction between the CVD gas mixture and the substrate surface. In contrast, alternative deposition techniques such as those based on physical vapor deposition or spraying produce coating/substrate attachment which is usually mechanical. Additional advantages of CVD include its ability to uniformly coat parts with complex shapes and its ability to be scaled-up to produce commercial quantities.

The development of the coating configuration and the CVD processes for applying the coating was guided by mathematical modeling. A model based on finite element analysis was developed to calculate relationships between thickness of the various coating layers and residual stress levels in the coating and substrate. Although predictive capability was not achieved, the model did give insight into control of stress build-up in the coating. Mathematical models were also used to determine (1) feasibility of growing the desired coating under various sets of CVD operating conditions, (2) dependence of coating yield and growth rate on operating conditions, and (3) relationships between coating composition and operating conditions. Results were plotted in the form of "CVD phase diagrams" for growth of $Al_2O_3+ZrO_2$ composite and AlN coatings.

During this program, the CVD processes were developed and coatings were deposited on three substrates—reaction bonded Si_3N_4 (RBSN), hot isostatically pressed Si_3N_4 (HSN), and sintered SiC (SSC) (Table 1). Work was done on test bars measuring 2 in. x 1/4 in. x 1/8 in. that were either whole or cut into three equal size pieces before coating. Adherence of the coating was assessed using a conventional scratch test (Revetest type). The effect of the coating on the flexure strength of each substrate material was measured at room and elevated temperature. The thermal shock resistance was tested by rapidly and repeatedly cycling samples to typical engine operating temperatures. Long term, high temperature oxidation resistance in static air was also studied. In each case, the effect of the test on coating adhesion was evaluated. Finally, a set of samples was coated for contact stress tests which

will be conducted by Garrett Turbine Engine Company, Auxiliary Power Division.

The results obtained in this phase of the program demonstrated significant potential for the use of this coating configuration on ceramic engine components to reduce contact stress damage of the substrate. The coatings generally remained intact during performance tests at temperatures of 1000°C. However, the AlN and Al_2O_3+ZrO_2 coatings, deposited by CVD, were cracked. Finite element analysis was used to show that these coatings, deposited by convential CVD, would always crack, and that the concept of "graded" layers would not prevent the cracking problem.

EXECUTIVE SUMMARY

This report summarizes the Phase II findings on the development of an $Al_2O_3+ZrO_2$ composite coating, intended to reduce the contact stress damage of Si_3N_4 and SiC ceramics. An AlN interlayer (~5 microns thick) was demonstrated to be an effective means of providing good adhesion between $Al_2O_3+ZrO_2$ (~1 micron thick) and the ceramic substrates. During this program, CVD processes were developed and used to successfully deposit the multilayer coating. The performance of the coatings produced in Phase II was assessed by oxidation tests, scratch tests, and pin-on-disk sliding contact.

Modeling the diffusion of oxygen through an Al_2O_3 layer at elevated temperatures suggested that the coating would be an adequate diffusion barrier to oxygen. However, experimental results revealed that the composite coating configuration was not oxidation resistant for 500 hours at temperatures above 1000°C. The lack of protection is attributed to cracks in the $Al_2O_3+ZrO_2$ layer, which allowed oxygen to penetrate and react with AlN. The kinetics of oxidation of AlN are sufficiently slow at 1000°C for the coating to protect the substrate for 500 hours. However, above 1000°C, the oxidation rate of AlN is rapid enough to cause the AlN to fully oxidize to Al_2O_3.

A major aspect of this program has dealt with the use of finite element methods and fracture mechanics to model the behavior of brittle multilayer coatings. Detailed analysis of the residual stresses in uncracked coatings on ceramic substrates revealed that the coating thickness, order of coating layers (including grading of the coefficient of thermal expansion), and elastic modulus of the coating all have a negligible effect on the residual stress in the coating. It was concluded that due to the high temperatures used in CVD processing and inherent thermal expansion mismatch between the materials, the $Al_2O_3+ZrO_2$ coatings would contain cracks upon cooling to room temperature.

To better understand the behavior of cracks in the coating and possibly identify a means to eliminate them from the coating, additional modeling was performed. The effect of crack propagation during solid body contact was studied using interface fracture mechanics coupled with finite element analysis. Several geometries were studied; one coating layer with a vertical

flaw, two coating layers with a vertical flaw, and two coating layers with a horizontal flaw. Thermal residual stress and point contact loads (which simulated the scratch test) were applied to the coated system and the crack was allowed to propagate. For vertical flaws, the cracks always propagated into the substrate. Further analysis showed that improving the fracture toughness of the interface would not improve the performance of the coating, since the interface was not a weak point. In contrast, the horizontal crack did not reach the substrate. A crack in the middle layer of a two layer coating, stayed within that layer. A crack in the outer layer of a coating moved away from the substrate and towards the free surface. Therefore, cracks of this type would not degrade the oxidation performance of a coated substrate.

The possibilities for working around the problem inherent to thin brittle coatings could lie in the area of controlled brittle fracture of multilayers, controlling the residual stress in the deposited film, or by the use of "ductile" layers which would permit stress relief and alleviate pre-service cracking. Physical vapor deposition (PVD) methods, which allow the residual stress state to be controlled, or low temperature CVD processes may allow for crack-free coatings to be deposited. The coating would then be in a compressive stress state at the service temperature and would not crack. It is anticipated that without cracks, the Al_2O_3+ZrO_2 composite coating would be an effective means of reducing the contact stress damage and oxidation of Si_3N_4 ceramics.

A single point scratch test was used to assess the protective nature of the coatings during contact loading on unoxidized samples at room temperature. The coating protected the SiC (SSC) and reaction bonded Si_3N_4 (RBSN) substrates by reducing chipping and cracking of the substrates. No significant differences were seen in the scratch resistance of the uncoated and coated hot pressed Si_3N_4 (HSN).

A method was developed to measure the ultimate tensile strength, fracture toughness, and Weibull modulus of thin brittle coatings on substrates. The technique is based on measuring the radius of curvature of a coated substrate, and equating the resulting calculated stress with a theoretical shear-lag stress distribution model. The Weibull modulus and fracture stress of Al_2O_3 CVD coatings on SiC substrates were measured. The

fracture stresses for coatings of these materials ranged from 190 MPa to 480 MPa, the Weibull modulus ranged from 16 to 28, and the fracture toughness ranged from 0.5 - 1.1 MPa$\sqrt{m}$. This work has shown that the tensile strength of Al_2O_3 and Al_2O_3+ZrO_2 coatings can be approximated by bulk values, however, the fracture toughness of these coatings was found to be significantly lower than bulk values.

Additional contact stress tests on Phase I coatings were carried out by Garrett Turbine Engine company. These tests were deemed inconclusive due to the lack of coating oxidation resistance at 1200°C.

Pin-on-disk tests were used to measure the breakaway and kinetic friction coefficients for coated and uncoated materials. Room temperature results showed that the Al_2O_3+ZrO_2 coating reduces the kinetic friction coefficient of RBSN and HSN by as much as 50% in self-mated tests. No apparent reduction in friction was observed for the SSC substrate. An improvement in sliding wear resistance was obtained with Al_2O_3+ZrO_2 coated HSN in the pin-on-disk test, whereas the coatings on RBSN and SSC were ineffective.

DESIGN OF COATING CONFIGURATION

REQUIREMENTS OF THE APPLICATION

Advanced heat engine components are subjected to high localized stresses in contacting areas during operation. In addition, they are exposed to extreme conditions of thermal cycling. The use of thin (<100 microns) ceramic coatings on various components has been shown to reduce contact stress damage by reducing the relative coefficient of friction and elastic modulus of the contacting parts. However, the coating must be strongly adherent and not degrade under thermal shock and oxidizing conditions at engine operating temperatures. These requirements dictate six major design criteria:

1. Strong coating/substrate adherence.
2. Low residual stress in the coating and at the coating/substrate interface.
3. Excellent oxidation resistance and low permeability of oxygen through the coating.
4. High thermal shock resistance.
5. Improved mechanical strength and low coefficient of friction at room and elevated temperatures.
6. Minimum chemical interaction between the substrate and the coating and coating stability at operating temperatures.

A single monolithic ceramic coating which could satisfy all of these criteria could not be identified. Hence, a multilayered coating configuration was proposed (see Figure 1). This coating consists of an intermediate layer whose primary function is to promote bonding with the substrate, and an outer layer which provides the required mechanical properties and oxidation resistance.

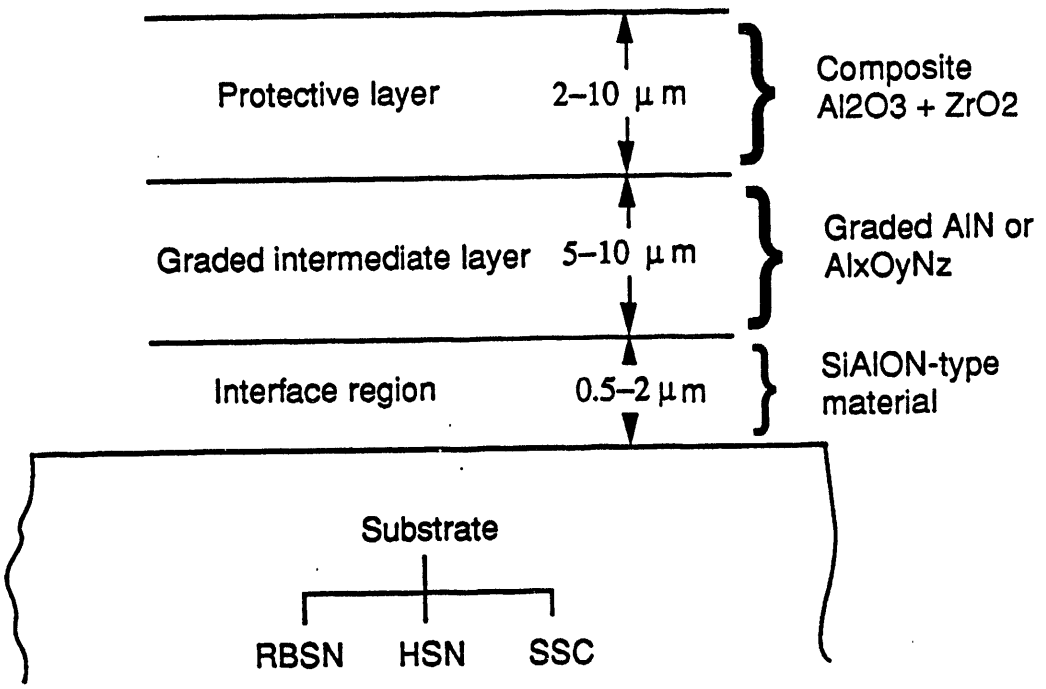

Figure 1. Schematic of coating design.

CHEMICAL, PHYSICAL, AND MECHANICAL PROPERTY CONSIDERATIONS

The important chemical properties required of the outer coating layer are oxidation resistance and low permeability to oxygen. The oxidation resistance of Al_2O_3 is well known. Even with this outer layer, it would still be possible for oxygen to diffuse through the layer via pores or cracks. Hence, an intermediate layer which can dissolve or react with oxygen is necessary. Aluminum nitride forms polytypes and solid solutions with oxygen over wide ranges of composition, so it is a candidate for the intermediate layer. In addition, AlN forms solid solutions with Si_2N_2O, and these solutions are the basis for some SiAlON-type compounds. Since Si_3N_4 readily oxidizes to form Si_2N_2O, the surface of Si_3N_4 materials generally contains Si_2N_2O. Hence the potential for SiAlON formation exists at the Si_3N_4/coating interface. It is therefore expected that if AlN is used as the intermediate layer, it will act as a chemical oxygen barrier and as a bonding agent with Si_3N_4-based substrates.

Physical and mechanical properties which are considered to be relevant to coating design include density, thermal expansion coefficient,

fracture toughness, elastic modulus, hardness, and Poisson's ratio. The composition and selected properties are listed in Table 1 for the substrate materials as well as for the candidate coating materials. The values reported are for bulk materials; it is assumed for purposes of coating design that the property values are the same for thin films.

Table 1. Properties of the materials used in this study.

Material	Nominal Composition (wt%)	Density (actual/ theoretical) (g/cm^2)	KHN (GPa) Face/Edge	Identation Fracture Toughness ($MPa\sqrt{m}$) Face/Edge
RBSN (Airesearch)	> 95% Si_3N_4 < 3 Si < 2 Fe	2.75/3.19	9.846 ± 0.56 9.395 ± 0.80	3.5 ± 0.3 4.0 ± 0.6
SSC (Hexalloy SA)	> 95.5 SiC < 0.5 B < 0.1 impurities	3.17/3.21	25.29 ± 0.91 23.91 ± 0.46	2.2 ± 0.2 2.3 ± 0.2
HSN (GTE AY6)	92 Si_3N_4 2 Al_2O_3 6 Y_2O_3 < 0.1 impurities	3.25/3.26	13.22 ± 0.15 13.11 ± 0.17	3.4 ± 0.2 3.3 ± 0.3
Al_2O_3		3.99	13-15	2-5
AlN		3.28	---	2-3

COATING PROCESS DEVELOPMENT

THERMODYNAMIC ANALYSIS OF COATING PROCESS

Thermodynamic analysis of the coating procedure was preformed in Phase I of this program. The results are listed in Appendix B of the Phase I final report.

HIGH TEMPERATURE COATING DEPOSITION REACTOR

A new CVD reactor was built, the Phase II reactor. This reactor is a hot-wall, crucible type reactor that is heated resistively with graphite heating elements. The system was leak checked and found to be leak-free down to a pressure of 10^{-6} torr. Source gases enter at the bottom, flow upward past the parts to be coated, and exit through exhaust tubes terminating above the deposition zone. This is illustrated in Figure 2. A perforated plate defines the upper limit of the deposition zone. Graphite rods are hung from this plate to form a fixture for supporting the substrates. The substrates are placed on a grid of thin alumina rods that pass through holes in the graphite rods. The volume of the reactor is 5 liters. An internal reactor is used for generating volatile $AlCl_3$ and $ZrCl_4$, which are the aluminum and zirconium source materials being used for the AlN and $Al_2O_3+ZrO_2$ coatings.

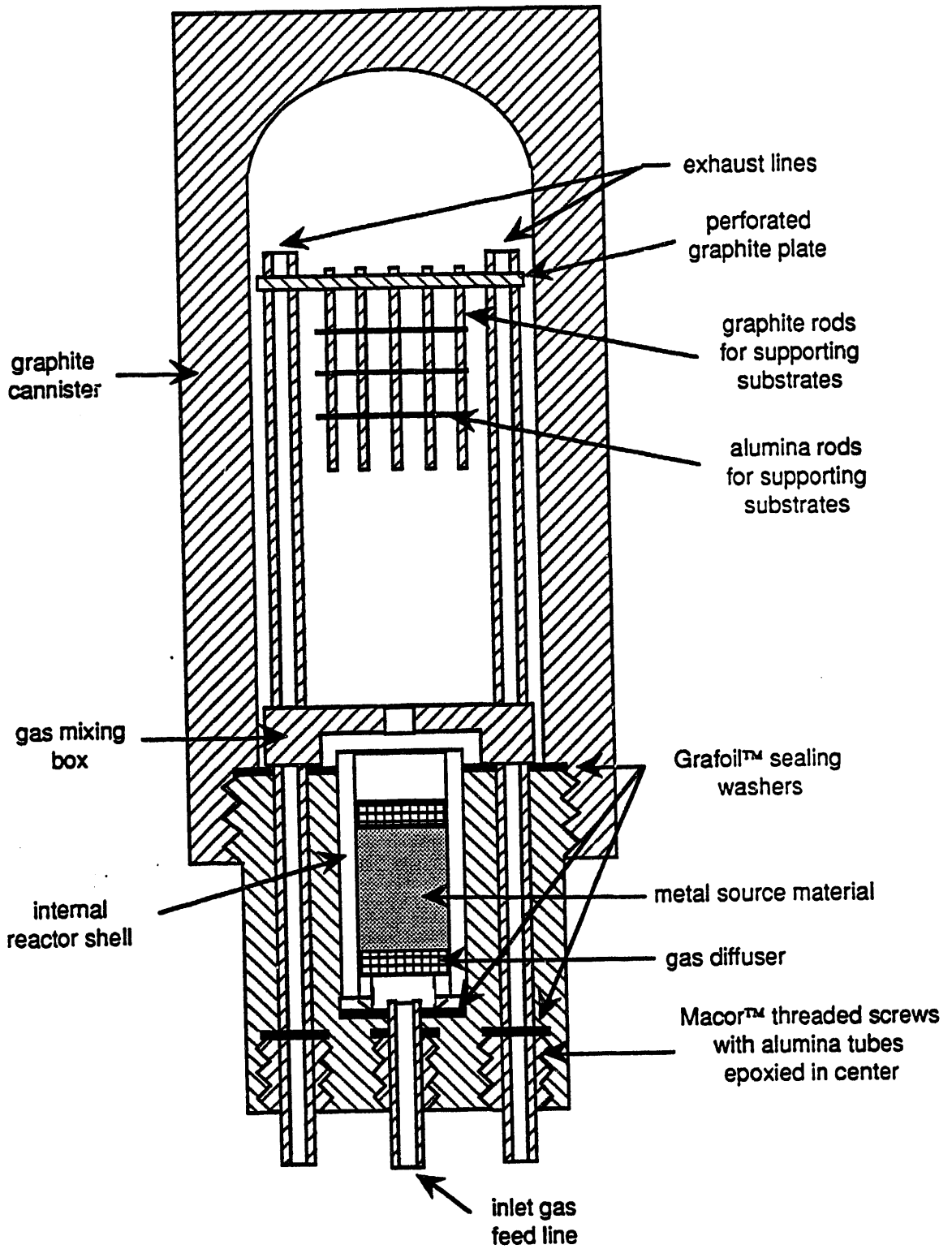

Figure 2. Phase II high temperature CVD reactor being used for coating deposition.

Formation of a coating at high temperatures (T > 1000°C) was complicated by the tendency for gas phase nucleation to occur in CVD processes that use $AlCl_3$ as a source material. To compensate for the higher thermal driving force for gas phase nucleation, we reduced the pressure to 10 torr. The system can be operated at pressures as low as 1 torr depending on the total gas flow rate.

The CVD reactor which was previously being used for Phase I of this program was modified to incorporate two internal reactors for simultaneously generating two different source materials. Previously, all source materials were generated in one internal reactor. This resulted in poor control over the relative amounts and distribution of ZrO_2 and Al_2O_3 in the Al_2O_3+ZrO_2 composite layer. Details of the composite layer composition were discussed in the October, 1989 Bimonthly Progress Report. The new design was expected to allow better control of the relative rates of generation of $AlCl_3$ and $ZrCl_4$ for deposition of the Al_2O_3+ZrO_2 composite layer.

EXPERIMENTAL COATING PROCESS

Process development for deposition of the coating at temperatures above 1000°C was carried out for the Phase II graphite high temperature CVD reactor (Figure 2). Initially, attempts were made to deposit a pure Al_2O_3 coating. The first experiment was done at 1000°C to establish reproducibility of coatings obtained in the Phase I CVD reactor. The coating produced was not analyzed, although it appeared to be similar to those obtained in the Phase I reactor. Based on weight gain, the deposition rate was approximately 0.5 microns/hour, which was typical of the deposition rate obtained in the other reactor. The deposition temperature was then raised to 1200°C. This gave a 1.5 micron thick coating in one hour. However, Al_2O_3 powder also formed due to gas phase nucleation. Most of this powder was easily removed from the samples, and the remaining coating appeared to be nonporous and smooth on the surface. In order to determine if there was a relationship between deposition temperature and gas phase nucleation, an experiment was done at 1120°C. This run produced extensive amounts of powder, causing the reactor exhaust line to plug. In addition, melting of the Al metal in the $AlCl_3$

generator occurred, so samples from this run were not analyzed. The remainder of the experiments done were deposition of $Al_2O_3+ZrO_2$ or AlN.

Since some success was achieved with deposition of pure Al_2O_3 at 1200°C, the first $Al_2O_3+ZrO_2$ experiment was done at 1200°C. This resulted in extensive gas phase nucleation. The deposit that collected on the substrates was loosely adherent and easily rubbed off. No weight gain of the substrate was detected, which suggested that no coating had formed. Another experiment was done at this temperature, but with the relative amounts of $AlCl_3$ and $ZrCl_4$ source varied; i.e., a higher ratio of Zr/Al. This resulted in a moderate amount of powder formation due to gas phase nucleation. In addition, a very thick, loosely adherent coating was again easily removed. A third experiment was done at 1200°C with the same ratio of source materials but with a steeper temperature profile so that the source gases did not get preheated to as high a temperature. It was hypothesized that this would reduce the amount of gas phase nucleation. This succeeded in producing less powder. Additional experiments were done with the original Zr/Al ratio in the source gases and with deposition temperatures of 1300°C and 1375°C. The experiment at 1300°C produced a thick, nonporous, well adherent coating and a small amount of powder. The coating thickness indicated a deposition rate of 11 microns/hour. The experiment at 1375°C gave a moderate amount of powder and a thick coating.

Analysis of the high temperature Al_2O_3 and $Al_2O_3+ZrO_2$ experiments suggests that there is a transition temperature, below which gas phase nucleation dominates, and above which surface nucleation dominates. At the lowest deposition temperature used in this program (975°C used throughout Phase I and early Phase II), gas phase nucleation was not measurable, but the deposition rate was very low (<1 micron/hour for either Al_2O_3 or $Al_2O_3+ZrO_2$). At 1200°C for pure Al_2O_3 and 1300°C for $Al_2O_3+ZrO_2$, the deposition rate was much higher and an adherent coating was formed with only moderate amounts of powder from gas phase nucleation. At intermediate temperatures, extensive powder formation took place, and little or no adherent coating was formed. The only experiment that did not fit this trend was the one in which $Al_2O_3+ZrO_2$ was deposited at 1375°C. It should be emphasized that these results are specific to our deposition system and should therefore not be generalized

to predict the behavior of other systems. This is especially important since the temperature profile in the gas phase upstream of the deposition zone appears to strongly influence the results.

The remainder of the experiments were directed towards the deposition of AlN. Initially, an experiment was done at 1000°C to establish reproducibility of coatings obtained in the low temperature CVD reactor. This resulted in quite different behavior than that which typically occurred in the low temperature reactor. Specifically, an adherent, thick coating formed along with an extensive amount of powder. The coating thickness varied substantially on a given sample, corresponding to a deposition rate of 6-9 microns/hour. The difference in behavior can be attributed to the different temperature profile experienced by the gas phase, suggesting that the AlN system is very sensitive to this parameter. A second experiment at 1200°C also gave extensive powder formation, but a lower and more variable deposition rate (1-5 microns/hour). It should be emphasized that the reported deposition rates are only apparent rates since they are determined by measuring coating thickness at several locations and dividing by the total deposition time. Loss of loosely adherent coating or flaking or chipping of strongly adherent coating, during fracture of the sample, could skew the measurement.

In Phase I of this work Al and Zr metals were mixed together to generate the $AlCl_3$ and $ZrCl_4$ reactant gases for composite layer deposition. This led to a nonuniform distribution of Zr in the coating. The Zr reacted first and a layer of pure ZrO_2 was deposited followed by an Al_2O_3 layer. In Phase II an Al-Zr metal alloy was used as the metal source to generate the $AlCl_3$ and $ZrCl_4$ reactant gases for composite layer deposition. The Al-Zr alloy was prepared by melting under argon and had a composition of 88 wt% Al-12 wt% Zr. Use of this Al-Zr alloy produced a composite film with a uniform Zr distribution. The "best set" of deposition conditions used to deposit AlN and Al_2O_3+ZrO_2 coatings are listed in Table 2. The microstructure of these coatings is detailed in the next section.

Table 2. Process conditions for CVD deposition of AlN and Al_2O_3+ZrO_2.

Pressure = 11 torr			
Temperature = 950°C			
Internal reactor;	AlN coatings;		30 gm Al
	Al_2O_3+ZrO_2 coatings;		10 gm Al+12 w/o Zr alloy
Ar flows;	750 sccm inner	2000 sccm outer	
H_2 flows;	1000 sccm inner	3500 sccm outer	
Cl_2 flows;	75 sccm inner		
CO_2 flow;	300 sccm outer	(only for Al_2O_3+ZrO_2 coatings)	
NH_3 flow;	250 sccm outer	(only for AlN coatings)	

MATERIAL CHARACTERIZATION

MICROSTRUCTURE OF COATING

Phase I Coating

Figure 3 shows the surface of an Al_2O_3 coating deposited on SSC substrate. The rough surface topology is attributed to Ni contamination from the Inconel vessel in the CVD reactor [COL86]. This problem was eliminated in the Phase II coating where a graphite CVD reactor was used.

Figure 4 shows a cross-section of the $AlN/Al_2O_3+ZrO_2$ coating on the SSC substrate, the coating had the same morphology on the RBSN and HSN substrates. The Zr is concentrated at the AlN/composite interface.

The microstructure of the $Al_2O_3+ZrO_2$ composite layer has been studied by TEM and analytical electron microscopy. A sample of the Phase I $Al_2O_3+ZrO_2$ coating on a TiC whisker reinforced Al_2O_3 substrate was analyzed. This substrate was used because previous attempts at preparing a thin foil specimen of coated silicon nitride-based materials were unsuccessful. The failure was attributed to uneven milling rates of the coating and substrate during ion beam milling. The coating was 3 microns thick and contained approximately 3 w/o Zr. It was found that the majority of the coating was essentially pure Al_2O_3 with the Zr concentrated at the interface between the coating and the substrate. The Zr was present as 30 nanometer particles containing impurities that were identified as silicon, tungsten, and probably oxygen. These impurities are very likely introduced during deposition of the coating as a result of residue inside the CVD equipment from coating of other substrate materials. The TEM study did not determine that the Zr was present as ZrO_2. An amorphous Si-rich phase was also present at the interface. This glass probably formed from the binder material in the substrate. The grain size of the Al_2O_3 in the coating ranged from 40 to 200 nanometers with the majority being 50 nanometers.

The TEM results are consistent with earlier studies done using electron microprobe. In particular, ZrO_2 was found to be concentrated at the interface.

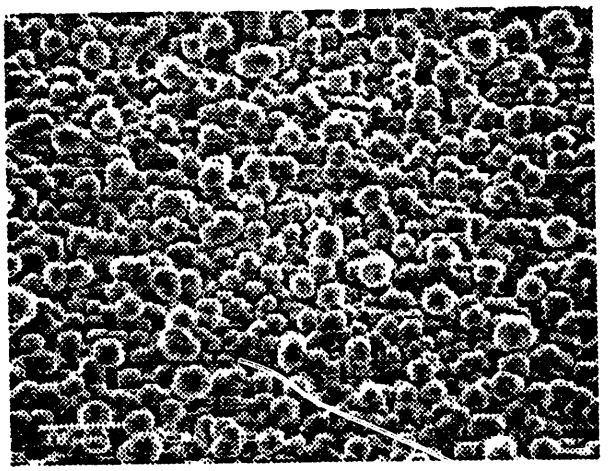

Figure 3. SEM micrograph of the surface of a Phase I Al_2O_3 coating on SSC.

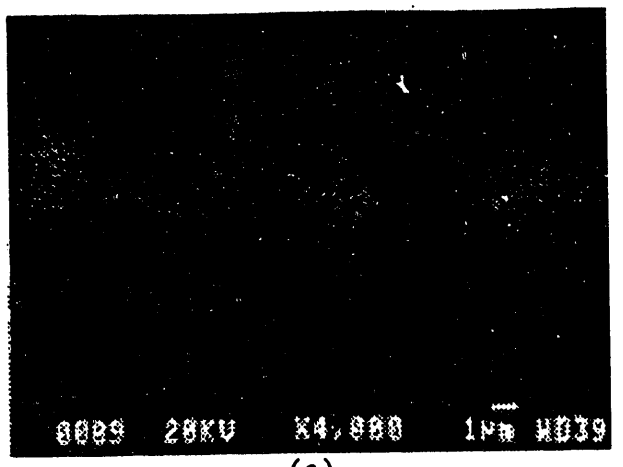

(a)

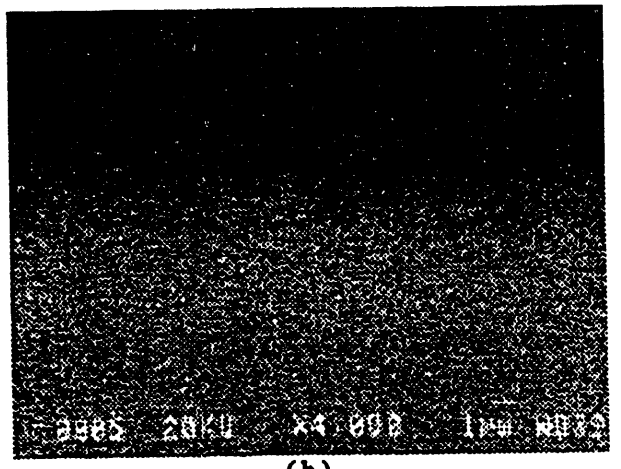

(b)

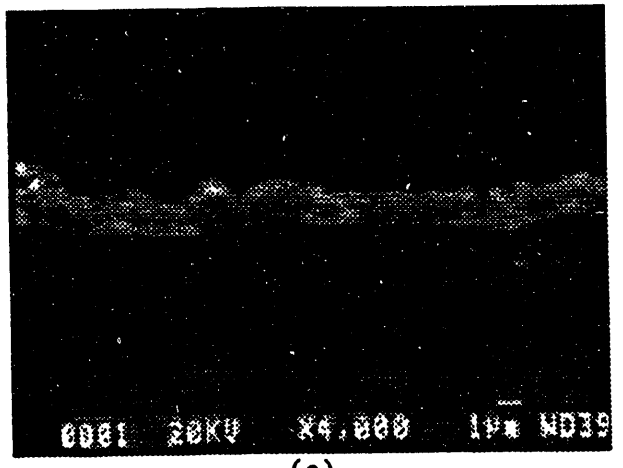

(c)

Figure 4. SEM micrograph of a Phase I Al_2O_3+ZrO_2 coating on SSC. a) Back scattered electron image, b) Al X-ray map, c) Zr X-ray map.

Phase II Coating

Figure 5 shows the surface of an Al_2O_3 coating deposited on SSC substrate. The smooth surface topology is contrasted with the rough surface of the Phase I coatings, Figure 3.

Figure 6 shows a cross-section of the $AlN/Al_2O_3+ZrO_2$ coating on the SSC substrate, the coating morphology on the RBSN and HSN substrates were identical. The Zr is uniformly dispersed throughout the composite region. A sample was prepared for transmission electron microscopy (TEM). This sample showed that the Al_2O_3 grain size was 30 - 50 nm and was alpha Al_2O_3. ZrO_2 particles were not identified, this is believed to be due to the small volume fraction of ZrO_2 (5 %) in the composite making it very difficult to identify ZrO_2 particles directly. While the phase of ZrO_2 was not identified it is believed that the ZrO_2 grain size was the same as the Al_2O_3 (30 - 50 nm).

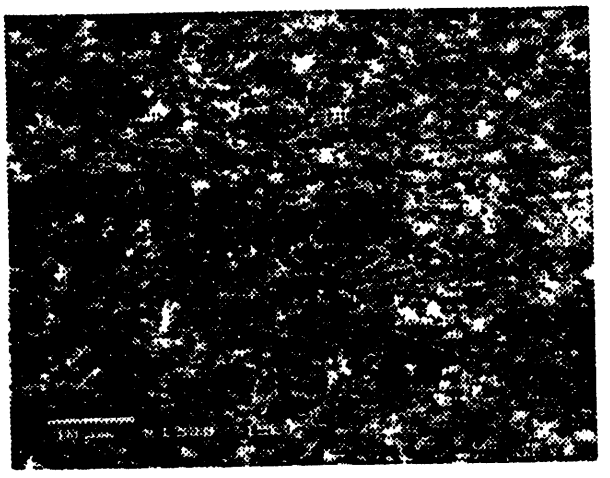

Figure 5. SEM micrograph of the surface of Phase II Al_2O_3 coating on SSC.

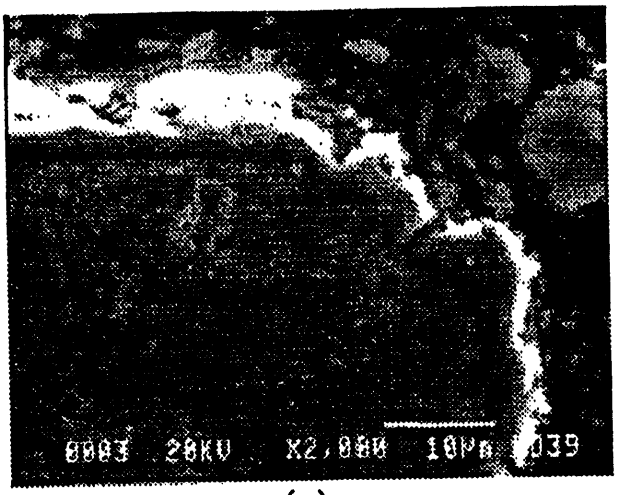

(a)

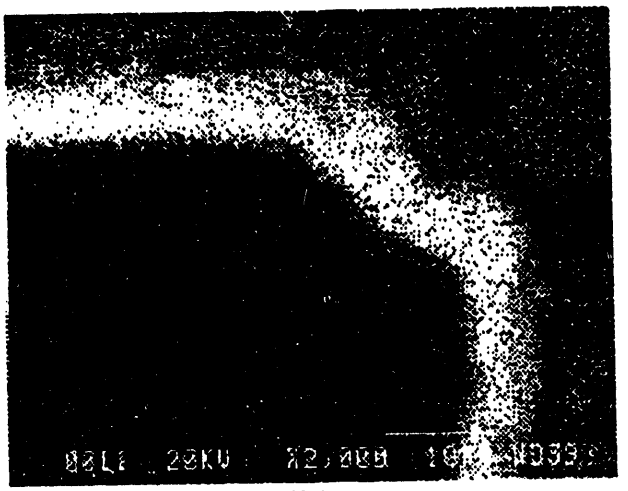

(b)

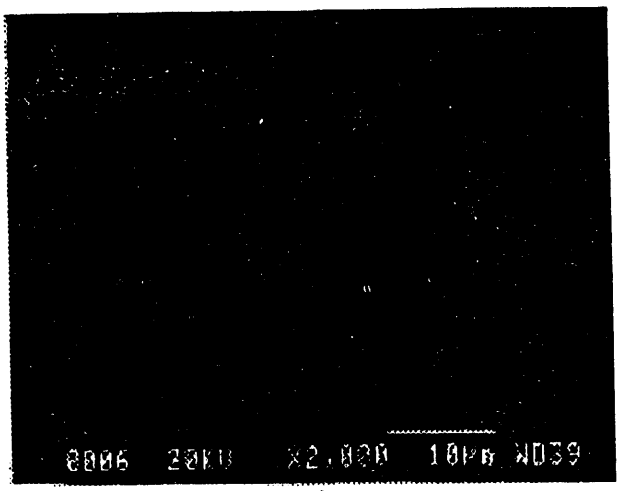

(c)

Figure 6. SEM micrograph of a Phase II $Al_2O_3+ZrO_2$ coating on SSC. a) Back scattered electron image, b) Al X-ray map, c) Zr X-ray map.

PHYSICAL PROPERTIES OF COATING

Oxidation-Literature Review

During Phase I, the oxidation resistance of the coating in static air was studied. The coating was found to be oxidation resistant for up to 500 hours at 1000°C, but was not oxidation resistant at 1200°C or higher. The lack of oxidation resistance at elevated temperatures was studied in Phase II.

The oxidation behavior of silicon nitride, silicon carbide, and aluminum nitride were the subjects of several previous studies. A brief summary of the literature is provided in the following sections. These summaries are intended to provide basic information and to indicate some relevant articles in the literature.

Oxidation of Silicon Nitride

The oxidation of Si_3N_4 depends on the type and amount of porosity, the flow rate of the oxidizing gas, and the types of additives and/or impurities present. Figure 7 shows the weight gain versus time for liquid phase sintered Si_3N_4 [BAB83, SIN76a] and RBSN [POR84] for comparison. All samples were oxidized at ~1300°C, except RBSN-1100°C which was oxidized at 1100°C. The oxidation rate was strongly dependant on the type of Si_3N_4 under study. The general oxidation reaction is:

$$Si_3N_4 + 3\ O_2 = 3\ SiO_2 + 2\ N_2 \qquad \text{Eq. 1}$$

However, when impurities are present, a mixed glass phase forms instead of SiO_2. This mixed glass may have a lower viscosity and can have a significant effect on the oxidation rate. Full oxidation of Si_3N_4 to SiO_2 is accompanied by a 28.3% increase in weight.

The oxidation of liquid phase sintered Si_3N_4 probably depends on the diffusion rate of the cation impurities. An activation energy of 374 kJ/mole (~93 kcal/mole) was reported [SIN76a]. During oxidation the cations became concentrated in the outer SiO_2 layer. MgO and CaO increase the oxidation rate. This increase in oxidation rate was probably due to a lowering of the melting point of the glassy phase which increases the diffusion rate. Impurities can increase the oxidation rate by two orders of magnitude or more [BAB83].

Varying the N_2 and/or O_2 partial pressures had no effect on the oxidation rate of liquid phase sintered Si_3N_4 [SIN76a]. The velocity of the oxidizing gas over the sample had no effect on the oxidation rate of liquid phase sintered Si_3N_4 [SIN76a], however it did effect the oxidation rate of RBSN [MAE89, BAR79]. During oxidation of RBSN a SiO boundary layer forms which reduces the oxygen partial pressure at the surface and therefore favors internal oxidation of the RBSN.

Oxidation of RBSN is very dependent on the amount of open porosity [POR84]. Open porosity results in the effective surface area of the sample changing with time in a complex way. Open porosity allows oxygen to reach the interior of the sample. As oxidation continues, the SiO_2 which forms will slowly close the pores. The closing of the pores is accompanied by a sharp decrease in the oxidation rate.

Below 900°C the oxidation was parabolic with time and an activation energy of 198 kJ/mole (~50 kcal/mole) was reported [POR84]. At 1200°C, oxidation effectively stopped after 1.5 hours, due to the pores being closed by the viscous SiO_2 layer. At 1100°C the weight gain was faster than at 1200°C and the oxidation stopped after 8 hours. This increased oxidation at lower temperatures is due to the pores being open longer which allows more internal oxidation to occur, and therefore larger weight gains were reported.

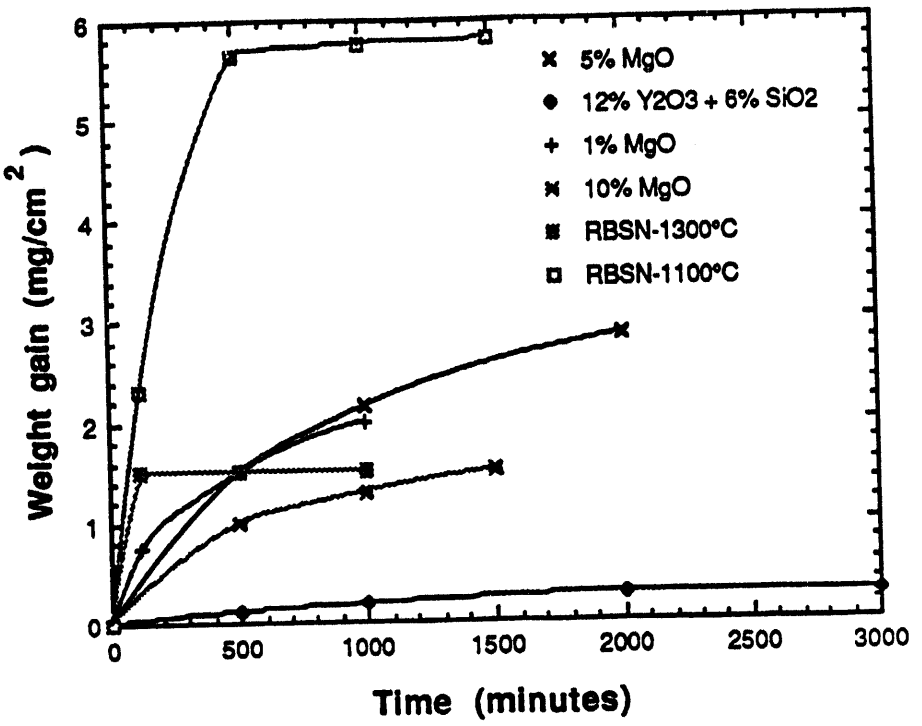

Figure 7. Plot of silicon nitride oxidation data [BAB83, SIN76a, POR84].

Oxidation of Silicon Carbide

Several studies dealt with the oxidation of SiC powders [ERV58, JOR59, JPR61]. For times less than 10 hours the oxidation of SiC powder was parabolic with time. At longer times the oxidation was faster, which was probably due to cracking of the SiO_2 surface film [ERV58]. Oxidation of SiC in air, O_2, and CO_2 showed the same behavior.

Figure 8 shows weight gain versus time for two types of sintered SiC [DUT84] in air and a hot pressed SiC [SIN76b] in dry oxygen. The oxidation of the sintered SiC was sensitive to the sintering aid, SiC-1 had no reported sintering aids and SiC-2 had B and C additions. The oxidation reaction is:

$$2\,SiC + 3\,O_2 = 2\,SiO_2 + 2\,CO \qquad \text{Eq. 2}$$

Complete conversion of SiC to SiO_2 is accompanied by a 49.9% increase in weight.

Impurities concentrate in the SiO_2 film. Above 1200°C the SiO_2 layer was crystalline and the activation energy increased, ~50 kcal/mole [JOR59]. This indicated that diffusion, probably molecular CO, through the SiO_2 film was rate controlling [JOR59, MIE84, FUN84]. At low oxygen partial pressures, less than 10^{-6} Pa, the protective SiO_2 film cannot form and volatile oxidation products result in rapid oxidation of SiC [WAR84].

The presence of water vapor in the oxidizing atmosphere increased the oxidation rate [WAR84, JOR61]. Hydrogen prevented the protective SiO_2 film from forming and increased the oxidation rate of SiC.

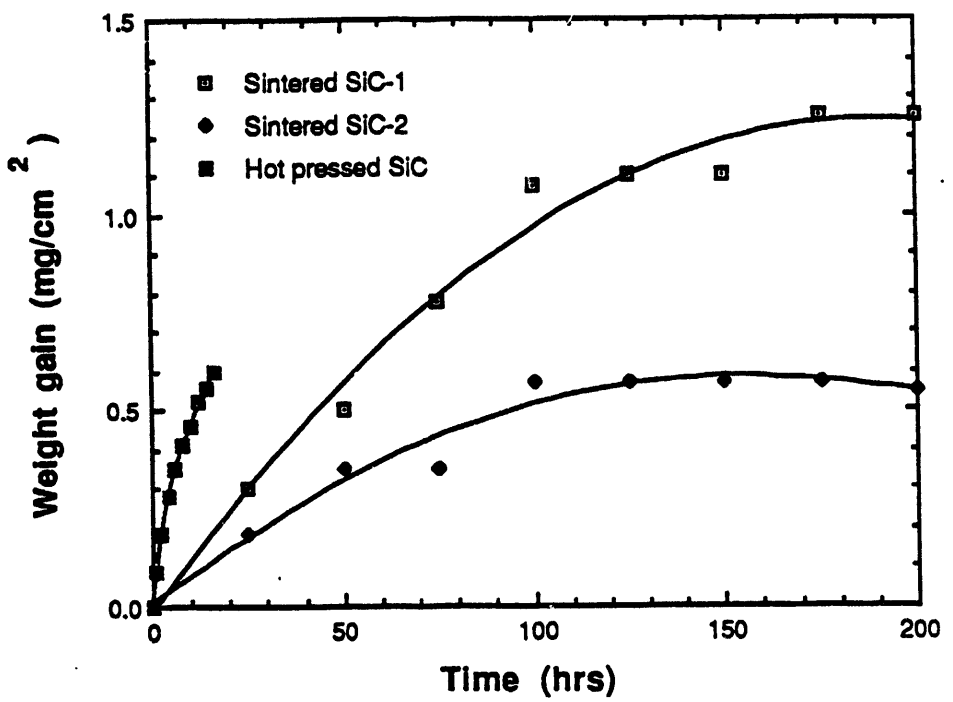

Figure 8. Plot of silicon carbide oxidation data [DUT84, SIN76b].

Oxidation of Aluminium Nitride

The oxidation of AlN is not clearly understood and the literature indicates that the "oxidation rate" of AlN has little meaning. The oxidation

rate must be determined for the specific oxidizing conditions the AlN part will experience. The reaction was very sensitive to the water content of the oxidizing atmosphere, which may explain the discrepancies between the different studies. Oxidation was faster in wet N_2 than in dry air [SAT87] and increased with increasing water partial pressure.

Oxidation starts at 800 - 1150°C. The weight gain began as a linear relationship with time and became parabolic with time. The parabolic rate constant had an activation energy of 60 - 65 kcal/mole [KAT87, LAV83], which is reasonable for a diffusional process. The probable reaction is:

$$4\ AlN + 3\ O_2 = 2\ Al_2O_3 + 2\ N_2 \qquad \text{Eq. 3}$$

NO_2 and aluminum oxynitride may also form. Complete conversion of AlN to Al_2O_3 is accompanied by a 24.4% increase in weight.

The weight gains due to oxidation are in the range of 0 - 10 mg/cm^2. Figure 9 is a plot of weight gain versus time for the data in references LAV83 and BOC82. Reference LAV83 studied the oxidation behavior of AlN in O_2 (at 900°C, 1000°C, 1050°C, and 1100°C) and reference BOC82 studied the oxidation behavior of AlN in air (at 1300°C, 1420°C, 1490°C, 1620°C, and 1680°C).

The Al_2O_3 oxide layer that formed was very adherent [BOC82]. Sato et al [SAT87] found that porous Al_2O_3 formed at low temperatures, 1250°C, and solid Al_2O_3 formed at high temperatures, 1400°C. However, Boch et al [BOC82] found that porous Al_2O_3 formed above 1600°C and solid Al_2O_3 formed below 1600°C. The reason for this disagreement is unclear.

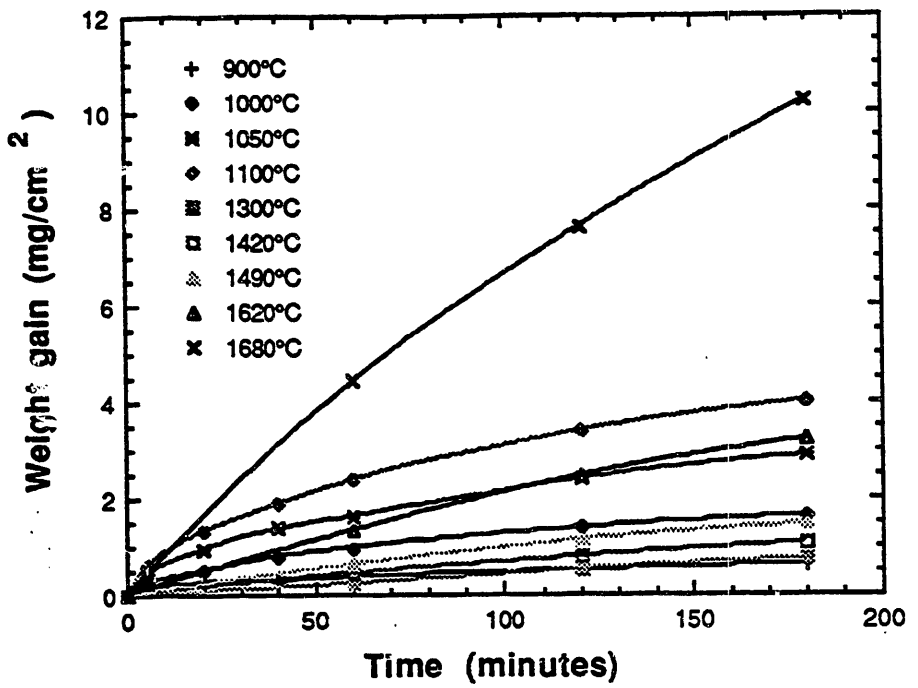

Figure 9. Plot of AlN oxidation data [LAV83, BOC82].

Oxygen Diffusion through Al_2O_3

The possibility of oxygen diffusion, either grain boundary or lattice, was theoretically evaluated. This was done by calculating the oxygen concentration in an Al_2O_3 coating as a function of temperature, time, and distance. The approach used was taken from Fisher [FIS51]. Three types of diffusion were included in the calculation: 1) diffusion from the surface down the grain boundary, 2) diffusion normal to the grain boundary into the grain, and 3) diffusion from the surface through the grain (bulk diffusion). Fisher's treatment was used for the first two types of diffusion, and the constant surface concentration solution to Fick's second law was used for the third type. For purposes of the calculation, the coating was treated as pure Al_2O_3.

Oxygen concentration profiles calculated at temperatures of 1100°C, 1200°C, 1300°C, 1400°C, and 1500°C for times up to 234 years (2,048,000 hours)

and diffusion distances of 0.5 microns, 1.0 micron, and 1.5 microns. The following parameters were used: grain boundary width = 5 x 10^{-8} cm, bulk diffusivity for oxygen in Al_2O_3 at 1500°C = 3.5 x 10^{-16} cm^2/s, grain boundary diffusivity of oxygen in Al_2O_3 at 1500°C = 5.0 x 10^{-15} cm^2/s, activation energy for oxygen lattice diffusion in Al_2O_3 = 152,000 cal/mole K, pre-exponential factor for oxygen lattice diffusion in Al_2O_3 = 1.9 x 10^3 cm^2/s, activation energy for oxygen grain boundary diffusion in Al_2O_3 = 57,600 cal/mole°K, pre-exponential factor for oxygen lattice diffusion in Al_2O_3 = 6.3 x 10^{-8} cm^2/s. The activation energies and pre-exponential factors were taken from Oishi and Kingery [OIS60]. The calculations indicated that, at 1200°C, the oxygen concentration 0.5 microns below the surface of the coating was less than 10^{-4} atomic per cent at 500 hours. At 1200°C and 1.0 micron below the surface, the oxygen concentration was zero after 500 hours and 1 x 10^{-2} atomic per cent after 8000 hours. At a depth of 1.5 microns at 1200°C, the oxygen concentration was 2 x 10^{-4} atomic percent after 8000 hours. The oxygen concentration only became significant for a depth of 1.5 microns and a temperature of 1500°C after 8000 hours. This combination of time and temperature is well beyond the anticipated service range of these coatings. Hence, these results suggest that the coating should not fail due to oxygen diffusion through an Al_2O_3 layer and that the composite layer is an adequate diffusion barrier.

Oxidation Testing

Oxidation tests of coated RBSN, SSC, and HSN were conducted with substrates measuring 1" x 0.25" x 0.02". For oxidation tests of coated sapphire the substrate size was 1" x 0.25" x 0.08". This sample size was selected to maximize the weight of the coating while minimizing the weight of the substrate, thereby increasing the magnitude of the weight gain due to oxidation and allowing for more sensitive weight gain measurements.

The oxidation treatments were done in a Lindberg box furnace, model 51314, in static air. The samples were weighed using a Mettler analytical balance with a readability of 1 μg and an accuracy of ~0.5 μg. After oxidation testing, some samples are analyzed by X-ray diffraction (XRD) to identify the oxidation products.

Coatings on Sapphire Substrates

Substrates of single crystal alumina (sapphire) were used to eliminate the contribution of substrate oxidation from the weight gain experiments. Three coating configurations were examined, AlN/sapphire, Al_2O_3/AlN/sapphire, and Al_2O_3+ZrO_2/AlN/sapphire, these were oxidized in static air at 1000°C, 1100°C, 1200°C, and 1275°C for up to 500 hours. The samples were periodically removed from the furnace and weighed (after 2, 8, 30, 125, and 500 hours). One sample was removed and set aside for X-ray diffraction analysis at each weighting. Due to flaking of the AlN coating, the weight gain as a function of time did not provide useful information, however, X-ray diffraction allowed the degree of AlN oxidation to be estimated.

AlN Coated Sapphire Substrates

Three samples with this coating configuration were examined at 1000°C for 2, 8, 30, 125, and 500 hour oxidation times. Table A-1 (in Appendix A) lists the times and weights gains of these samples, and Table A-2 (in Appendix A) shows the phases present after oxidation identified by XRD. The AlN coatings appeared to have flaked off during the oxidation treatments since the weight gains in Table A-1 did not increase with time. The flaking was attributed to poor adhesion between the AlN and the optically polished sapphire. The weight gain data is plotted versus oxidation time at 1100°C, 1200°C, and 1275°C in Figures A-1 - A-3 respectively.

XRD results indicated that some AlN was present in all of the samples up to 500 hours and Al_2O_3 formed with its c-axis perpendicular to the plane of the substrate. Two unidentified peaks of low intensity were found at 0.418 nm and 0.432 nm in all of the samples in Table A-1.

Al_2O_3/AlN Coated Sapphire Substrates

Three samples with this coating configuration were examined at 1100°C, 1200°C, and 1275°C for 2, 8, 30, 125, and 500 hour oxidation times. Table A-3 below lists the times and weights gains of these samples. The weight gains listed in Table A-3 were expected to increase with time but did not due to flaking of the coating.

X-ray diffraction of the oxidized samples (Table A-2) indicated that AlN was seen in some of the samples in Table A-3, however, the AlN peak intensity appeared to be reduced in the sample oxidized for 500 hours at 1100°C. Additional low intensity peaks were found indicating that AlON may be present.

The samples oxidized at 1200°C were similar to those oxidized at 1100°C except the AlN peak intensity was reduced after 125 hours, and at 1275°C the AlN peak intensity was reduced after 30 hours. In all of the samples discussed above the Al_2O_3 was present in the alpha form.

Al_2O_3+ZrO_2/AlN Coated Sapphire Substrates

Three samples with this coating configuration were examined at 1100°C, 1200°C, and 1275°C for 2, 8, 30, 125, and 500 hour oxidation times. Table A-4 lists the times and weights gains of these samples.

X-ray diffraction of the oxidized samples (Table A-2) indicated that AlN was seen in some of the samples in Table A-4. The AlN peak intensity was reduced in the samples oxidized for 2 hours and longer at 1100°C. The samples oxidized at 1200°C were similar to those oxidized at 1100°C except that the AlN peak intensity was not observed for oxidation times longer than 2 hours, and at 1275°C only a very faint AlN peak was detected after 2 hours. In all of the above samples α-Al_2O_3 was the predominate Al_2O_3 phase, however, χ-Al_2O_3 may have been present in the oxidized coatings. Also, both the orthorhombic and monoclinic forms of ZrO_2 were found in the oxidized and unoxidized coatings.

Oxidation Kinetics of Uncoated and AlN Coated Substrates

Results of the tests are summarized in Tables 3, A-5 and A-6 and Figures A-4 - A-21. The growth exponents listed in Table 3 were calculated by fitting the data to an equation of the form:

$$(\text{wt. gain, mg})^n = C * (\text{time, hr}) \qquad \text{Eq. 1}$$

where 'C' is a constant and 'n' is the growth exponent. A value of 2.0 for 'n' is typical of growth processes which are diffusion controlled.

In all of the oxidation tests, 3 samples were oxidized at each condition in Table 3. In the cases of large variability, samples with the highest weight gains are reported. The discrepancy between samples oxidized under identical conditions was thought to be due to flaking of the oxidized layer.

The weight gain versus time plots for the substrates with AlN coatings had two distinct regions (Figures A-4 - A-21). The first region lasted from 8 to 30 hours and was thought to be due to the rapid oxidation of the AlN layer. The second region exists at longer times and is essentially flat, was probably due to the oxidation of the substrate.

The results in Table 3 show that the oxidation of the AlN coating on SSC and HSN substrates had a growth exponent of ~2. This implies diffusion controlled oxidation at 1200°C and 1275°C. The growth exponent of the AlN coated substrates after the AlN coating was fully oxidized were 4 or higher. A growth exponent larger than 2 can be due to cracking of the oxidized layer or "ageing" of the oxide layer [MEI59]. Growth exponents of 1 are attributed to interface controlled kinetics.

Table 3. Summary of oxidation tests for uncoated and AlN coated RBSN, SSC, and HSN substrates. The tests were done in static air at 1200°C and 1275°C in a box furnace.

Sample	Number of Samples	Average Weight Gain ± 1 std. dev. (mg/cm^2)	Time to 100% AlN conversion (hrs)	Growth Exponent† ± 1 std. dev.
Uncoated RBSN				
1200°C	1	0.931	---	---
1275°C	2	0.994 ± 0.007	---	1.2 ± 0.1
Uncoated SSC				
1200°C	3	0.167	---	4.5 ± 0.4
1275°C	2	0.219 ± 0.039	---	1.6 ± 0.1
Uncoated HSN				
1200°C	3	0.279 ± 0.014	---	2.6 ± 0.2
1275°C	2	0.990 ± 0.007	---	2.2 ± 0.1
AlN/RBSN				
1200°C	3	0.334 ± 0.219	<30	1.0 ± 0.3
1275°C	1	2.736	<8	2.6
AlN/SSC				
1200°C	1	0.456	<30	2.1 ± 0.1
1275°C	2	1.511 ± 0.283	<8	1.9 ± 0.4
AlN/HSN				
1200°C	3	0.483 ± 0.091	<8	1.9 ± 0.1
1275°C	2	1.816 ± 0.057	<8	1.9 ± 0.3

† the growth exponents for the AlN coated substrates are only for oxidation times up to the "Time to 100% AlN conversion".

Phase Formation During Oxidation of Uncoated and Coated Substrates

The phases identified after the full 500 hours of oxidation on uncoated and AlN coated RBSN, SSC, and HSN are listed in Table A-5 for all temperatures tested. Uncoated RBSN was predominantly α-Si_3N_4 and tended to form SiO_2 when oxidized. Uncoated SSC consisted of predominantly the 8H and 12H polytypes and formed SiO_2 when oxidized. Uncoated HSN was predominantly β-Si_3N_4 and formed α-$Y_2Si_2O_7$, Y_2SiO_5, and SiO_2 when oxidized. The yittrium came from the grain boundary phase. Yttria was added to this material as a densification aid.

The oxidation of the AlN coated materials resulted in similar phase formation as the uncoated materials with the addition of Al_2O_3. The Al_2O_3 came from the oxidation of the AlN phase. No phases were identified that suggested a reaction between the AlN and Si_3N_4 or SiC.

The conventional coating (Al_2O_3+ZrO_2/AlN) was tested, along with Al_2O_3/AlN, Table A-6. The latter coating was evaluated to eliminate the effect of ZrO_2 to make the interpretation of the oxidation results simpler. ZrO_2 undergoes a phase transformation and 10% volume change at ~1200°C which may cause the coating to crack or flake.

The oxidation tests showed that all coating/substrate configurations failed at all temperatures. A post-failure analysis was initiated to determine the cause(s). One possibility was porosity in the oxide layer of the coating. Examination of as-grown coatings has shown a variety of features ranging from cauliflower shaped clusters of grains to faceted grains. Examination of the cauliflower shaped clusters at 5000x shows the presence of large gaps between clusters. Due to the thinness of the oxide layer of the coating (typically less than 2 microns), these gaps could penetrate to the AlN layer. An attempt was made to determine if AlN was exposed by doing a nitrogen map using an electron microprobe analyzer. Two samples were examined, and neither gave a nitrogen signal, suggesting that the Al_2O_3+ZrO_2 coating was continuous. However, the sensitivity of the microprobe to nitrogen was ~3 weight per cent and the detection limit for gaps was ~1 micron ; i.e., only gaps larger than 1 micron could be detected.

The results indicate that the current coating configuration is not oxidation resistant for 500 hours at temperatures above 1000°C. The lack of

protection is attributed to cracks in the $Al_2O_3+ZrO_2$ layer, which allow oxygen to penetrate and react with AlN. The kinetics of oxidation of AlN are sufficiently slow at 1000°C for the coating to protect the substrate for 500 hours. However, above 1000°C, the oxidation rate of AlN is rapid enough to cause the AlN to fully oxidize to Al_2O_3 before 500 hours. This oxidation is accompanied by further cracking, which in turn increases the oxidation of the substrate. The cause of cracking in the $Al_2O_3+ZrO_2$ layer is large residual stress due to thermal expansion mismatch between Al_2O_3 or ZrO_2 and Si_3N_4 or SiC. The stress in the $Al_2O_3+ZrO_2$ layer is approximately 1900 MPa for a Si_3N_4 substrate and 1300 MPa for a SiC substrate, which is well in excess of the fracture strength of the $Al_2O_3+ZrO_2$ layer. Physical vapor deposition (PVD) methods, which allow the residual stress state to be controlled, or low temperature CVD processes may allow for crack-free coatings to be deposited. When these coatings are heated to 1200°C the stress in the coatings would be compressive and they would not crack, although they may fail by buckling. The thermal stress and coating cracking problems are addressed in a following section.

Contact Stress Testing

The contact stress testing from Phase I of the program was completed by Garrett Turbine Engine Company. Twenty coated MOR bars (dimensions 2" x 1/4" x 1/8") and pins of each substrate (RBSN, SSC, and HSN) were tested for contact stress using point sliding contact. The test procedure was described elsewhere [SCH87]. Each sample had a ~5 micron thick AlN intermediate layer and a 1 micron thick outer layer of $Al_2O_3+ZrO_2$ composite. The coated MOR bars were oxidized in static air at 1200°C for 100 hours before application of the contact stress. After oxidation, the composite coatings exhibited good adherence to the RBSN and SSC substrates and poor adherence to the HSN substrates. Flexure strength (using 4-point bending) was measured after application of the contact stress. The friction coefficient was also calculated by Garrett.

Tables 4 - 6 show the strength loss and maximum friction coefficient measured for each set of conditions. The "As-coated strengths" were taken from samples that were oxidized at 1200°C for 500 hours and tested at 25°C and

from unoxidized samples tested at 1000 and 1200°C. These measurements were made at GTE on a separate set of samples. All samples contact stress tested showed a strength loss of 30 - 50%. The increase in strength of the HSN samples tested at 1200°C (see Table 5) is not understood.

It was previously reported [DAN89] that the $Al_2O_3+ZrO_2$ coatings flaked off the substrates and that the samples were fully oxidized after 100 hours of oxidation at 1200°C. Based on the previous oxidation data and the multiple factors involved in the contact stress testing (oxidation, contact stress, and variable friction), no firm conclusions are drawn from this contact stress data.

Table 4. Summary of contact testing and post-contact MOR strength testing for CVD coated RBSN.

Test Temp. (°C)	Applied Load (lbs)	Max. Friction	As-Coated Strength (MPa)	Retained Strength (MPa)	Contact Damage	Change in Strength (%)
25	25	0.44	197	154	yes	-22
"	"	0.47	"	157	yes	-20
"	"	0.54	"	137	yes	-30
"	50	0.35	"	188	yes	-5
"	"	0.43	"	130	yes	-34
"	"	0.37	"	124	yes	-37
"	60	0.50	"	116	yes	-41
"	"	0.48	"	119	yes	-40
"	"	0.45	"	131	yes	-34
1000	25	1.36	245	150	yes	-39
"	"	1.65	"	137	yes	-44
"	50	0.82	"	164	yes	-33
"	"	0.63	"	115	yes	-53
1200	25	1.02	224	90	yes	-60
"	"	1.03	"	105	yes	-53
"	50	0.94	"	92	yes	-59
"	"	0.81	"	95	yes	-58

Table 5. Summary of contact testing and post-contact MOR strength testing for CVD coated HSN.

Test Temp. (°C)	Applied Load (lbs)	Max. Friction	As-Coated Strength (MPa)	Retained Strength (MPa)	Contact Damage	Change in Strength (%)
25	50	0.81	520	267	yes	-49
"	"	0.43	"	564	no	+8
"	"	0.69	"	330	yes	-37
"	60	0.71	"	318	yes	-39
"	"	0.72	"	322	yes	-38
"	"	0.65	"	368	yes	-29
"	75	0.54	"	334	yes	-36
"	"	0.71	"	310	yes	-40
"	"	0.67	"	316	yes	-39
1000	50	0.60	557	316	yes	-43
"	"	0.68	"	--*	---	---
"	75	0.87	"	--*	---	---
"	"	0.85	"	109	yes	-80
1200	50	0.36	393	466	no	+19
"	"	0.48	"	453	no	+15
"	75	0.43	"	531	no	+35
"	"	0.42	"	545	no	+39

* Tested improperly

Table 6. Summary of contact testing and post-contact MOR strength testing for CVD coated SSC.

Test Temp. (°C)	Applied Load (lbs)	Max. Friction	As-Coated Strength (MPa)	Retained Strength (MPa)	Contact Damage	Change in Strength (%)
25	40	0.23	328	248	yes	-24
"	"	0.48	"	180	yes	-45
"	"	0.50	"	209	yes	-36
"	50	0.35	"	195	yes	-41
"	"	0.49	"	178	yes	-46
"	"	0.30	"	192	yes	-41
"	60	0.55	"	202	yes	-38
"	"	0.76	"	183	yes	-44
"	"	0.51	"	162	yes	-51
1000	40	0.59	258	172	yes	-33
"	"	0.69	"	173	yes	-33
"	60	0.45	"	165	yes	-36
"	"	0.49	"	152	yes	-41
1200	40	0.85	320	141	yes	-56
"	"	0.89	"	115	yes	-64
"	60	0.64	"	169	yes	-47
"	"	0.91	"	155	yes	-52

Friction Coefficient Tests

Self-mated sliding wear tests have been carried out at room temperature with uncoated and coated samples. In the tests of uncoated substrates the pin and disk were of the same material. In the tests of coated substrates the pin and disk were both coated. These samples included RBSN, SSC, and hot-pressed silicon nitride (HPSN). Hot-pressed material was used in place of hot isostatically pressed material (HSN) for this study due to the availability of HPSN of the proper size for fabricating into pins and disks.

Tests were conducted using a pin-on-disk set-up, Figure 10. The tip of the pin is spherical, which gives similar results to those obtained in a ball-on-disk test. The testing procedure is based upon the conditions used for the VAMAS round-robin on wear test methods [RUF89]. Tests are carried out in air with an applied force of 10 N and a sliding velocity of 0.01 m/s.

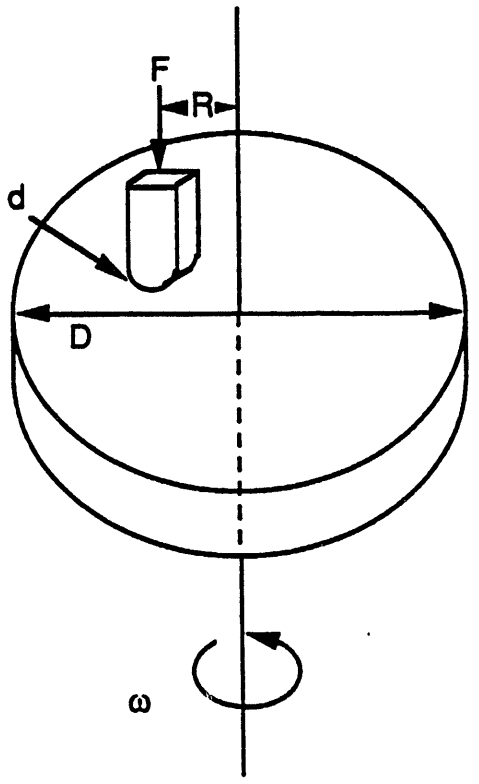

Figure 10. Schematic of pin-on-disk wear test system. F is the normal force on the pin, d is the pin diameter, D is the disk diameter, R is the wear track radius, and ω is the rotation velocity of the disk.

Table 7 summarizes the friction results obtained. The breakaway friction coefficients were measured prior to wear testing on surfaces polished to a 1 micron finish. The values reported for the kinetic friction coefficients are the steady state values obtained after 500 meters of sliding. These results show that in some instances the $Al_2O_3+ZrO_2$ coatings reduce friction. A significant reduction in kinetic friction value is obtained in the case of HPSN and RBSN, while no apparent benefit is observed with SSC at room temperature. The results at 1000°C were not sufficient to determine coating performance. The wear surfaces of uncoated HPSN, RBSN, and SSC are shown in Figure 11 and the wear surfaces of coated HPSN, RBSN, and SSC are shown in Figure 12. Figure 11 shows the worn pin and disk surfaces of uncoated ceramics after 500 meters of sliding contact. The spherical tip of the pins develop a circular wear scar, the extent of which is a measure of wear resistance. Coating the pin and disk materials leads to a noticeable improvement in wear resistance for HPSN as seen by the reduced wear scar on the pin and the polished wear track surface of the disk, Figure 12. The RBSN and the SSC materials were not protected as effectively by the coating, which is in part attributed to the poor adhesion of these coatings to the substrates. The wear results obtained with coated materials do agree with the lower kinetic friction results for HPSN and RBSN in Table 7.

Table 7. Results from pin-on-disk friction tests of uncoated and Al_2O_3+ZrO_2/AlN coated RBSN, HPSN, and SSC. All tests were done on self-mated samples. Reported values, unless otherwise indicated, are an average of three tests on the same pair of samples.

Material	Test Temperature (°C)	Breakaway Friction Coefficient	Kinetic Friction Coefficient	
			initial	after 1 km
RBSN				
uncoated	25	0.10	0.5	0.8
coated	25	0.17	0.3	0.4
HPSN				
uncoated	25	0.3	---	0.8
uncoated	1000	0.15	0.5	0.9*
coated	25	0.14	0.3	0.4
SSC				
uncoated	25	0.1	---	0.3
uncoated	1000	0.25	0.5	0.7
coated	25	0.17	0.3	0.4

* only 1 sample has been tested at this condition.

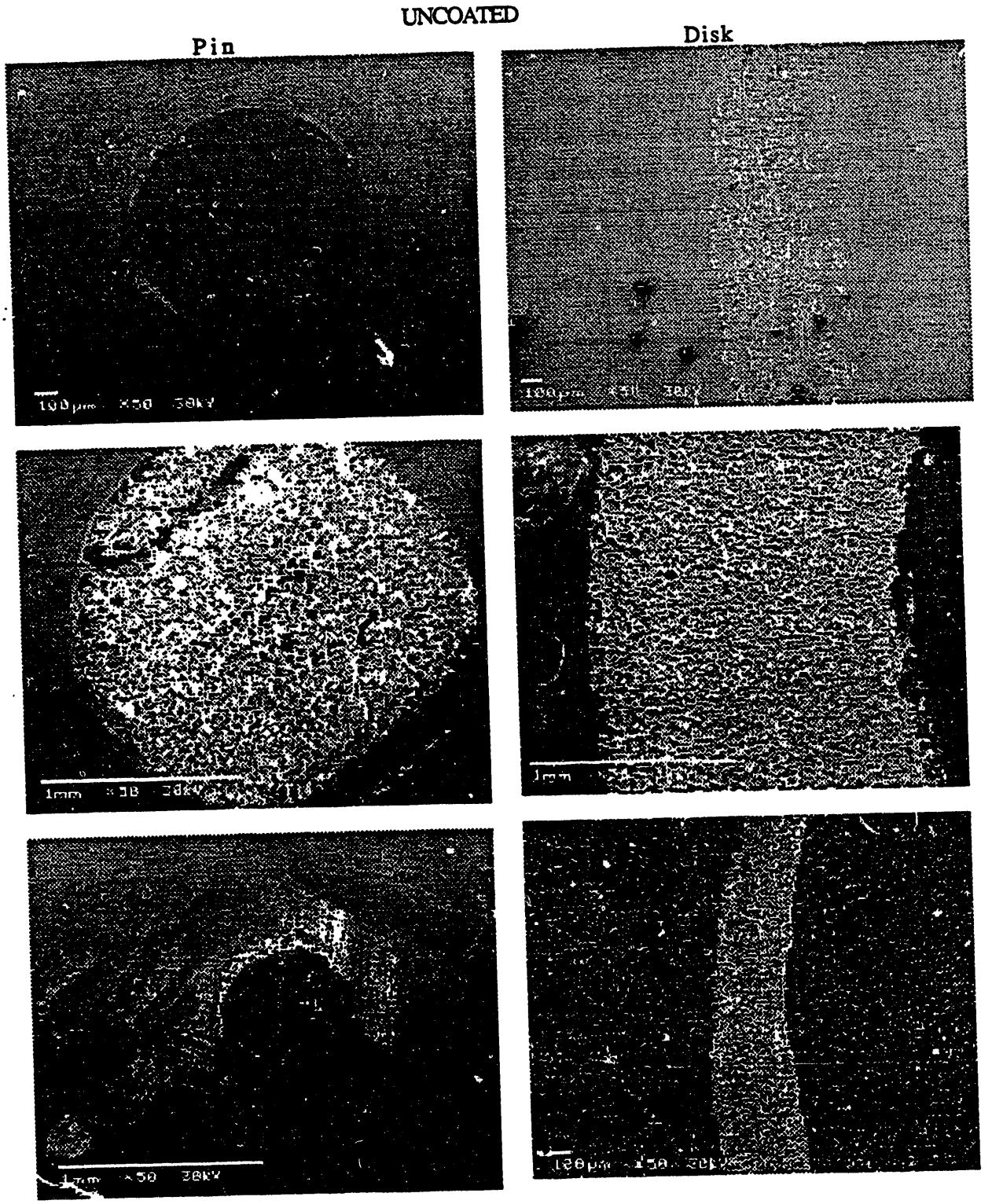

Figure 11. Wear tracks on the pins and disks for uncoated HPSN (top), RBSN (middle), and SSC (bottom), after a sliding distance of 500 meters at a sliding velocity of 0.01 m/s.

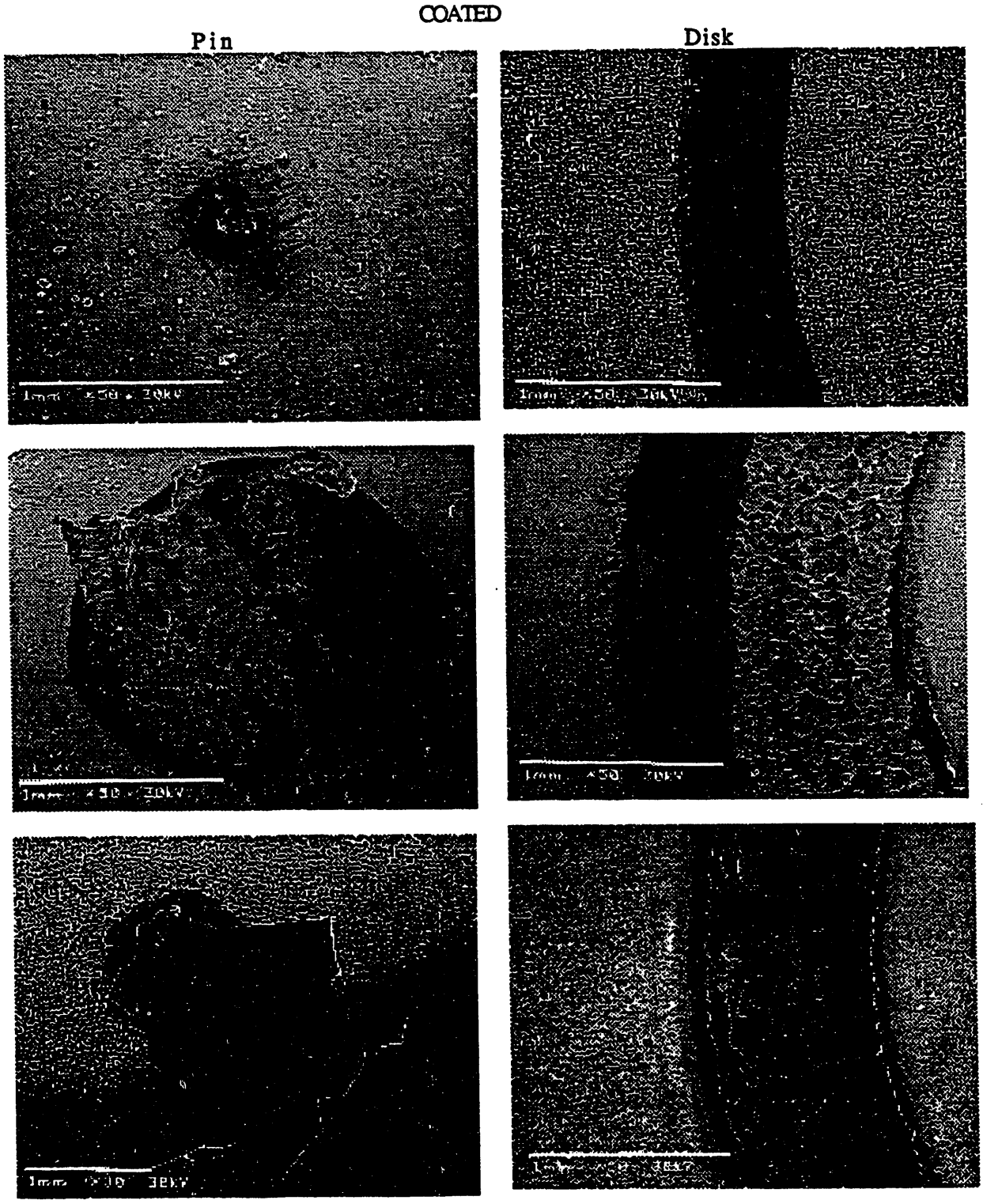

Figure 12. Wear tracks on the $AlN/Al_2O_3+ZrO_2$ coated pins and disks for HPSN (top), RBSN (middle), and SSC (bottom), after a sliding distance of 500 meters at a sliding velocity of 0.01 m/s.

Scratch Tests

In a scratch test a diamond indenter (Rockwell C) is drawn over a sample at a constant velocity while the normal force is monotonically increased (0 to 100 N). An acoustic pick-up is attached to the sample holder and both the force and acoustic signals are recorded during the test.

The uncoated and Al_2O_3+ZrO_2/AlN coated disks of HSN, RBSN, and SSC from the pin-on-disk wear tests were scratch tested. Figures 13 - 18 show the load, acoustic emission, and wear traces for each sample. Several points can be made from these figures. The force traces of the uncoated and coated samples were similar with the exception of uncoated SSC, which showed several large load drops. In general, the acoustic emission of the coated samples was less than the acoustic emission of the uncoated samples. Acoustic emission is regarded as an indicator of substrate cracking. The scratches themselves are very informative and vary from sample to sample. The individual samples are discussed below.

Cracking of the uncoated SSC disk began at ~40 N (Figure 13). As the force increased the cracking became massive failure of the SSC disk. The coated SSC disk (Figure 14) had a lower acoustic signal than the uncoated SSC disk, indicating that the coating protected the SSC substrate from damage. The scratches on the uncoated and coated SSC are very different. The uncoated SSC showed massive cracking and chipping, while the coated SSC showed no chipping and less cracking. The major damage to the coated SSC was in the form of flaking of the coating in the scratch track beginning at ~30 N, indicating low adhesion of the coating to the SSC.

Vent cracks began to form in the uncoated RBSN disk ~30 N (Figure 15). As the force increased the size of the vent cracks increased, however, the RBSN did not chip. The coated RBSN disk (Figure 16) had a lower acoustic signal than the uncoated RBSN disk indicating that the coating protected the RBSN substrate from damage. The scratches on the uncoated and coated RBSN were similar. The major damage to the coated RBSN was in the form of flaking of the coating in the scratch track beginning at very high forces, ~90 N, indicating high adhesion of the coating to the RBSN.

Uncoated HSN behaved differently than the SSC and RBSN (Figure 17). HSN did not exhibit massive chipping (like SSC) or vent crack formation (like

RBSN). The uncoated HSN failed at a high force, ~90 N, by small scale chipping at the edge of the scratch track. The coated HSN (Figure 18) was similar to the coated RBSN. The coated began to flake at ~50 N. However, the flaking was not continuous at forces greater than 50 N. The discontinuous nature of the flaking may be related to processing defects in the coating.

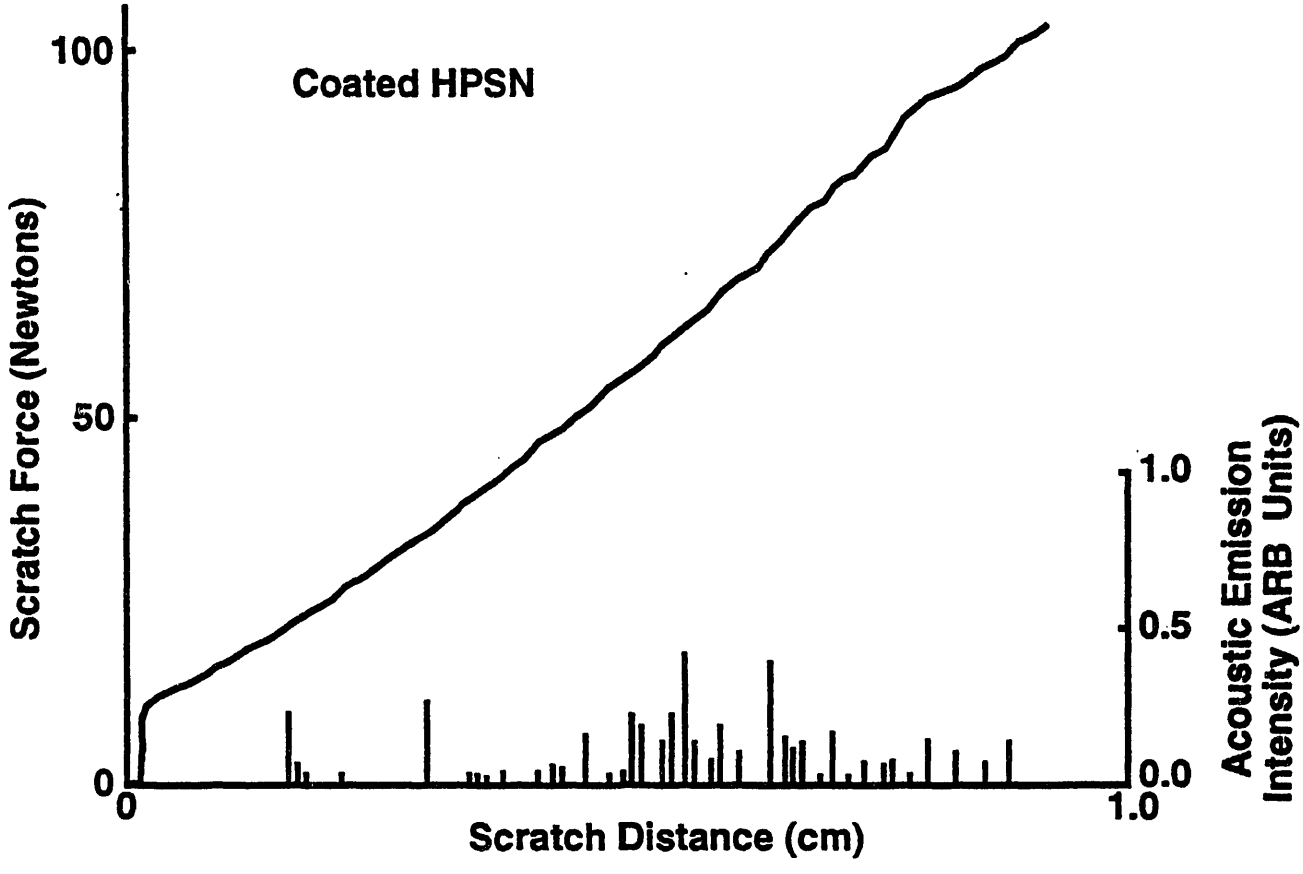

Figure 13. Scratch test results of uncoated HSN. The load trace is the solid line (left axis) and the acoustic signal is represented by the spikes (right axis).

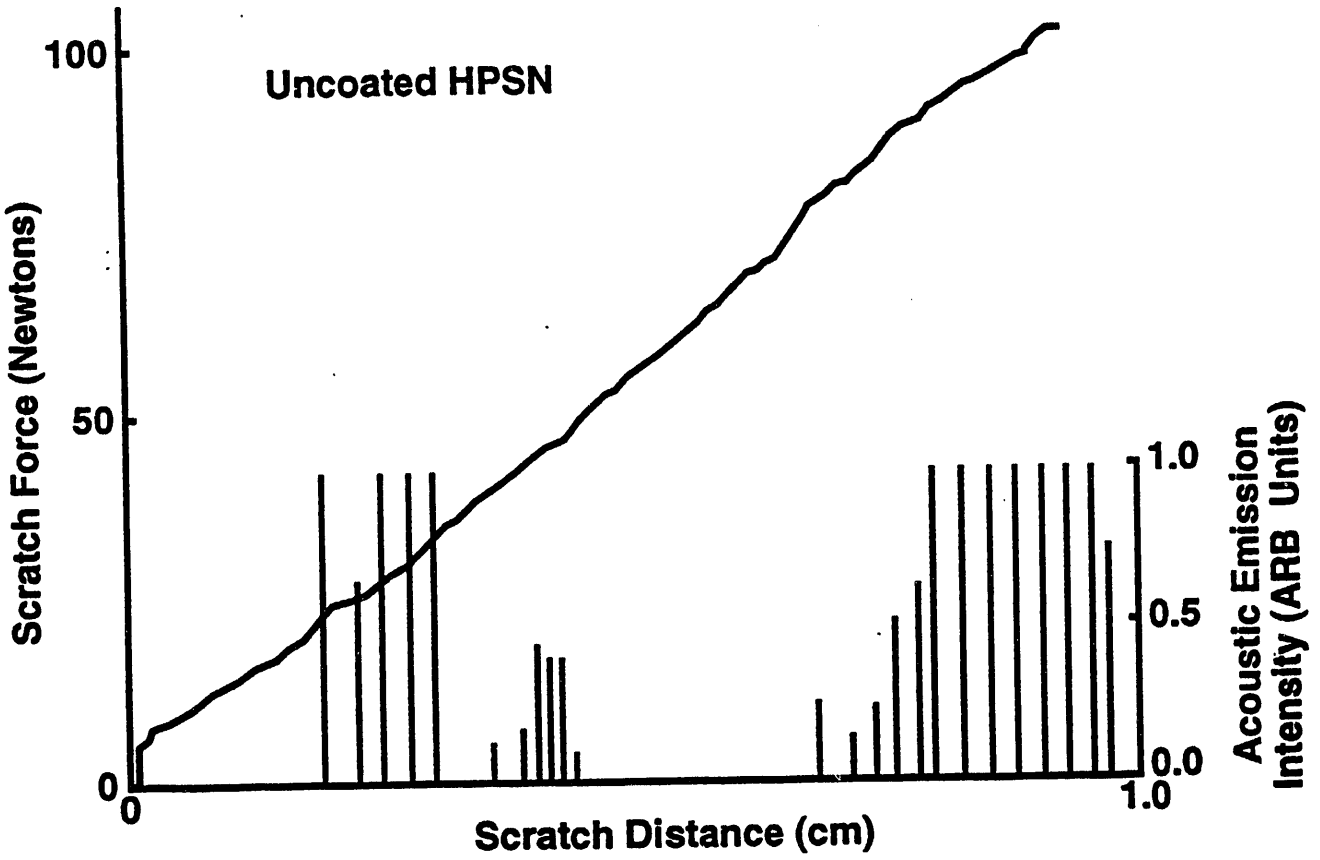

Figure 14. Scratch test results of coated HSN. The load trace is the solid line (left axis) and the acoustic signal is represented by the spikes (right axis).

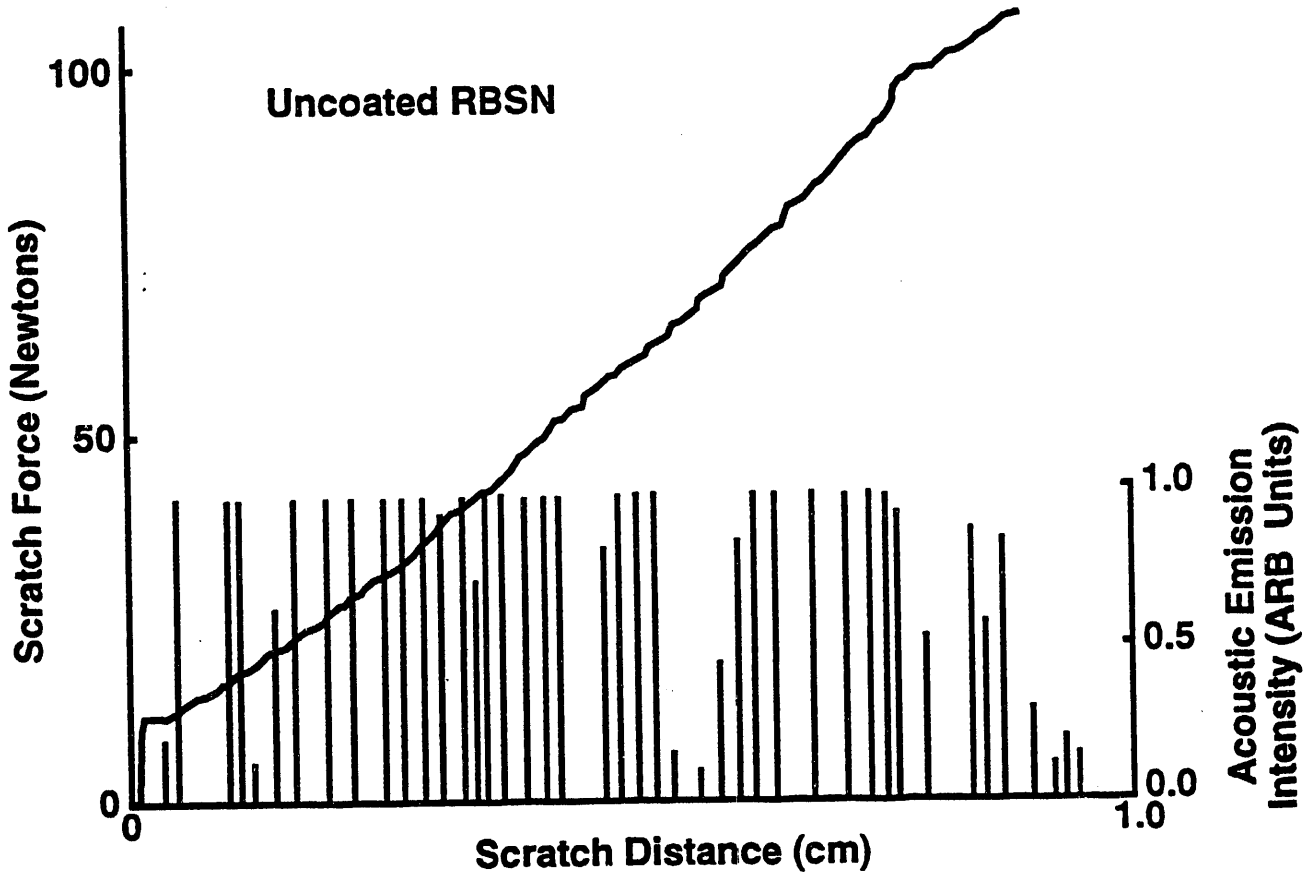

Figure 15. Scratch test results of uncoated RBSN. The load trace is the solid line (left axis) and the acoustic signal is represented by the spikes (right axis).

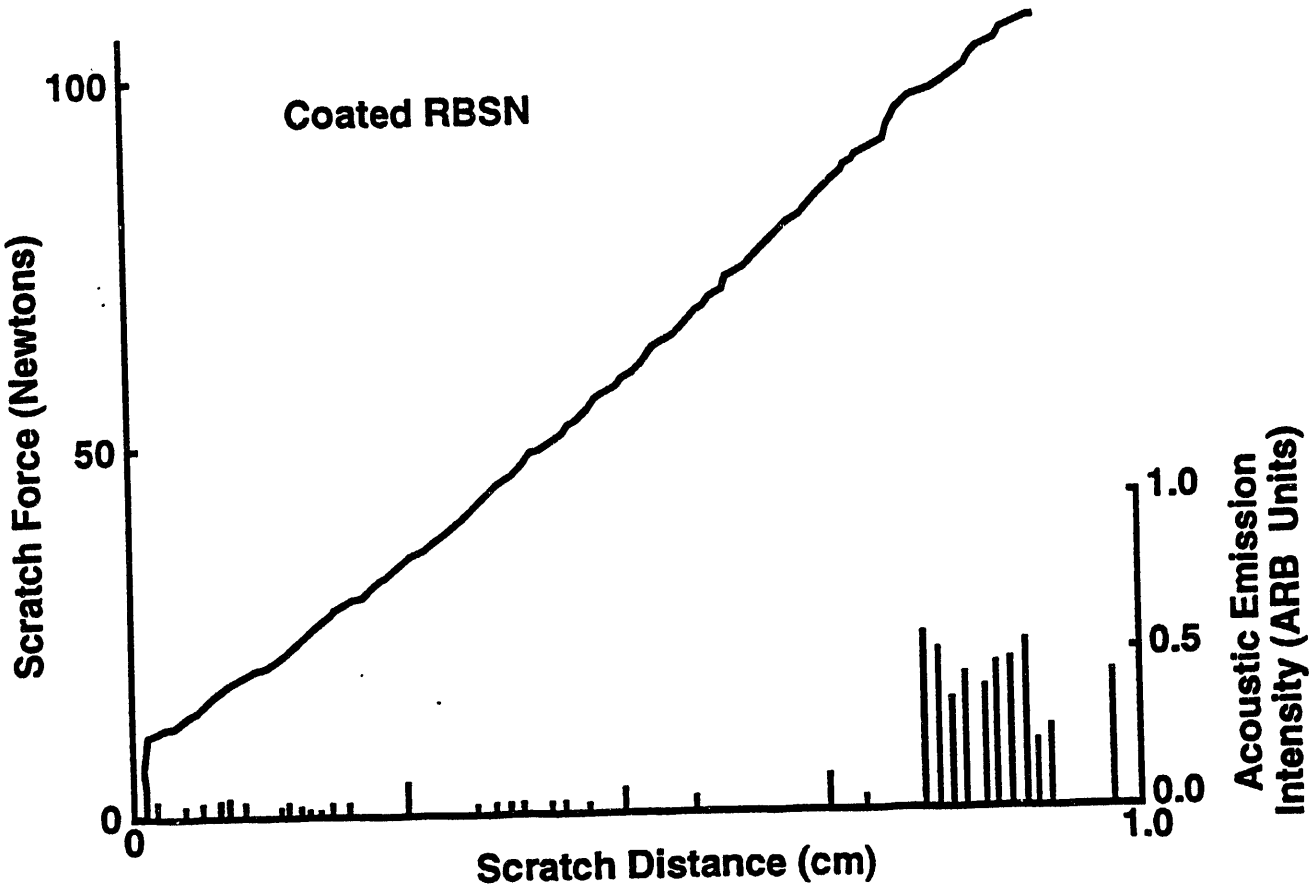

Figure 16. Scratch test results of coated RBSN. The load trace is the solid line (left axis) and the acoustic signal is represented by the spikes (right axis).

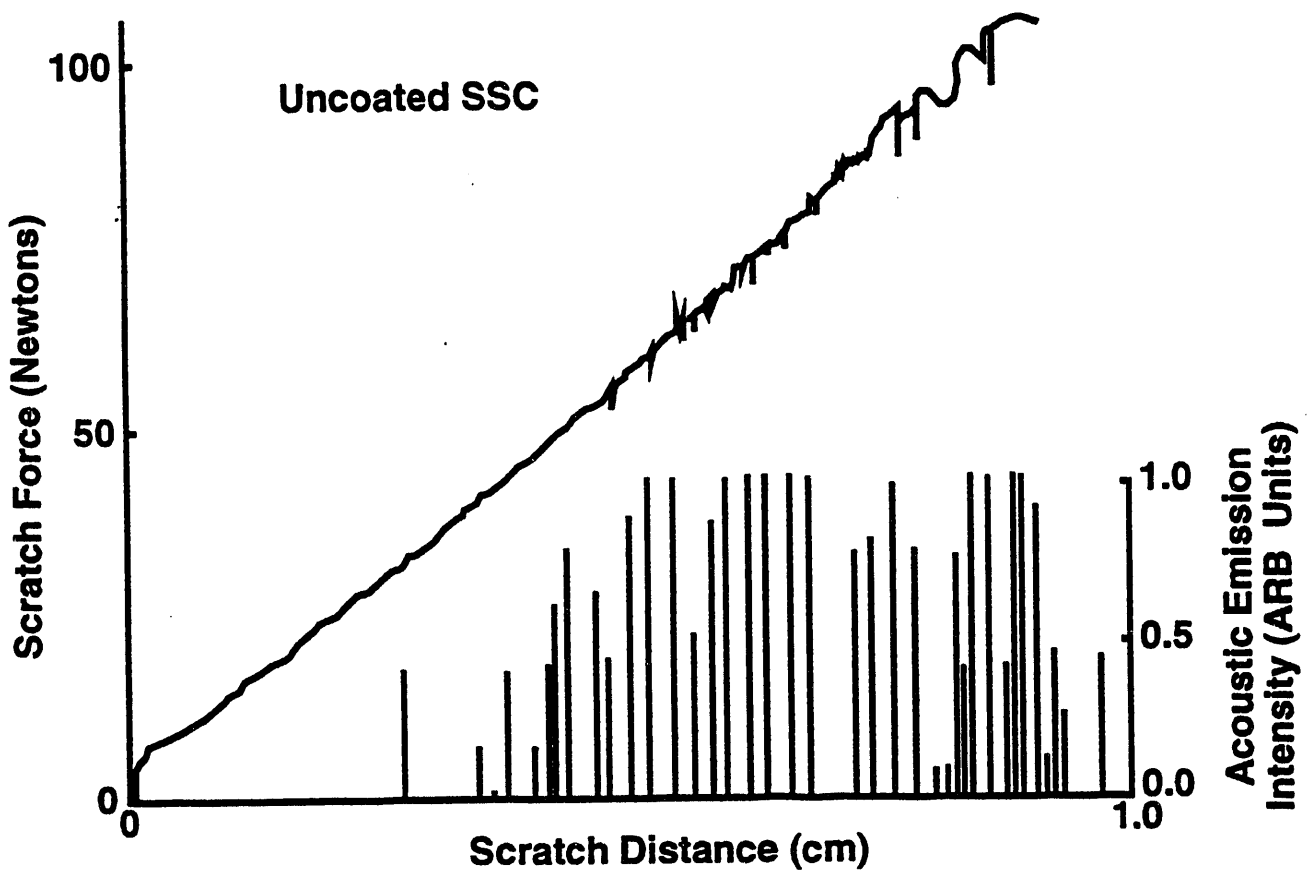

Figure 17. Scratch test results of uncoated SSC. The load trace is the solid line (left axis) and the acoustic signal is represented by the spikes (right axis).

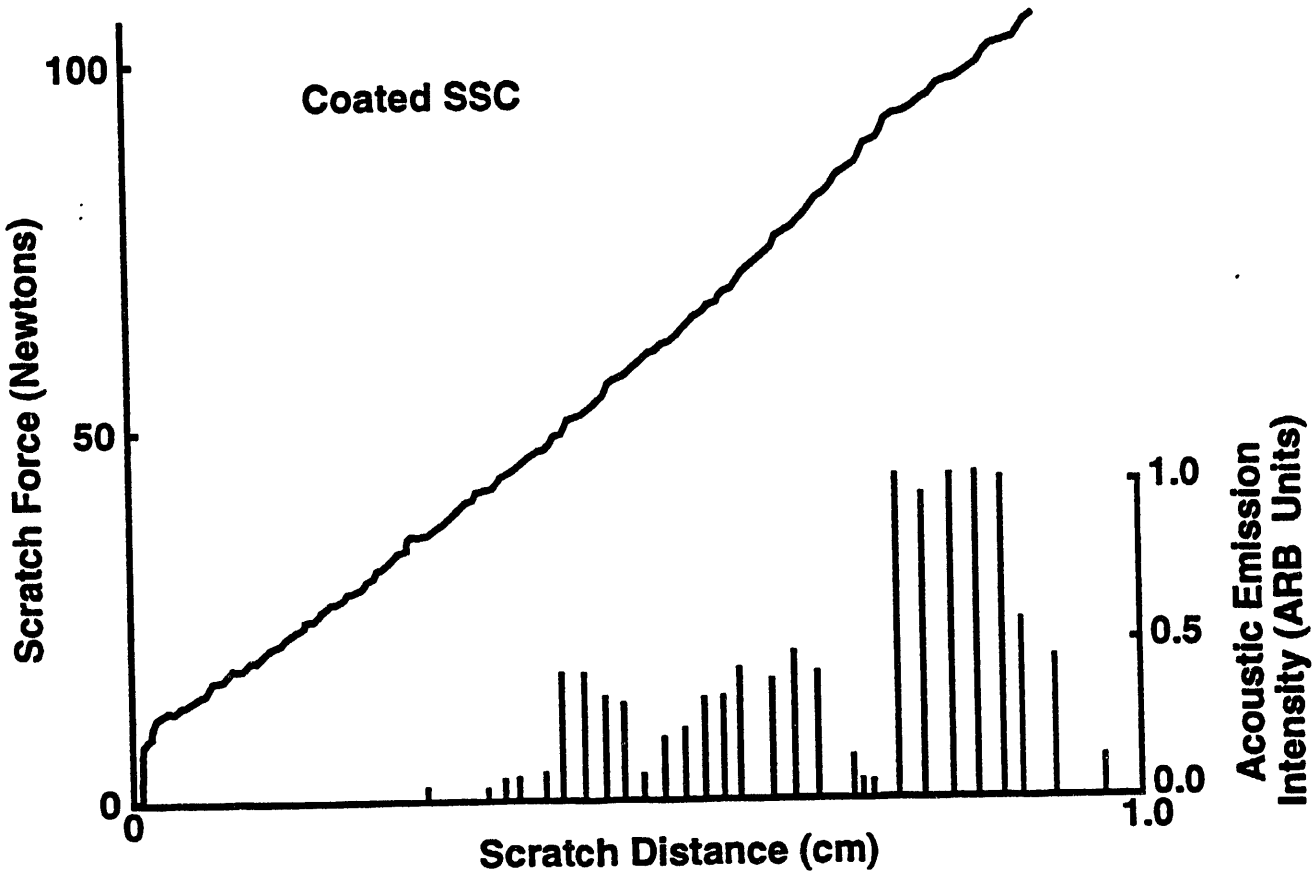

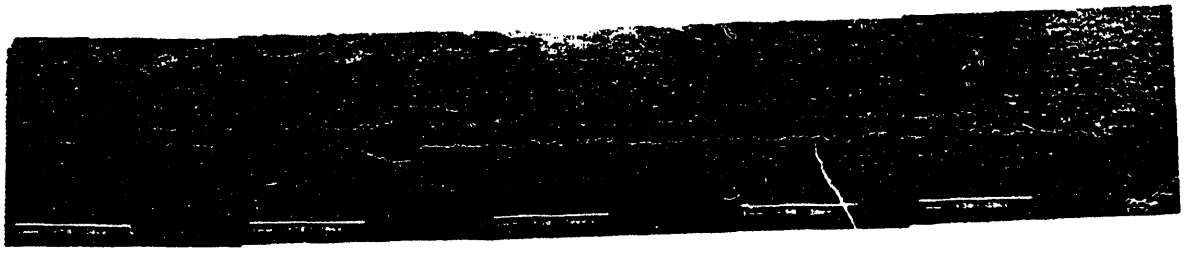

Figure 18. Scratch test results of coated SSC. The load trace is the solid line (left axis) and the acoustic signal is represented by the spikes (right axis).

Measurement of Fracture Stress and Toughness of Coatings on Substrates

Conventional mechanical property measurement techniques usually cannot be applied to thin ceramic coatings because of the small amount of material involved. A method is described to determine the ultimate tensile strength, Weibull modulus, and crack density of micron-sized ceramic coatings. This technique is based on measuring the radius of curvature of a coated substrate, and equating the resulting calculated stress with a theoretical shear-lag stress distribution model. The Weibull modulus and fracture stress of chemical vapor deposited coatings of Al_2O_3 have been measured on SiC and Si_3N_4 substrates. The fracture stresses for coatings of these materials ranged from 190 MPa to 480 MPa, the Weibull modulus ranged from 16 to 28, and the fracture toughness ranged from 0.5 - 1.1 $MPa\sqrt{m}$. These results are summarized in Table 8. This work has shown that the tensile strength of Al_2O_3 and $Al_2O_3+ZrO_2$ coatings can be approximated by bulk values, however, the fracture toughness of these coatings was found to be significantly lower than bulk values. This method is detailed in Appendix B.

Table 8. Calculated fracture stress, fracture toughness, and Weibull modulus for Al_2O_3 and $Al_2O_3+ZrO_2$ coatings.

Sample (coating/substrate)	Temp.of First Cracking (°C)	Fracture Stress, σ_f (MPa)	Fracture Toughness, K_{Ic} ($MPa\sqrt{m}$)	Weibull Modulus
Al_2O_3/SiC				
Inconel reactor	800	190	0.5	19
Graphite reactor	770	240	0.5	28
Al_2O_3+5 v/o ZrO_2	590	480	1.1	16

COMPUTER MODELLING OF BRITTLE COATINGS

COMPUTER SIMULATION OF RESIDUAL STRESS

Numerical models were developed to predict residual stresses in the coating and substrate. The goal was to develop a model with predictive capability which could be used to determine the optimum thickness of each layer.

In coatings deposited at elevated temperatures, where the coating and substrate materials have different coefficients of thermal expansion (CTE), large stresses are generated in the coating after cooling to room temperature. Figure 19 shows CTE values for the materials in this study. If tensile, these stresses often lead to cracking of the coating. The stress component we are most concerned with is the in-plane normal stress away from the edges of a coated sample. The word "stress" is used here to describe this component.

As a coated substrate is cooled, stresses build-up in the coating. For most ceramic coatings these stresses can be described by elastic relationships. Because the coating is often a ceramic, it has a distribution of fracture strengths. Once the fracture stress of the weakest part of the coating is reached, the coating will crack. The coating will not crack again until it is cooled further because of the distribution of failure strengths and because the remaining uncracked coating has a smaller volume and therefore a higher failure strength.

In phase I conventional FEA was used to predict residual stresses for the case of AlN coatings on pure Si_3N_4 and SiC substrates. The model assumed linear elastic behavior, constant physical properties within a coating layer, and zero deposition stresses. Calculations for 10 micron thick coatings gave residual stresses which oscillated between elements, regardless of mesh pattern. This was found to be caused by the large aspect ratios of the finite elements. Consequently, a technique for varying the mesh size was incorporated [SHA88]. The model was used to predict edge effects (Figure A-2).

One drawback of the second generation model was that the predicted stress was insensitive to edge effects. In addition, the model used 90° angles at corners. In an effort to overcome these problems, the model was modified to use a hybrid-stress technique [SHA88].

In phase II, a generalized treatment of the thermal expansion mismatch problem was carried out. In addition, finite element analysis involving the complex combination of thermal stress, linear elastic fracture mechanics and fracture mechanics of bimaterial interfaces was implemented. This work was based on contact stress issues for ceramic coatings. The method has been applied to the single and multilayer coatings of this study and deal with the presence of pre-existing flaws which are in the form of vertical or horizontal cracks. The driving force for crack initiation and propagation stems from thermal loads and a resultant normal load which simulates single point contact. The following sections describe theory and results of the newly developed technique.

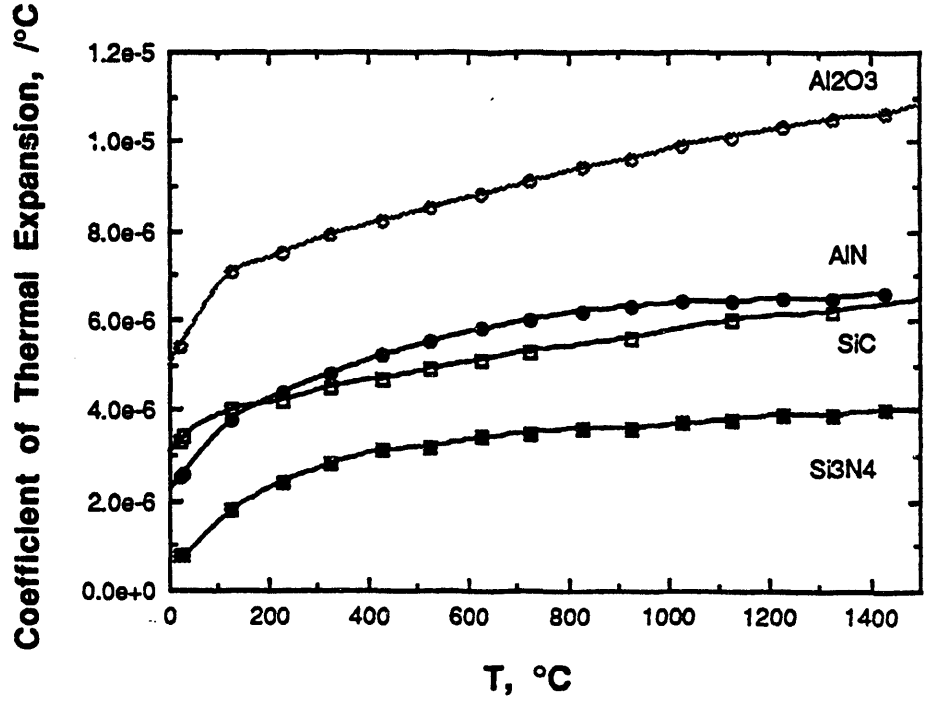

Figure 19. Thermal expansion coefficients of the various materials present in this system over the temperature range 25°C to 1500°C.

Simple Beam Theory

The in-plane stress in a narrow bimaterial strip generated by a change in temperature was derived by Timoshenko [TIM25].

$$\frac{1}{\rho} = \frac{(\alpha_2 - \alpha_1)(T_d - T_i)}{\frac{t}{2} + \frac{2(E_1 I_1 + E_2 I_2)}{t}\left(\frac{1}{E_1 t_1} + \frac{1}{E_2 t_2}\right)} \qquad \text{Eq. 2}$$

$$\sigma_{max} = \frac{1}{\rho}\left(\frac{2}{t t_1}(E_1 I_1 + E_2 I_2) + \frac{t_1 E_1}{2}\right) \qquad \text{Eq. 3}$$

where ρ is the radius of curvature, α is the coefficient of thermal expansion, T_i is the final temperature, T_d is the initial temperature, "E" is the elastic modulus, "I" is the moment of inertia, "$t_{1,2}$" is the layer thickness, and "t" is the total thickness ($t=t_1+t_2$). More details are given in Appendix B. For systems of interest in this study a coating is thin if it less than 10% of the substrate. Figure 20 shows the bending and axial contributions to the stress in a coating. The coefficient of thermal expansion and elastic modulus of the materials are treated as temperature dependent quantities and Equations 2 and 3 are numerically integrated over temperature range (T_d to T_i) to solve for the stress in the coating. The treatment of the coefficients of thermal expansion as temperature *independent* constants can lead to significant errors in materials where these coefficients are strong functions of temperature. An example of such a material is diamond.

The stresses in AlN and Al_2O_3 coatings deposited onto SiC and Si_3N_4 at 1000°C are shown as a function of cooling temperature in Figure 21. Al_2O_3 coatings on SiC and Si_3N_4, and AlN coatings on Si_3N_4 have very large stresses at room temperature, while AlN has only moderate stress level at room temperature. Based on these calculated stresses the Al_2O_3 coatings would be expected to be cracked at room temperature. The presence of cracks in the Al_2O_3 coating has obvious consequences for the ability of the coating to act as an oxidation barrier for the substrate.

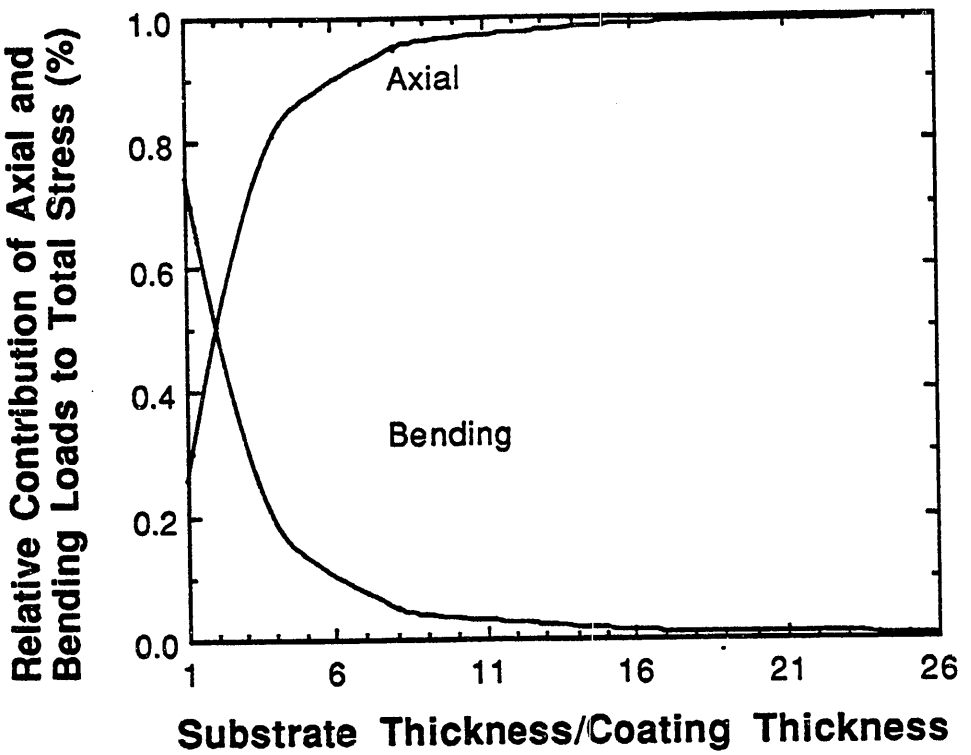

Figure 20. At coating thicknesses less than 10% of the substrate thickness most of the stress in the coating is due to the axial component and is therefore independent of the coating and substrate thicknesses.

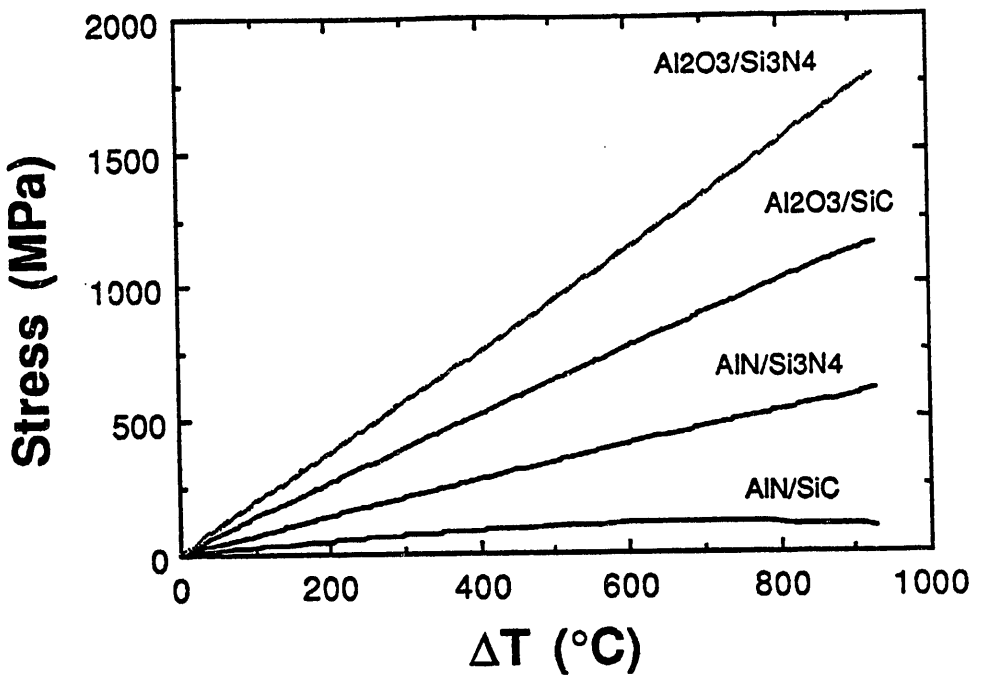

Figure 21. Stress in coating versus ΔT for AlN coatings on SiC and Si_3N_4, and Al_2O_3 coatings on SiC and Si_3N_4.

Composite Plate Theory

The method follows the flow chart illustrated in Figure 22. Nomenclature is given at the end of the report. The geometry of the coated system is shown in Figure 23, and Figure 24 illustrates the numbering scheme for a multi-coated substrate. In figure 24, layer 1 could be the substrate, and 5 coating layers could be represented by layers 2 through 6. The method is flexible for describing any number of coating layers. Note that h is the total thickness of the substrate and all the coatings. (See appendix D for details).

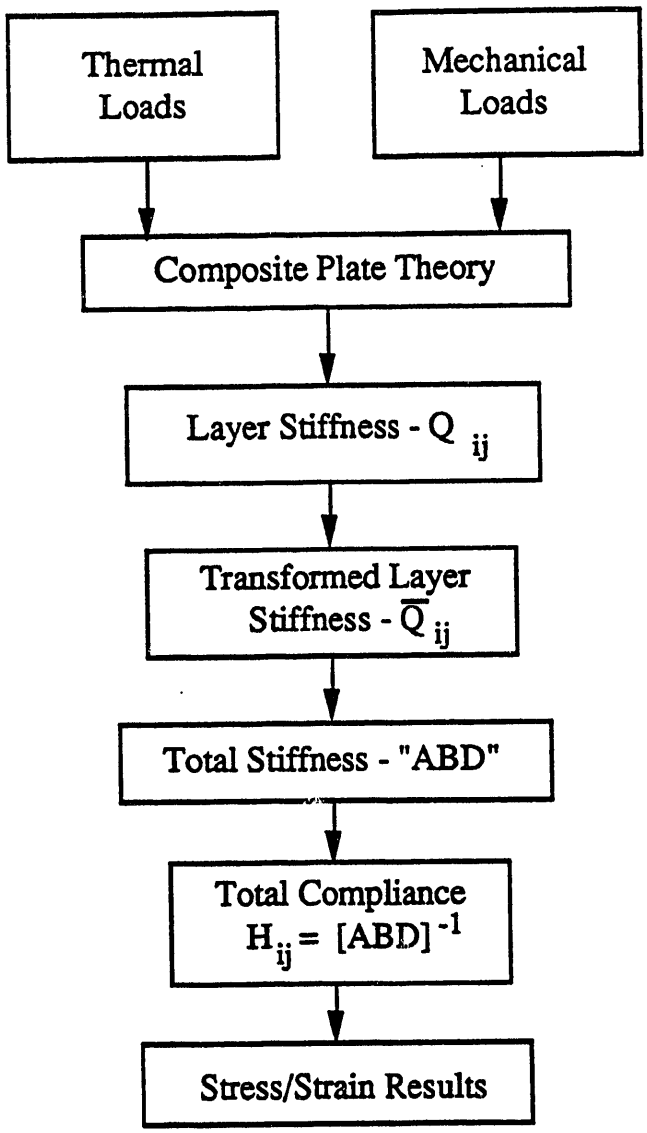

Figure 22. Flow chart for computer code implementation of composite plate theory. Layer properties were used to get transformed stiffnesses for each layer, and these were cumulated into a total stiffness matrix for the entire coated system. Unknown mid-plane strains were then solved for, and stresses in each of the layers recovered.

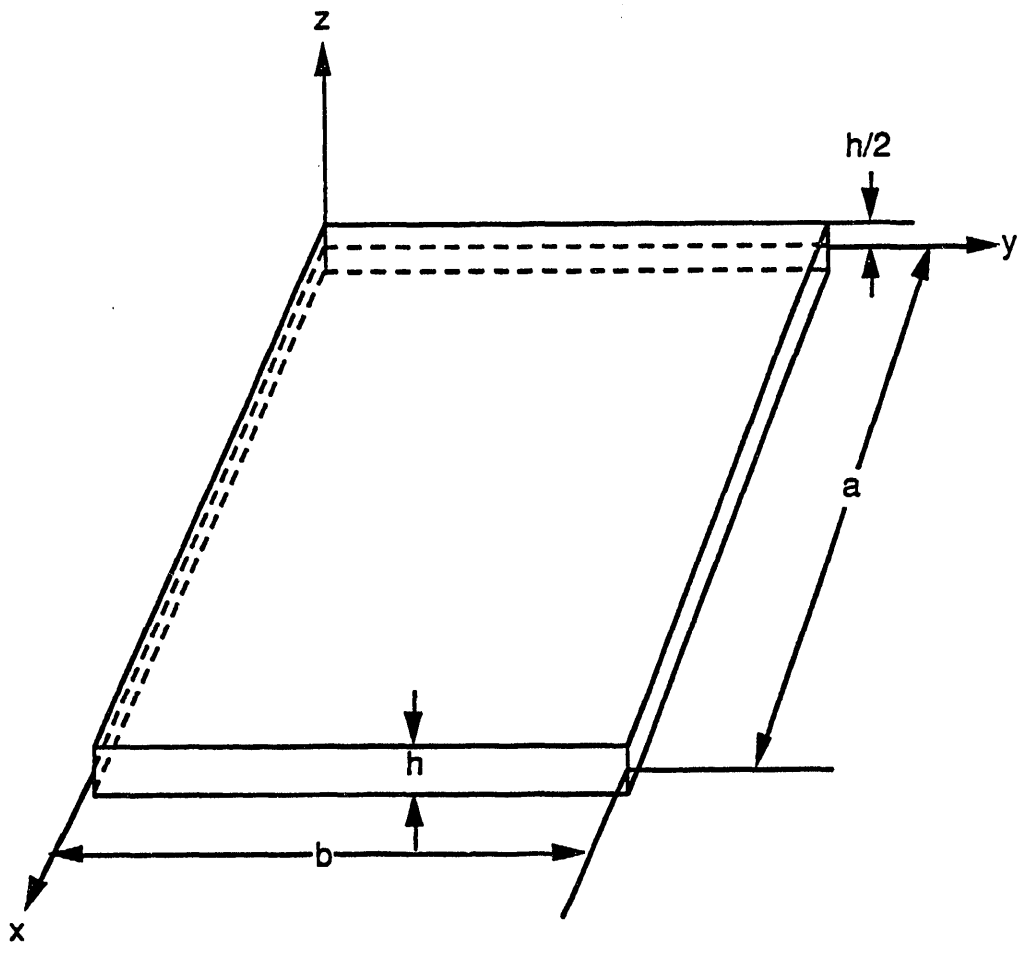

Figure 23. Schematic of the coated substrate model; h is the total thickness, and the mid-plane is at $h/2$. The z direction is normal to the plane of the coatings.

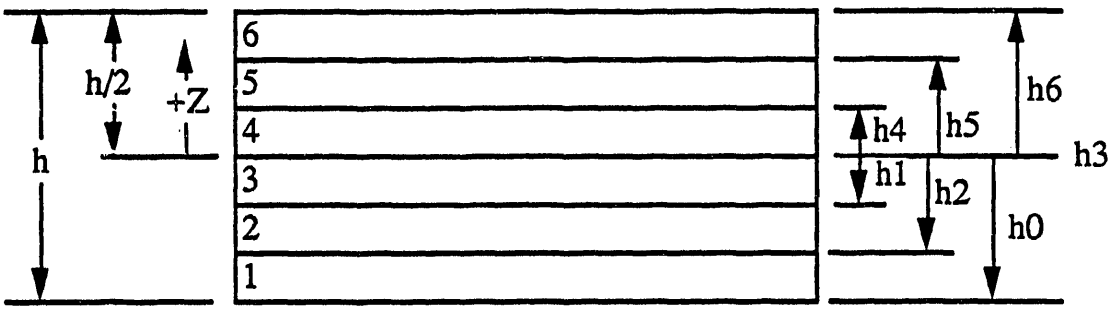

Figure 24. Numbering scheme for a multicoated system. h is the total coating thickness, and all interface positions are measured relative to the mid-plane at $h/2$, which the $z = 0$ plane. Note that layers below this plane have negative interlayer position values.

Comparison to Finite Element Results

Numerical experiments were performed to compare the generalized composite plate theory to those obtained by the finite element method.. Table 9 shows the material properties used in all stress analyses. Each of the systems was cooled from 1000°C to find the residual stress in each of the materials present. The substrate was 6350 microns thick for all studies.

Table 9. Material properties used for substrates and coating layers in this part of the study.

Material	Young's Modulus (GPa)	Poisson's Ratio	Fracture Toughness ($MPa\sqrt{m}$)	Thermal Expansion Coeff. (/°C) x 10^{-6}
Al_2O_3	390	0.22	-	7.8
AlN	340	0.24	1.0	4.9
Interface	320	0.255	-	3.8
SiC	207	0.22	-	4.3
Al_2O_3+ZrO_2	380	0.22	5.0	9.4
Si_3N_4	296	0.27	3.5	2.7

To ensure that the composite plate theory code was working correctly, the stress results were compared to a finite element solution of a similar problem [SHA88]. The finite element method used in Sham and Sarin [SHA88] was specially formulated to exploit hybrid finite elements because of the relative size of the elements used for the coating and for the substrate.

Results for both substrate materials are shown in Table 10. Excellent agreement between the two methods is shown, thus confirming the applicability of composite plate theory to this problem.

Si_3N_4 Substrate

Three numerical experiments were performed with the silicon nitride substrate. Firstly, residual stress with no interlayer but with varying thickness of the alumina-zirconia coating was calculated. Next an AlN interlayer *between* the alumina-zirconia and Si_3N_4 substrate was varied in thickness and residual stresses found for each material. Lastly, the AlN coating was placed *above* the Si_3N_4 coating to illustrate the irrelevance of thermal expansion grading.

Results are shown in Figures D-1, D-2, and D-3 (see Appendix D). The results indicate that the presence or absence of an interlayer, thickness of the coating layers, and order of the coatings on the substrate have negligible effect on residual stress in each of the layers.

Table 10. Comparison of 2-D finite element results using special hybrid elements to the composite plate theory described here. Stress values are from reference [SHA88], values in parentheses are results from the composite plate code described here. For both tables $\Delta T = -1000°C$. Note use of Si_3N_4 and SiC substrates.

Layer	Young's Modulus (GPa)	Poisson's Ratio	Thermal Expansion Coeff. (/°C)	Residual Stress (MPa) [Layer Thickness, μm] (a)	(b)
Al_2O_3*	390	0.22	7.8×10^{-6}	2475 (2527) [10]	2482 (2534) [4]
AlN*	340	0.24	4.9×10^{-6}	938 (964) [3]	943 (970) [9]
Interface*	320	0.255	3.8×10^{-6}	442 (453) [1]	448 (459) [1]
Si_3N_4*	296.5	0.27	2.7×10^{-6}	-16 (-17)	-11 (-12)
Al_2O_3†	390	0.22	7.8×10^{-6}	1731 (1728) [10]	1740 (1738) [4]
AlN†	340	0.24	4.9×10^{-6}	282 (249) [3]	290 (258) [9]
SiC†	207	0.22	4.3×10^{-6}	-11 (-11.5)	-6 (-6)

†SiC substrate. *Si_3N_4 substrate.

SiC Substrate

Since it has been shown that coating stresses are not sensitive to thickness or coating order variations, all pertinent stresses for the SiC substrate coating systems can be found with a single residual stress analysis.

The stresses shown in Figure D-4 (appendix D) are applicable for changes in any of the layer thickness or order sequence.

Based on these studies, our conclusions for brittle ceramic coatings on Si_3N_4 and SiC substrates are:

- Verifying that coating thickness has *negligible* effect on residual stress in any of the coating layers.

- The *order* (i.e., grading the thermal expansion mismatch in a multilayer coated system) has *negligible* effect on residual stress in any of the coating layers.

- Modulus of elasticity has almost no effect on residual stress in any of the coating layers.

- Because each of the coatings are thin films relative to the size of the substrate thickness, the strain in the coatings is the same as the strain at the top fiber of the substrate, that zone which has an interface with the first coating layer.

- If material properties vary as a function of temperature, magnitudes of stress will be different, but the above conclusions still hold.

It should be noted that these conclusions apply to brittle thin films, and that simulations were performed on uncracked coating layers. The stresses calculated in each of the layers would be those which induce cracking in any of the layers, and as such are indicators of the tendency for cracking during cooling from the CVD process.

The effect of crack propagation during solid body contact of these elastic layers is not known, so thickness and layer ordering may have an effect in that case. The possibilities for working around the problem inherent to brittle coatings could lie either in the area of controlled brittle fracture using multilayer coating, or by the use of "ductile" layers which would permit stress relief of the ceramic layers when they are bonded to

other brittle layers. However, the required thickness of the ductile interlayer wqould probably be too thick for practial applications [SCH92].

COMPUTER SIMULATION OF COATING FRACTURE

Single Layer with Interface - *Initial Vertical Flaw*

Studies were performed on a single-layer coating of $Al_2O_3+ZrO_2$ on a substrate of silicon nitride. Subsequent sections will describe results for a multi-layer coated substrate. Loads were imposed on the body in the form of residual thermal stress, and mechanical loads resulting from solid body contact with friction. The finite element model allows automatic changes in mesh topology due to crack growth, and a bimaterial fracture model which takes into account the different fracture toughnesses of the coating, interface, and substrate when the cracks are at or near the interface. Results indicate that, subject to these loads, a vertical flaw in the coating propagates approximately downward until the coating-substrate interface region. Once the crack has entered the interface, it moves away from the contact loads along the interface a distance of approximately half the coating thickness, after which it continues in a direction nearly normal to the net direction of the applied load. Since the crack did not continue along the interface, improvements in the interface bond strength would not have significantly influenced the crack growth direction.

Geometry

A finite element mesh was created to simulate the cross-section of a wide sample (plane-strain) of a single layer coated substrate. Coating thickness was 2 microns, substrate thickness was arbitrary, and assigned a value of 58 microns.

The plane of the mesh is shown in Figure 25. For the single layer analysis the AlN interlayer was not used. The model was simply $Al_2O_3+ZrO_2$ on a Si_3N_4 substrate. The width of the model was 60 microns. A set of boundary markers exists between the elements which describe the coating and those that define the substrate. These boundary markers locate the bimaterial fracture boundary. During remeshing, this boundary must lie on element

boundaries to keep the interface coherent. The model initially was crack-free. A vertical flaw 0.5 microns long was positioned 1 micron from the mechanical load. As the crack propagated, the model was automatically remeshed to take into account the change in surface, the bimaterial interface, and the stress concentration at the crack tip. Eight noded quadratic elements were used for the original mesh. Mesh changes were mapped with 6 noded triangular elements, and the crack tip was modeled with 6 noded singularity elements. When the crack tip was at or near the bimaterial interface, singularity elements were not used. For each crack increment, the next propagation direction was predicted by using a maximum energy release rate criterion, which is also applicable in the region of the interface. The energy release rate was calculated by comparing the energy released by the system for candidate directions in each of the materials in the vicinity of the crack tip. Once a direction was found, the crack length was increased a small amount and the calculation repeated. This procedure was continued until no significant change in the direction of crack propagation was seen.

Boundary Conditions

Thermal loads were applied to the entire body by including a temperature change of -1000°C into the analysis. This temperature is typical of temperatures used in the CVD process for this material system. It was assumed that the coating was applied to the substrate in the CVD chamber in a stress-free state and that stresses were generated upon cooling by thermal expansion mismatch between the coating and the substrate. A mechanical load was also applied to the coating. The mechanical loads represents the load applied by solid body contact. The load was distributed over a 1 micron region; the shape of the distribution was parabolic. The magnitude of the maximum value of the distribution was scaled such that the stress results were normalized from zero to one. The coefficient of friction used was 0.5, resulting in the same form of the distribution of shear stress on the surface of the coating. Figure 26 is a schematic of the boundary conditions. As previously mentioned, the AlN interlayer, while shown in Figure 25, was not used in the single layer analysis. On the lower edge of the model, the central node of the

edge was pinned, and all other nodes on the edge were constrained in the vertical direction.

Material Properties

The coating material was $Al_2O_3+ZrO_2$ and the substrate was silicon nitride. Both materials were modeled as elastic in both thermal and mechanical properties. Material properties were assigned to the coating, substrate and interface. Elastic and thermal properties for the coating and substrate are shown in Table 9. The interface energy release rate as a function of mode-mixity is shown in Figure 27.

Crack Propagation Studies

The crack propagation occurred over 14 crack increments, after which the direction of crack growth remained constant. Since the crack crossed the bimaterial interface, the bimaterial interface fracture model was used for several crack growth steps. Other crack growth steps used linear elastic fracture mechanics theory solved using finite element methods. This bimaterial fracture model has been implemented into a finite element framework [FRA91], and the key concept in the numerical scheme is that the crack is predicted to propagate in the direction of maximum energy release rate. This energy release rate is analogous to that described for homogeneous fracture theory. The difference is that there may be several candidate directions where the energy release rate is a maximum. All candidate directions for all materials must be considered and compared. The method was developed to apply in cases where the crack tip is in or near a bimaterial interface. Figure 28 shows the finite element mesh prior to crack growth. The upper four elements comprise the coating region. Elements below the upper four comprise the substrate. An enlargement of the initial vertical flaw, showing the original and deformed shape of the coated system is shown in Figure 29. Note that the deformed shape was a result of the thermal, normal and shear loads on the structure. Figure 30 illustrates the direction of crack growth prior to crossing the bimaterial interface. The crack has begun a slight turn away from the applied mechanical loading. Figures 31 shows the deformed shape for the final crack increment. Note that the crack did not

remain in the interface, as it would for a material with a lower range of interface fracture toughnesses (lower G_{Ic} curve), and also that the final crack direction is approximately normal to the applied mechanical loading direction. The fracture modeling of coated systems continues in the next section with a two-layered coated substrate; under the same thermal and mechanical loads.

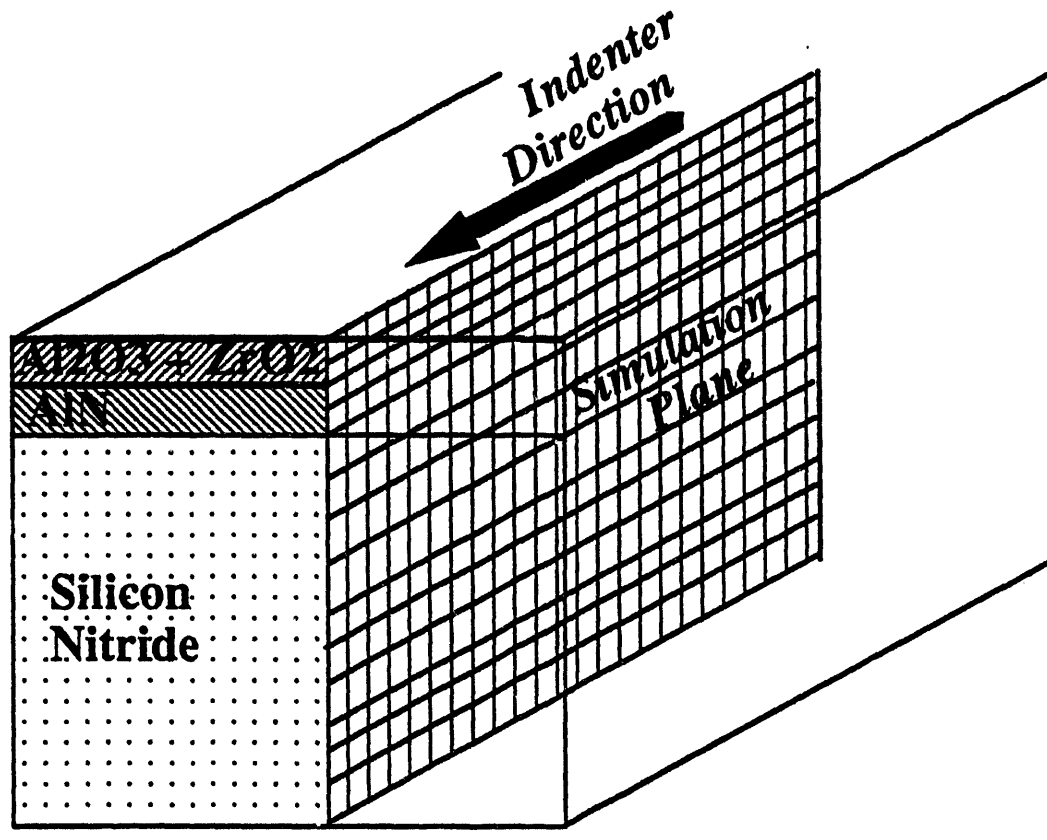

Figure 25. Schematic of the finite element mesh relative to microstructural cross section. Direction and positioning of scratch test indenter is shown.

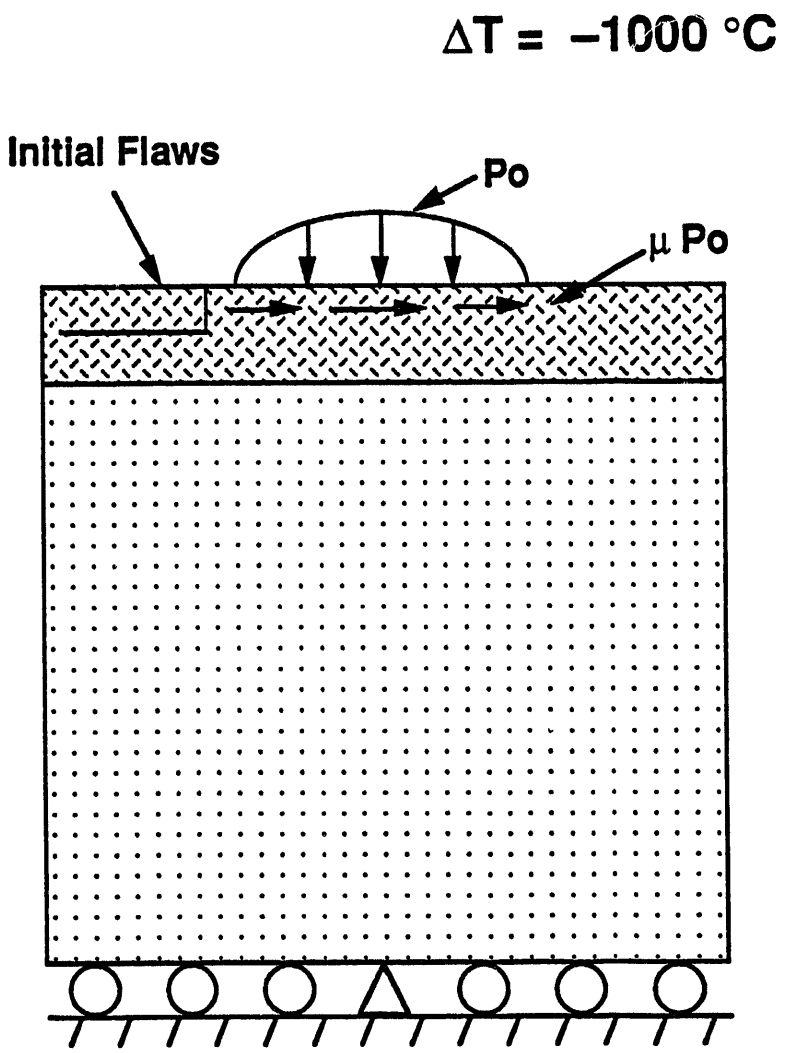

Figure 26. Schematic of the boundary conditions used in the fracture simulation. Coefficient of friction was 0.5. The value of `p' (the maximum magnitude of the load distribution) was assigned a value such that the stress results are normalized.

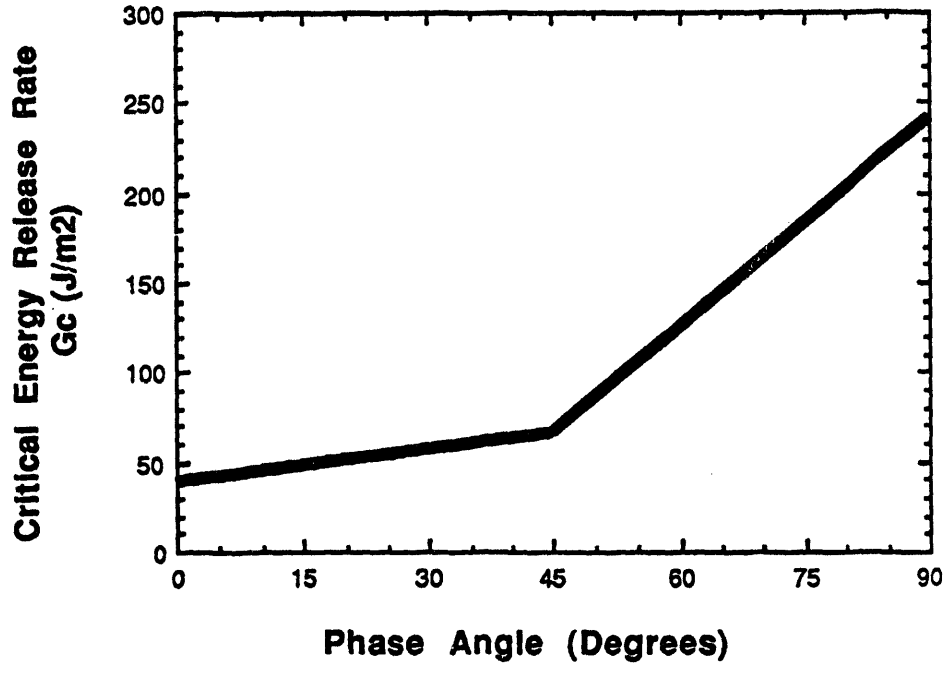

Figure 27. Energy release rate for the interface as a function of mode mixity. A mode-mixity of 0.0 describes pure mode I loading at the crack tip, and a mode-mixity of 90 (degrees) describes pure mode II loading at the crack tip.

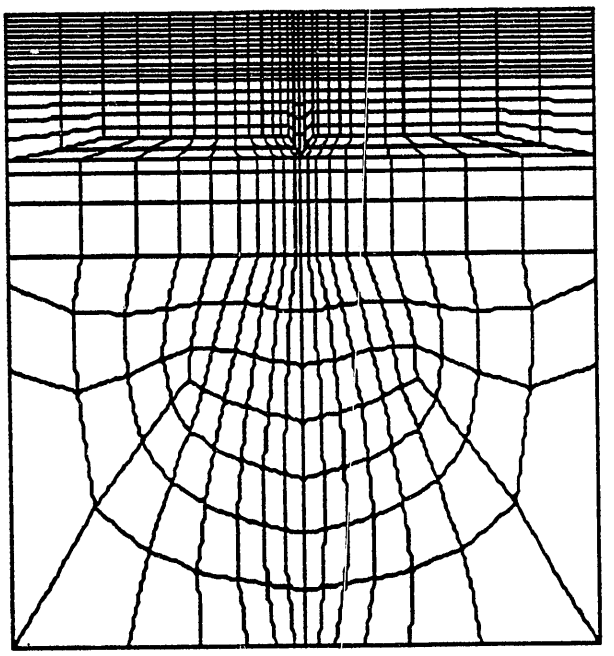

Figure 28. Initial (uncracked) mesh used in the fracture simulation study. The top four elements are the $Al_2O_3+ZrO_2$ coating material.

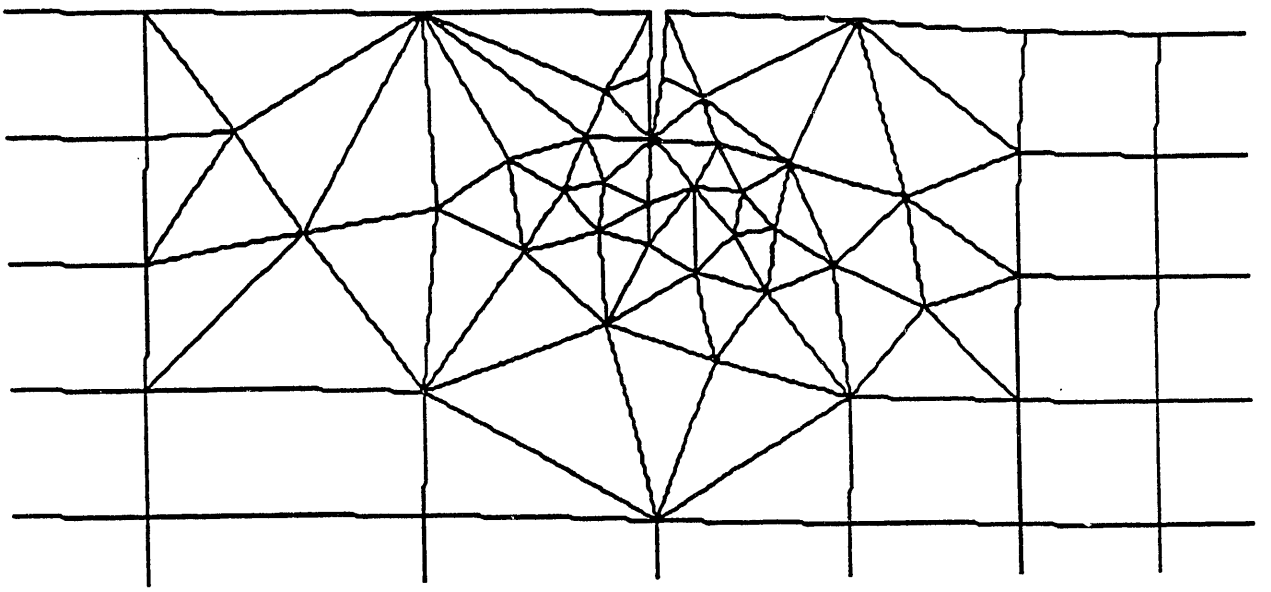

Figure 29. Initial vertical flaw, 0.5 microns long (1/4 coating thickness).

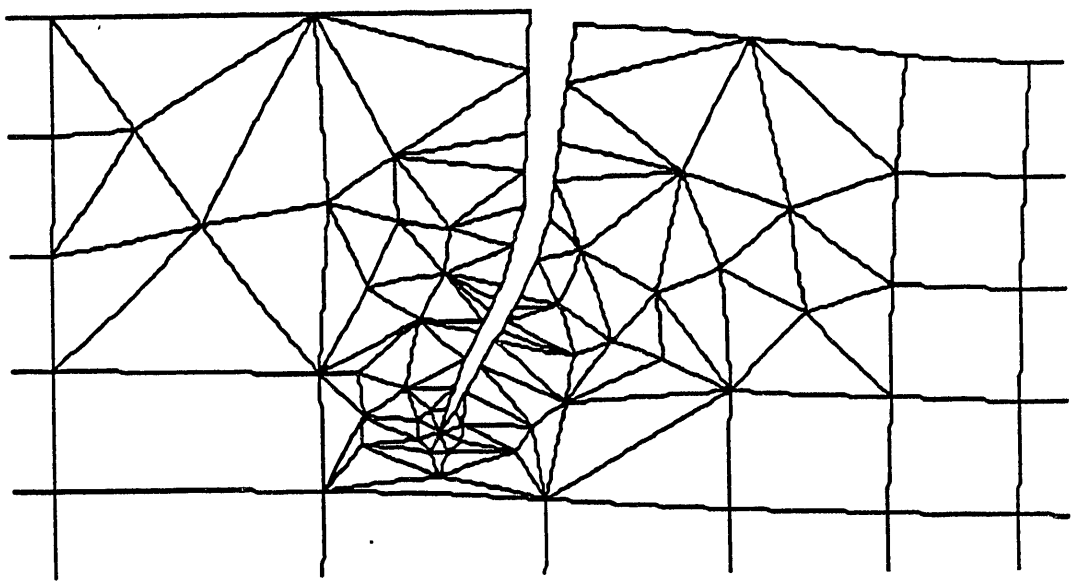

Figure 30. Deformed shape and crack growth direction prior to crossing the bimaterial interface.

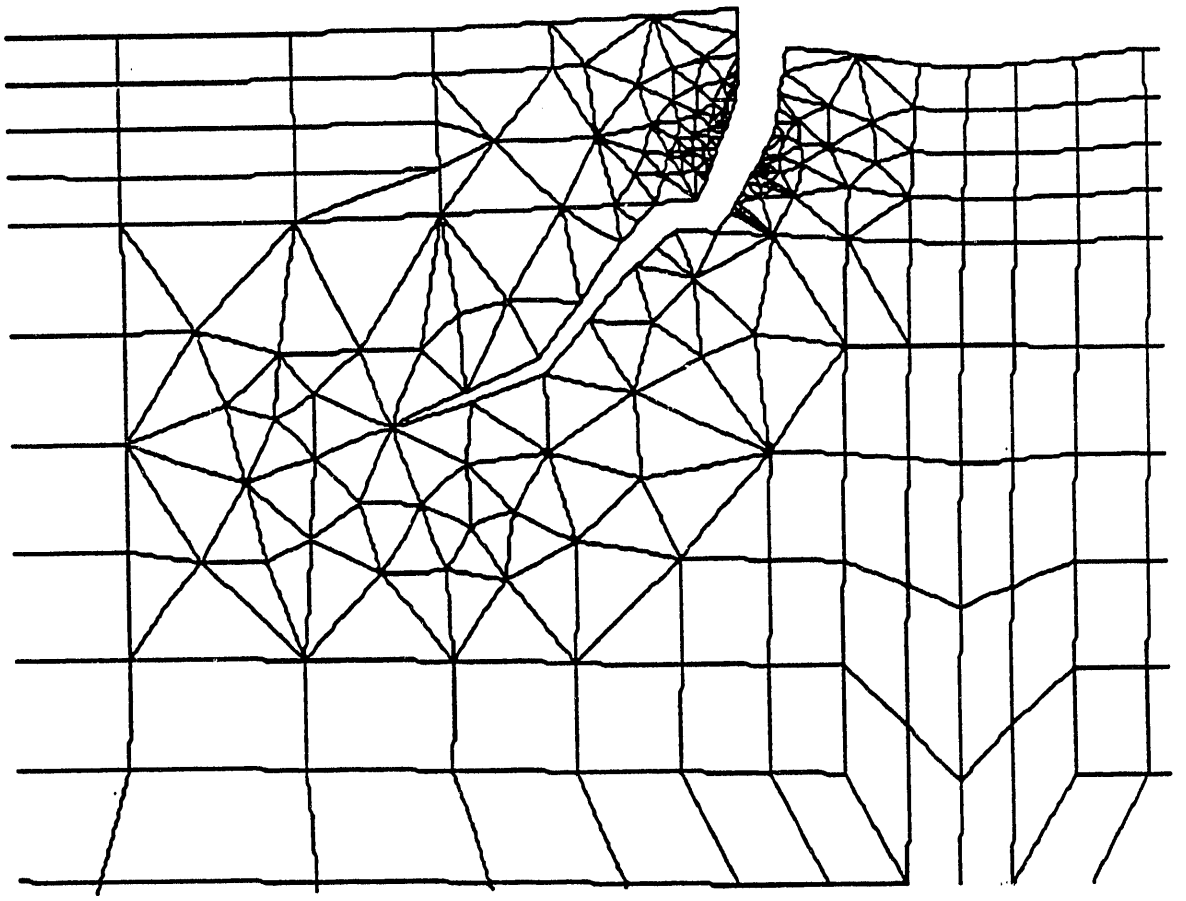

Figure 31. Deformed shape and crack path in final increment.

Multilayer Analysis - *Initial Vertical Flaw*

Simulations of a single-layer fracture were reported in the previous section. Here we describe the model and results for numerical simulation of a single-pass scratch test of a substrate with two coating layers, and crack propagation due to an initial vertical flaw.

Geometry

The finite element mesh was created to simulate the cross-section of a wide sample (plane-strain) of a double-layer coated substrate. Coating thicknesses were 2 microns, substrate thickness was arbitrary, and assigned a value of 58 microns. The plane of the mesh is shown in Figure 25. The boundary conditions are those shown in Figure 26.

Material Properties

The top-layer coating material was $Al_2O_3+ZrO_2$, the second (middle) coating layer as AlN, and the substrate was silicon nitride. All materials were modeled as elastic in both thermal and mechanical properties. Material properties were assigned to the coatings, substrate and interface. The interface energy release rate as a function of mode-mixity for both material interfaces is shown in Figure 32.

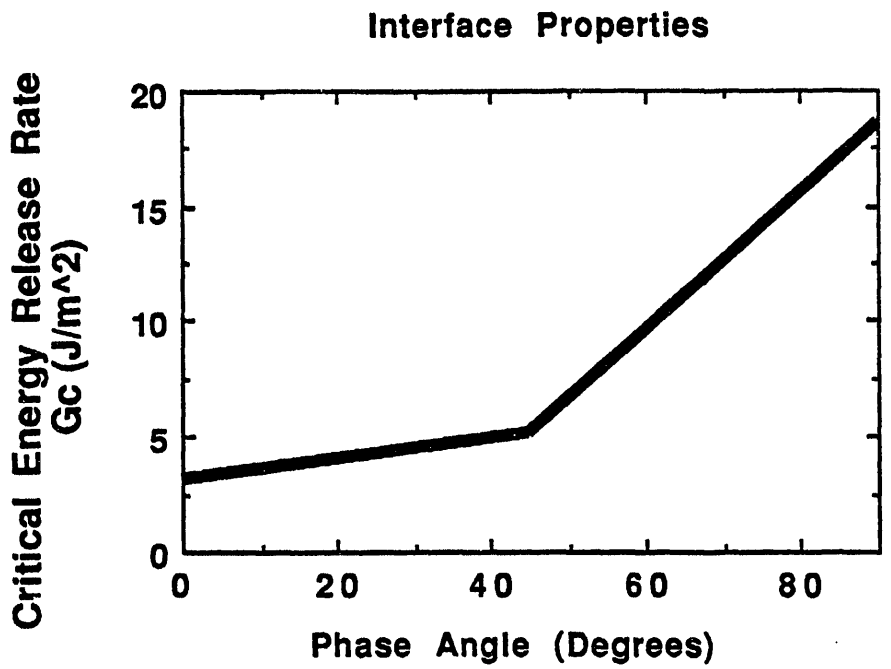

Figure 32. Energy release rate for both interfaces as a function of mode mixity. A mode-mixity of 0.0 describes pure mode I loading at the crack tip, and a mode-mixity of 90 (degrees) describes pure mode II loading at the crack tip.

Crack Propagation Studies

The crack propagation occurred over 27 crack increments, after which the direction of crack growth remained constant; along the AlN-substrate interface. Since the crack crossed both bimaterial interfaces, the bimaterial interface fracture model was used for several crack growth steps. Other crack growth steps used linear elastic fracture mechanics theory which was solved using finite element methods.

Figure 33 shows the finite element prior to crack growth. The upper four elements (in the vertical direction) comprised the top-layer (Al_2O_3+ZrO_2). The next four elements in the vertical direction comprised the second layer (AlN). Elements below the upper eight modeled the substrate. A zoom of the initial vertical flaw, showing the original and deformed shape of the coated system is shown in Figure 34. Note that the deformed shape was a result of the thermal, normal and shear loads on the structure.

Figure 35 illustrates the direction of crack growth as the crack entered the first material interface. The $Al_2O_3+ZrO_2$ layer would no longer provide oxidation resistance. The crack has begun a slight turn away from the applied mechanical loading at this stage in the crack history.

Figure 36 shows the deformed shape for the final crack increment. Note that the crack did not remain in the top interface, but continued through the middle AlN layer to the silicon nitride substrate. These results indicate that both coating layers have been completely fractured. A solution to this type of failure could be to design the first material interface (increased toughness) such that the crack would not penetrate into the second coating layer.

Results indicated that, subject to these loads, a vertical flaw in the coating propagated approximately downward until the first coating-substrate interface region. Once the crack entered this first interface, it traveled for a distance of about 20% of the coating thickness, then changed direction and advanced into the second coating material. While traversing both coating layers, the crack traveled in a direction nearly normal to the net direction of the applied load. Since the crack continued to the substrate surface, it was anticipated that the surface would be exposed to outer gaseous conditions.

The fracture modeling of coated systems continues with a two-layered coated substrate with initial horizontal flaws; under the same thermal and mechanical loads.

Multilayer Analysis - *Initial Horizontal Flaw*

Two analyses have been performed. The first had the initial horizontal flaw positioned at the middle of the second coating layer. In this case, the crack did not cross any of the material interfaces during crack growth. Figures 25 and 26 show the model and boundary conditions prior to crack growth. With regard to the mesh the upper four elements (in the vertical direction) comprised the $Al_2O_3+ZrO_2$ layer coating. The next four element in the vertical direction comprised the second layer (AlN) coating region. Elements below the upper eight modeled the substrate. A zoom of the initial horizontal flaw, showing the original and deformed shape of the coated system is shown in Figure 37. Note that the deformed shape was a result of the

thermal, normal and shear loads on the structure. Figure 38 illustrates the direction of crack growth in the final stage of simulation. The crack is directed upwards toward the free surface, then curves away from the applied mechanical load.

The second simulation was performed with an initial horizontal crack in the top coating layer. It was positioned in the middle of this layer. A zoom of the initial horizontal flaw, showing the original and deformed shape of the coated system is shown in Figure 39. Note that the deformed shape was a result of the thermal, normal and shear loads on the structure. Figure 40 illustrates the direction of crack growth in the final stage of simulation. The crack is directed upwards toward the free surface, and the analysis was halted as the crack neared the surface. Since the horizontal cracks were directed away from the substrate, an opportunity exists to design the coating layer such that manufacturing flaws are highly oriented in the horizontal direction, which would promote coating stability and thus oxidation resistance of the substrate.

Since cracks were predicted to move away from the substrate material, the oxidation resistance of the substrate could be preserved during crack growth of this type. It should also be emphasized that this was not the case with initial vertical flaws, which propagated to the substrate.

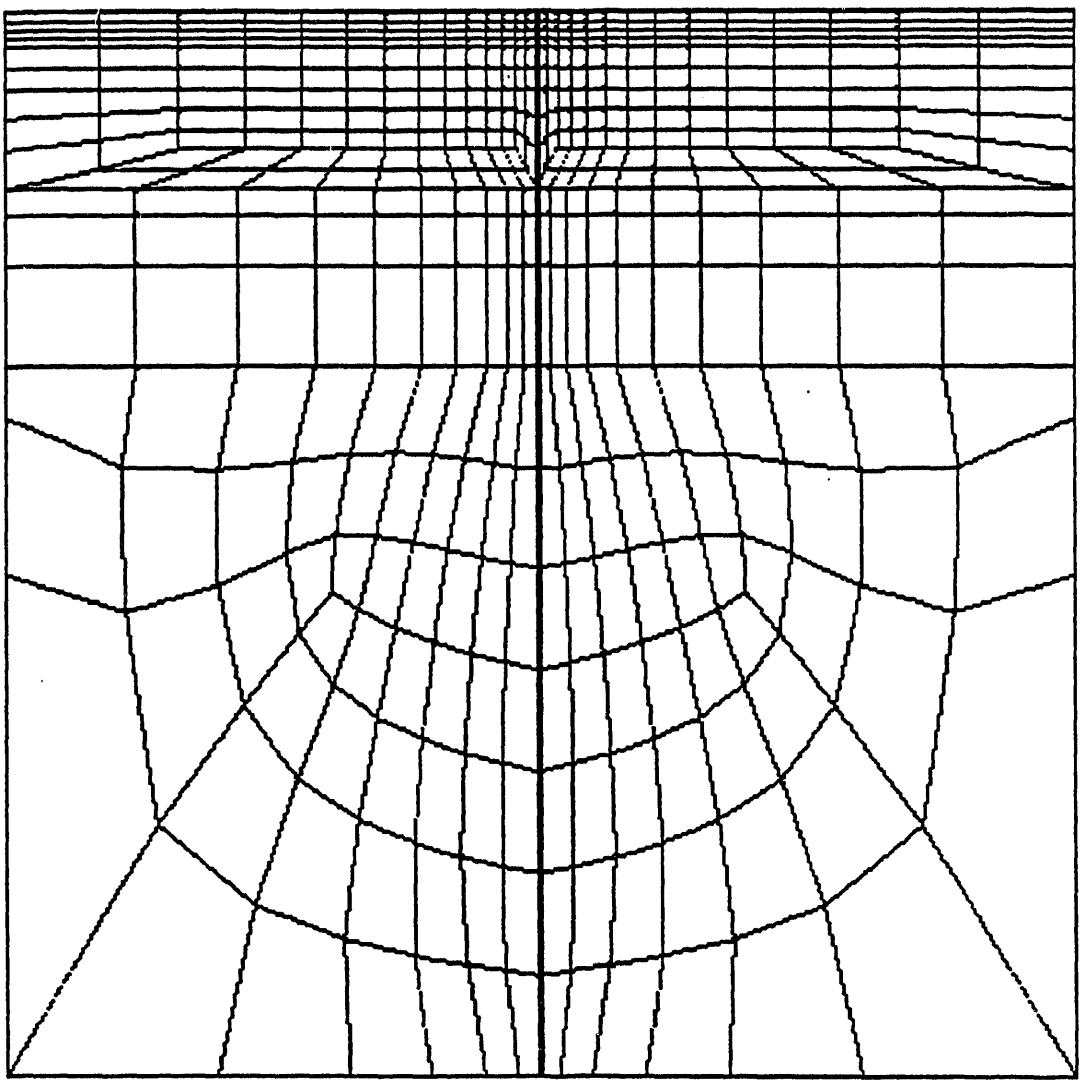

Figure 33. Initial (uncracked) mesh used in the fracture simulation study. The top four elements are the Al_2O_3 + ZrO_2 coating material. The next four were the AlN coating material.

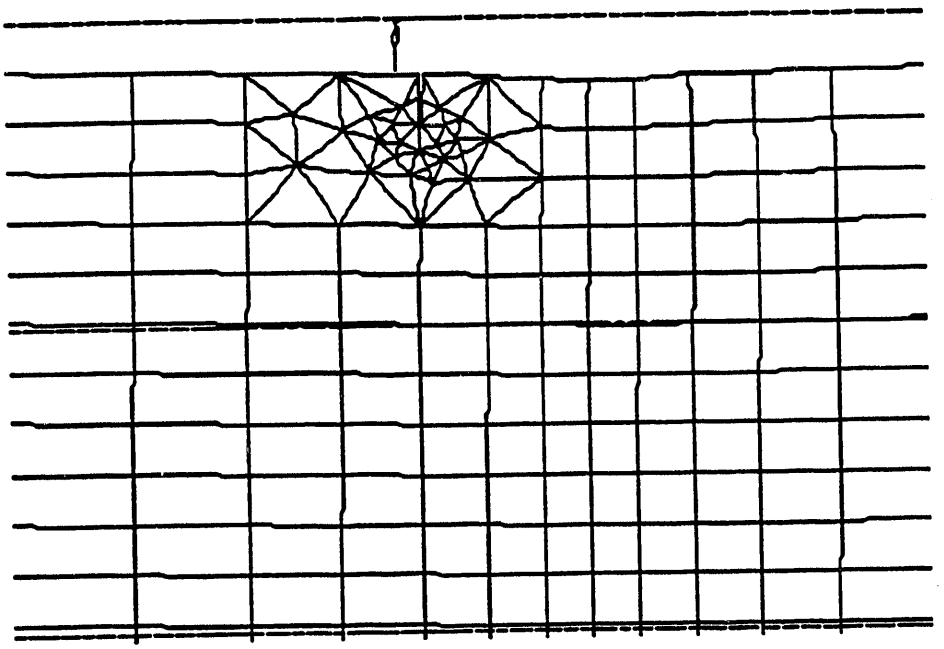

Figure 34. Initial vertical flaw, 0.5 microns long (1/4 coating thickness). Solid lines are deformed geometry (thermal and mechanical loads). Dashed lines are undeformed geometry.

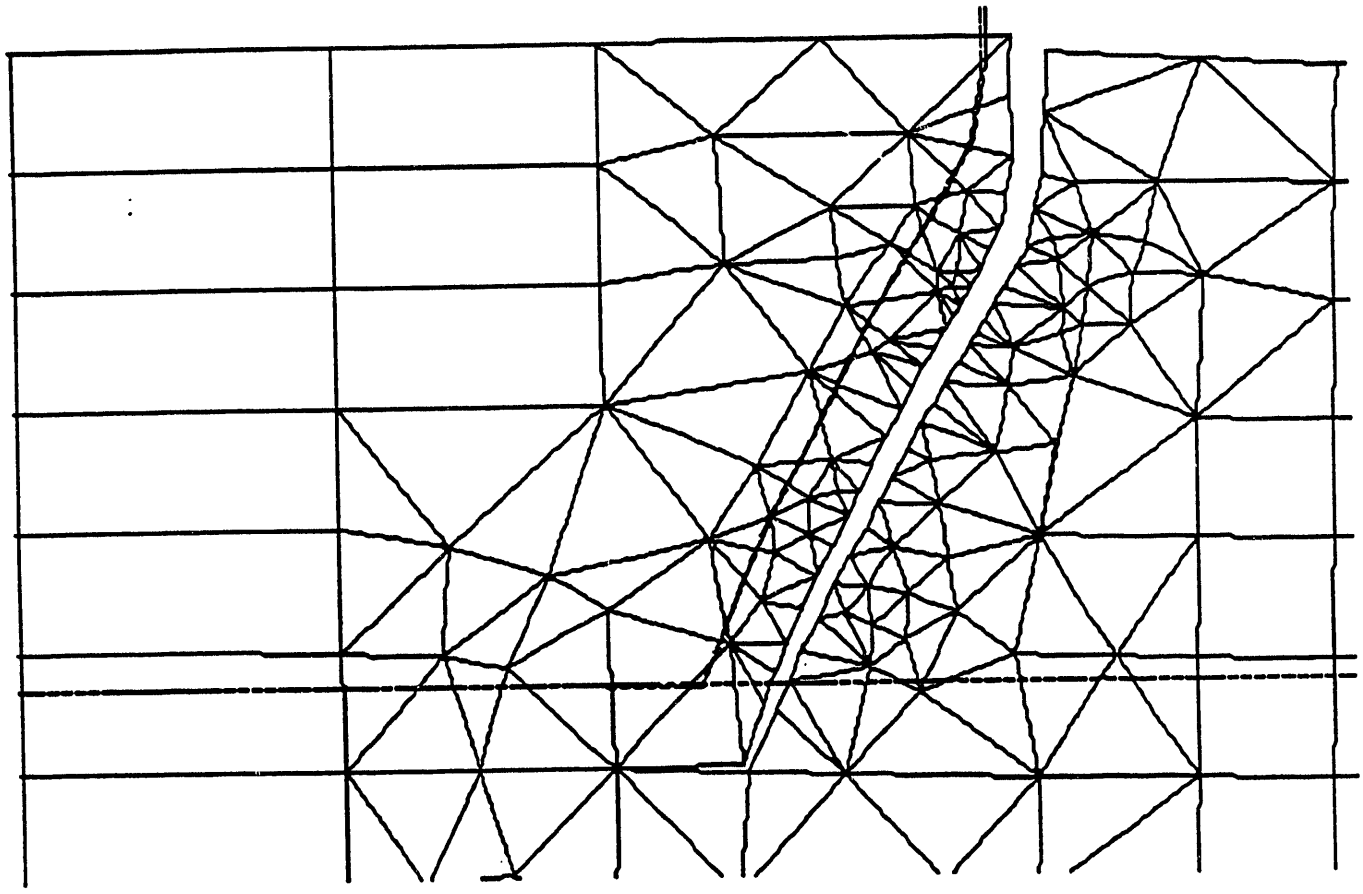

Figure 35. Deformed shape and crack growth direction as the crack encountered the top bimaterial interface.

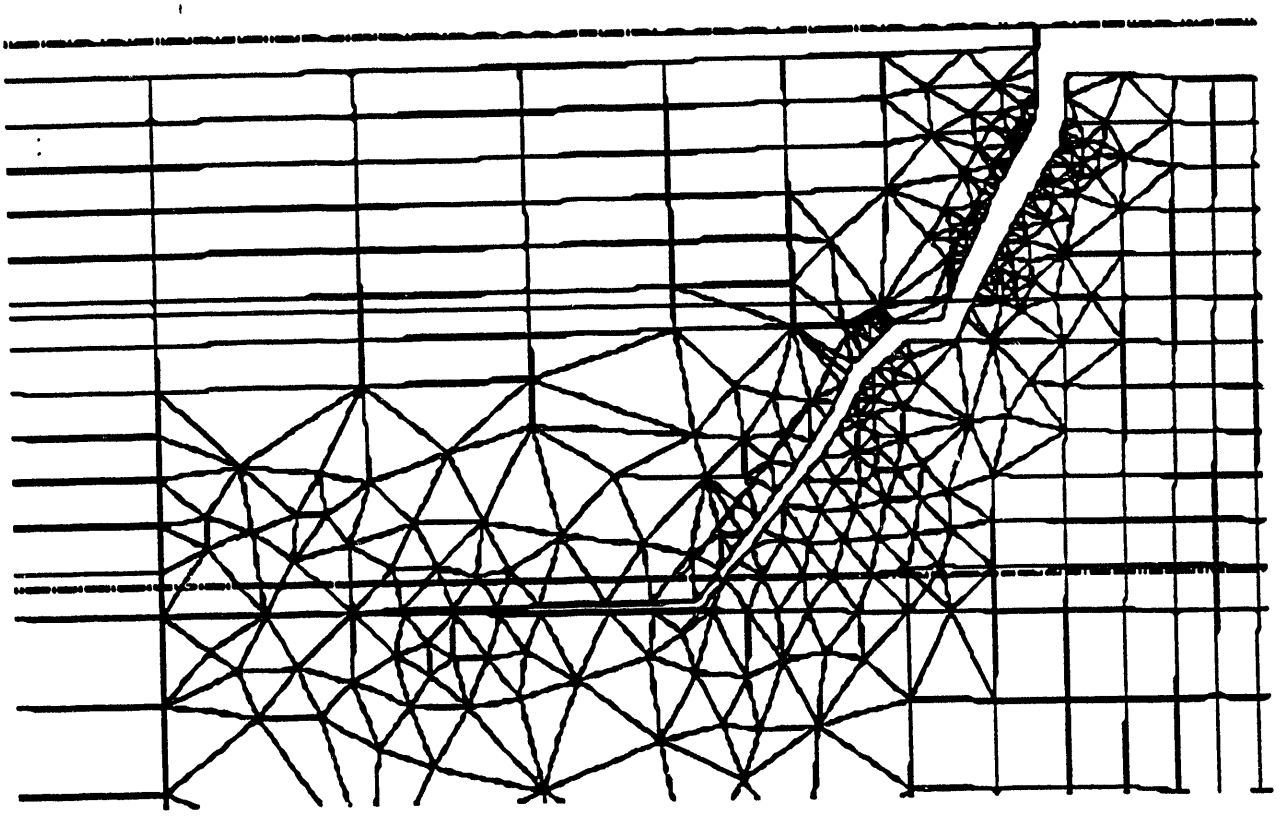

Figure 36. Deformed shape and crack path in final increment. The crack has propagated through both coating layers.

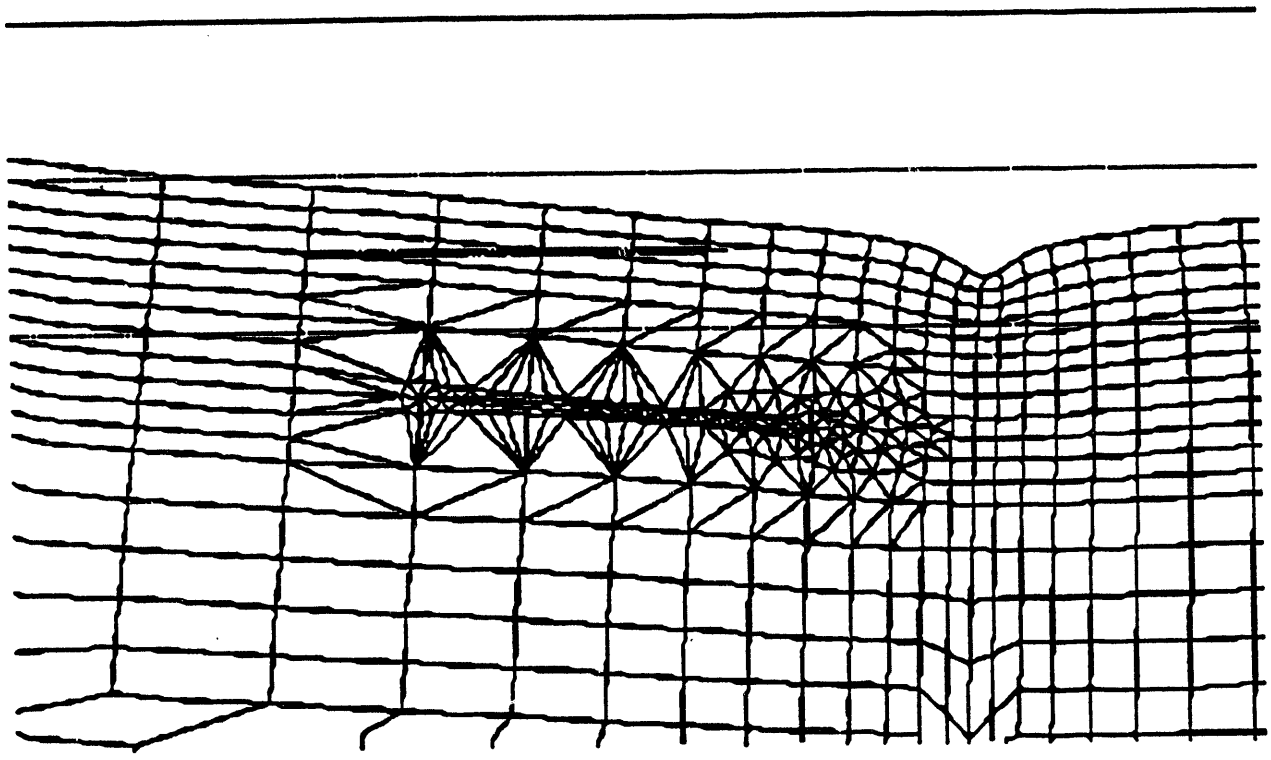

Figure 37. Initial horizontal flaw in the second coating layer. The flaw is positioned at the middle of the layer. Solid lines are deformed geometry (thermal and mechanical loads). Dashed lines are undeformed geometry.

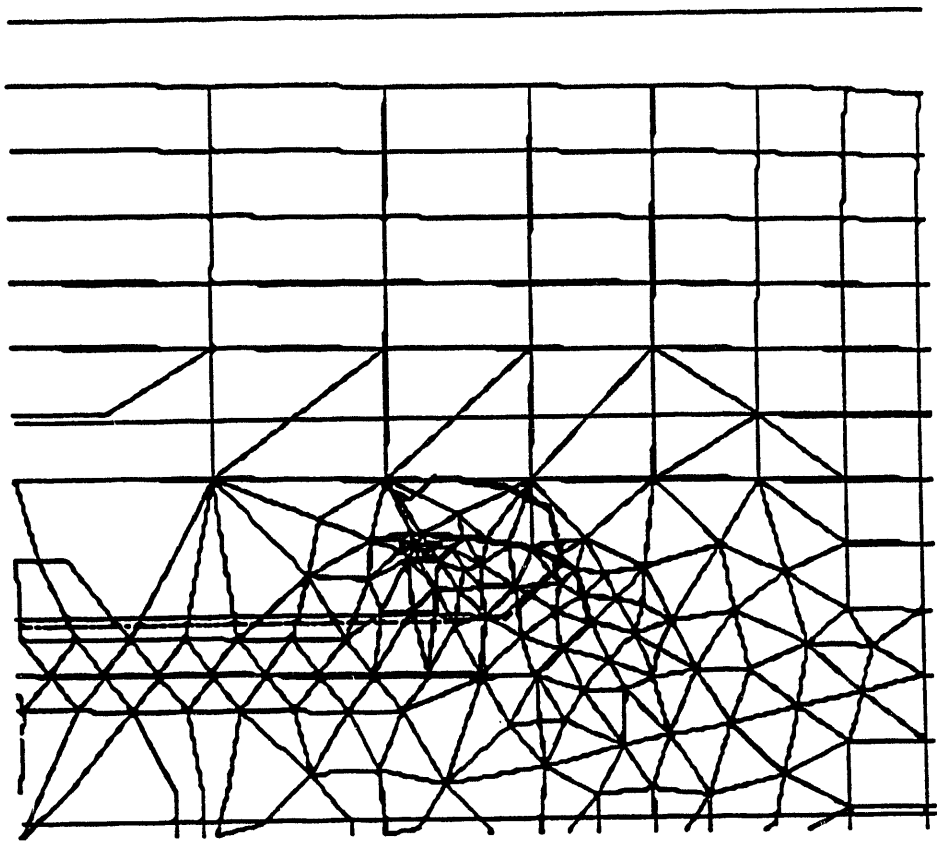

Figure 38. Deformed shape and crack path in final increment for the case where the initial flaw was in the second (middle) coating layer. The crack has been directed away from the substrate.

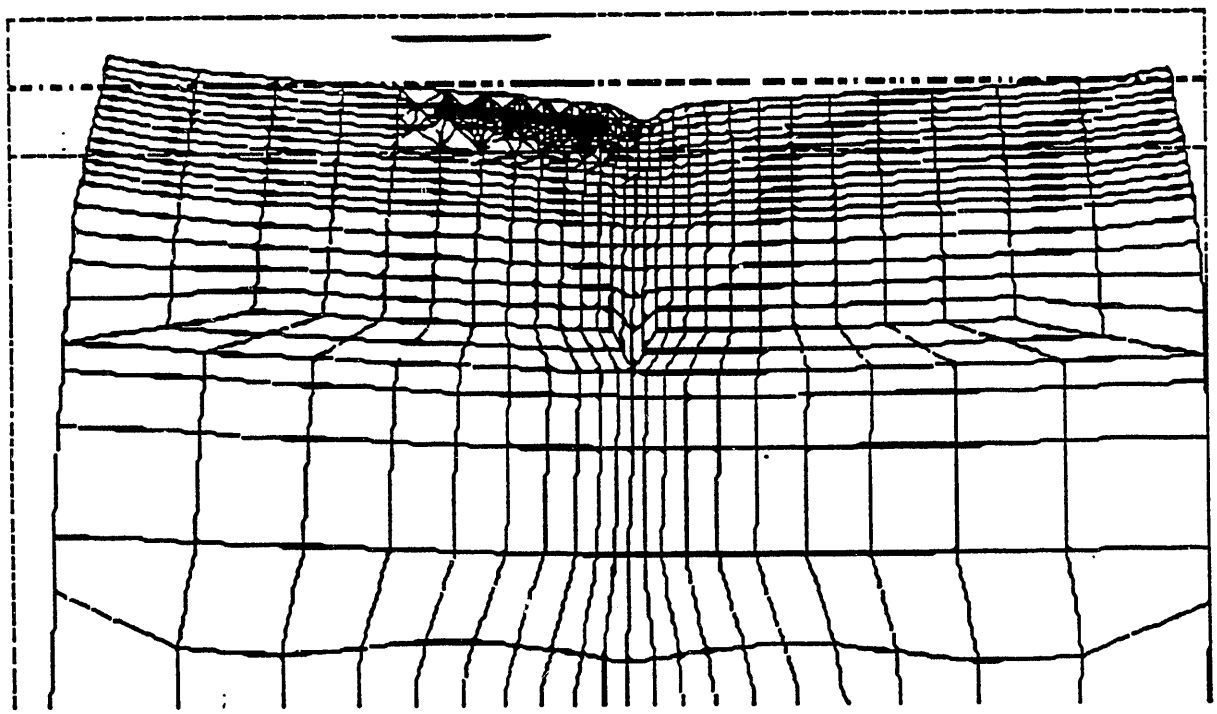

Figure 39. Initial horizontal flaw in the top coating layer. The flaw is positioned at the middle of the top layer. Solid lines are deformed geometry (thermal and mechanical loads). Dashed lines are undeformed geometry.

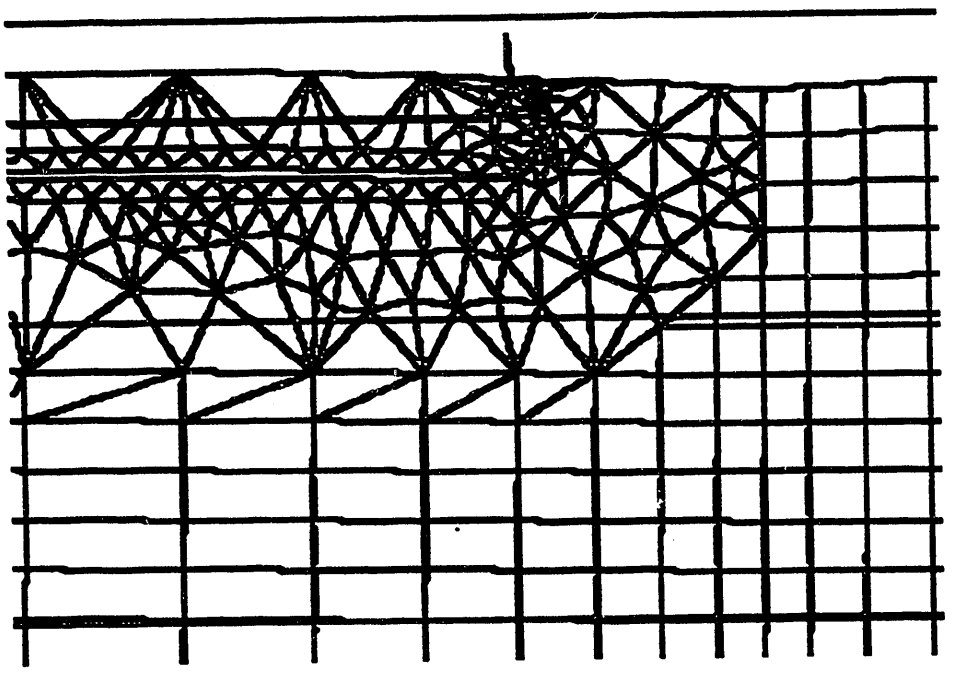

Figure 40. Deformed shape and crack path in final increment for the initial flaw in the top coating layer. The crack has been directed away from the substrate.

CONCLUSIONS

A multilayered coating configuration for protection of Si_3N_4 and SiC-based ceramics used in advanced heat engines was designed, deposited, and tested. It consists of an intermediate layer of AlN (~5 microns) and an outer layer of $Al_2O_3+ZrO_2$ (~1 micron). The coatings were deposited by CVD onto the three substrate materials specified by the DOE; reaction bonded Si_3N_4 (RBSN), sintered SiC (SSC), and HIP'ed Si_3N_4 (HSN). The AlN interlayer was demonstrated to be an effective means of providing good adhesion between the $Al_2O_3+ZrO_2$ coating and the ceramic substrates.

Modeling the grain boundary and lattice diffusion of oxygen through an Al_2O_3 layer at elevated temperatures suggested that the coating would be a good diffusion barrier to oxygen. However, experimental results revealed that the composite coating was not oxidation resistant at temperatures above 1000°C. The lack of protection was attributed to cracks in the $Al_2O_3+ZrO_2$ layer, which allowed oxygen to penetrate and react with AlN.

Finite element methods and fracture mechanics were to model the behavior of brittle multilayer coatings. Detailed analysis of the residual stresses in uncracked coatings on ceramic substrates revealed that the coating thickness, order of coating layers (including grading of the coefficient of thermal expansion), and elastic modulus of the coating all have little effect on the residual stress in the coating. Based on these numerical results, it was concluded that the $Al_2O_3+ZrO_2$ coatings would contain cracks upon cooling to room temperature. These cracks result from the high temperatures used in CVD processing and inherent thermal expansion mismatch between the materials.

Additional modeling was performed to better understand the behavior of cracks in a coating and possibly identify a means to eliminate or stabilize them. The effect of crack propagation during solid body contact was studied using interface fracture mechanics coupled with finite element analysis. For coatings which contain vertical flaws, the cracks always propagated into the substrate. Further analysis showed that improving the fracture toughness of the interface would not improve the performance of the coating, since the interface was not a weak point. In contrast, the horizontal crack did not

reach the substrate; it either stayed within that layer or moved away from the substrate and towards the free surface. Therefore, horizontal cracks would not degrade the oxidation performance of a coated substrate.

The possibilities for working around the problem inherent to thin brittle coatings could lie in the area of controlled brittle fracture of multilayers, or by the use of "ductile" layers which would permit stress relief and alleviate pre-service cracking. However, the ductile interlayer would have to be too thick to be effective. PVD methods, which allow the residual stress state to be controlled, or low temperature CVD processes may allow for crack-free coatings to be deposited which would be in a compressive stress state at the operation temperature. It is anticipated that without cracks, the $Al_2O_3+ZrO_2$ composite coating would be an effective means of reducing the contact stress damage and oxidation of Si_3N_4 ceramics.

A method was developed to measure the ultimate tensile strength, fracture toughness, and Weibull modulus of thin brittle coatings on substrates. The fracture stresses of CVD Al_2O_3 coatings on SiC substrates ranged from 190 MPa to 480 MPa, the Weibull modulus ranged from 16 to 28, and the fracture toughness ranged from 0.5 - 1.1 $MPa\sqrt{m}$. This work has shown that the tensile strength of Al_2O_3 and $Al_2O_3+ZrO_2$ coatings can be approximated by bulk values, however, the fracture toughness of these coatings was found to be 10 - 20% of bulk values.

A single point scratch test was used to assess the protective nature of the Phase II coatings during contact loading on unoxidized samples at room temperature. The coating protected the SSC and RBSN substrates by reducing chipping and cracking of the substrates, however, no significant differences were seen in the scratch resistance of the uncoated and coated HPSN.

Pin-on-disk tests were used to measure the breakaway and kinetic friction coefficients for coated and uncoated materials at room temperature. The $Al_2O_3+ZrO_2$ coating reduced the kinetic friction coefficient of RBSN and HSN by as much as 50% in self-mated tests. No apparent reduction in friction was observed for the SSC substrate. An improvement in sliding wear resistance was obtained with $Al_2O_3+ZrO_2$ coated HSN in the pin-on-disk test, whereas the coatings on RBSN and SSC were ineffective.

ACKNOWLEDGMENTS

The authors gratefully acknowledge Dr. D. R. Johnson and D. P. Stinton of Oak Ridge National Laboratory for providing technical guidance and support for this project.

The contributions of the following people at GTE Laboratories are also acknowledged: D. Bazinet, C. D'Angelo, M. J. Downey, J. Heftner, H. Kim, H. S. Mackel, A. Moschetti, D. Oblas, H. Rebenne, S. A. Robillard, F. E. Sivo, and C. Sung.

This research was sponsored in part by the U.S. Department of Energy, Assistant Secretary for Conservation and Renewable Energy, Office of Transportation Systems, as part of the Ceramic Technology Project of the Materials Development Program, under subcontract # 86X-95915C with Martin Marietta Energy Systems, Inc.

PUBLICATIONS

1. J.H. Selverian and D. ONeil, "Mechanical Property Measurement of Ceramic Thin Films on Ceramic Substrates," submitted to Thin Solid Films, March 1992.

2. J.H. Selverian, "Errors in Curve Fitting of Profilometer Data," J. of Vacuum Science & Technology A, Sept/Oct, (1992).

3. H.E. Rebenne and J.H. Selverian, "Adherent Ceramic Coatings to Reduce Contact Stress Damage of Ceramics," Proc. 26th Automotive Technology Development Contractors' Coordination Meeting, (1990).

4. D.W. Oblas, C. D'Angelo, H.E. Rebenne, and V.K. Sarin, "Ceramics Coatings to reduce Contact Stress Damage of Ceramics: Performance Testing," Proc. 26th Automotive Technology Development Contractors' Coordination Meeting, P-219, p.221-226, (1989).

5. H.E. Rebenne and S.K. Sarin, "Ceramic Coatings to Reduce Contact Stress Damage of Ceramics - Thermodynamic Modeling," Proc. 25th Automotive Technology Development Contractors' Coordination Meeting, P-209, 199-206 (1988)

6. T.-L. Sham and V.K. Sarin, "Residual Stress Calculations in Coating Configurations Using Finite Element Analysis," Ceramics Eng. and Sci., Proc., Vol. 9, (9/10), p. 1189-1198 (1988).

7. V.K. Sarin, "Design Criteria for a Coating to Reduce Contact Stress Damage," Proc. DOE Workshop on Coatings for Advanced Heat Engines, Castine, ME (1987), III, p. 83-89.

PRESENTATIONS

1. J.H. Selverian and D. ONeil, "Fracture Toughness and Strength of Thin Films on Substrates," Amer. Cer. Soc. Conf., Minn., MN, April, 1992.

2. J.H. Selverian and D. ONeil, "Strength and Weibull Modulus of Thin Films on Substrates," MRS Fall Conf., Boston, MA, Dec. 3, 1991.

3. J.H. Selverian and H.E. Rebenne, "Effect of CVD Coatings of Al_2O_3+ZrO_2 on the MOR Strength of Si_3N_4 and SiC," Amer. Cer. Soc. Conference, Cincinnati, OH, April, 1991.

4. H. E. Rebenne, "High Temperature Oxidation of Ceramic Coatings on Silicon Nitride and Silicon Carbide-Based Substrates," 91st Annual Meeting of the Amer. Cer. Soc., April 24, 1989, Cincinatti, OH, 1989.

5. D.W. Oblas, C. D'Angelo, V.K. Sarin, and H.E. Rebenne, "Ceramic Coatings to Reduce Contact Stress Damage: Characterization," 26th Automotive Technology Development CCM, Dearborn, MI, Oct. 26, 1988.

6. V. K. Sarin, "Fundamentals of Coating Design," 2nd Intl. Conf. on Surface Modification Technology, Chicago, IL, September, 1988.

7. V. K. Sarin, "Residual Stress Calculations in Coating Configurations Using Finite Element Analysis," 12th Annual Conf. on Composites and Advanced Ceramics, Cocoa Beach, FL, January 17, 1988.

8. V.K. Sarin, "Ceramic Coatings to reduce Ceramic-Ceramic Contact Stress," DOE Coatings for Advanced Heat Engines Workshop, Castine, ME, July 27, 1987.

9. H.E. Rebenne and V.K. Sarin, "Ceramic Coatings to Reduce Contact Stress Damage of Ceramics - Thermodynamic Modeling," 25th Automotive Technology Development CCM, Dearborn, MI, Oct. 19, 1987.

PATENTS

1. "Composite Coatings on Cemented Carbide Substrates," U.S. Patent 4,701,384.

2. "Composite Coatings on Ceramic Substrates," U.S. Patent 4,702,970.

3. "Process for Depositing a Composite Ceramic Coating on a Cemented Carbide Substrate," U.S. Patent 4,745,010.

4. "Ultrathin Laminate Oxide Coatings and Methods," U.S. Patent 4,749,629.

5. "A Process for Depositing a Composite Ceramic Coating on a Hard Ceramic Substrate," U.S. Patent 4,751,109.

6. "A Method for Depositing Composite Coatings," filed 1986.

7. "Composite Coatings on Refractory Substrates," filed 1986.

8. "Oxidation Resistant, High Temperature Thermal Cycling Resistant Coatings on Silicon-Based Substrates and Process for the Production Thereof, filed 1986.

9. "Aluminum Nitride Coated Silicon Nitride-Based Cutting Tools," filed 1987.

10. "Aluminum Nitride Coated Silicon Nitride-Based Cutting Tools," filed 1988.

REFERENCES

ABI86 A. Abid, R. Bensalem, B.J. Sealy, "The thermal stability of AlN", J. Mat. Sci., vol 22, 1301-1304 (1986).

BAB83 G.N. Babini, P. Vicenzini, "Oxidation kinetics of hot-pressed silicon nitride", Progress in Nitrogen Ceramics, 427-438 (1983).

BAR79 P. Barlier, J.P. Torre, "On the influence of a gaseous boundary layer on the oxidation of reaction-bonded silicon nitride at 1400 C", J. Mat. Sci. Lett., vol. 14, 235-237 (1979).

BOC82 P. Boch, J.C. Glandus, J. Jarrige, J.P. LeCompte, J. Mexmain, "Sintering, oxidation and mechanical properties of hot pressed aluminum nitride", Ceramics International, vol. 8(1), 34-40 (1982).

CHE78 J.L. Chermant, A. Deschanvres, and F. Osterstock, in R.C. Bradt, D.P.H. Hasselman, and F.F. Lange (eds.) Fracture Mechanics of Ceramics Vol. 4 Crack Growth and Microstructure, Plenum Press, New York, (1978), p. 891.

COL86 C. Colombier, J. Peng, H. Altena, and B. Lux, "Influence of Trace Impurities on the α-Al_2O_3 CVD in the $AlX_3/CO_2/H_2$-Systems (X=Cl, Br, I)," Refractory & Hard Metals, June, 82-87 (1986)

CS91 *Ceramic Source 1991-1992*, vol. 7, Pub. The American Ceramic Society, Westerville, Ohio, 1992, Tables 101, 136, & 139, p. 310, 321, & 322.

DAN89 C. D'Angelo, H.J. Kim, D.W. Oblas, H. Rebenne, and V.K. Sarin, "Development of Adherent Ceramic Coatings to Reduce Contact Stress Damage of Ceramics," Final Report, DoE Contract 86X95915C, submitted March, (1989).

DAV80 R.W. Davidge, Mechanical Behaviour of Ceramics, Pub. Cambridge Solid State Science Series, Cambridge University Press, (1980), p. 138.

DUT84 S. Dutta, "Sinterability, strength and oxidation of alpha silicon carbide powders", J. Mat. Sci., vol 19, 1307-1313 (1984).

ERV58 G. Ervin, Jr, "Oxidation Behavior of Silicon Carbide", J. American Ceramic Society, vol. 41(9), 347-352 (1958).

FIS51 J. C. Fisher, "Calculation of Diffusion Penetration Curves for Surface and Grain Boundary Diffusion," J. App. Phys., vol. 22(1), 74-7 (1951).

FLI87 P.A. Flinn, D.S. Gardner, and W.D. Nix, "Measurement and Interpretation of Stress in Aluminum-Based Metallization as a Function of Thermal History," IEEE Transactions on Electron Devices, vol. ED-34, no. 3, p. 689-698, March (1987).

FUN84 C.D. Fung, J.J. Kopanski, "Thermal oxidation of 3C silicon carbide single-crystal layers on silicon", Applied Physics Lett., vol 45(7), 757-759 (1984).

GTE81 Advanced Gas Turbine (AGT) Powertrain System Development for Automotive Applications, 2nd semiannual progress report, Contract No. CR-165329, Garrett Turbine Engine Co., Report No. 31-3725(2) (1981).

JOR59 P.J. Jorgensen, M.E. Wadsworth, I.B. Cutler, "Oxidation of Silicon Carbide", J. American Ceramics Soc., vol. 42(12), 613-616 (1959).

JOR61 P.J. Jorgensen, M.E. Wadsworth, I.B. Cutler, "Effects of Water Vapor on Oxidation of Silicon Carbide", J. American Ceramics Soc., vol. 44(6), 258-261 (1961).

KAT83 A.P. Katz, H.A. Lipsitt, T.Mah, and M.G. Mendiratta, J. Mat. Sci., vol. 18, p. 1983, (1983).

KAT87 A.D. Katnani and K.I. Papathomas, "Kinetics and initial stages of oxidation of aluminum nitride: Thermogravimetric analysis and X-ray photoelectron spectroscopy study", J. Vac. Sci. Technol. A, vol. 5(4), 1335-1340 (1987).

KRE85 A. Krell, J. Woltersdorf, E. Pippel, and D. Schulze, Philo. Mag. A, vol. 51(5), p. 765, (1985).

LAC84 W.J. Lackey, D.P. Stinton, G.A. Cerny, L.L. Fehrenbacher, and A.C. Schaffhauser, ORNL Report, ORNL/TM-8959 (1984).

LAV83 V.A. Lavrenko, A.F. Alexeev, "Oxidation of sintered AlN", Ceramics International, vol. 9(3), 80-82 (1983).

LAW75 B.R. Lawn and T.R. Wilshaw, Fracture of Solids, Cambraidge Solid State Science Series, Cambridge University Press, New York, (1975), p. 65.

LIV56 D.T. Livey and P. Murray, J. American Ceramic Society, vol. 39(11), 363, (1956).

LON59 G. Long, L.M. Foster, "Aluminum nitride, a refractory for aluminum to 2000°C", J. American Ceramic Soc., vol. 42(2), 5359 (1959).

MAE89 M. Maeda, K. Nakamura, A. Tsuge, "Scale effect of the testing furnace on the oxidation of silicon nitride ceramics", J. Mat. Sci. Lett., vol. 8, 195-197 (1989).

MEI59 J.L. Meijering and M.L. Verheijke, "Oxidation Kinetics in the Case of Ageing Oxide Films", Acta Metallurgica, 7(5), p. 331-338, (1959).

MIE84 D.M. Mieskowski, T.E. Mitchell, A.H. Heuer, "Bubble Formation in Oxide Scales on SiC", J. American Ceramic Soc., January, C-17, (1984).

NIX89 W. D. Nix, Metall. Trans. A **20A**, 2217 (1989).

OIS60 Y. Oishi and W. D. Kingery, "Self-Diffusion of Oxygen in Single and Polycrystalline Aluminum Oxide," J. Chem. Phys., vol. 33(2), 480-86 (1960).

POR84 F. Porz, F. Thummler, "Oxidation mechanism of porous silicon nitride", J. Mat. Sci., vol. 19, 1283-1295 (1984).

RUF89 A. W. Ruff and S. Jahanmir, "Measurements of Tribological Behavior of Advanced Materials: Summary of U.S. Results on VAMAS Round-Robin No. 2," NISTIR 89-4170, U.S. Dept. of Commerce, Gaithersburg, MD, (1989).

SAT87 T. Sato, K. Haryu, T. Endo, M. Shimada, "High temperature oxidation of hot-pressed aluminum nitride by water vapour", J. Mat. Sci., vol. 22, 2277-2280 (1987).

SCH87 J. Schienle, and J. Smyth, "High Temperature Coating Study to Reduce Contact Stress Damage of Ceramics," Final Report, Contract No. DE-AC05-84R21400, Garrett Turbine Engine Co, (1987).

SCH92 L.S. Schadler and L.C. Noyan, "Experimental Determination of the Strain Transfer Across a Flexible Intermediate Layer in Thin Film Structures as a Function of Flexible Layer Thickness," Mat. Res. Symp. Proc., Vol. 239, 151-156 (1992).

SHA88 T.-L. Sham and V.K. Sarin, "Residual Stress Calculations in Coating Configurations using Finite Element Analysis," Ceramics Eng. and Sci. Proc., Vol. 9 (9,10), 1189-98 (1988).

SIN76a S.C. Singhal, "Thermodynamics and kinetics of oxidation of hot-pressed silicon nitride", J. Mat. Sci., vol. 11, 500-509, (1976).

SIN76b S.C Singhal, "Oxidation kinetics of hot-pressed silicon carbide", J. Mat. Sci., vol 11, 1246-1253 (1976).

SWA89 S.R. Swanson, J. of Engineering Materials and Technology, vol. 111, 145 (1989) .

TAY60 K.M. Taylor, C. Lenie, "Some properties of aluminum nitride", J. Electrochemical Soc., vol. 107(4), 308-314 (1960).

THO90 M.D. Thouless, J. American Ceramic Society, vol. 73(7), p. 2144, (1990).

TIM25 S.P. Timoshenko, "Analysis of Bi-Metal Thermostats," J. Optical Soc. Amer., vol. 11, p.233-255, (1925).

TOR87 E. Tòr ök and A. J. Perry, Thin Solid Films, vol. 153, p. 37, (1987).

TOU75 Y. S. Touloukian, R. K. Kirby, R. E. Taylor, and T. Y. R. Lee, Thermal Expansion - Nonmetallic Solids - vol. 13 - Thermophysical Properties of Matter, Plenum Press, New York, 1975.

WAR84 R. Warren, C-H. Anderson, "Silicon carbide fibers and their potential for use in composite materials. Part II", Composites, vol 15(2), 101-111, (1984).

APPENDIX A - OXIDATION RESULTS

Table A-1. Weight gain as a function of oxidation time for AlN coated sapphire oxidized in static air at 1000°C. The weight gain at a given time was calculated from the original weight and the measured weight after a given oxidation time.

Sample	Original Weight (gm)	Weight Gain as a Function of Time				
		2 hr	8.75	30.5	125	500
A	2.048404	0.022 mg	0.014	0.022	0.011	0.062
B	1.885474	0.332	0.428	0.408	0.493	0.544
C	1.887054	0.192	0.191	0.155	0.066	0.079

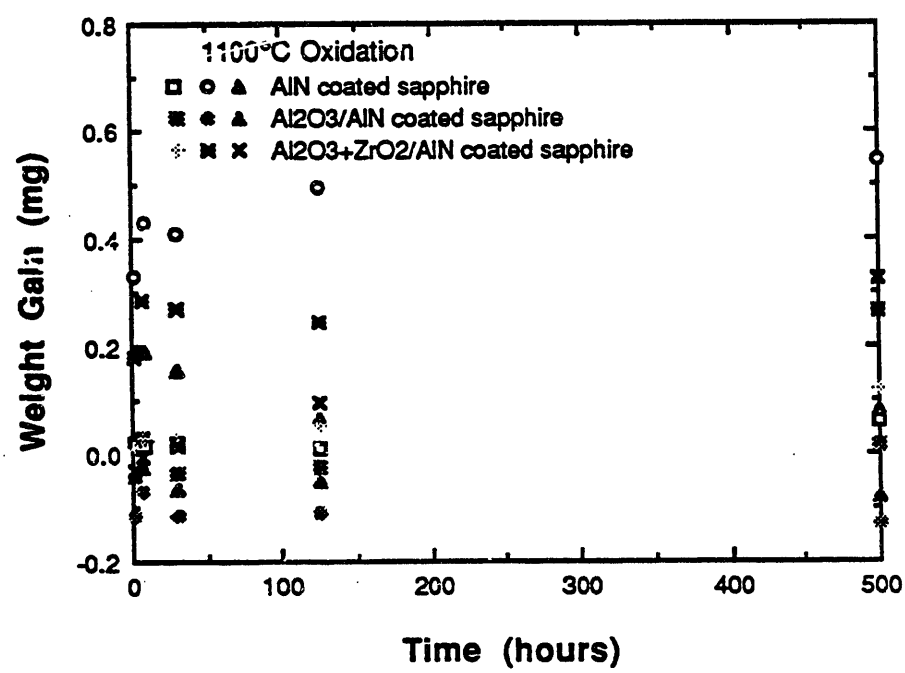

Figure A-1. Weight gain versus time for AlN, Al_2O_3/AlN, and Al_2O_3+ZrO_2/AlN coated sapphire oxidized in static air at 1100°C.

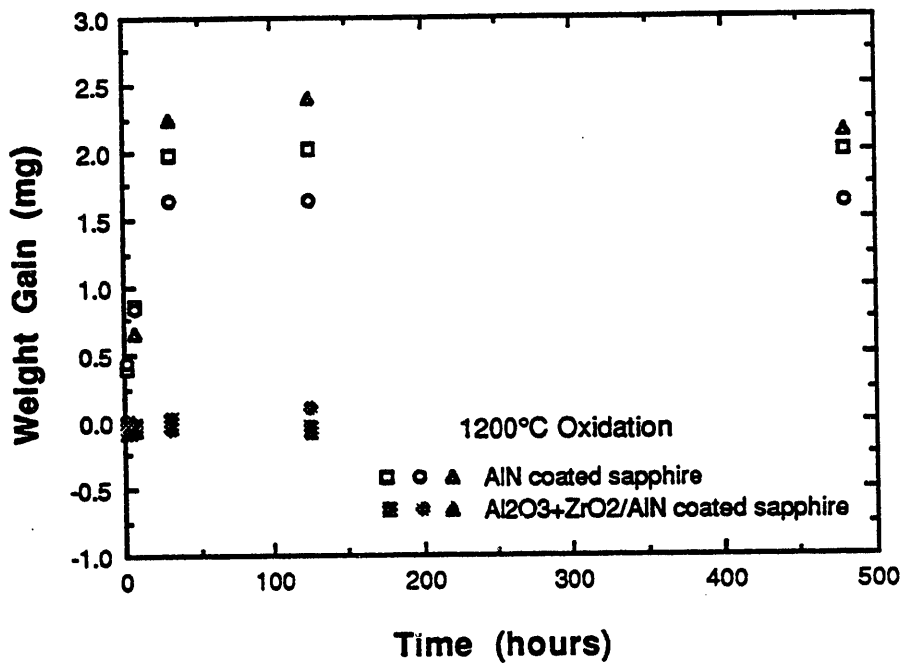

Figure A-2. Weight gain versus time for AlN and $Al_2O_3+ZrO_2/AlN$ coated sapphire oxidized in static air at 1200°C.

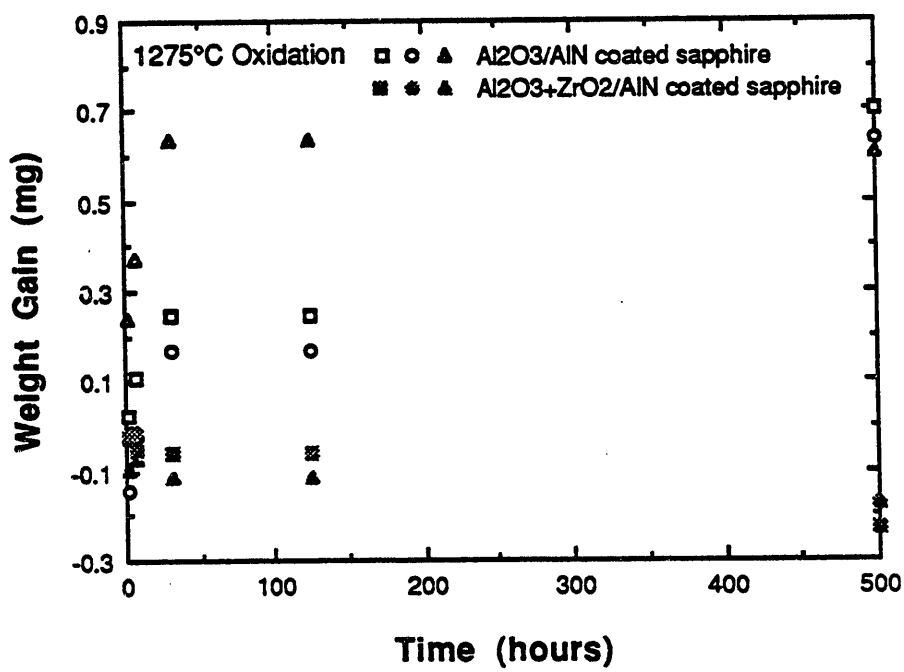

Figure A-3. Weight gain versus time for Al_2O_3/AlN and $Al_2O_3+ZrO_2/AlN$ coated sapphire oxidized in static air at 1275°C.

Table A-2. Phases identified by X-ray diffraction after oxidation in static air. Samples were sapphire with AlN, Al_2O_3/AlN, and Al_2O_3+ZrO_2/AlN coating. Phases associated with substrate reflection are not listed.

Oxidation Time (hours)	Oxidation Temperature		
	1000°C	1200°C	1275°C
AlN coated			
2	α-Al_2O_3	α-Al_2O_3	α-Al_2O_3
8	α-Al_2O_3	α-Al_2O_3	α-Al_2O_3
30	α-Al_2O_3	α-Al_2O_3	α-Al_2O_3
125	α-Al_2O_3	α-Al_2O_3	α-Al_2O_3
500	α-Al_2O_3	---	α-Al_2O_3
Al_2O_3/AlN coated			
2	---	α-Al_2O_3, AlN	α-Al_2O_3, AlN
8	---	α-Al_2O_3, AlN	α-Al_2O_3, AlN
30	---	α-Al_2O_3, AlN	α-Al_2O_3, AlN
125	---	α-Al_2O_3	α-Al_2O_3
500	---	α-Al_2O_3	---
Al_2O_3+ZrO_2/AlN coated			
2	---	α-Al_2O_3	α-Al_2O_3, ZrO_2
8	---	α-Al_2O_3, ZrO_2	α-Al_2O_3, ZrO_2
30	---	α-Al_2O_3, ZrO_2	α-Al_2O_3, ZrO_2
125	---	α-Al_2O_3, ZrO_2	α-Al_2O_3, ZrO_2
500	---	α-Al_2O_3, ZrO_2	---

Table A-3. Weight gain as a function of oxidation time for Al_2O_3/AlN coated sapphire oxidized in static air at 1100°C, 1200°C, and 1275°C. The weight gain at a given time was calculated from the original weight and the measured weight after a given oxidation time.

Sample	Original Weight (gm)	Weight Gain as a Function of Time				
		2 hr	8	30	125	500
1100°C						
A	1.678948	---	0.032	-0.033	-0.023	0.017
B	1.788780	-0.115 mg	-0.070	-0.115	-0.112	-0.129
C	1.697396	-0.041	-0.026	-0.066	-0.051	-0.082
1200°C						
A	1.417758	-0.105	---	---	---	---
B	1.296831	-0.077	---	---	---	---
C	1.229500	-1.080	---	---	---	---
1275°C						
A	1.483679	-0.023	-0.056	-0.059	---	---
B	1.433669	-0.019	-0.014	-0.061	---	---
C	1.464726	-0.098	-0.074	-0.111	---	---

Table A-4. Weight gain as a function of oxidation time for $Al_2O_3+ZrO_2/AlN$ coated sapphire oxidized in static air at 1100°C, 1200°C, and 1275°C. The weight gain at a given time was calculated from the original weight and the measured weight after a given oxidation time.

Sample	Original Weight (gm)	Weight Gain as a Function of Time				
		2 hr	8	30	125	500
1100°C						
A	1.529552	0.008 mg	0.028	0.023	0.053	0.120
B	1.430195	0.181	0.285	0.268	0.245	0.265
C	1.582685	-0.030	-0.005	0.015	0.095	0.325
1200°C						
A	1.280131	-0.006	-0.013	0.013	---	---
B	1.250632	-0.077	-0.072	-0.061	---	---
C	1.213560	-0.080	-0.060	-0.046	---	---
1275°C						
A	1.448246	0.024	0.111	0.244	---	---
B	1.302016	-0.146	-0.026	0.168	---	---
C	1.467992	0.239	0.372	0.633	---	---

Table A-5. Phases identified by X-ray diffraction after 500 hours of oxidation in static air. Samples include uncoated and AlN coated RBSN, SSC, and HSN.

Sample	Major Phases	Minor Phases
Temperature = 1100°C		
Uncoated RBSN	α-Si_3N_4	β-Si_3N_4, SiO_2
Uncoated SSC	SiC(8H), SiC(12H)	SiO_2
Uncoated HSN	β-Si_3N_4	α-$Y_2Si_2O_7$, Y_2SiO_5, SiO_2
AlN/RBSN	α-Al_2O_3, α-Si_3N_4	α-Si_3N_4, β-Si_3N_4, SiO_2
AlN/SSC	α-Al_2O_3, SiC(8H), SiC(12H)	-----
AlN/HSN	α-Al_2O_3	β-Si_3N_4, α-$Y_2Si_2O_7$, Y_2SiO_5, SiO_2
Temperature = 1200°C		
Uncoated RBSN	SiO_2, α-Si_3N_4	β-Si_3N_4(?)*
Uncoated SSC	SiC(12H)	SiO_2
Uncoated HSN	β-Si_3N_4	SiO_2, $Y_2Si_2O_7$
AlN/RBSN	α-Al_2O_3	β-Si_3N_4, SiO_2(?)
AlN/SSC	SiC(12H), α-Al_2O_3	SiO_2(?)
AlN/HSN	β-Si_3N_4	$Y_2Si_2O_7$, α-Al_2O_3, SiO_2(?)
Temperature = 1275°C		
Uncoated RBSN	α-Si_3N_4, SiO_2	β-Si_3N_4
Uncoated SSC	SiC(12H)	SiO_2, α-Si_3N_4(?)
Uncoated HSN	$Y_2Si_2O_7$	β-Si_3N_4, SiO_2
AlN/RBSN	α-Al_2O_3	Si_3N_4(?)
AlN/SSC	SiC(12H), α-Al_2O_3	α-Si_3N_4(?), SiO_2(?)
AlN/HSN	AlN	$Y_2Si_2O_7$

* The question mark denotes uncertainty.

Table A-6. Phases identified by X-ray diffraction after 500 hour oxidation in static air. Samples had coating of AlN, Al_2O_3/AlN, and Al_2O_3+ZrO_2/AlN. Phases associated with substrate reflection are not listed.

Sample	Oxidation Temperature		
	1000°C	1200°C	1275°C
AlN coated			
RBSN	α-Al_2O_3	α-Al_2O_3	α-Al_2O_3
SSC	α-Al_2O_3	α-Al_2O_3	α-Al_2O_3
HSN	α-Al_2O_3	α-Al_2O_3	AlN
Al_2O_3/AlN coated			
RBSN	---	α-Al_2O_3, AlN	α-Al_2O_3, AlN, AlON(?)
SSC	---	α-Al_2O_3, AlN	α-Al_2O_3, AlN
HSN	---	α-Al_2O_3, AlN(?), AlON(?)	α-Al_2O_3, AlN(?), AlON(?)
Al_2O_3+ZrO_2/AlN coated			
RBSN	---	α-Al_2O_3, ZrO_2	α-Al_2O_3, ZrO_2
SSC	---	α-Al_2O_3, ZrO_2	α-Al_2O_3, AlN, ZrO_2(?)
HSN	---	α-Al_2O_3, ZrO_2, AlN	ZrO_2, AlN(?), AlON(?)

* the question mark indicates uncertainty.

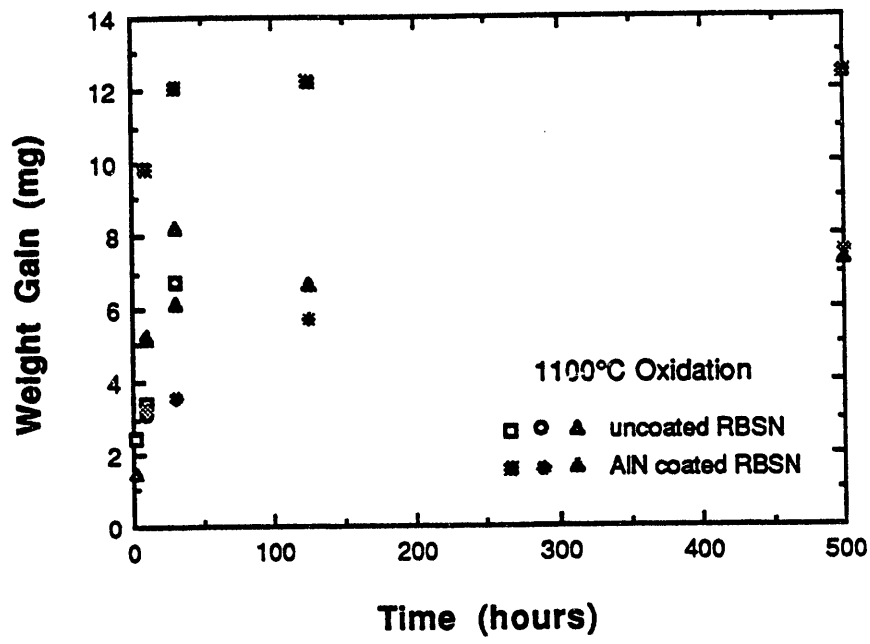

Figure A-4. Weight gain versus time for uncoated and AlN coated RBSN oxidized in static air at 1100°C.

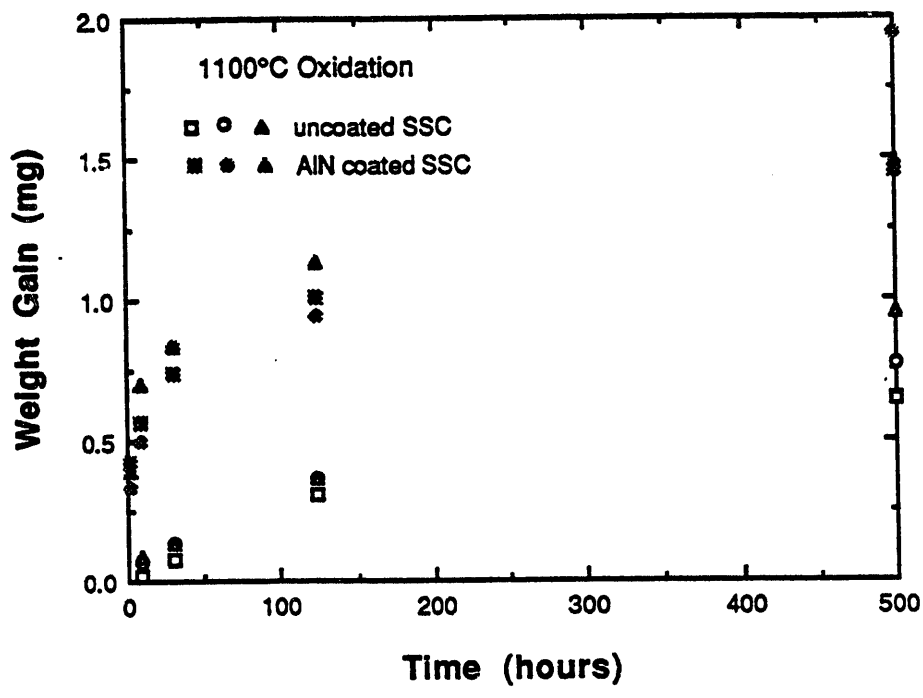

Figure A-5. Weight gain versus time for uncoated and AlN coated SSC oxidized in static air at 1100°C.

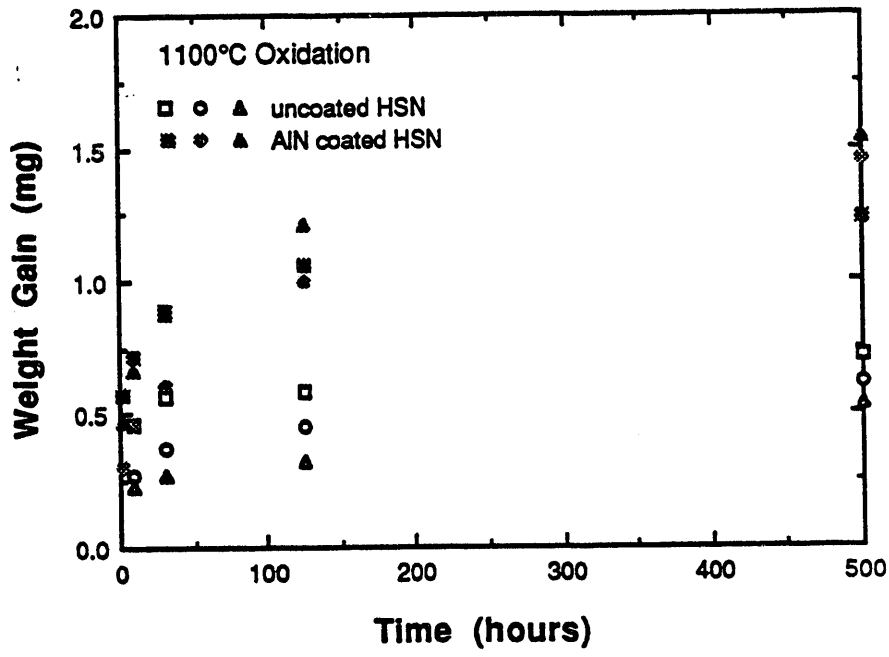

Figure A-6. Weight gain versus time for uncoated and AlN coated HSN oxidized in static air at 1100°C.

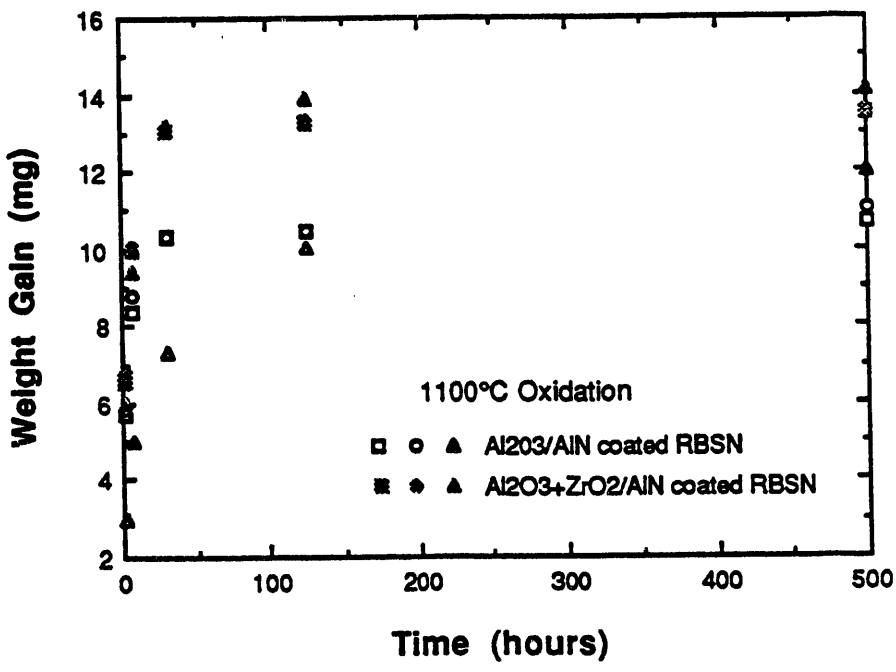

Figure A-7. Weight gain versus time for uncoated and Al_2O_3/AlN and Al_2O_3+ZrO_2/AlN coated RBSN oxidized in static air at 1100°C.

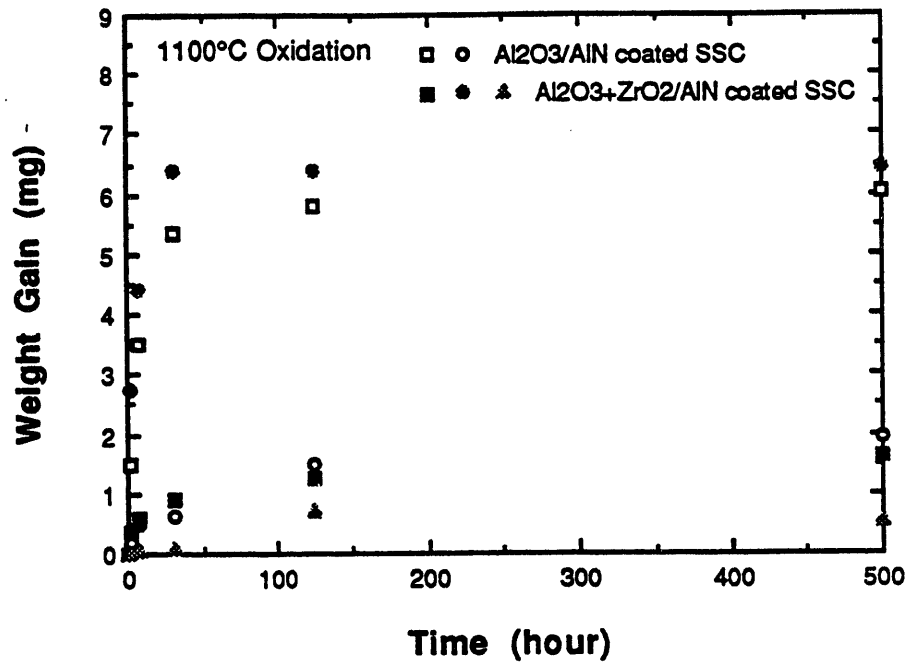

Figure A-8. Weight gain versus time for uncoated and Al_2O_3/AlN and Al_2O_3+ZrO_2/AlN coated SSC oxidized in static air at 1100°C.

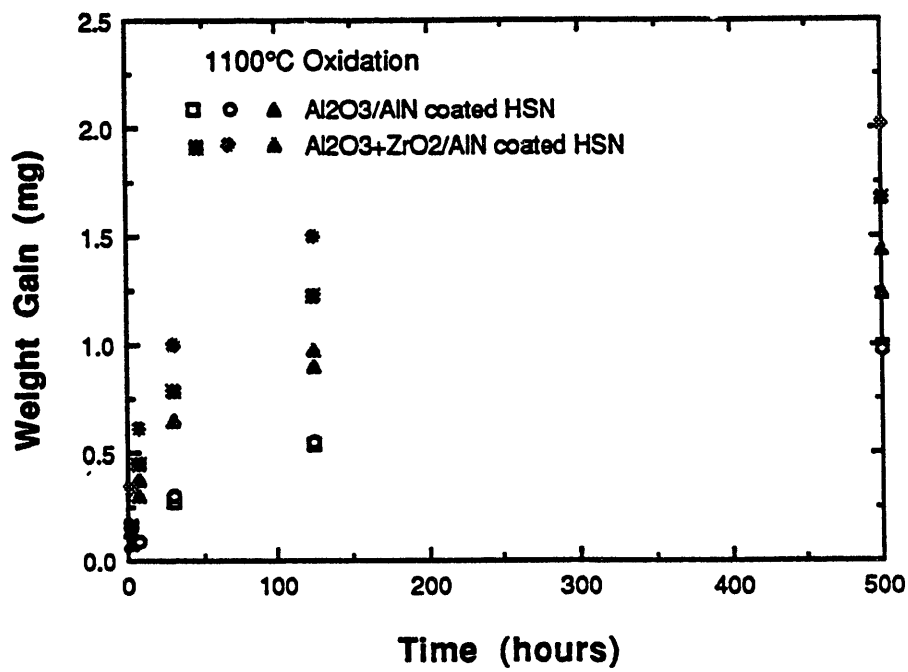

Figure A-9. Weight gain versus time for uncoated and Al_2O_3/AlN and Al_2O_3+ZrO_2/AlN coated HSN oxidized in static air at 1100°C.

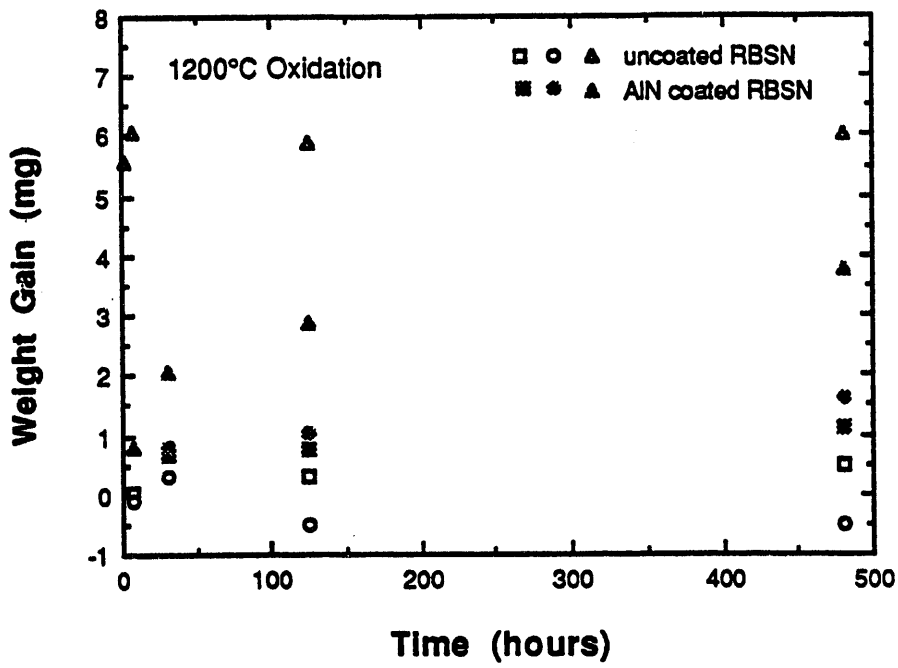

Figure A-10. Weight gain versus time for uncoated and AlN coated RBSN oxidized in static air at 1200°C.

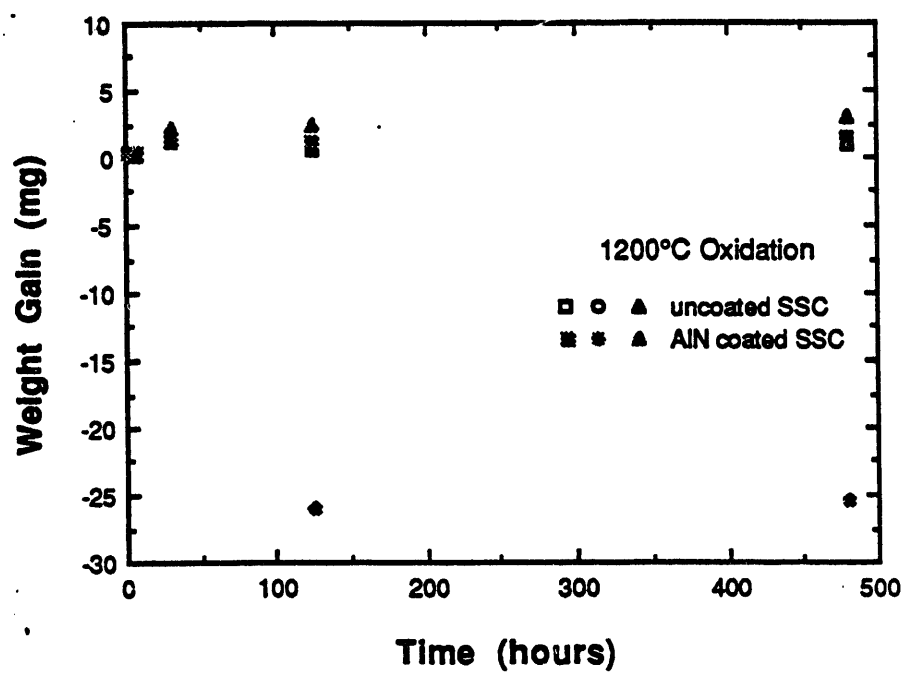

Figure A-11. Weight gain versus time for uncoated and AlN coated SSC oxidized in static air at 1200°C.

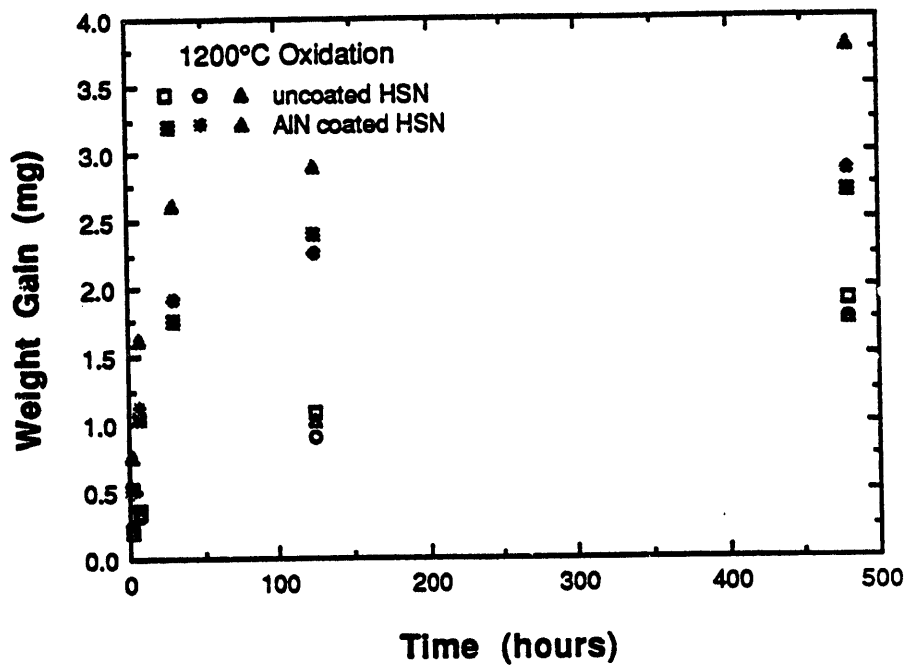

Figure A-12. Weight gain versus time for uncoated and AlN coated HSN oxidized in static air at 1200°C.

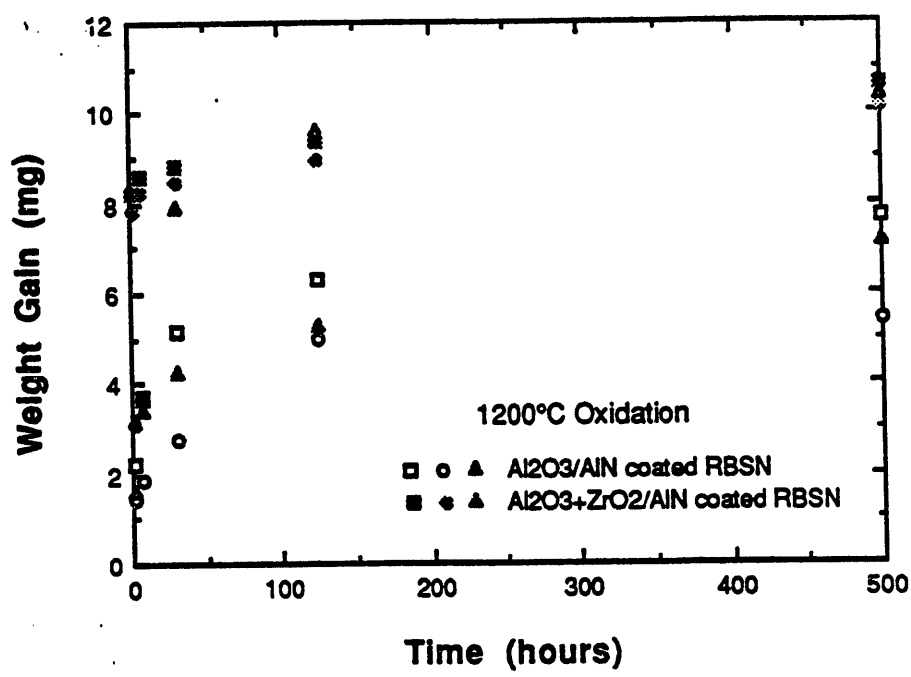

Figure A-13. Weight gain versus time for Al_2O_3/AlN and Al_2O_3+ZrO_2/AlN coated RBSN oxidized in static air at 1200°C.

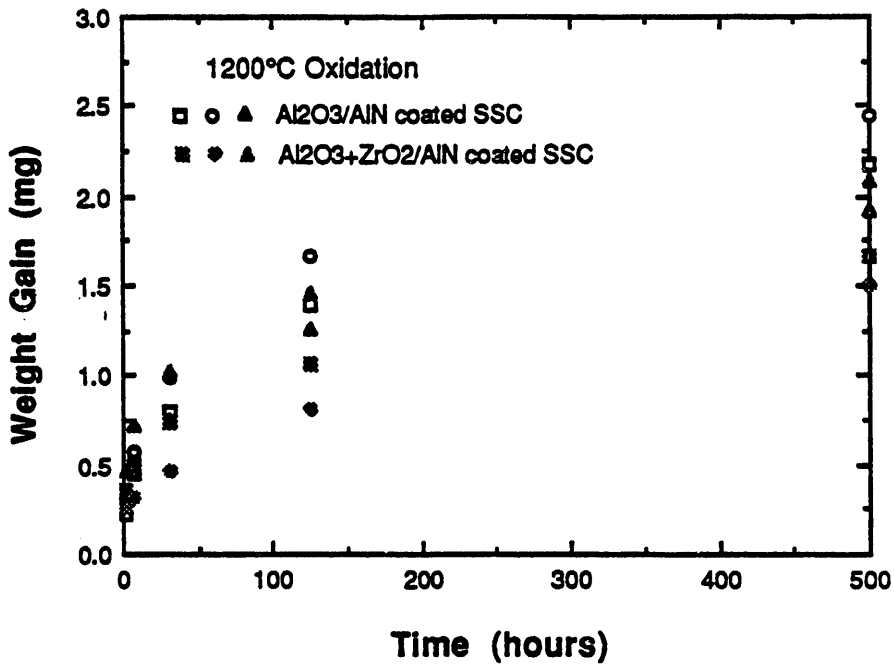

Figure A-14. Weight gain versus time for Al_2O_3/AlN and Al_2O_3+ZrO_2/AlN coated SSC oxidized in static air at 1200°C.

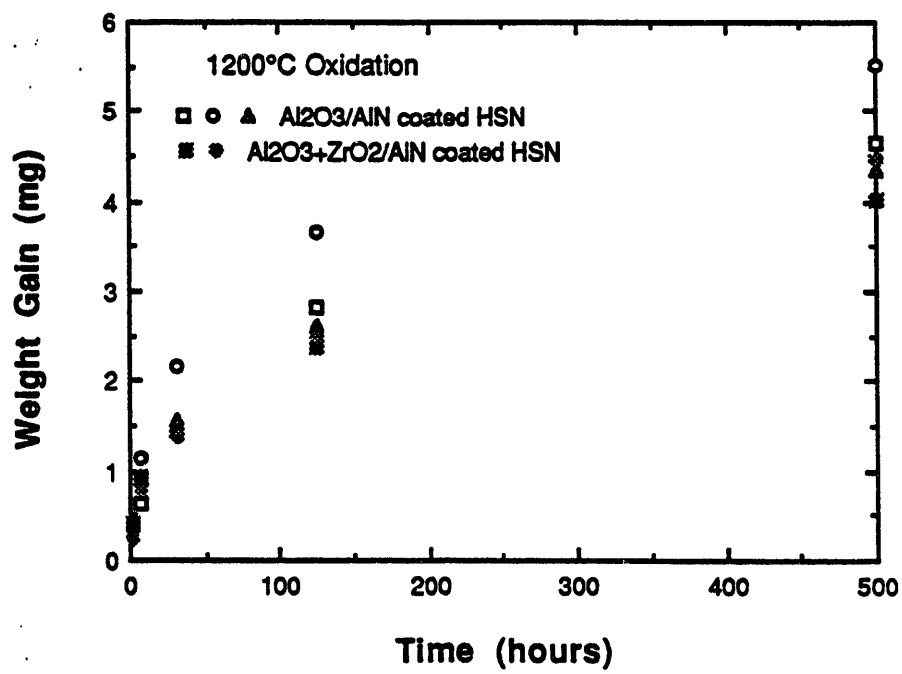

Figure A-15. Weight gain versus time for Al_2O_3/AlN and Al_2O_3+ZrO_2/AlN coated HSN oxidized in static air at 1200°C.

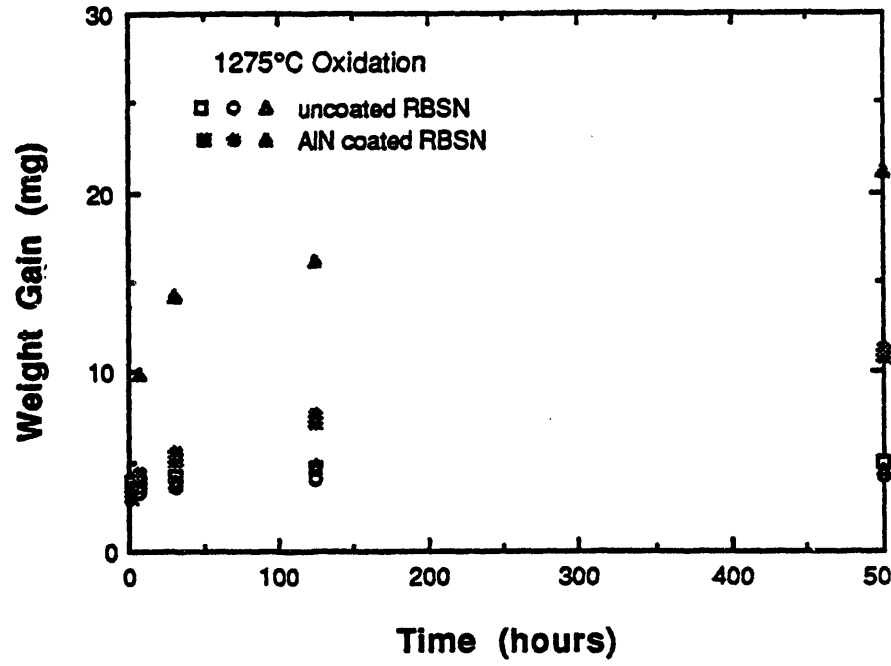

Figure A-16. Weight gain versus time for uncoated and AlN coated RBSN oxidized in static air at 1275°C.

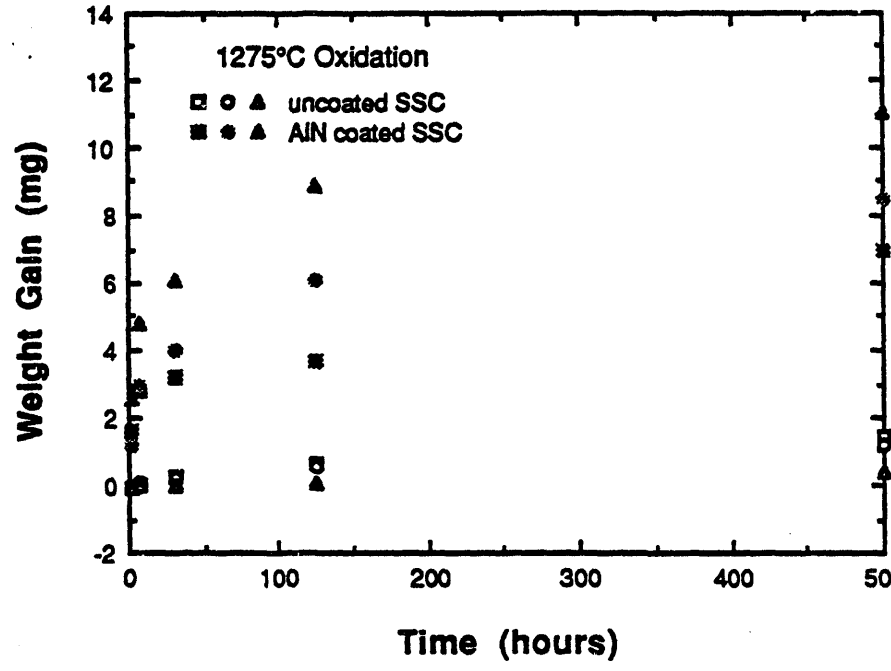

Figure A-17. Weight gain versus time for uncoated and AlN coated SSC oxidized in static air at 1275°C.

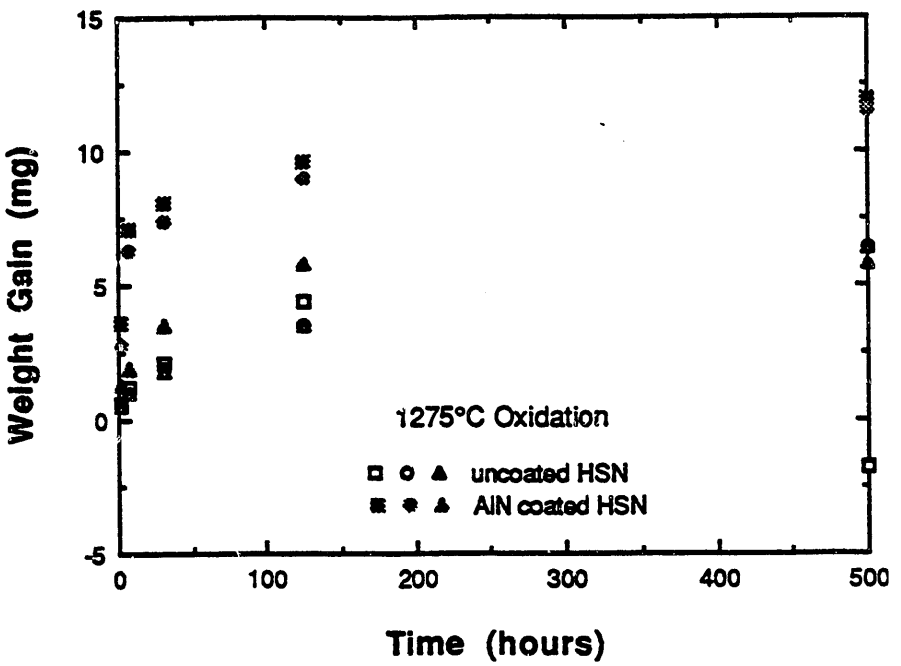

Figure A-18. Weight gain versus time for uncoated and AlN coated HSN oxidized in static air at 1275°C.

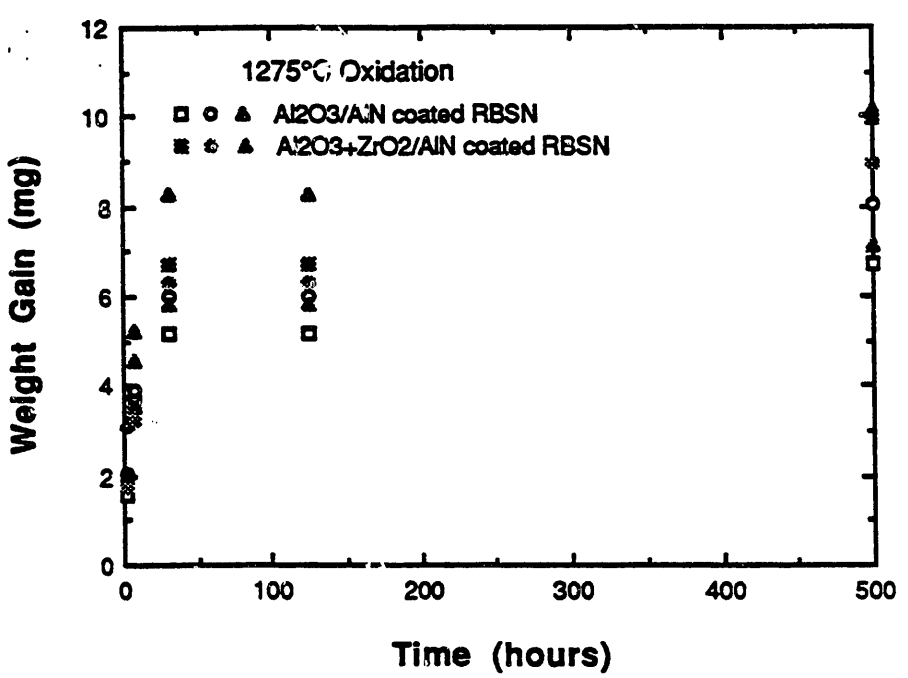

Figure A-19. Weight gain versus time for Al_2O_3/AlN and Al_2O_3+ZrO_2/AlN coated RBSN oxidized in static air at 1275°C.

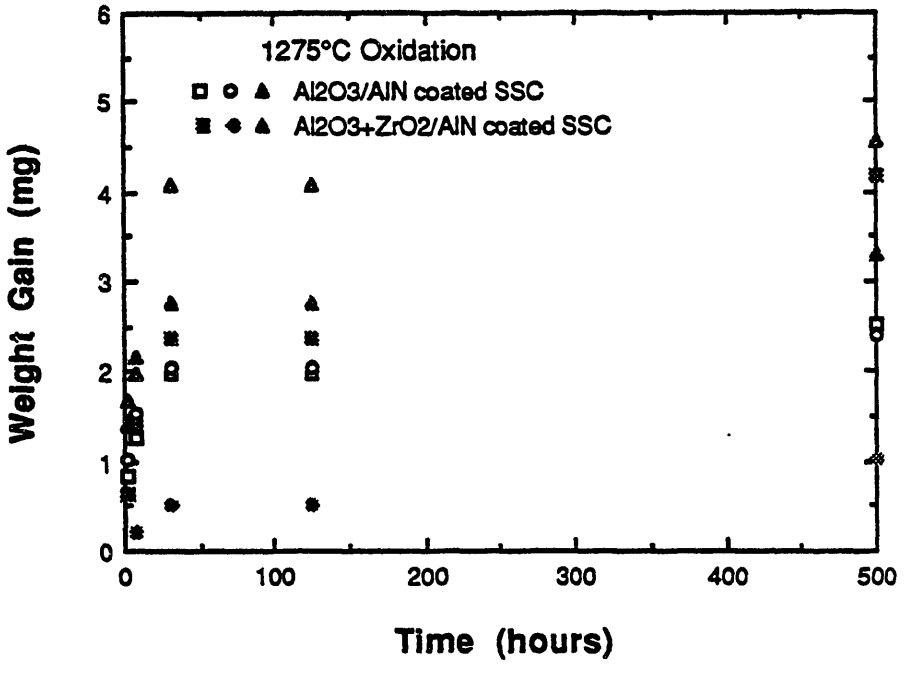

Figure A-20. Weight gain versus time for Al_2O_3/AlN and Al_2O_3+ZrO_2/AlN coated SSC oxidized in static air at 1275°C.

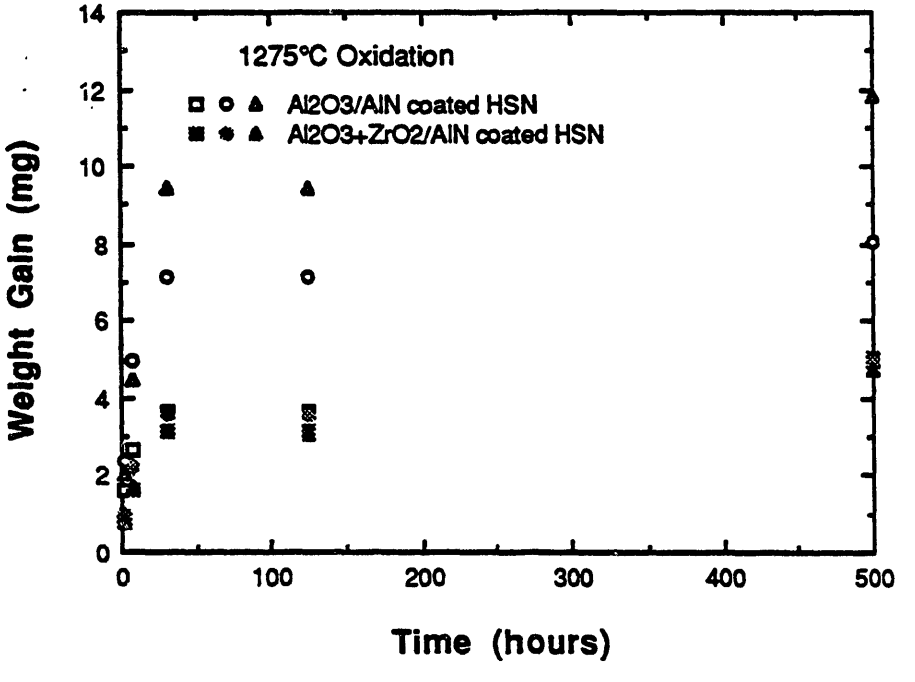

Figure A-21. Weight gain versus time for Al_2O_3/AlN and Al_2O_3+ZrO_2/AlN coated HSN oxidized in static air at 1275°C.

APPENDIX B - METHOD TO MEASURE FRACTURE STRESS AND FRACTURE TOUGHNESS OF COATINGS ON SUBSTRATES

SUMMARY

Conventional mechanical property measurement techniques usually cannot be applied to thin ceramic coatings because of the small amount of material involved. A method is described to determine the ultimate tensile strength, fracture toughness, Weibull modulus, and surface energy of micron-sized ceramic coatings on substrates. This technique is based on measuring the radius of curvature of a coated substrate, and equating the resulting calculated stress with a theoretical shear-lag stress distribution model using a force balance. The properties of chemical vapor deposited coatings of Al_2O_3 and TiN were measured on SiC and Si_3N_4 substrates. The fracture stresses of these coatings were 190 - 480 MPa, the fracture toughnesses were 0.4 - 1.1 $MPa\sqrt{m}$, the Weibull modulii were 10 - 28, and the surface energies were 0.3 - 1.6 J/m^2. This work has shown that the tensile strength of thin brittle coatings can be approximated by bulk values, however, the fracture toughness of a coating can be significantly lower than bulk values.

INTRODUCTION

In coatings deposited at elevated temperatures, where the coating and substrate materials have different coefficients of thermal expansion, large stresses are generated in the coating after cooling to room temperature. If tensile, these stresses often lead to cracking of the coating, Figure B-1. Nitride, carbide, and oxide chemical vapor deposited (CVD) coatings on silicon nitride substrates for cutting tool applications are examples of coatings which crack on cooling. The technique presently described can be used for coatings deposited by any technique as long as the coating cracks due to thermal stresses and the deposition stress is known.

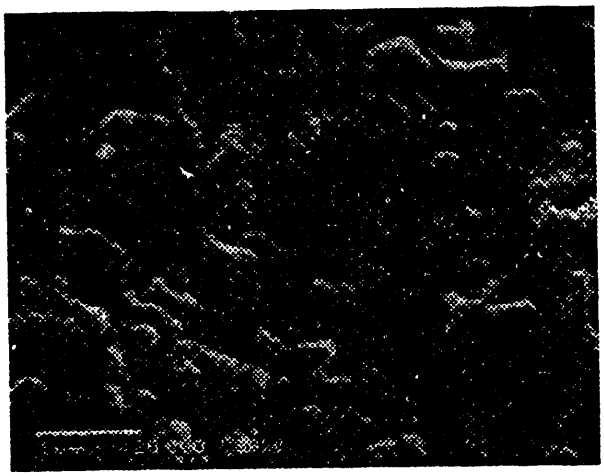

Figure B-1. Scanning electron micrograph of a crack in a coating.

As a coated substrate cools, stress builds up in the coating, Figure B-2. The stress component we are most concerned with is the in-plane normal stress. The word "stress" is used here to denote this component, and for most ceramic coatings this stress can be described by elastic relationships. Since the coating is a ceramic it is described by a distribution of fracture strengths. Once the fracture stress of the weakest part of the coating is reached, the coating will crack (σ_f in Figure B-2). During continued cooling, the peak stress increases, additional cracks form in the coating, and the overall stress (σ_m) is relaxed. The serrations in Figure B-2 indicate the drop in stress due to cracking and their magnitudes are exaggerated. The coating does not crack again until it is cooled further because of the distribution of failure strengths and because the remaining uncracked coating has a smaller volume and therefore a higher failure strength. The relationship between the stressed volume and failure strength of a ceramic is described by Eq. (B-1) from Davidge [DAV80]:

$$\frac{\sigma_1}{\sigma_2}=\left(\frac{V_2}{V_1}\right)^{1/m} \qquad \text{(B-1)}$$

where V_1 is stressed volume 1, V_2 is stressed volume 2, σ_1 is the failure stress for volume V_1, σ_2 is the failure stress for volume V_2, and 'm' is the Weibull modulus of the material.

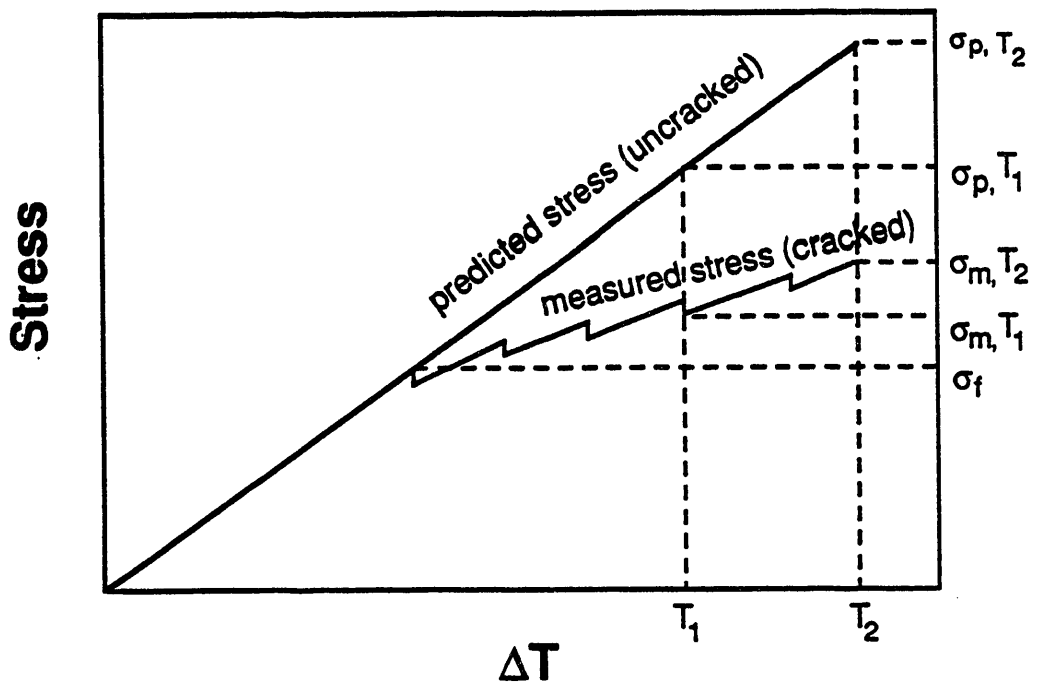

Figure B-2. Schematic of stress versus ΔT plot for a cracked ceramic coating on a substrate. ΔT is the deposition temperature minus the instantaneous temperature, σ_p is the predicted stress at T_1 and T_2 (Eq. B-3), σ_m is the measured stress at T_1 and T_2 (Eq. B-4), and σ_f is the fracture stress of the coating.

The drop in stress that occurred from cracking during cooling of a coated substrate was exploited in this research to extract material properties for the coating. The objective of the study was to determine fracture strength, fracture toughness, and Weibull modulus for a range of coating-substrate material systems by equating the predicted theoretical residual thermal stress

in the coating (taking into account the stress distribution between cracks in the coating) to the experimentally measured average stress in the coating.

No previous technique has been described which determines the fracture stress of thin coatings *in situ* on a substrate. In the present study, the theory and methodology are presented for determining the fracture stress (σ_f), fracture toughness (K_{Ic}), and Weibull modulus (m) of brittle thin coatings. A useful function of this technique is to study the effect of varying the deposition parameters or microstructure on the strength and Weibull modulus of a coating. An example of this last application is provided as an example.

Stresses in Coatings - Theory

Stresses in Uncracked Coatings

The in-plane stress in a narrow flat bimaterial strip (consisting of materials 1 and 2) generated by a change in temperature was derived by Timoshenko [TIM25].

$$\frac{1}{\rho} = \frac{(\alpha_2 - \alpha_1)(T_d - T_i)}{\frac{t}{2} + \frac{2(E_1 I_1 + E_2 I_2)}{t}\left(\frac{1}{E_1 t_1} + \frac{1}{E_2 t_2}\right)} \tag{B-2}$$

$$\sigma = \frac{1}{\rho}\left(\frac{2}{t t_1}(E_1 I_1 + E_2 I_2) + \frac{t_1 E_1}{2}\right) \tag{B-3}$$

where ρ is the radius of curvature of the strip, α is the coefficient of thermal expansion, T_i is the final temperature, T_d is the deposition temperature, E is Young's modulus, I is the moment of inertia, $t_{1,2}$ are the individual layer thicknesses, and t is the total thickness ($t=t_1+t_2$). The geometry of the beam is shown in Figure B-3. To convert from narrow beams to wide beams; $E/(1-\upsilon^2)$ is substituted for E; and $I = t^3/12$ in Eqs. (B-2) and (B-3), where υ is Poissons ratio.

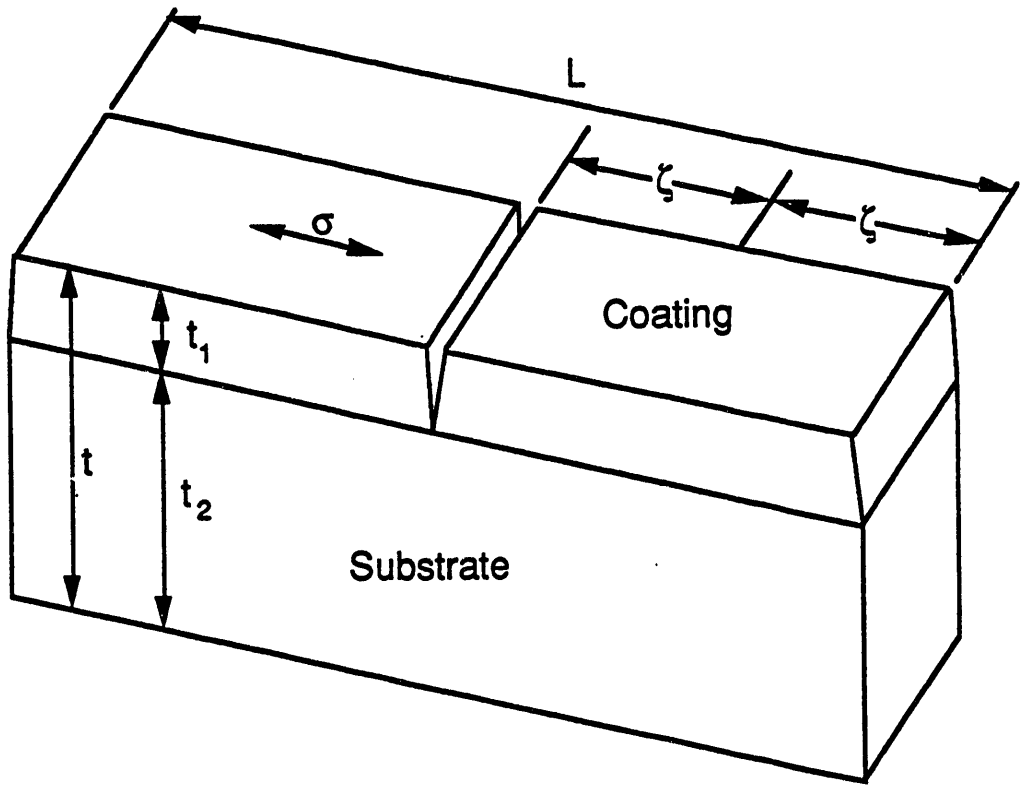

Figure B-3. Schematic of coating on substrate with a single crack. The ends are treated as crack faces. The relative size of the coating was greatly exaggerated to show detail.

The coefficient of thermal expansion and Young's modulus of the materials are treated as temperature dependent quantities and Eqs. (B-2) and (B-3) are numerically integrated to solve for the stress in the coating. Treating the coefficient of thermal expansion as a temperature independent constant can lead to significant errors in materials where these coefficients are strong functions of temperature.

Equation (B-3) was used to predict the stress in an uncracked coating on a substrate subjected to a change in temperature. This predicted stress was referred to as σ_p in Figure B-2. Use of Eq. (B-3) assumed that the coating was deposited with a known stress at the deposition temperature (assumed 0 in this work) and was crack free. Equation (B-3) gave the maximum stress in

material 1, which we treated as the coating. The stress in a thin coating is nearly uniform through the thickness, and the stress in Eq. (B-3) was set equal to the stress in the coating. For a "thin" coating, the stress was independent of coating and substrate thicknesses. For material systems of interest in this study, a coating is considered thin if it was less than 10% of the substrate thickness. Figure B-4 shows the bending and axial contributions to the stress in a coating as a function of relative coating to substrate thickness from Equation (B-3). At coating thicknesses less than 10% of the substrate thickness, most of the stress is due to axial loading, and hence, will scale as the coating thickness changes. A "thin film" approximation to Eq. (B-3) was derived by setting t_1 to zero in the relevant terms [FLI87];

$$\sigma = \frac{E_2 t_2^2}{6 t_1 (1-\upsilon_2^2)} \left(\frac{1}{\rho_c} - \frac{1}{\rho_{uc}} \right) \tag{B-4}$$

where subscripts 'c' and 'uc' on ρ refer to the coated and uncoated strip respectively. The term in the parenthesis is used to correct for nonflat uncoated strips. If the uncoated strip is flat $1/\rho_c$ approaches zero and Eq. (B-3) is regained, with $t_1 = 0$. The primary advantage of Eq. (B-4) over Eq. (B-3) is that only substrate properties and the coating thickness are needed to calculate stress in the coating. Measured radii of curvature were substituted into Eq. (B-4) to arrive at a value for the average stress in the coating. This stress was valid for coatings which are cracked or plastically deformed and was referred to as σ_m (measured stress) in Figure B-2.

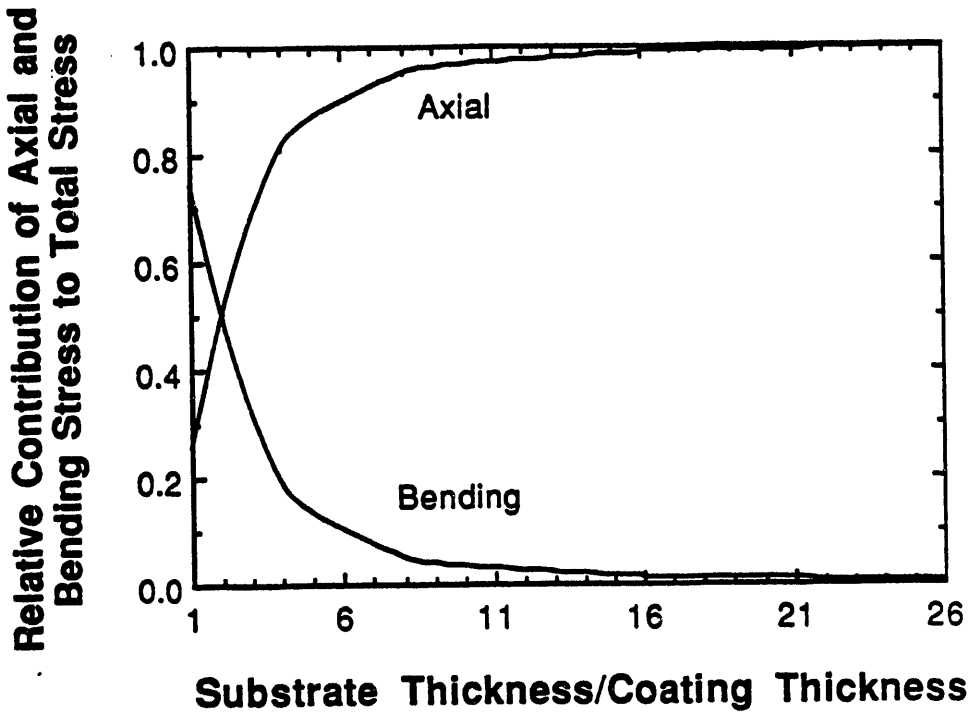

Figure B-4. At coating thicknesses less than 10% of the substrate thickness most of the stress in the coating was due to the axial component and was therefore independent of the coating and substrate thicknesses.

Stresses in Cracked Coatings

When a coating cracks, stress relaxation occurs in the coating around the crack. The in-plane stress is bounded by zero stress at the crack surface and reaches a steady state level "far" from the crack. The distance over which the stress is reduced is related to the elastic properties of the coating and substrate and to the thickness of the coating. Swanson [SWA89] described the stress distribution in fiber-reinforced materials near a crack, commonly known as shear-lag. It can be applied to thin coatings by considering the fiber as the coating material, and the surrounding matrix as the substrate. His model considered approximate stress distributions, and the equilibrium was considered in an average sense through the thickness of a cracked layer.

Swanson's treatment was for a fiber in a ply within a composite. However, since shear-lag is a general phenomenon, the form of the shear-lag distribution in a ply near a crack should be similar to that in a coating near a crack.

The in-plane normal stress distribution in a fiber near a free surface (a crack) was given by Swanson as:

$$\sigma(x) = \sigma_p\{\tanh(\beta\zeta)\sinh(\beta x) - \cosh(\beta x) + 1\} \tag{B-5}$$

where

$$\beta^2 = \frac{G_f}{t_f}\left\{\frac{1}{t_f Q_f} + \frac{1}{t_m Q_m}\right\} \tag{B-6a}$$

$$Q_f = \frac{E_f}{2(1-\upsilon_f^2)} \quad \text{and} \quad Q_m = \frac{E_m}{2(1-\upsilon_m^2)} \tag{B-6b}$$

'x' is the position along the coating between cracks (x = 0 is the crack face position), σ_p is the stress far from the crack for noninteracting cracks, ζ is one-half of the distance between cracks, G_f is the shear modulus of the fiber, $t_{f,m}$ is one-half the thickness of the fiber or matrix, and $E_{f,m}$ is Young's modulus of the fiber or matrix. For the case of a coating on a substrate t_f and t_m were set to the thickness of the coating and substrate, respectively, resulting in;

$$\beta^2 = \frac{G_1}{t_1}\left\{\frac{1}{t_1 Q_1} + \frac{1}{t_2 Q_2}\right\} \tag{B-7}$$

Figure B-5 shows a plot of normalized stress versus distance from a crack face in a coating. The shear-lag stress distribution shown in Figure B-5 is for a 4.7 microns thick Al_2O_3 coating on a SiC substrate for crack spacings of 50, 10, and 5 microns.

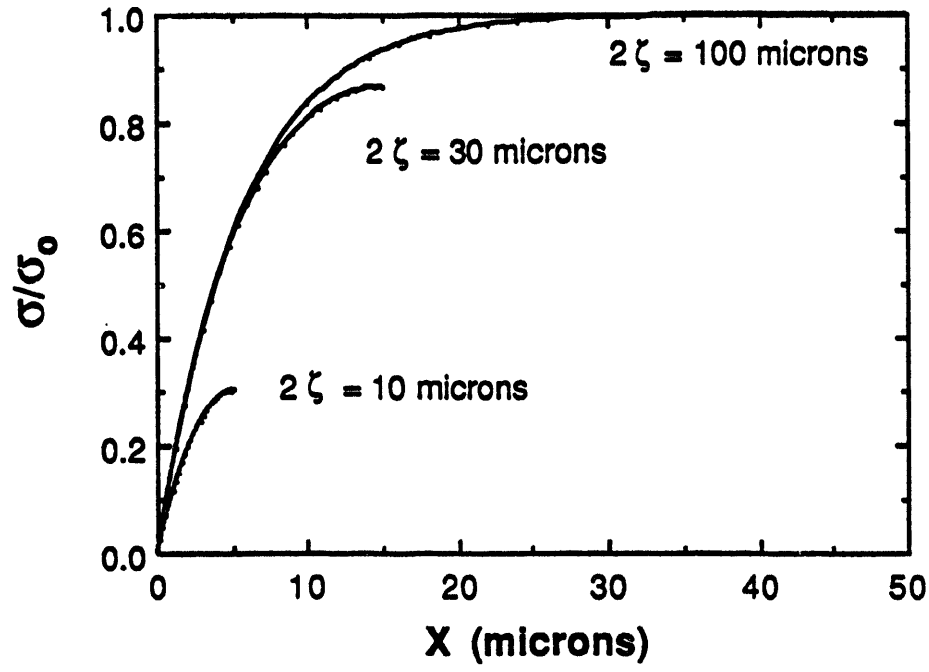

Figure B-5. Plot of the stress distribution in a 4.7 microns Al_2O_3 coating on a SiC substrate according to Eq. (B-5) for three different crack spacings (10, 30, and 100 microns). The crack is located at x = 0.

Determination of the Weibull Modulus - Theory

The difference between the predicted stress in an uncracked coating σ_p (calculated with Eq. (B-3)) and the measured stress in the cracked coating σ_m (calculated with Eq. (B-4)) was used to determine the number of cracks at the temperature of interest. The experimentally determined average stress (σ_m) was set equal to the integral of the theoretical stress, including reductions due to shear-lag drops at the crack faces, Figure B-6.

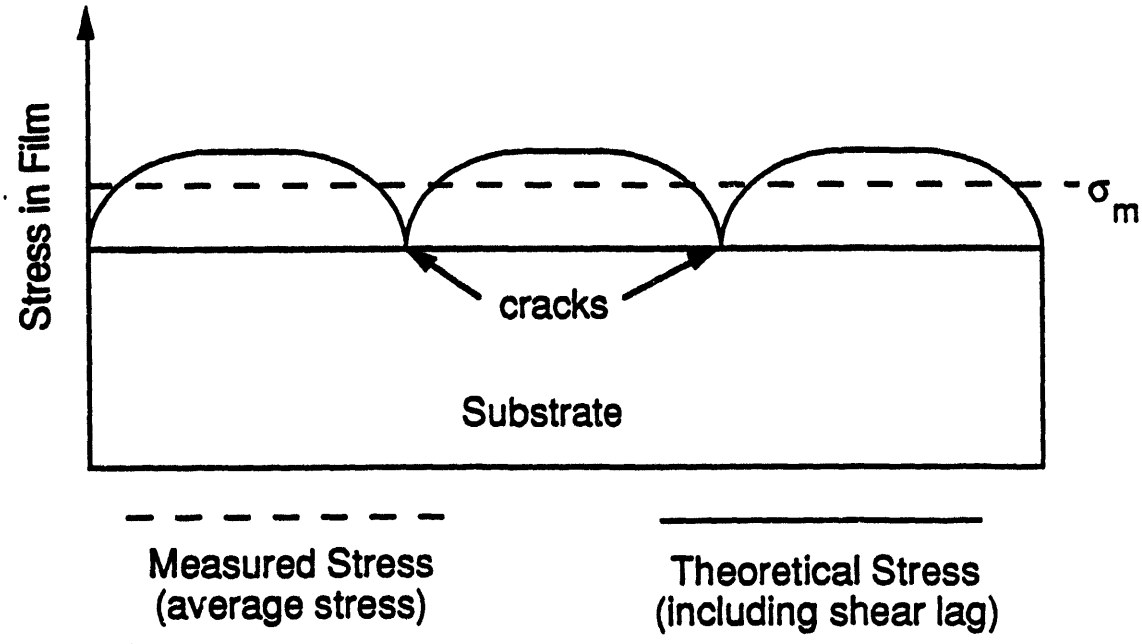

Figure B-6. Plot of theoretical stress in coating and measured stress in coating.

The presence of a crack in a coating caused a drop off in stress near the free edge in accordance with Eq. (B-5). Figure B-7 shows the average stress in a coating as a function of the number of cracks (NC). At a certain crack spacing the stress fields around the cracks begin to interact and the plot of stress versus the number of cracks becomes nonlinear. Equation (B-8) was used to solve for the number of cracks in a coating. The only unknown (NC) was solved for by an iterative procedure.

$$\sigma_m = \frac{2(NC+1)}{L} \int_0^{\zeta} \sigma_p \{\tanh(\beta\zeta)\sinh(\beta x) - \cosh(\beta x) + 1\}\, dx \qquad \text{(B-8)}$$

where $\zeta = \frac{L}{2(NC+1)}$,

σ_m is the measured stress in the cracked coating, σ_p is the calculated stress in the uncracked coating (from Eq. (B-3)), and L is the total length of the sample. The limits on the integral are determined by the length of the coating between cracks, where that length equals 2ζ. The factor of 2 in Eq. (B-8) arises because the stress distribution in the coating is integrated only over one-half of the distance between cracks due to the symmetry of the problem.

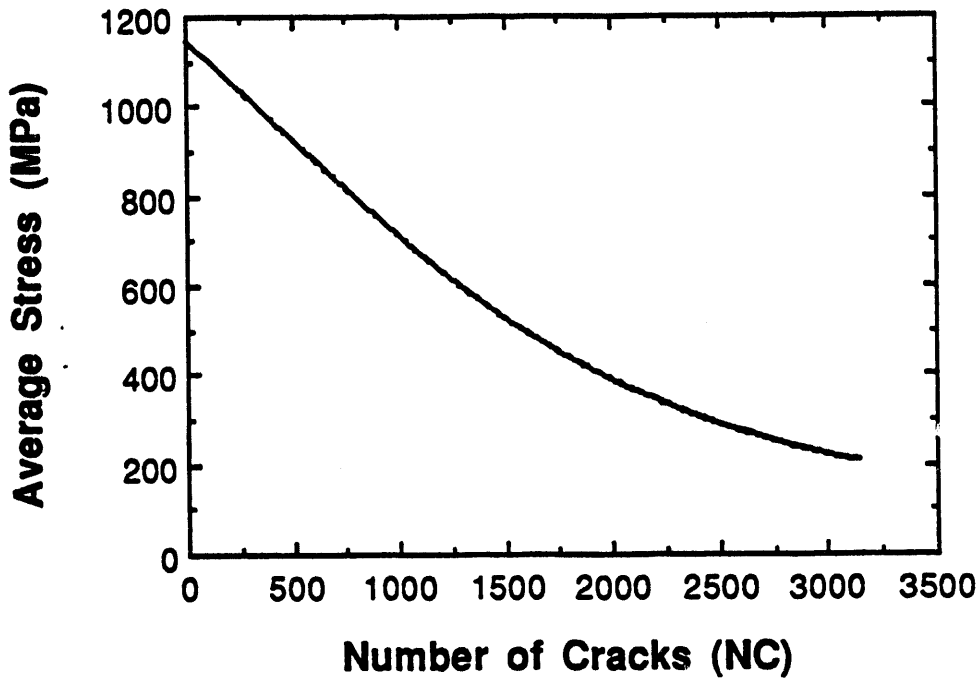

Figure B-7. Plot of number of cracks (NC) versus the average stress in the coating, for a 2.3 microns Al_2O_3 coating on SiC, Eq. (B-8).

Once the number of cracks is known the average crack spacing, related to V_2 in Eq. (B-1), was determined by;

$$\text{average crack spacing} = 2\zeta = \frac{L}{NC+1} \qquad \text{(B-9)}$$

and the volume of the coating that cracked, V_{bc}, was given by

$$V_{bc} = 2 \times \text{(average crack spacing)} \times t_1 \times w \qquad \text{(B-10)}$$

where t_1 and w were the thickness and width of the coating respectively. The calculations were done for a sample of unit width, i.e. w = 1.

The Weibull modulus was calculated by rearranging Eq. (B-1) and substituting in the appropriate values resulting in;

$$m = \frac{\ln\left(\frac{V_{T1}}{V_{T2}}\right)}{\ln\left(\frac{\sigma_{T2}}{\sigma_{T1}}\right)} \qquad \text{(B-11)}$$

The stress values used in Eq. (B-11) are derived from the number of cracks and the shear-lag distribution. The peak value of the shear-lag distribution (Figure B-5) was considered to be the fracture stress of the last segment of coating that cracked.

Determination of Surface Energy - Theory

Strain Energy Balance

We preform an energy balance on the cracked and uncracked system. This is summarized in the following equation:

$$U_s + U_c \text{ (uncracked system)} = U_s + U_c + 2t_c(NC)\gamma \text{ (cracked system)} \qquad \text{(B-12)}$$

where U represents an energy component of the system, either the substrate (U_s) or the coating (U_c), and the $2t_c(NC)\gamma$ term represents the surface energy in the system for NC cracks. Each of the components can be described as a function of the radius of curvature of the system (either cracked or

uncracked), and the material properties of the substrate and coating. The individual components of the energy balance in Eq. (B-12) are derived below.

The energy in the substrate depends on the radius of curvature and has the same form for the cracked and uncracked cases:

$$U_s = \int_v \frac{E_s}{2(1-\upsilon_s^2)} \varepsilon^2 \, dv \tag{B-13}$$

for a small arc of the substrate of thickness dr:

$$dU = \frac{E_s}{2(1-\upsilon_s^2)} \varepsilon^2 \, (\text{vol}) \tag{B-14}$$

where $\varepsilon = \frac{\Delta L}{L} = \frac{(r - R)\theta}{L}$ and $\text{vol} = \ell \, dr$ (unit thickness) (B-15)

where ℓ is the length of the substrate at a radius 'r'. Figure B-8 defines the geometry of the bent substrate. The length of the substrate changes at all values of 'r' except when r = NA at which $\ell = L$. Substitution of Eq. (B-15) into Eq. (B-14) gives:

$$dU = \frac{E_s}{2(1-\upsilon_s^2)} \frac{\Delta L^2}{L^2} \ell \, dr = \frac{E_s}{2(1-\upsilon_s^2)} \frac{(r\theta - L)^2}{L^2} r\theta \, dr \tag{B-16}$$

therefore

$$U_s = \int_u dU = \int_{R_{inner}}^{R_{outer}} \frac{E_s}{2(1-\upsilon_s^2)} \frac{(r\theta - L)^2}{L^2} r\theta \, dr \tag{B-17}$$

$$U_s = \int_{NA-a}^{NA+b} \frac{E_s}{2(1-\upsilon_s^2)} \frac{(r\theta - L)^2}{L^2} r\theta \; dr \qquad \text{(B-18)}$$

where NA is the location of the neutral axis. This was integrated to get:

$$U_s = \frac{E_s L t_s^3}{18(1-\upsilon_s^2)R^2} - \frac{5E_s L t_s^4}{216(1-\upsilon_s^2)R^3} \qquad \text{(B-19)}$$

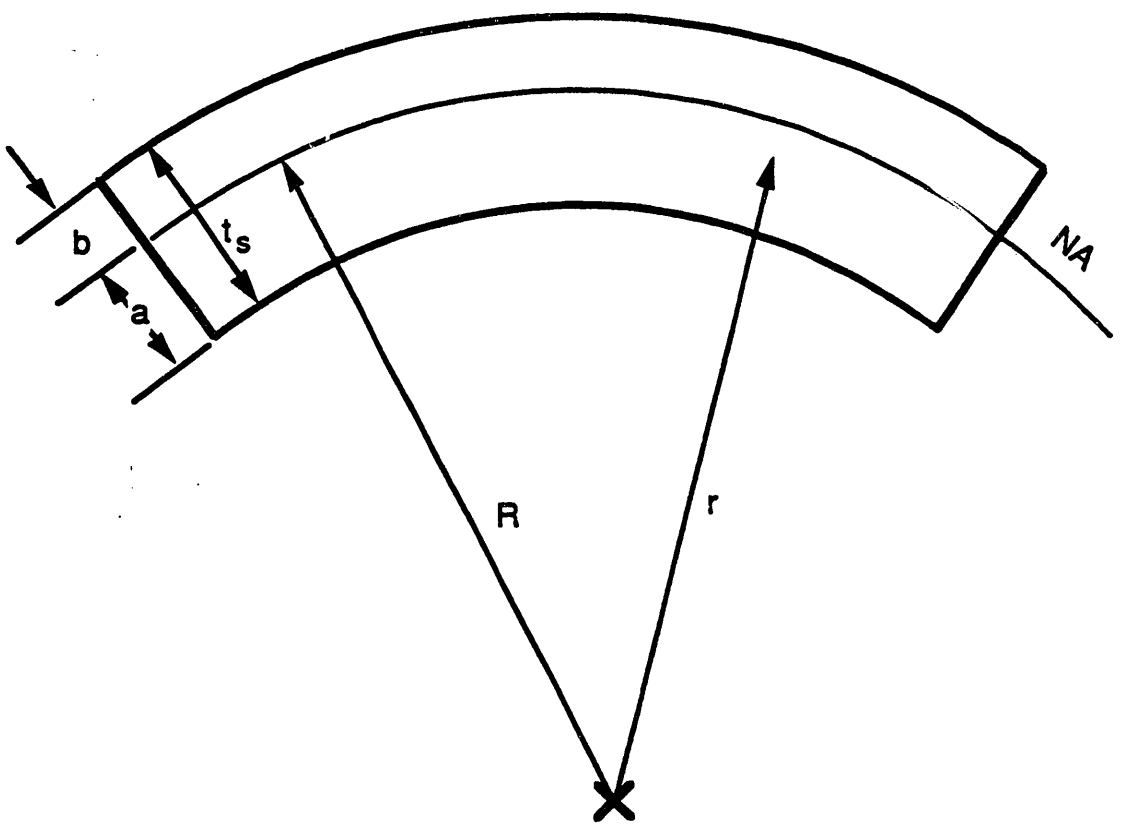

Figure B-8. Schematic of bent substrate. NA is the location of the neutral axis, 'b' is the distance from the NA to the uncoated side of the substrate, 'a' is the distance from the coated side to the NA, and 'r' is the radius to any given location in the substrate.

The energy of the substrate for the uncracked and cracked system is given by Eq. (B-19) with R equal to the radius of curvature of the uncracked and cracked coated sample, respectively.

The energy in the coating depends on the radius of curvature and has the same form for the cracked and uncracked cases:

$$U_c = \int_v \frac{E_c}{2(1-\upsilon_c^2)} \varepsilon^2 \, dv \qquad \text{(B-20)}$$

since the strain is essentially constant through the thickness of a thin film, the integral over the volume equals v_c (volume of the coating); Eq. (B-20) reduces to:

$$U_c = \frac{E_c}{2(1-\upsilon_c^2)} \varepsilon^2 v_c \qquad \text{(B-21)}$$

from the geometry of a bent beam:

$$\varepsilon_c = \frac{\Delta L}{L} = -\frac{a\theta}{L} \quad \text{and} \quad v_c = (L-a\theta)t_c \quad \text{(for unit width)} \qquad \text{(B-22)}$$

Substituting Eq. (B-22) into Eq. (B-21) gives:

$$U_c = \frac{E_c}{2(1-\upsilon_c^2)} \frac{(a\theta)^2}{L^2} (L - a\theta)\, t_c \qquad \text{(B-23)}$$

Setting $\theta = \frac{L}{R}$ and $a = \frac{2t_s}{3}$, gives:

$$U_c = \frac{2E_c t_c t_s^2 \left(L - \frac{2}{3}\frac{L t_s}{R}\right)}{9(1-\upsilon_c^2)R^2} \qquad \text{(B-24)}$$

This applies to both cracked and uncracked cases, with the appropriate radius of curvature. For the cracked case, the stress distribution is not uniform (as it is in the uncracked case), but the energy stored in all of the cracked segments of the coating is the same as the energy given by Eq. (B-24) using the cracked radius of curvature.

Once the energies of the substrate and coating are determined for the uncracked and cracked cases, the surface energy can be solved for by rearranging Eq. (B-12).

$$\gamma = \frac{\{U_s + U_c\,(\text{uncracked system})\} - \{U_s + U_c\,(\text{cracked system})\}}{2t_c NC} \tag{B-25}$$

where U_s and U_c are given by Eqs. (B-19) and (B-24), respectively, using the uncracked and cracked radius of curvature.

Griffith Energy Balance

Lawn and Wilshaw [LAW75] describe the relationship between the surface energy (γ) and fracture toughness (K_c) of a material derived from Griffith theory and fracture mechanics. Equation (B-26) below describes this relationship;

$$\gamma = \frac{(1-\upsilon_c^2)K_c^2}{2E_c} \tag{B-26}$$

EXPERIMENTAL DETAILS

Coating Procedure

Samples were coated in a hot-wall CVD reactor made of either graphite or Inconel. Coatings of Al_2O_3 and Al_2O_3+ZrO_2 were deposited at 950°C, while TiN coatings were deposited at 970°C. Metal chlorides, along with other reactant gases were used to deposit the coatings; Al_2O_3 ($AlCl_3$, CO_2, H_2, and Ar), Al_2O_3+ZrO_2 ($AlCl_3$, $ZrCl_4$, CO_2, H_2, and Ar), and TiN ($TiCl_4$, N_2, H_2, and Ar). The

Al_2O_3 and Al_2O_3+ZrO_2 coatings were deposited at low pressures (1.33 Pa), while TiN was deposited at atmospheric pressure. $AlCl_3$ and $ZrCl_4$ were generated by passing Cl_2 and H_2 over the metals held at ~600°C, while $TiCl_4$ was produced in a bubbler. Deposition of TiN required 1 hour while the Al_2O_3 and Al_2O_3+5 v/o ZrO_2 depositions required 2 - 3 hours.

Residual Stress Measurements

The stress in a coating was measured from the radius of curvature of the coated substrate using Eq. (B-4). Thin substrates of silicon nitride and silicon carbide (nominally 25.4 mm x 2.54 mm x 0.175 mm) were polished to a 0.1 micron surface finish and annealed at ~1200°C in vacuum (10^{-2} Pa at temperature) for one hour to relieve stresses induced during preparation.

Figures B-9 and B-10 show flow charts of the experimental procedure. The radius of curvature (ROC) of the sample was measured with a laser profilometer, and the measured shape was fitted to the equation of a circle to determine the ROC (see Appendix C). The ROC of the uncoated sample (ρ_{uc}) was measured at room temperature (20°C), then one side was coated and the ROC of the coated (ρ_c) substrate was measured at 20°C. These values were used in Eq. (B-4) to calculate σ_m at 20°C for the cracked coating with the number of cracks at 20°C. The coated substrate was then cooled in liquid nitrogen (-160°C) then warmed to 20°C and the ROC was measured. This value along with the ROC of the uncoated substrate were used in Eq. (B-4) to calculate σ_m at 20°C in the cracked coating with the number of cracks at -160°C. Room temperature elastic constants used in these calculations and are listed in Table B-1 and the thermal expansion data are plotted in Figure B-11.

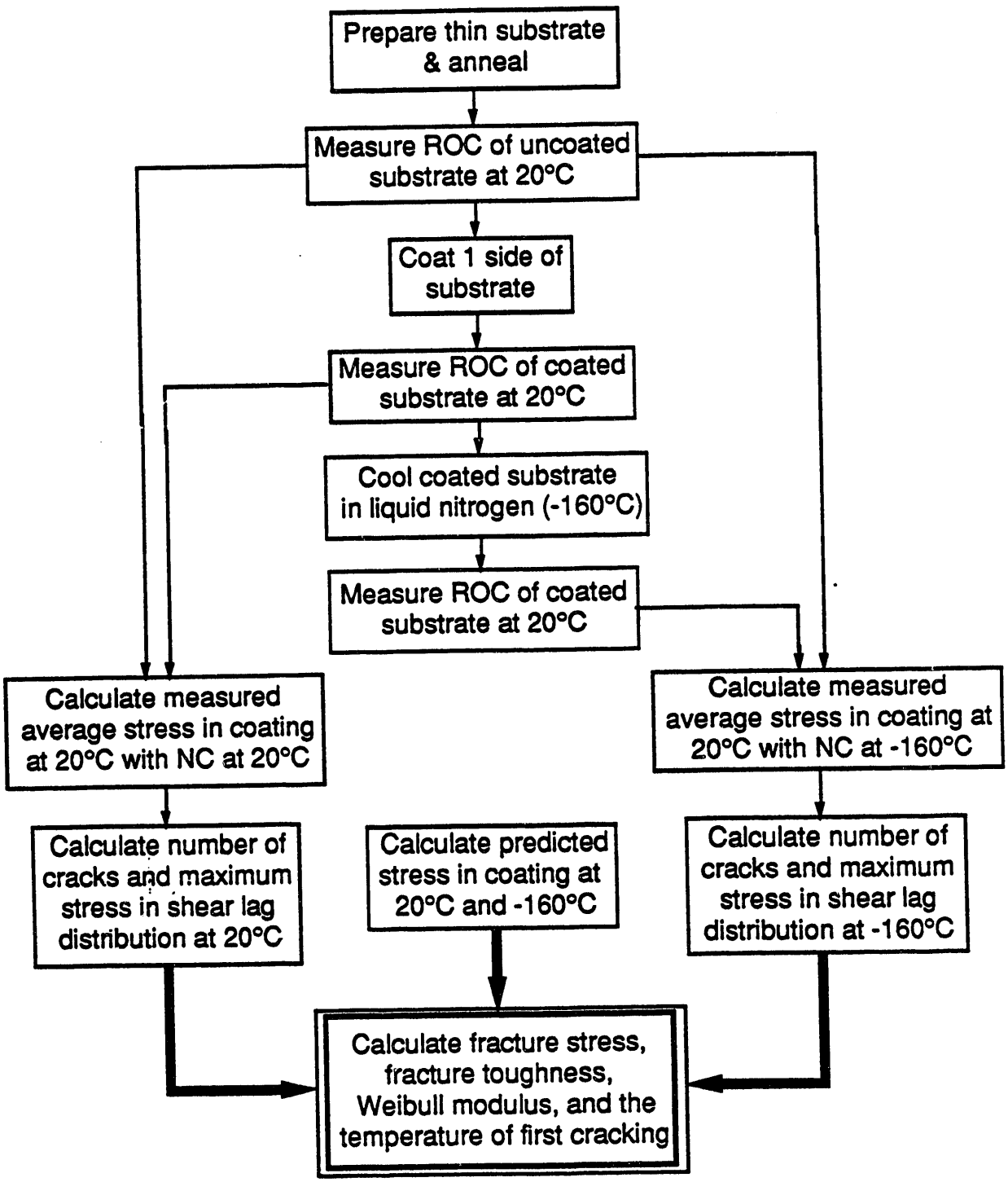

Figure B-9. Flow chart of experimental procedure outlining important steps in the force balance used to calculate the fracture strength, fracture toughness, Weibull modulus, and temperature of first cracking of thin coatings on substrates.

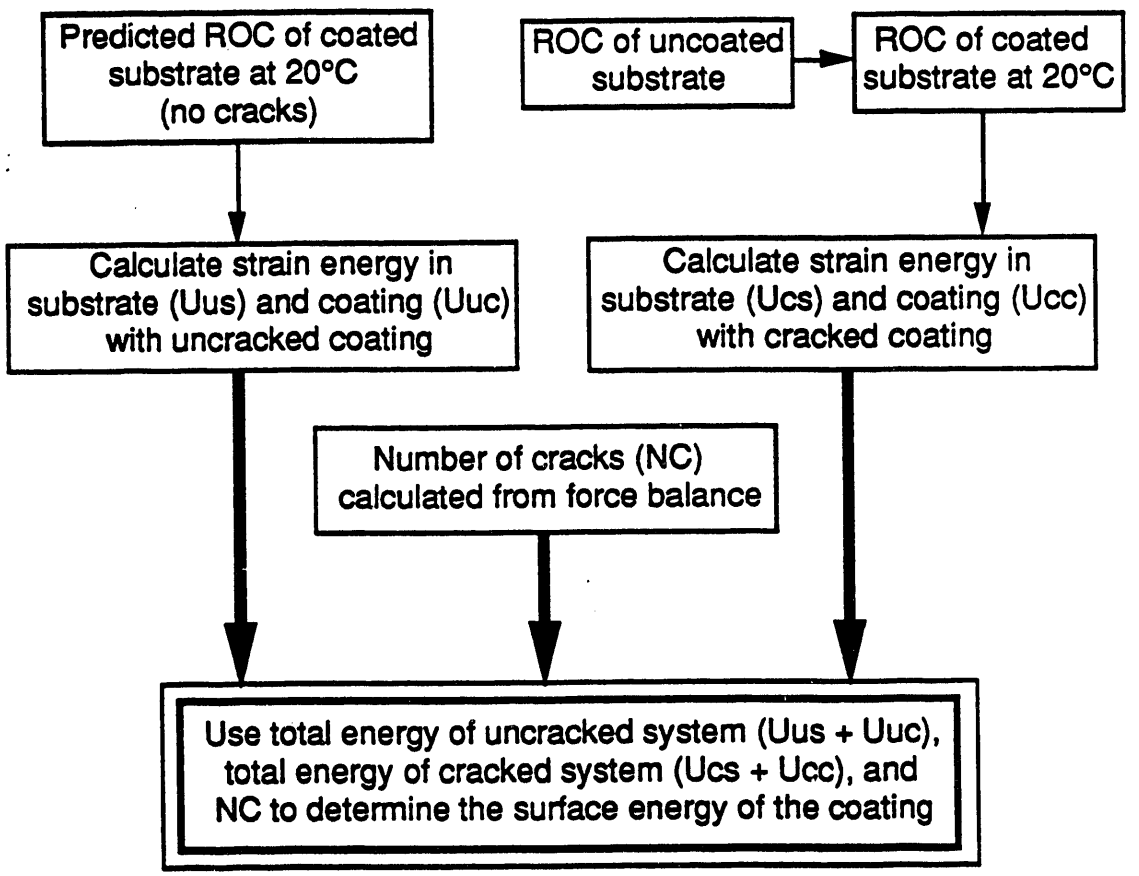

Figure B-10. Flow chart of experimental procedure outlining important steps in the energy balance used to calculate the surface energy of thin coatings on substrates.

Table B-1. Material elastic constants used in calculations.

Material	Young's Modulus, E (GPa)	Poisson's Ratio, υ	Shear Modulus, $G=\frac{E}{2(1-\upsilon)}$ (GPa)
Al_2O_3	380	0.26	257
Al_2O_3+5 v/o ZrO_2	340	0.26	135
SiC	405	0.19	250
Si_3N_4	300	0.23	195
TiN	300 - 600 [TOR87]	0.23	167

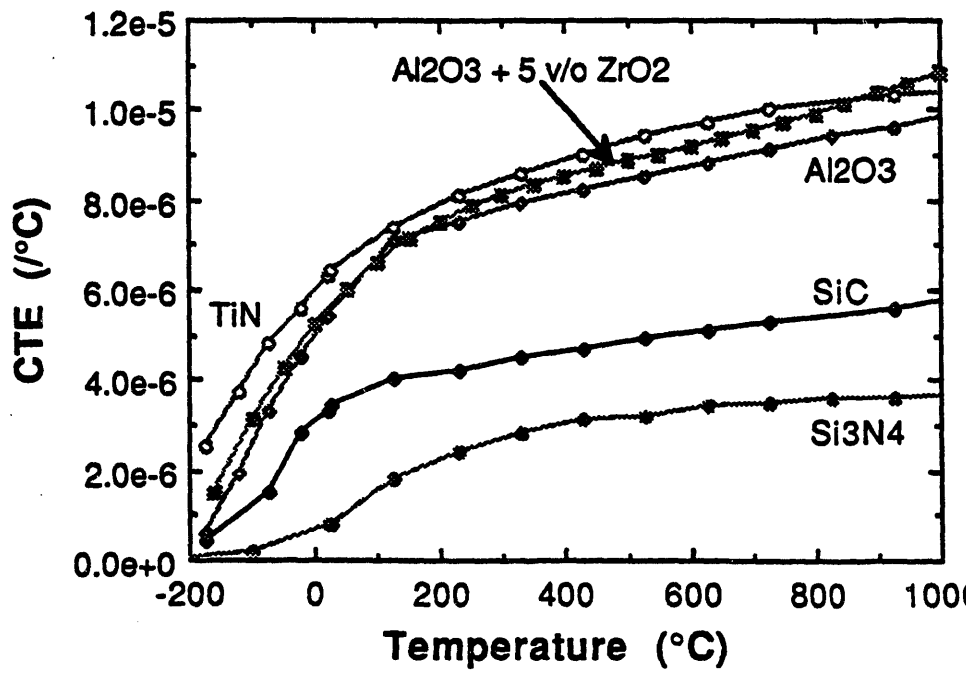

Figure B-11. Plot of the coefficients of thermal expansion for materials used in this study [TOU75]. Data for the Al_2O_3+5 v/o ZrO_2 coating is from the volume weighted average of Al_2O_3 and ZrO_2. Data for Si_3N_4 at temperatures below 20°C was extrapolated.

RESULTS

The data used in the calculations and results of these calculations are listed in Tables B-2 and B-3, respectively. A sample with a 2.34 microns Al_2O_3 coating deposited at 950°C on SiC in a reactor with a graphite chamber is used as an example to demonstrate these calculations. To determine the ROC, 2000 data points were collected and fit to the equation of a circle. Once the ROC was measured, Eq. (B-4) was used to determine the stress in the coating. The average stress in the coating at 20°C and at 20°C after cooling to -160°C was given by Eq. (B-12) and Eq. (B-13), respectively. Note that the stress at 20°C was lower in the sample that was first cooled to -160°C.

$$\sigma(20°C) = \frac{405\ \text{GPa}\ (217 \times 10^{-6}\ \text{m})^2}{6(2.34 \times 10^{-6}\ \text{m})(1-\{0.19\}^2)} \left(\frac{1}{4.7676\ \text{m}} - \frac{1}{15.525\ \text{m}}\right) = 203\ \text{MPa} \tag{B-27}$$

$$\sigma(20°C,-160°C) = \frac{405\ \text{GPa}\ (217 \times 10^{-6}\ \text{m})^2}{6(2.34 \times 10^{-6}\ \text{m})(1-\{0.19\}^2)} \left(\frac{1}{4.9232\ \text{m}} - \frac{1}{15.525\ \text{m}}\right) = 193\ \text{MPa} \tag{B-28}$$

With the average stress in the coating known (σ_m), the predicted stress (σ_p) in the coating as a function of temperature (below the deposition temperature) was calculated from Eq. (B-3). In calculating the predicted stress, a deposition temperature of 950°C and final temperatures of 20°C and -160°C were used. σ_m and σ_p were then used in Eq. (B-8) to solve for the number of cracks at 20°C and -160°C. The number of cracks in the sample at -160°C was determined using the sample that was cooled to -160°C and measured at 20°C.

For the coated substrate at 20°C, σ_p = 1146 MPa and σ_m = 203 MPa. These values were used in Eq. (B-8) to solve for NC, the crack spacing, and the maximum stress in the shear-lag distribution. For the sample cooled to -160°C and measured at 20°C; NC was solved for by using σ_p = 1146 MPa and σ_m = 193 MPa in Eq. (B-8). Crack spacings of 6.28 microns at 20°C and of 6.10 microns at -160°C were calculated, corresponding to stressed volumes of $2.94 \times 10^{-11}\ m^3$ and $2.85 \times 10^{-11}\ m^3$ for a unit width substrate, respectively.

Once the number of cracks and the crack spacing were known at -160°C, the maximum stress in the shear-lag distribution was solved for using σ_p = 1262 MPa (the predicted stress at -160°C) in Eq. (B-5). At 20°C the maximum stress was 301 MPa and at -160°C the maximum stress was 316 MPa, these values were defined as the fracture stress of the coating at 20°C and -160°C for NC cracks. The predicted stress as a function of ΔT is plotted along with the calculated/measured maximum stresses at 20°C and -160°C in Figure B-12. The intersection of these lines in Figure B-12 was taken as the fracture stress, 240 MPa. The fracture stress was the value of stress in the coating at which first fracture occurred. This value appears reasonable compared to reported values of bulk Al_2O_3 which are in the range of 100 - 300 MPa, Table B-4.

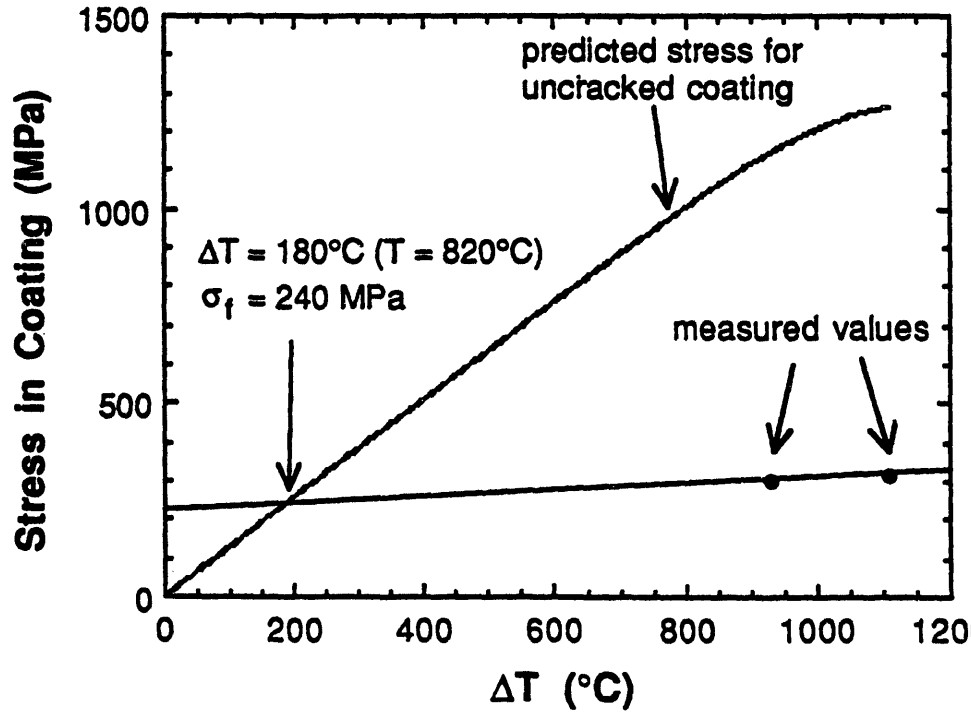

Figure B-12. Plot of stress versus ΔT for a 2.34 microns Al_2O_3 coating on SiC. The predicted stress was calculated from Eq. (B-3) and the measured maximum stress (•) was calculated from Eqs. (B-5) and (B-8).

Table B-2. Coating and substrate thicknesses, measured radius of curvature, predicted stress and predicted radius of curvature of samples tested.

Sample (coating/substrate)	Coating/Substrate Thickness (μm)	Measured Radius of Curvature at 20°C (m)			Predicted Values for Uncracked Coating	
		Uncoated (20°C)	Coated (20°C)	Coated (-160°C)	Stress in Coating 20°C/-160°C (MPa)	Radius of Curvature at 20°C (m)
Al_2O_3/SiC						
Inconel reactor	3.47/212	8.4836	3.1385	3.2025	1123/1238	0.7663
Graphite reactor	2.34/217	15.525	4.7676	4.9232	1146/1262	1.1733
Al_2O_3 + 5 v/o ZrO_2	2.51/164	4.9224	1.1721	1.1825	1136/1262	0.6273
TiN/Si_3N_4						
Sample #1	2.57/257	9.6008	3.1641	3.2625	1427/1658	0.8917
Sample #2	1.57/244	8.0190	3.6559	3.7680	1444/1678	1.3045

Table B-3. Calculated fracture stress, temperature at the onset of cracking, fracture toughness, Weibull modulus, and surface energy for coatings in this study. All of the reported values are valid at "The Temperature at First Cracking".

Sample (coating/substrate)	Fracture Stress, σ_f (MPa)	Temperature of First Cracking (°C)	Fracture Toughness, K_{Ic} (MPa$\sqrt{m}$)	Weibull Modulus	Surface Energy (J/m^2) From eqn. (25)	Surface Energy (J/m^2) From eqn. (26)
Al_2O_3/SiC						
Inconel reactor	190	800	0.5	19	0.5	0.3
Graphite reactor	240	770	0.5	28	0.2	0.3
Al_2O3 + 5 v/o ZrO_2	480	590	1.1	16	0.6	1.6
TiN/Si_3N_4†						
Sample #1	215 (195)	825 (910)	0.5 (0.4)	10 (9)	0.5 (1.8)	0.4 (0.2)
Sample #2	250 [345]	805 [740]	0.4 [0.6]	13 [27]	0.2 [0.2]	0.3 [0.6]

† These were calculated with E = 300 GPa, numbers in parenthesis are for sample # 1 with E = 600 GPa. The numbers in square brackets were calculated using the data for sample #2 but with the ROC at 20°C decreased by 1% and the ROC at -160°C increased by 1% from the values listed in Table B-2.

Table B-4. Fracture toughness, tensile strength, and surface energy of bulk ceramics from the literature.

Material	Fracture Toughness K_{Ic} (MPa$\sqrt{m}$) [CS91,CHE78]	Tensile Fracture Strength σ_f (MPa) [CS91,KAT83]	Surface Energy γ (J/m^2) [LIV56]
Al_2O_3	4	100 - 300	0.9
Al_2O_3+5 v/o ZrO_2	5†	250†	0.9**
TiN	3.8*	300*,††	1.2*

† this value includes effects of transformation toughening which is not expected to play a role in coatings.

†† values estimated with Eqs. (B-32) and (B-33).

* values taken to be the same as TiC.

** value form the volume weighted average of Al_2O_3 and ZrO_2.

The fracture stress was used with the maximum stresses at 20°C and -160°C along with the associated volumes to calculate the Weibull modulus of the coating according to Eq. (B-11). The average Weibull modulus for this coating is 29. These calculations are shown in Eqs. (B-29) and (B-30).

$$m = \frac{\ln\left(\frac{4.68 \times 10^{-8}\ m^3}{2.94 \times 10^{-11}\ m^3}\right)}{\ln\left(\frac{301\ MPa}{240\ MPa}\right)} = 32 \qquad \text{(B-29)}$$

$$m = \frac{\ln\left(\frac{4.68 \times 10^{-8}\ m^3}{2.85 \times 10^{-11}\ m^3}\right)}{\ln\left(\frac{316\ MPa}{240\ MPa}\right)} = 27 \qquad \text{(B-30)}$$

A relationship by Thouless [THO90] was used to calculate the mode I fracture toughness of the coating.

$$K_{Ic} = \frac{\sigma\sqrt{t_1}}{0.7} \qquad \text{(B-31)}$$

where σ was the fracture stress of the coating, taken as σ_f. Taking σ_f as 240 MPa, the fracture toughness is 0.5 $MPa\sqrt{m}$. In calculating K_{Ic} of the coating, the largest error arises from the uncertainty in the stressed volumes. The accuracy of these volumes depends on NC and the accuracy of the shear-lag distribution, Eq. (B-5). This same analysis was repeated for each sample and the results are summarized in Tables B-2 and B-3.

DISCUSSION

Coating Properties

Two Al_2O_3 coatings, with significantly different surface morphologies, were deposited at 950°C on SiC substrates for comparison. One coating was deposited in a hot wall reactor with an Inconel chamber, Figure B-13a. Al_2O_3 coatings deposited in this reactor were known to be contaminated with nickel which caused the textured morphology, Figure B-13a. A second Al_2O_3 coating was deposited in a hot wall reactor with a graphite chamber, Figure B-13b, producing a more compact and uniform coating as compared to that deposited in the Inconel reactor.

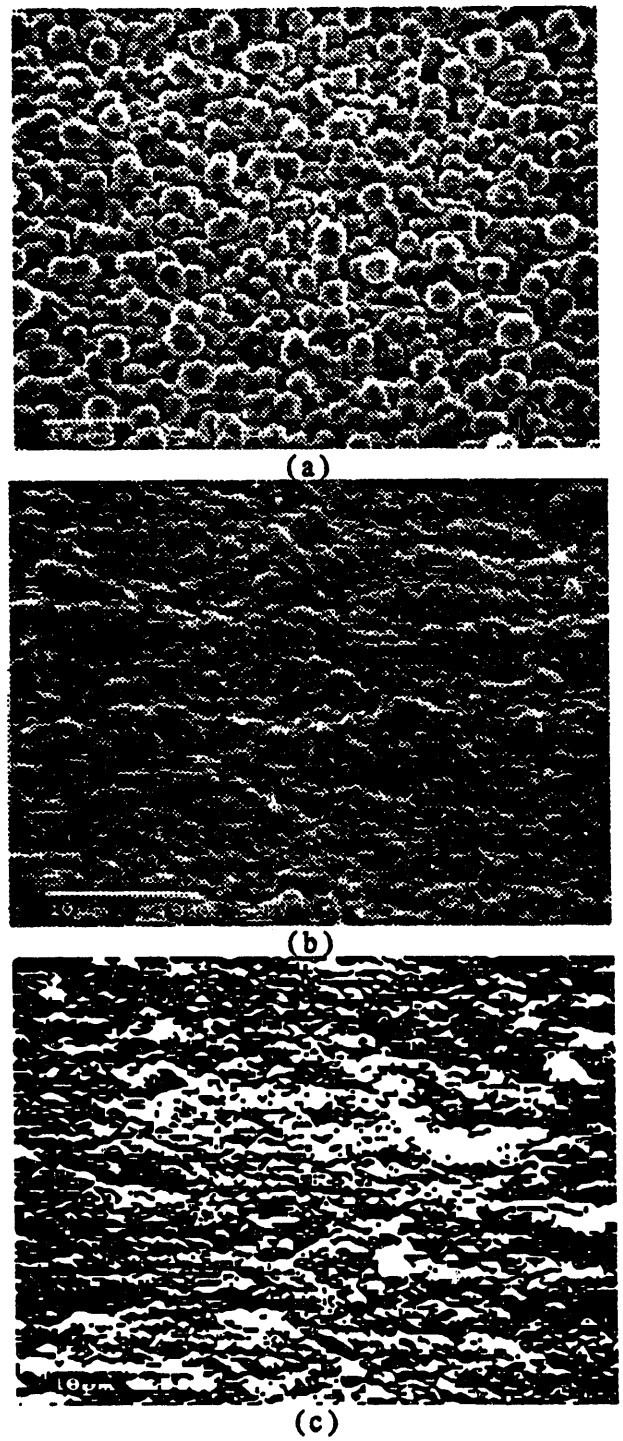

Figure B-13. Scanning electron micrograph of the coatings deposited on a SiC substrate at 950°C in a) Al_2O_3 deposited in an Inconel chamber, b) Al_2O_3 deposited in a graphite chamber, and c) Al_2O_3 + 5 v/o ZrO_2 deposited in a graphite chamber.

The coating in Figure B-13a was expected to have lower mechanical properties than the coating in Figure B-13b. The textured structure of the coating in Figure B-13a was expected to allow easier crack propagation compared to the uniform structure of the coating (Figure B-13b). Therefore, the coating in Figure B-13a was expected to have lower strength and toughness as compared to the coating in Figure B-13b. These properties were measured and reported in Table B-3. The coating in Figure B-13a had a fracture strength of 190 MPa, a fracture toughness of 0.5 $MPa\sqrt{m}$, and a Weibull modulus of 19, the coating in Figure B-13b had a fracture strength of 240 MPa, a fracture toughness of 0.5 $MPa\sqrt{m}$, and a Weibull modulus of 28. While the difference in properties between these coatings was anticipated due to their different morphologies, the method described in this work allowed the expected differences to be quantified. It should be noted that the fracture strength and fracture toughness values reported in this study are not room temperature values, but the values at the temperature of first cracking, 800°C and 770°C for the coatings in Figures B-13a and B-13b respectively.

Figure B-13c shows the surface morphology of the Al_2O_3+5 v/o ZrO_2 coating on a SiC substrate deposited in the graphite reactor. This coating has a smoother surface morphology than the pure Al_2O_3 coating (Figure B-13b). The Al_2O_3+5 v/o ZrO_2 coating had a fracture strength of 480 MPa, a fracture toughness of 1.1 $MPa\sqrt{m}$, and a Weibull modulus of 16. The higher strength and toughness of the Al_2O_3+5 v/o ZrO_2 coating is primarily attributed to grain refinement of the Al_2O_3 by the ZrO_2 phase.

Table B-4 lists tensile strength, fracture toughness, and surface energy values from bulk ceramics reported in the literature. Equations (B-32) and (B-33) were used to estimate tensile strength values from 3-pt and 4-pt bending tests [DAV80], since limited tensile strength data was available for ceramics in the literature.

$$\sigma_t = \frac{\sigma_{3b}}{1.7} \tag{B-32}$$

$$\sigma_t = \frac{\sigma_{4b}}{1.5} \tag{B-33}$$

where the Weibull modulus from the 3-pt and 4-pt bend tests was assumed to be 10; σ_t was the tensile strength, σ_{3b} is the 3-pt bend strength, and σ_{4b} is the 4-pt bend strength. The strengths of the Al_2O_3 and TiN coatings are generally higher than those expected for the bulk solid.

The fracture toughness of the Al_2O_3 and TiN coatings are generally lower that the bulk values. The coatings in this study have submicron grain sizes and large grain boundary area, therefore, cracking is expected to occur along the grain boundaries.

The grain boundary fracture toughness for a sintered Al_2O_3+0.3 vol % MgO was reported as 0.32 - 0.98 MPa$\sqrt{m}$, which was 0.1 - 0.4 of the bulk fracture toughness [KRE85]. this agrees well with the value of 0.5 MPa$\sqrt{m}$ (Table B-3). Further comparisons are made on the basis of grain boundary fracture toughness, defined as 0.1-0.4 of the bulk fracture toughness. The calculated fracture toughness value of a TiN coating on Si_3N_4 (0.5 MPa$\sqrt{m}$ in Table B-3) also compares well with the estimated grain boundary fracture toughness of bulk TiN, 0.4 - 1.5 MPa$\sqrt{m}$. Therefore, the properties used to describe coatings should be grain boundary properties when available.

The surface energy of the coatings were determined by two methods described in the introduction section, a strain energy balance, Eq. (B-25), and a Griffith energy balance, Eq. (B-26). The surface energies calculated with Eq. (B-25) are lower than those in Table B-4 from Livey and Murray [LIV56]. This is attributed to the value of NC used in Eq. (B-25). The crack spacing in the Al_2O_3 coating was calculated to be approximately 6 microns. As the degree of shear-lag increases NC decreases and γ increases. The other properties of the coating depend on NC to a much lesser extent then γ and are not significantly effected when NC changes. The surface energies calculated with Eq. (B-26) are also significantly different from those listed in Table B-4. This may be due to the cracking process not being at equilibrium, as suggested by Lawn and Wilshaw [LAW75]. In general, the present method does not allow for accurate values of the surface energy to be determined. However, a more rigorous form of the shear-lag distribution may give better agreement between measured and expected surface energies.

We attempted to measure the crack spacing directly as a check on the calculated value of NC but could only find isolated cracks which were

extremely fine. The crack opening was estimated for the $Al_2O_3+ZrO_2$ coating on SiC as follows:

$$\text{crack opening} = \frac{(\varepsilon_s - \varepsilon_c)L}{NC} \qquad \text{(B-34)}$$

where ε_s is the strain in the substrate due to the temperature change (from Eq. (B-2)) and ε_c is the strain in the coating due to the measured stress (σ_m).

$$\text{crack opening} = \frac{\left(3.6 \times 10^{-3} - \frac{480\ \text{MPa}}{340\ \text{GPa}}\right) 0.0254\ \text{m}}{1527} = 3.6 \times 10^{-8}\ \text{m} \qquad \text{(B-35)}$$

The crack is expected to be approximately 36 nanometers wide which is 0.7 mm wide on a micrograph taken at a magnification of 20,000 x. This indicates the difficulty in observing and photographing such a small feature on the relatively rough surfaces of the coatings studied.

Limitations on Modeling and Experimental Data

Young's modulus for TiN was reported to range from 300 - 600 GPa. Both values (300 and 600 GPa) were used with the experimental data from TiN coated Si_3N_4 sample #1 to determine the sensitivity of the analysis to uncertainty in the Young's modulus of the coating material. The calculated values of the fracture strength, fracture toughness, and Weibull modulus are 215 MPa, 0.5 MPa$\sqrt{m}$, and 10 for a Young's modulus of 300 GPa and 195 MPa, 0.4 MPa$\sqrt{m}$, and 9 for a Young's modulus of 600 GPa. Therefore, this analysis is essentially insensitive to uncertainty in the coating elastic properties, with the exception of the surface energy.

The TiN coated Si_3N_4 samples in Tables B-2 and B-3 were coated simultaneously and used to compare the repeatability of the measurement technique. Figure B-14 shows that these 2 samples have very similar surface morphologies and are expected to have similar microstructures. The fracture strengths of these samples are within 15%, the fracture toughnesses are within 20%, the Weibull modulus are within 30%, and the surface energies are within 25%. These percentages differences are taken to represent the relative error in each measured property.

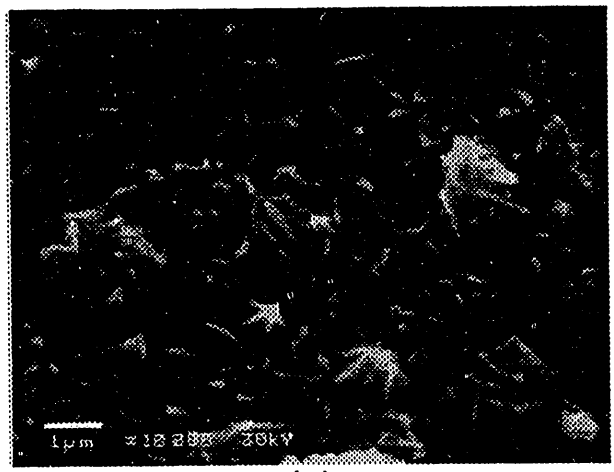

(a)

(b)

Figure B-14. Scanning electron micrograph of the coatings deposited on a SiC substrate at 970°C in a) TiN sample # 1, b) TiN sample #2.

The leading sources of error are the difficulty in determining the radius of curvature of the sample and the error in the thickness of the coating. A 1% error in the radius of curvature results in an error of 40% in the fracture strength, 50% in the fracture toughness, 100% in the Weibull modulus, and 0 - 100% in the surface energy. A 5% error in the thicknesses of the coating and substrate results in a 15% error in the fracture strength. The errors associated with measuring the radius of curvature are discussed in Appendix C.

In determining the fracture stress of the coating, σ_f, two values of measured stress were used (Figure B-12). Any non-linearity in measured stress as a function of measurement temperature will result in changes in the fracture stress of the coating. The curvature of this non-linear region was related to the Weibull modulus through Eq. (B-1). However, in order to fit a more accurate line to the data points, data at several more temperatures are needed. Since for practical reasons these additional temperatures would fall between the existing data (taken at 20°C and -160°C) these points would not allow a more accurate curve to be fit. The Weibull modulus calculated from σ_f and the corresponding values at 20°C and -160°C were 32 and 27, respectively. Since these two values are close to one another, the error introduced by the straight line approximation cannot be too large, thus the straight line approximation appears reasonable. The straight line approximation resulted in the calculated fracture stress of the coating being higher than the actual fracture stress of the coating. It would be more satisfactory if the error was conservative.

The largest error in calculating the Weibull modulus is from calculating the volume that corresponds to the fracture stress. This volume is calculated from the number of cracks. The number of cracks is a strong function of the shear-lag distribution. As the amount of lag increases the number of cracks decreases and the Weibull modulus decreases.

The approach taken in this work has demonstrated the viability of measuring the tensile strength, fracture toughness, and Weibull modulus of a coating. In comparing the measured properties of coatings to the bulk properties of the coating material, it was found that bulk properties provide a reasonable approximation to coating strength. However, the fracture

toughness of a coating was markedly lower than the bulk fracture toughness of the same material. The discrepancy between the fracture toughness of the coating and bulk materials was attributed to the large amount of intergranular fracture that occurred in fine grained coating materials.

CONCLUSIONS

In modelling and design applications the bulk properties of a material are used in place of coating properties due to the difficulty of measuring the mechanical of coatings. A simple method for quantitatively measuring the fracture stress, fracture toughness, and Weibull modulus of thin brittle coatings on a substrate was developed. This method involves measuring the radius of curvature of the coated sample at room temperature.

Two Al_2O_3 coatings on SiC substrates were compared. One had a compact coating structure and the other had a textured coating structure. The compact coating had a fracture strength of 240 MPa, a fracture toughness of 0.5 $MPa\sqrt{m}$, a Weibull modulus of 28, and a surface energy of 0.3 J/m^2. The textured coating had a fracture strength of 190 MPa, a fracture toughness of 0.5 $MPa\sqrt{m}$, and a Weibull modulus of 19, and a surface energy of 0.3 J/m^2.

A composite $Al_2O_3+ZrO_2$ coating on a SiC substrate had a fracture strength of 480 MPa, a fracture toughness of 1.1 $MPa\sqrt{m}$, a Weibull modulus of 16 and a surface energy of 1.6 J/m^2.

A TiN coating on a Si_3N_4 substrate had a fracture strength of 230 MPa $\pm$ 35, a fracture toughness of 0.5 $MPa\sqrt{m} \pm 0.1$, a Weibull modulus of 12 ± 3, and a surface energy of 0.3 ± 1 J/m^2.

Uncertainty in the coating and substrate thicknesses along with uncertainty in the radius of curvature are the leading sources of error in the method. The surface energies determined by this technique do not agree well with expected values. A more exact form of the shear-lag distribution is expected to result in more accurate surface energies.

APPENDIX C - CURVE FITTING OF PROFILOMETER DATA

BACKGROUND

Stresses in thin films on substrates can be measured by the beam bending technique [NIX89]. The technique involves measuring the radius of curvature of a coated substrate. The stress in the film (σ_f) is related to the Young's modulus of the film (E), the film thickness (t_f), the substrate thickness (t_s) and, the radius of curvature (R) by Equation C-1:

$$\sigma_f = \frac{t_s^2 E}{6 t_f R} \qquad \text{Eq. C-1}$$

A new technique was developed for measuring the fracture stress and fracture toughness of films on substrates which is based on measuring the radius of curvature of a coated substrate (Appendix B) The samples used to measure the fracture stress and fracture toughness were limited to lengths of 10 mm and 20 mm, due to material availability. The radii of curvature of the samples ranged from 0.5 m to 10.0 m. In developing this technique, the software supplied with the laser profilometer poorly fit the data to the equation of a circle. A new FORTRAN curve fitting routine was written and tested with simulated profilometer data to evaluate its accuracy.

EXPERIMENTS AND RESULTS

A PC-based laser profilometer (Rodenstock model RM600) was used for data acquisition. Software accompanying the profilometer included a routine to calculate the radius of curvature. This routine was tested with standards of known radius of curvature (0.500 m, 1.000 m and 5.000 m). In acquiring the profilometer data, 2000 data points were taken and scans of 10 mm and 20 mm were used, for reasons stated above. In most cases the results from the fitting routine were unsatisfactory, see Figure C-1. The results for the 0.5 m radius of curvature standard were accurate. However, for the 1.0 m and 5.0 m radius of

curvature standards the difference between the calculated and actual radii ranged from 5% to several thousand percent.

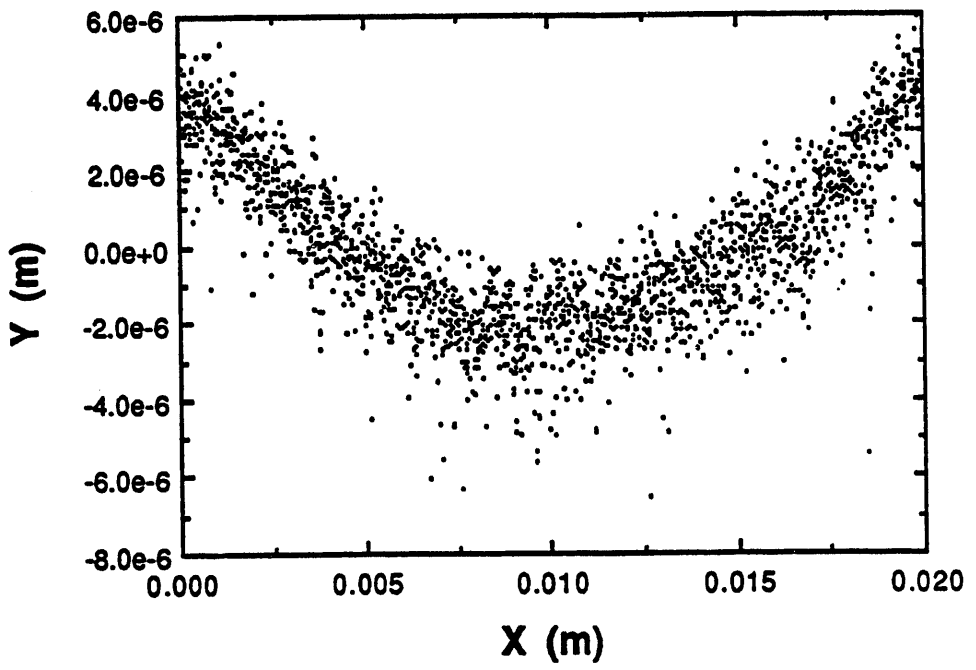

Figure C-1. Plot of experimental profilometer data. In this example the RMS noise is approximately 0.94 microns and the radius of curvature was calculated to be 7.861 m ±5% using the "GUESS" routine (see end of Appendix), compared to 6.229 m calculated by the Rodenstock software.

A new routine "POINT_FIT" was written to fit the profilometer data to the equation of a circle, Equation C-2.

$$R^2 = (x+A)^2 + (y+B)^2 \qquad \text{Eq. C-2}$$

where R is the radius of curvature, x and y are the data points, and A and B are constants. This subroutine is included at the end of this appendix along with a routine "GUESS" to supply an initial guess for R, A, and B.

Profilometer data simulating samples with different radii of curvature were computer generated and fitted to the equation of a circle using the

subroutines to test these routines for accuracy and robustness. Noise was introduced into the data to assess the sensitivity of the fitting procedure. All noise values reported refer to the root mean square (RMS) level. Two distributions were used to generate the noise, a Gaussian distribution and a uniform distribution, see Figure C-2. Each set of generated data contained 2000 points. The results were largely insensitive to the number of data points. Scan lengths of 10 mm, 20 mm, and 50 mm were tested and radius of curvature values from 0.5 m to 10.0 m were used. These scan lengths and radii of curvature values were selected because they were typical values encountered.

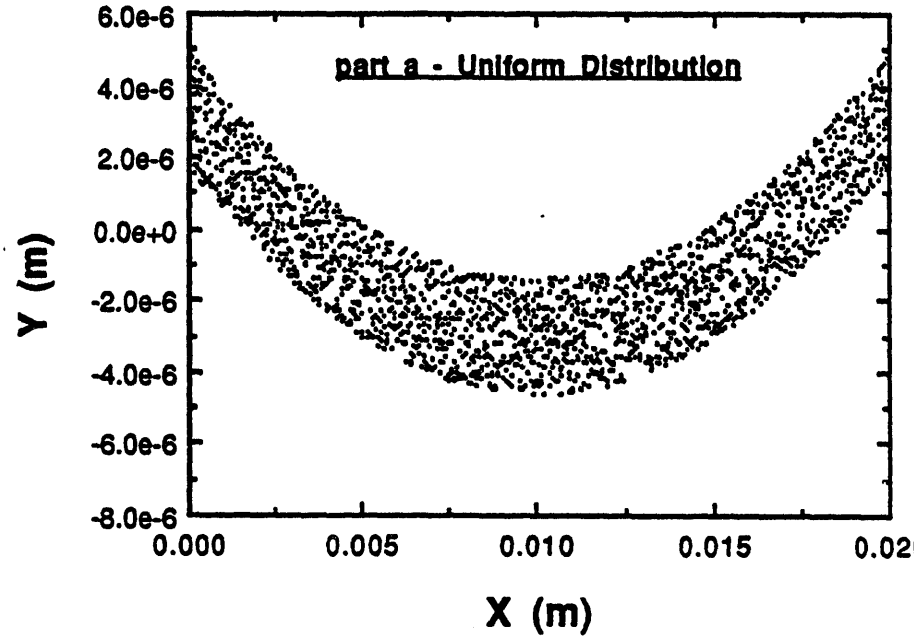

Figure C-2a. Plot of computer generated data for a radius of curvature of 7.861 m and an RMS noise level of 0.94 microns with a uniform distribution, calculated R = 8.002 m. The calculated radius of curvature value is within 2% of the actual radius of curvature of 7.861 m.

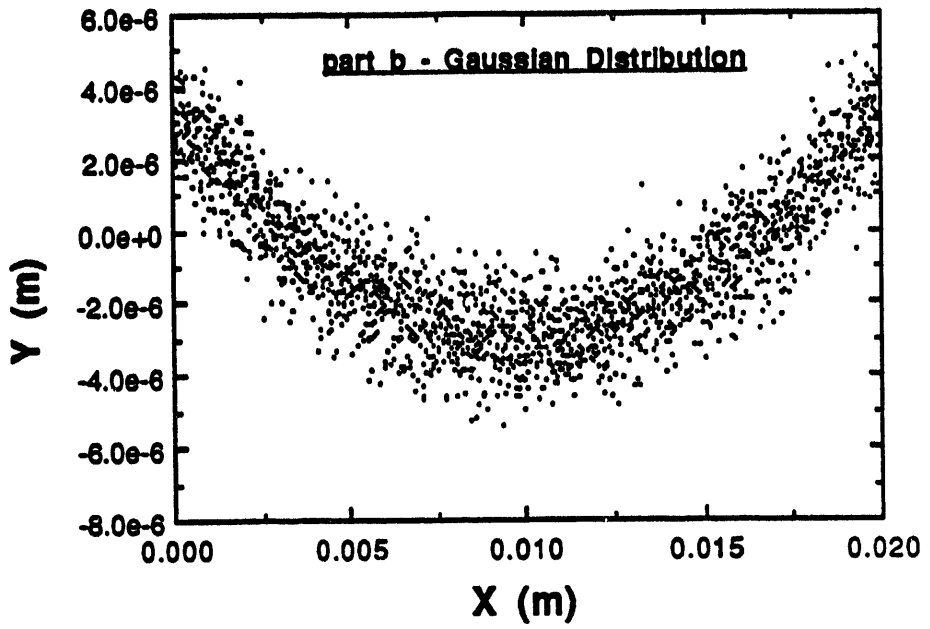

Figure C-2b. Plot of computer generated data for a radius of curvature of 7.861 m and an RMS noise level of 0.94 microns with a Gaussian distribution, calculated R = 8.204 m. The calculated radius of curvature value is within 4% of the actual radius of curvature of 7.861 m.

A plot of the fitted radius of curvature versus the signal-to-noise ratio (S/N) is shown in Figure C-3 for the Gaussian noise distribution. This plot shows that as the signal-to-noise ratio decreases (noise increases) the accuracy decreases to the point that the calculated radius of curvature is unreliable. The critical value of the signal-to-noise ratio was 1.8 for the Gaussian distribution and 0.7 for the uniform distribution. A S/N ratio of 1.8 was used as the minimum acceptable S/N ratio for the profilometer data because the Gaussian distribution (Figure C-2b) matched the experimental distribution (Figure C-1) better than the uniform distribution (Figure C-2a). Figure C-4 shows the value of the noise which corresponds to the signal-to-noise ratio of 1.8 as a function of radius of curvature. Figure C-5 shows the error in the radius of curvature as a function of S/N. As S/N increases the error approaches zero, and when the S/N drops below the critical S/N value of

1.8 the error increases very rapidly. In general, as the radius of curvature increases the accuracy of the fit decreases; as the noise increases the accuracy of the fit decreases; and as the scan length increases the accuracy of the fit increases.

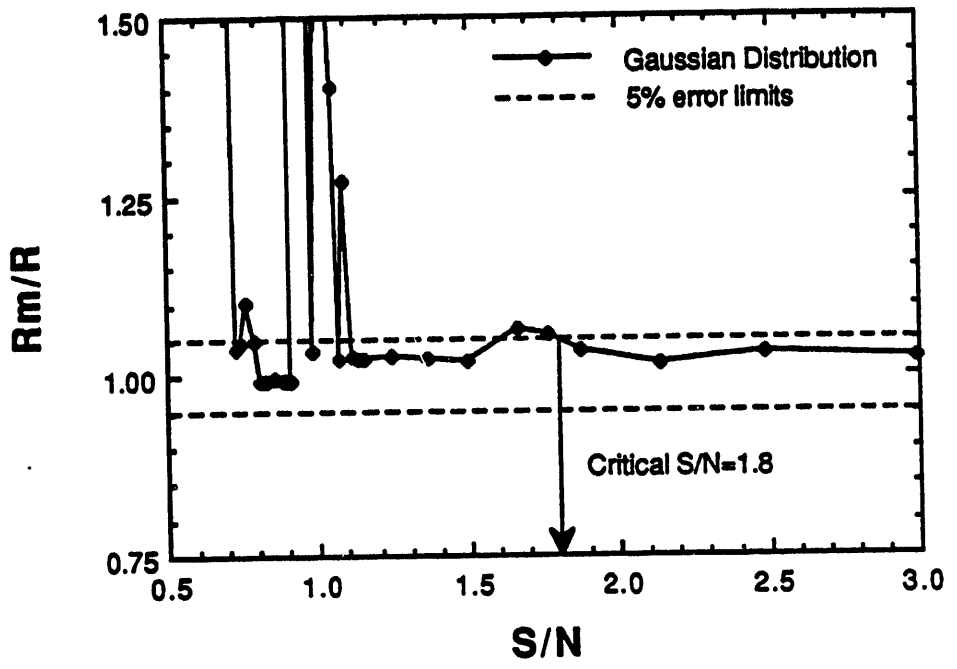

Figure C-3. Ratio of the calculated radius of curvature to the actual radius of curvature versus the signal-to-noise ratio for data sets with 2000 data points. For the Gaussian distribution the critical S/N ratio was 1.8 and for the uniform distribution it was 0.7. Only the results from the Gaussian distribution are shown.

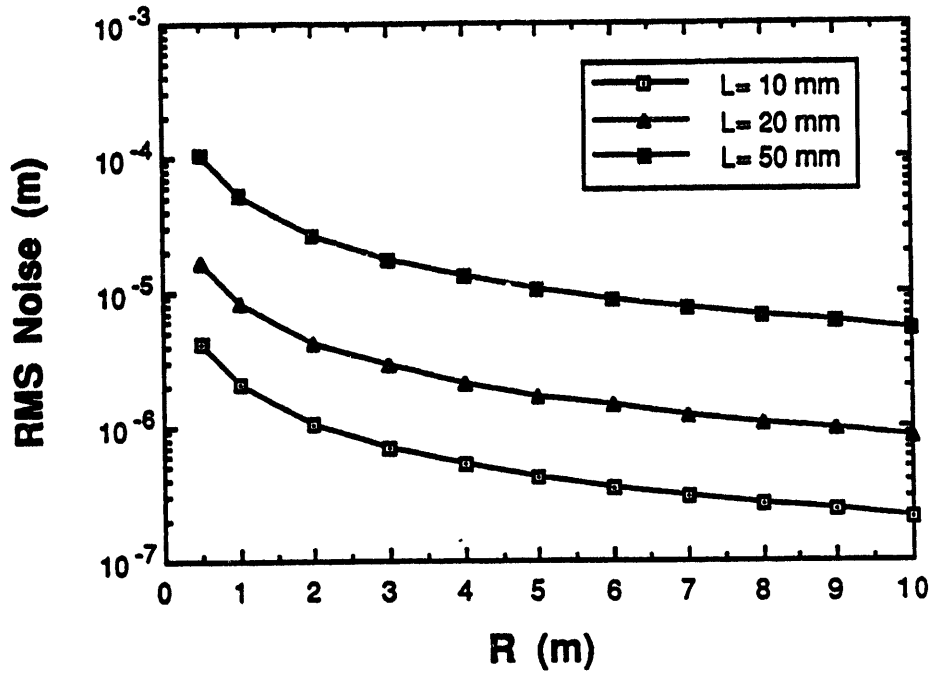

Figure C-4. Values of the maximum RMS noise level for which the fitted radius of curvature is within 5% of the true radius of curvature. A critical S/N ratio of 1.8 was used.

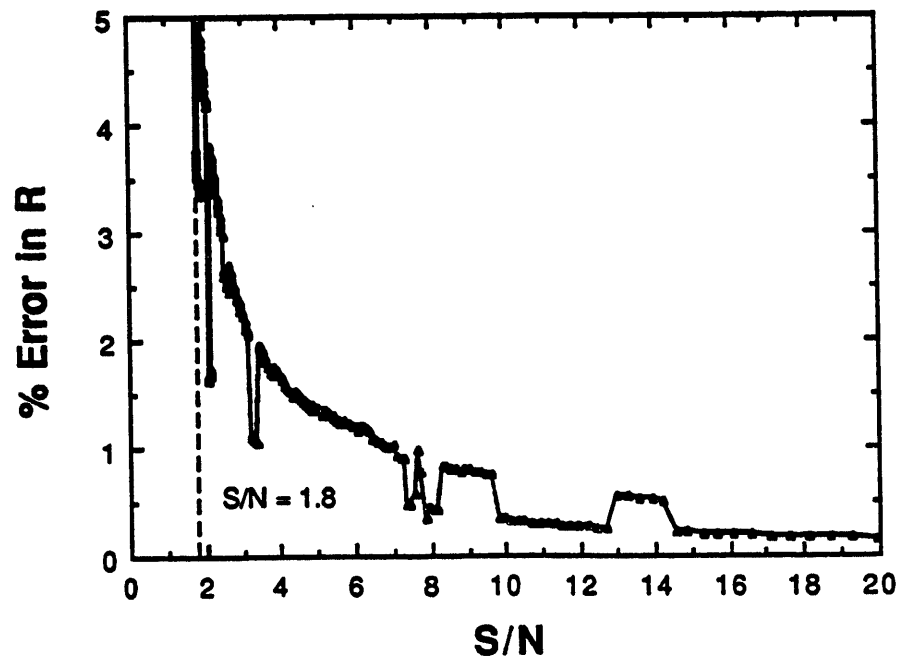

Figure C-5. Plot of error in the radius of curvature versus S/N.

CONCLUSIONS

Routines used to fit profilometer data to the equation of a circle are very sensitive to noise in experimental data, the scan length, and the actual radius of curvature being measured. A routine for fitting profilometer data to the equation of a circle was described and its behavior was characterized with simulated data of known radius of curvature and noise level.

The signal-to-noise ratio has to be greater than 1.8 to measure the radius of curvature within 5% of the true value. High values of the signal-to-noise ratio are favored by small radius of curvatures, small scatter in the data, and long scan lengths.

COMPUTER ROUTINES FOR CURVE FITTING OF PROFILOMETER DATA

These subroutines are written in FORTRAN and fit experimental data to the Equation of a circle by solving for the A, B, and R values in Equation C-2.

Subroutine GUESS supplies the initial guess for the fitting routine, POINT_FIT. GUESS works by evaluating Equation C-2 at 3 different points and solving these 3 equations for values of R, A, and B. To reduce the effects of data scatter NCP sets of points are used and averaged to obtain an initial guess. GUESS requires input arrays of X and Y values of dimension NP, and the number of sets of equations that are averaged (NCP), and stores the initial values of R, A, and B in variables RO, AO, and BO.

```
      SUBROUTINE GUESS(X,Y,AO,BO,RO,NP,NCP)
      IMPLICIT NONE
      REAL*8 X(5000),Y(5000),AO,BO,RO,XNCP,X1,X2,X3,Y1,Y2,Y3,
     +          T1,T2,T3,BO_S(100),AO_S(100),RO_S(100),Y1_SAVE,Y2_SAVE
      INTEGER I,NCP,NP
      AO=0.
      BO=0.
      RO=0.
      Y1_SAVE=0.
      Y2_SAVE=0.
      XNCP=FLOAT(NCP)
      DO 1 I=1,NCP
       X1=X(I)
        Y1=Y(I)
       Y1_SAVE=Y1_SAVE+Y1
        X2=X(NP/2-NCP/2+I)
```

```
      Y2=Y(NP/2-NCP/2+I)
     Y2_SAVE=Y2_SAVE+Y2
     X3=X(NP-NCP+I)
      Y3=Y(NP-NCP+I)
      T1=(X2*X2+Y2*Y2-X1*X1-Y1*Y1)/(X1-X2)
      T2=(X3*X3+Y3*Y3-X1*X1-Y1*Y1)/(X1-X3)
      T3=(Y3-Y1)/(X1-X3) - (Y2-Y1)/(X1-X2)
      BO_S(I)=0.5*(T1-T2)/T3
      AO_S(I)=(X2*X2+Y2*Y2+2.*BO_S(I)*Y2-X1*X1-Y1*Y1-
     +                2.*BO_S(I)*Y1)/2./(X1-X2)
      RO_S(I)=SQRT((X1+AO_S(I))**2+(Y1+BO_S(I))**2)/3. +
     +              SQRT((X2+AO_S(I))**2+(Y2+BO_S(I))**2)/3. +
     +              SQRT((X3+AO_S(I))**2+(Y3+BO_S(I))**2)/3.
1    CONTINUE
     DO 2 I=1,NCP
      AO=AO+AO_S(I)/XNCP
      BO=BO+BO_S(I)/XNCP
      RO=RO+RO_S(I)/XNCP
2    CONTINUE
     RO=ABS(RO)
     IF(Y1_SAVE .LT. Y2_SAVE)RO=-RO
     RETURN
     END
```

Subroutine POINT_FIT fits experimental data to Equation C-2. It requires arrays of X and Y values of dimension NP, an initial guess for the R, A, B values (R_AVE, AO, and BO), and the value of NCP. R_AVE contains the initial guess of R at the beginning and the final value of R on exit. Several parameters control the accuracy of the calculation; NUM_C controls the number of fitting steps used to solve for A and B, NUM_TOTAL controls the number of fitting steps used to solve for R_AVE, STEP is the increment size used to change the values of A and B during fitting, D is how much STEP is reduced by, and TOL is used to terminate the routine. The routine is ended when either NUM_C or NUM_TOTAL is reached, or when the change in R_AVE is less than TOL*ERR_R. ERR_R is defined as the absolute magnitude of the average deviation of R(i) from R_AVE.

```
     SUBROUTINE POINT_FIT(X,Y,NP,AO,BO,A,B,R_AVE,ERR_R,NCP)
     IMPLICIT NONE
     REAL*8 AO,BO,A_SIGN,B_SIGN,OLD_R_AVE,DA,DB,OLD_ERR_R,C(2),
    +          R_AVE,XNP,ERR_R,D_ERR,TOL,X(5000),Y(5000),R(5000),
    +          A,B,T1,T2,STEP(2),STEP_I,SIGN,RA,D
```

```
      INTEGER TOTAL_FIT,I,NP,NUM_C,NUM_TOTAL,FIT(2),II,NCP
      COMMON/CC2/NUM_C,NUM_TOTAL,STEP_I,D,TOL

C
C     GET 'BEST' A & B VALUES BY MINIMIZING VARIATION IN R
C                A = C(1);       B=C(2)
C     APPROXIMATE STARTING VALUES OF STEP=0.25, D=5., TOL=1.E-4
C
      XNP=FLOAT(NP)
      C(1)=AO
      C(2)=BO
      STEP(1)=STEP_I
      STEP(2)=STEP_I
      TOTAL_FIT=0
      SIGN=1.0
      OLD_R_AVE=1.E6
      TOTAL_FIT=0
100   DO 999 I=1,2
       OLD_ERR_R=1.E6
        FIT(I)=0

22     CONTINUE
       R_AVE=0.0
       DO 20 II=1,NP
           R(II)=SQRT((X(II)+C(1))**2+(Y(II)+C(2))**2)
         R_AVE=R_AVE+R(II)
20     CONTINUE
       R_AVE=R_AVE/XNP

       ERR_R=0.0
       DO 21 II=1,NP
          ERR_R=ERR_R+ABS(R_AVE-R(II))/XNP
21     CONTINUE
       D_ERR=ERR_R-OLD_ERR_R
       OLD_ERR_R=ERR_R

        FIT(I)=FIT(I)+1
       IF(FIT(I) .EQ. NUM_C)GOTO 30

       IF(D_ERR .GT. 0.)THEN
         SIGN=-SIGN
          STEP(I)=STEP(I)/D
       ENDIF
       IF( ABS(D_ERR) .LT. TOL*ERR_R )GOTO 30
         C(I)=C(I)*(1.+SIGN*STEP(I))
       GOTO 22
30     CONTINUE
999   CONTINUE

      A=C(1)
      B=C(2)
      TOTAL_FIT=TOTAL_FIT+1
```

```
      T1=0.
      T2=0.
      DO 1901 I=1,NCP
        T1=T1+Y(I)
         T2=T2+Y(NP/2-NCP/2+I)
1901  CONTINUE

      RA=ABS(R_AVE)
      IF(T1 .LT. T2)RA=-R_AVE
      IF(TOTAL_FIT .EQ. NUM_TOTAL)GOTO 918
      IF(ABS(OLD_R_AVE-R_AVE) .GT. TOL*R_AVE)THEN
       OLD_R_AVE=R_AVE
       GOTO 100
      ENDIF
      R_AVE=ABS(R_AVE)
918   IF(T1 .LT. T2)R_AVE=-R_AVE
      RETURN
      END
```

APPENDIX D - SIMPLE COMPOSITE PLATE AND BEAM THEORY

COMPOSITE PLATE THEORY

Firstly, individual layer stiffnesses are calculated by

$$Q_{11}^k = \frac{E_1^k}{1 - v_{12}^k v_{21}^k} \qquad Q_{12}^k = Q_{21}^k = \frac{v_{21}^k E_1^k}{1 - v_{12}^k v_{21}^k}$$

$$Q_{22}^k = \frac{E_2^k}{1 - v_{12}^k v_{21}^k} \qquad Q_{66}^k = G_{12}^k$$

If the layer is anisotropic, the stiffnesses of each of the layers are rotated to the principal directions of the plate by using the tensor rotation transformation

$$\begin{bmatrix} \sigma_x \\ \sigma_y \\ \tau_{xy} \end{bmatrix}_k = [T]^{-1} [Q]^k [T] \begin{bmatrix} \varepsilon_x \\ \varepsilon_y \\ \frac{1}{2}\gamma_{xy} \end{bmatrix}_k$$

$$[T] = \begin{bmatrix} m^2 & n^2 & 2mn \\ n^2 & m^2 & -2mn \\ -mn & mn & m^2-n^2 \end{bmatrix}$$

where

$$m = \cos\theta \quad \text{and} \quad n = \sin\theta$$

where θ is described in a counter-clockwise direction. Next, each of the transformed layer stiffnesses are assembled into a global stiffness matrix of the form:

$$\begin{bmatrix} N_x \\ N_y \\ N_{xy} \\ M_x \\ M_y \\ M_{xy} \end{bmatrix} = \begin{bmatrix} A_{11} & A_{12} & A_{16} & B_{11} & B_{12} & B_{16} \\ A_{12} & A_{22} & A_{26} & B_{12} & B_{22} & B_{26} \\ A_{16} & A_{26} & A_{66} & B_{16} & B_{26} & B_{66} \\ B_{11} & B_{12} & B_{16} & D_{11} & D_{12} & D_{16} \\ B_{12} & B_{22} & B_{26} & D_{21} & D_{22} & D_{26} \\ B_{16} & B_{26} & B_{66} & D_{61} & D_{62} & D_{66} \end{bmatrix} \begin{bmatrix} \varepsilon_x^o \\ \varepsilon_y^o \\ \gamma_{xy}^o \\ \kappa_x \\ \kappa_y \\ \kappa_{xy} \end{bmatrix}$$

where

$$A_{ij} = \sum_{k=1}^{N} \bar{Q}_{ij}^k \, (h_k - h_{k-1})$$

$$B_{ij} = \frac{1}{2} \sum_{k=1}^{N} \bar{Q}_{ij}^k \, (h_k^2 - {}_{k-1}^2) \qquad (i,j=1,2,6)$$

$$D_{ij} = \frac{1}{3} \sum_{k=1}^{N} \bar{Q}_{ij}^k \, (h_k^3 - {}_{k-1}^3)$$

The goal is to solve for the mid-plane strain and curvatures of the coated structure, due the applied loads, then to use the strain values to back-calculate for all the stress components through the thickness of each of the materials in the structure. Thermal forces (due to cooling) are

$$N_x^t = \sum_{k-1}^{N} (\bar{Q}_{11}^k \, \alpha_x^k + \bar{Q}_{12}^k \, \alpha_y^k + \bar{Q}_{16}^k \, \alpha_{xy}^k) \, (h_k - h_{k-1}) \, \Delta T^k$$

$$N_y^t = \sum_{k-1}^{N} (\bar{Q}_{12}^k \, \alpha_x^k + \bar{Q}_{22}^k \, \alpha_y^k + \bar{Q}_{26}^k \, \alpha_{xy}^k) \, (h_k - h_{k-1}) \, \Delta T^k$$

$$N_{xy}^t = \sum_{k-1}^{N} (\bar{Q}_{16}^k \, \alpha_x^k + \bar{Q}_{26}^k \, \alpha_y^k + \bar{Q}_{66}^k \, \alpha_{xy}^k) \, (h_k - h_{k-1}) \, \Delta T^k$$

$$M_x^t = \frac{1}{2} \sum_{k-1}^{N} (\bar{Q}_{11}^k \alpha_x^k + \bar{Q}_{12}^k \alpha_y^k + \bar{Q}_{16}^k \alpha_{xy}^k)(h_k^2 - h_{k-1}^2) \Delta T^k$$

$$M_y^t = \frac{1}{2} \sum_{k-1}^{N} (\bar{Q}_{12}^k \alpha_x^k + \bar{Q}_{22}^k \alpha_y^k + \bar{Q})_{26}^k \alpha_{xy}^k)(h_k^2 - h_{k-1}^2) \Delta T^k$$

$$M_{xy}^t = \frac{1}{2} \sum_{k-1}^{N} (\bar{Q}_{16}^k \alpha_x^k + \bar{Q}_{26}^k \alpha_y^k + \bar{Q})_{66}^k \alpha_{xy}^k)(h_k^2 - h_{k-1}^2) \Delta T^k$$

and the total load on the structure is the sum of any mechanical loads and moments (here zero) with these thermal loads. The global stiffness matrix is then inverted to get

$$\begin{bmatrix} \varepsilon_x^o \\ \varepsilon_y^o \\ \gamma_{xy}^o \\ \kappa_x \\ \kappa_y \\ \kappa_{xy} \end{bmatrix} = \begin{bmatrix} H_{11} & H_{12} & H_{13} & H_{14} & H_{15} & H_{16} \\ H_{12} & H_{22} & H_{23} & H_{24} & H_{25} & H_{26} \\ H_{13} & H_{23} & H_{33} & H_{34} & H_{35} & H_{36} \\ H_{14} & H_{24} & H_{34} & H_{44} & H_{45} & H_{46} \\ H_{15} & H_{25} & H_{35} & H_{45} & H_{55} & H_{56} \\ H_{16} & H_{26} & H_{36} & H_{46} & H_{56} & H_{66} \end{bmatrix} \begin{bmatrix} N_x \\ N_y \\ N_{xy} \\ M_x \\ M_y \\ M_{xy} \end{bmatrix}$$

and the mid-plane strain and curvature can then be solved for by any matrix solution method. Mid-plane strain and curvatures are used to find the strains through the entire thickness of the coated substrate

$$\varepsilon_x = \varepsilon_x^o + z\kappa_x$$

$$\varepsilon_y = \varepsilon_y^o + z\kappa_y$$

$$\gamma_{xy} = \gamma_{xy}^o + z\kappa_{xy}$$

Now that strains have been resolved, stress can be found by

$$\sigma_x^k = \bar{Q}_{11}^k (\varepsilon_x^k - \alpha_x^k \Delta T^k) + \bar{Q}_{12}^k (\varepsilon_y^k - \alpha_y^k \Delta T^k) + \bar{Q}_{16}^k (\gamma_{xy}^k - \alpha_{xy}^k \Delta T^k)$$

$$\sigma_y^k = \bar{Q}_{21}^k (\varepsilon_x^k - \alpha_x^k \Delta T^k) + \bar{Q}_{22}^k (\varepsilon_y^k - \alpha_y^k \Delta T^k) + \bar{Q}_{26}^k (\gamma_{xy}^k - \alpha_{xy}^k \Delta T^k)$$

$$\tau_{xy}^k = \bar{Q}_{61}^k (\varepsilon_x^k - \alpha_x^k \Delta T^k) + \bar{Q}_{62}^k (\varepsilon_y^k - \alpha_y^k \Delta T^k) + \bar{Q}_{66}^k (\gamma_{xy}^k - \alpha_{xy}^k \Delta T^k)$$

Each of the ε_{ij}^k terms vary through the thickness a very small amount relative to the $\alpha \Delta T$ strain terms, thus leading to the sharp discontinuities in the in-plane stress terms when traversing material interfaces.

This theory has been implemented in a FORTRAN computer code, which also includes material properties of the specific material systems used here.

NOMENCLATURE

E_i	-	Young's Modulus
γ_{ij}	-	Poisson's Ratio
G_{ij}	-	Shear Modulus
Q_{ij}	-	Stiffness Component
T_{ij}	-	Rotation Transformation Component
ε_i^o	-	Mid-plane Strain
κ_i	-	Mid-plane Curvature
N_i	-	Applied Forces
M_i	-	Applied Moments
h	-	Total Thickness
h_i	-	Distance from Mid-plane to Interfaces
α_i	-	Coefficient of Thermal Expansion
ΔT	-	Temperature Change

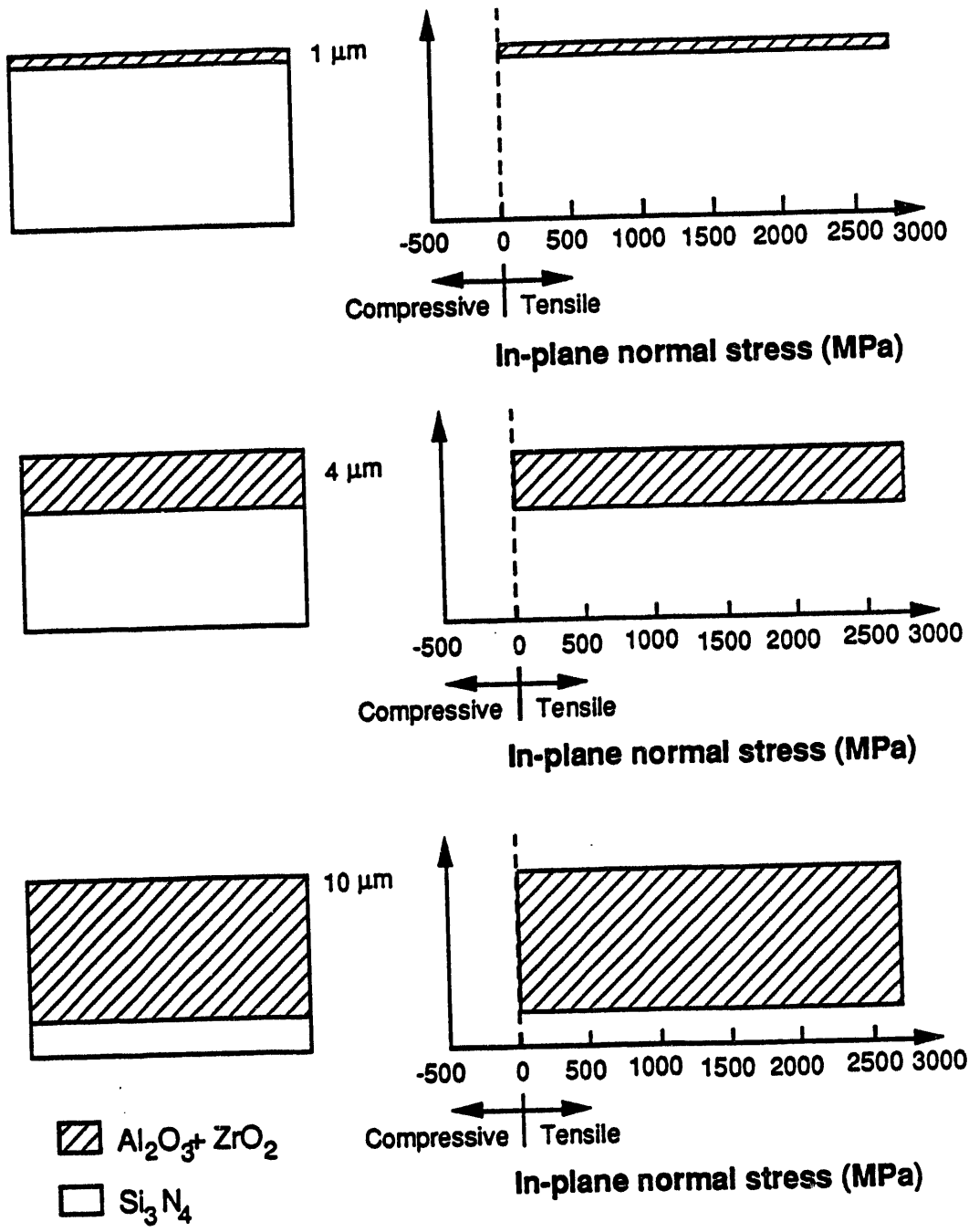

Figure D-1 In-plane residual stresses for a Si_3N_4 substrate coated with alumina-zirconia without an interlayer. Stresses for 1, 4 and 10 microns coating thicknesses are shown. Thickness of the coating layer has negligible effect on residual stress.

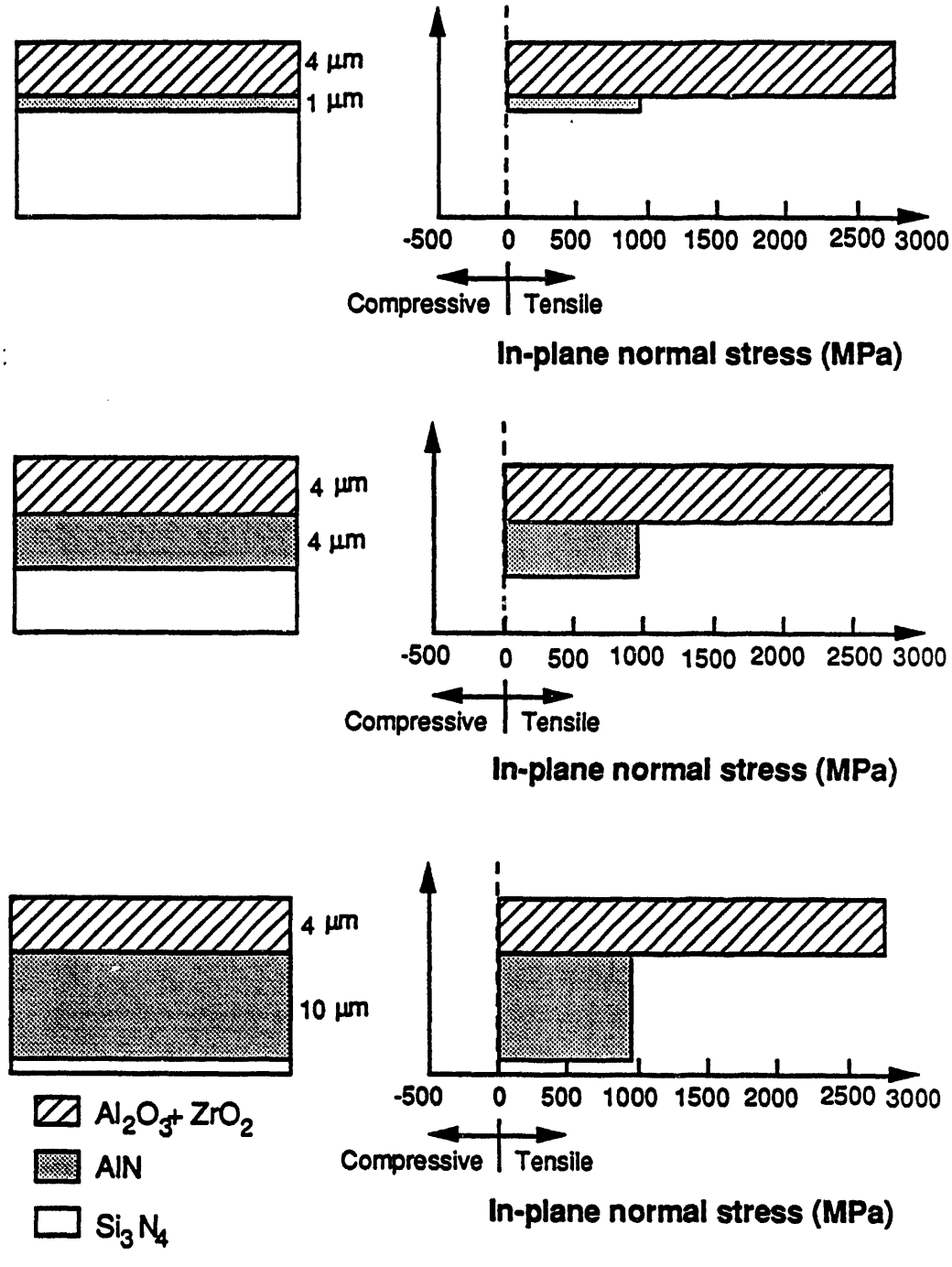

Figure D-2. In-plane residual stresses for a Si_3N_4 substrate coated with alumina-zirconia with an AlN interlayer. Stresses for 1, 4 and 10 microns interlayer thicknesses are shown. Thickness of the interlayer has negligible effect on residual stress.

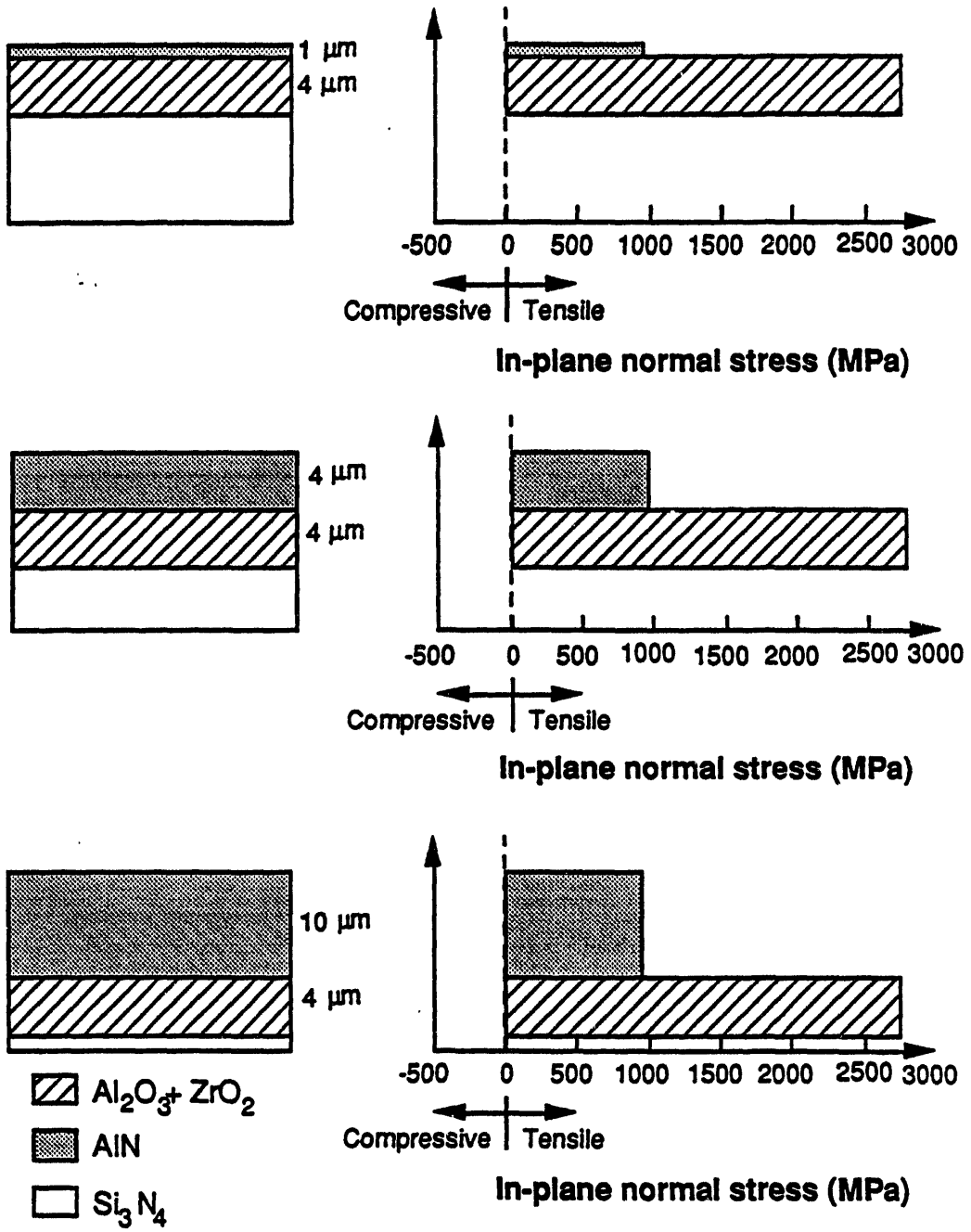

Figure D-3. In-plane residual stresses for a Si_3N_4 substrate coated with AlN and an alumina-zirconia interlayer (coating order is reversed from the previous figure). Stresses for 1,4 and 10 microns interlayer thicknesses are shown. Comparing to the previous figure, order of the coating layers has negligible effect on residual stress.

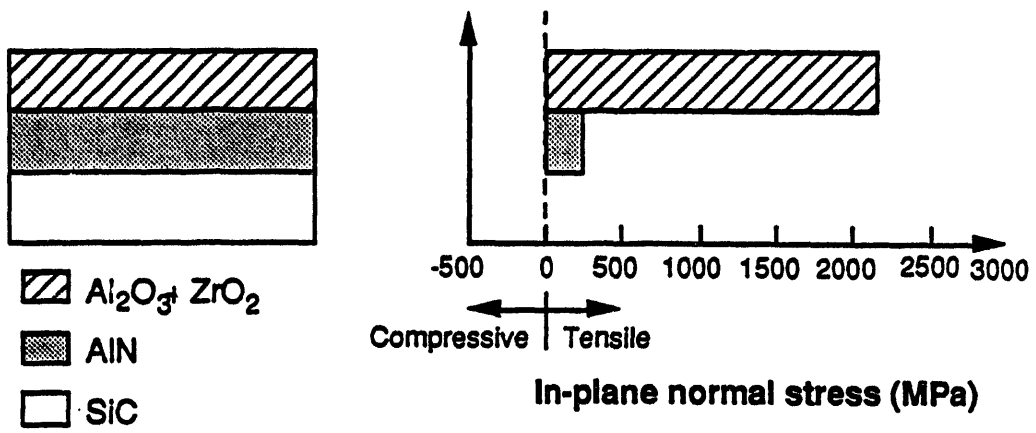

Figure D-4. In-plane residual stresses for a SiC substrate coated with AlN and alumina-zirconia. Stresses shown are applicable for a wide range of coating thicknesses.

INTERNAL DISTRIBUTION

Central Research Library (2)
Document Reference Section
Laboratory Records Department (2)
Laboratory Records, ORNL RC
ORNL Patent Section
M&C Records Office (3)
L. F. Allard, Jr.
L. D. Armstrong
P. F. Becher
R. F. Bernal
T. M. Besmann
P. J. Blau
A. Bleier
E. E. Bloom
K. W. Boling
R. A. Bradley
C. R. Brinkman
V. R. Bullington
R. S. Carlsmith
P. T. Carlson
G. M. Caton
S. J. Chang
R. H. Cooper, Jr.
B. L. Cox
D. F. Craig
S. A. David
J. H. DeVan
J. L. Ding
M. K. Ferber
F. M. Foust
W. Fulkerson
R. L. Graves
D. L. Greene
M. H. Harris
E. E. Hoffman
C. R. Hubbard
M. A. Janney
M. G. Jenkins
D. R. Johnson
D. Joslin
R. R. Judkins
M. A. Karnitz
M. R. Kass
B. L. P. Keyes
H. D. Kimrey, Jr.
K. C. Liu
E. L. Long, Jr.
W. D. Manly
R. W. McClung
D. J. McGuire
J. R. Merriman
T. A. Nolan
A. E. Pasto
J. L. Rich
J M Robbins
M. L. Santella
A. C. Schaffhauser
S. Scott
G. M. Slaughter
E. J. Soderstrom
D. P. Stinton
R. W. Swindeman
V. J. Tennery
T. N. Tiegs
J. R. Weir, Jr.
B. H. West
F. W. Wiffen
S. G. Winslow
J. M. Wyrick
C. S. Yust

EXTERNAL DISTRIBUTION

Pioneering Research Information Center
E. I. DuPond de Nemours & Co., Inc.
Experimental Station
P. O. Box 80302
Wilmington, DE 19880-0302

James H. Adair
University of Florida
Materials Science and Engineering
317 MAE Bldg.
Gainesville, FL 32611-2066

Donald F. Adams
University of Wyoming
Mechanical Engineering Department
P. O. Box 3295
Laramie, WY 82071

Jalees Ahmad
AdTech Systems Research, Inc.
1342 North Fairfield Road
Dayton, OH 45432-2698

Yoshio Akimune
NISSAN Motor Co., Ltd.
Materials Research Laboratory
1 Natsushima-Cho
Yokosuka 237
JAPAN AIR MAIL

Mufit Akinc
Iowa State University
322 Spedding Hall
Ames, IA 50011

Ilhan A. Aksay
University of Washington
Materials Science and Engineering
Department, FB-10
Seattle, WA 98195

R. G. Alexander
BASE, 26 Malvern Close
Kettering Northants NN16 AJP
UNITED KINGDOM AIR MAIL

Richard L. Allor
Ford Motor Company
Material Systems
Reliability Department
20000 Rotunda Drive
P.O. Box 2053, Room S-2031
Dearborn, MI 48121-2053

Richard T. Alpaugh
U.S. Department of Energy
Advanced Propulsion Division
CE-322, Forrestal Building
Washington, DC 20585

Joseph E. Amaral
Instron Corporation
Corporate Engineering Office
100 Royale Street
Canton, MA 02021

Edward M. Anderson
Aluminum Company of America
North American Industrial
Chemicals Division
P.O. Box 300
Bauxite, AR 72011

Norman C. Anderson
Ceradyne, Inc.
Ceramic-to-Metal Division
3169 Redhill Avenue
Costa Mesa, CA 92626

Don Anson
Battelle Columbus Laboratories
Thermal Power Systems
505 King Avenue
Columbus, OH 43201-2693

Thomas Arbanas
G.B.C. Materials Corporation
580 Monastery Drive
Latrobe, PA 15650-2698

Frank Armatis
3M Company
3M Center
Building 60-1N-01
St. Paul, MN 55144-1000

Everett B. Arnold
Detroit Diesel Corporation
Mechanical Systems Technology
13400 Outer Drive, West
Detroit, MI 48239-4001

Richard M. Arons
PA Consulting Group
279 Princeton Road
Hightstown, NJ 08550

Bertil Aronsson
Sandvik AB
S-12680
Stockholm Lerkrogsvagen 19
SWEDEN AIR MAIL

Dennis Assanis
University of Illinois
Department of Mechanical Engineering
1206 W. Green Street
Urbana, IL 61801

William H. Atwell
Dow Corning Corporation
3901 South Saginaw Road
MS:540
Midland, MI 48686-0995

V. S. Avva
North Carolina A&T State University
Department of Mechanical Engineering
Greensboro, NC 27411

Patrick Badgley
Adiabatics, Inc
3385 Commerce Drive
Columbus, IN 47201

Sunggi Baik
Pohang Institute of Science & Technology
Department of Materials Science and Engineering
P.O. Box 125
Pohang 790-600
KOREA AIR MAIL

John M. Bailey
Caterpillar, Inc.
Technical Center, Building L
P.O. Box 1875
Peoria, IL 61656-1875

Bob Baker
Ceradyne, Inc.
3169 Redhill Avenue
Costa Mesa, CA 92626

Frank Baker
Aluminum Company of America
Alcoa Technical Center
Alcoa Center, PA 15069

J. G. Baldoni
GTE Laboratories Inc.
40 Sylvan Road
Waltham, MA 02254

Clifford P. Ballard
Allied-Signal, Inc.
Ceramics Program
P.O. Box 1021
Morristown, NJ 07962-1021

B. P. Bandyopadhyay
Toyohashi University of Technology
School of Production Systems Engineering
Tempaku-Cho Toyohashi 440
JAPAN AIR MAIL

P. M. Barnard
Ruston Gas Turbines Limited
Metallurgical Laboratory
P. O. Box 1
Lincoln LN2 5DJ
ENGLAND AIR MAIL

Harold N. Barr
Hittman Corporation
9190 Red Branch Road
Columbia, MD 21045

Renald D. Bartoe
Vesuvius McDanel
510 Ninth Avenue
Box 560
Beaver Falls, PA 15010-0560

David L. Baty
Babcock & Wilcox-LRC
P.O. Box 11165
Lynchburg, VA 24506-1165

Donald F. Baxter, Jr.
ASM International
Advanced Materials and Processes
Materials Park, OH 44073-0002

M. Brad Beardsley
Caterpillar, Inc.
Advanced Materials Technology
Technical Center Bldg. E
P.O. Box 1875
Peoria, IL 61656-1875

John C. Bell
Shell Research Limited
Thornton Research Centre
P.O. Box 1, Chester, Ch1 3SH
ENGLAND AIR MAIL

Albert H. Bell, III
General Motors Technical Center
30200 Mound Road
Engineering Building/W3 Turbine
Warren, MI 48090-9010

M. Bentele
Xamag, Inc.
259 Melville Avenue
Fairfield, CT 06430

Larry D. Bentsen
BF Goodrich Company
R&D Center
9921 Brecksville Road
Brecksville, OH 44141

Joseph C. Bentz
ENCERATEC
2525 Sandcrest Drive
Columbus, IN 47203

Louis Beregszazi
Defiance Precision Products
P.O. Drawer 428
Defiance, OH 43512

Tom Bernecki
Northwestern University
BIRL
1801 Maple Avenue
Evanston, IL 60201-3135

Charles F. Bersch
Institute for Defense Analyses
1801 North Beauregard Street
Alexandria, VA 22311

Ram Bhatt
NASA Lewis Research Center
21000 Brookpark Road
Cleveland, OH 44135

Deane I. Biehler
Caterpillar, Inc.
Engineering and Research Materials
Technical Center, Building E
P.O. Box 1875
Peoria, IL 61656-1875

John. W. Bjerklie
Consolidated Natural Gas
Service Co., Inc.
Research Department
CNG Tower
Pittsburgh, PA 15222-3199

William D. Bjorndahl
TRW, Inc.
One Space Park
Building 01, Room 2040
Redondo Beach, CA 90278

Keith A. Blakely
Advanced Refractory Technologies, Inc.
699 Hertel Avenue
Buffalo, NY 14207

Edward G. Blanchard
Netzsch Inc.
119 Pickering Way
Exton, PA 19341

Keith Blandford
Boride Products, Inc.
2879 Aero Park Drive
Traverse City, MI 49684

Bruce Boardman
Deere and Company Technical Center
3300 River Drive
Moline, IL 61265

Russell Bockstedt
Hoechst Celanese Corporation
150 JFK Parkway
Short Hills, NJ 07078

M. Boehmer
DLR German Aerospace Research
Establishment
Postfach 90 60 58
D-5000 Koln 90
GERMANY AIR MAIL

Lawrence P. Boesch
EER Systems Corp.
1593 Spring Hill Road
Vienna, VA 22182-2239

Donald H. Boone
Boone & Associates
2412 Cascade Drive
Walnut Creek, CA 94598-4313

Tom Booth
Allied-Signal Aerospace Company
AiResearch Los Angeles Division
2525 West 190th Street
Torrance, CA 90509-2960

Tibor Bornemisza
Sundstrand Power Systems
4400 Ruffin Road
San Diego, CA 92186-5757

J.A.M. Boulet
University of Tennessee
Department of Engineering
Science and Mechanics
310 Perkins Hall
Knoxville, TN 37996-2030

H. Kent Bowen
Massachusetts Institute of Technology
77 Massachusetts Avenue
Room E40-434
Cambridge, MA 02139

Leslie J. Bowen
Materials Systems
53 Hillcrest Road
Concord, MA 01742

Steven C. Boyce
Air Force Office of
Scientific Research
AFOSR/NA Bldg. 410
Bolling AFB DC 20332-6448

Steve Bradley
UOP Research Center
50 East Algonquin Road
Des Plaines, IL 60017-6187

Michael C. Brands
Cummins Engine Company, Inc.
P.O. Box 3005
Mail Code 50179
Columbus, IN 47201

Raymond J. Bratton
Westinghouse Science and
Technology Center
1310 Beulah Road
Pittsburgh, PA 15235

John J. Brennan
United Technologies Corporation
Research Center
Silver Lane, MS:24
East Hartford, CT 06108

Jeff D. Bright
Ceramatec, Inc.
2425 South 900 West
Salt Lake City, UT 84108

Terrence K. Brog
Coors Ceramics Company
Corporate Development and Technology
4545 McIntyre Street
Golden, CO 80403

Gunnar Broman
317 Fairlane Drive
Spartanburg, SC 29302

Al Brown
High-Tech Materials Alert
P.O. Box 882
Dayton, NJ 08810

Jesse Brown
Virginia Polytechnic Institute
and State University
Center for Advanced Ceramic Materials
Blacksburg, VA 24061-0256

Sherman D. Brown
University of Illinois
Materials Science and
Engineering Department
105 South Goodwin Avenue
204 Ceramics Building
Urbana, IL 61801

S. L. Bruner
Ceramatec, Inc.
2425 South 900 West
Salt Lake City, UT 84119

Adolfo Brusaferro
Keramont Corporation
4231 South Fremont Avenue
Tucson, AZ 85714

Walter Bryzik
U.S. Army Tank Automotive Command
R&D Center
Propulsion Systems Division
Warren, MI 48397-5000

S. T. Buljan
GTE Laboratories, Inc.
40 Sylvan Road
Waltham, MA 02254

S. J. Burden
GTE Valenite
1711 Thunderbird
Troy, MI 48084

Curt V. Burkland
AMERCOM, Inc.
8928 Fullbright Avenue
Chatsworth, CA 91311

Bill Bustamante
AMERCOM, Inc.
8928 Fullbright Street
Chatsworth, CA 91311

Oral Buyukozturk
Massachusetts Institute of Technology
77 Massachusetts Avenue
Room 1-280
Cambridge, MA 02139

David A. Caillet
Ethyl Corporation
451 Florida Street
Baton Rouge, LA 70801

Frederick J. Calnan
Heany Industries, Inc.
249 Briarwood Lane
P.O. Box 38
Scottsville, NY 14546

Roger Cannon
Rutgers University
Ceramics Department
P.O. Box 909
Piscataway, NJ 08855-0909

Scott Cannon
P.O. Box 567254
Atlanta, GA 30356

Harry W. Carpenter
19945 Acre Street
Northridge, CA 91324

David Carruthers
Kyocera Industrial Ceramics Company
P.O. Box 2279
Vancouver, WA 98668-2279

Calvin H. Carter, Jr.
Cree Research, Inc.
2810 Meridian Parkway
Durham, NC 27713

J. David Casey
35 Atlantis Street
West Roxbury, MA 02132

Jere G. Castor
J. C. Enterprise
5078 North 83rd Street
Scottsdale, AZ 85250

James D. Cawley
Case Western Reserve University
Materials Science and
Engineering Department
Cleveland, OH 44106

Thomas C. Chadwick
Den-Mat Corporation
P.O. Box 1729
Santa Maria, CA 93456

Ronald H. Chand
Chand Kare Technical Ceramics
2 Coppage Drive
Worcester, MA 01603

Robert E. Chaney
EG&G Idaho, Inc.
Idaho National Engineering Laboratory
P.O. Box 1625
Idaho Falls, ID 83415-3525

Frank C. Chang
U.S. Army Materials
Technology Laboratory
AMTL-EMM
405 Arsenal Street
Watertown, MA 02172

Robert M. Chapman
Allied-Signal Aerospace Company
1001 Pennsylvania Avenue, N.W.
Suite 700 South
Washington, DC 20004

William Chapman
Williams International Corporation
2280 West Maple Road
Walled Lake, MI 48390-0200

Charlie Chen
LECO Corporation
P.O. Box 211688
Augusta, GA 30917

Frank Childs
EG&G Idaho, Inc.
Idaho National Engineering Laboratory
P.O. Box 1625
Idaho Falls, ID 83415-3527

William J. Chmura
Torrington Company
59 Field Street
Torrington, CT 06790-4942

Tsu-Wei Chou
University of Delaware
Center for Composite Materials
201 Spencer Laboratory
Newark, DE 19716

R. J. Christopher
Ricardo Consulting Engineers
Bridge Works
Shoreham-By-Sea West Sussex
BN43 5FG
ENGLAND AIR MAIL

Joel P. Clark
Massachusetts Institute of Technology
Room 8-409
Cambridge, MA 02139

Giorgio Clarotti
Commission of the European Communities
DGXII-C3, M075, 1-53;
200 Rue de la Loi
B-1049 Brussels
BELGIUM AIR MAIL

W. J. Clegg
ICI Advanced Materials
P.O. Box 11
The Heath, Runcorn Cheshire
WA7 4QE
ENGLAND AIR MAIL

Joseph Cleveland
GTE Products Corporation
Hawes Street
Towanda, PA 18848-0504

Gloria M. Collins
ASTM
1916 Race Street
Philadelphia, PA 19103

William C. Connors
Sundstrand Aviation Operations
Materials Science and
Engineering Department
4747 Harrison Avenue
P.O. Box 7002
Rockford, IL 61125-7002

John A. Coppola
Carborundum Company
P.O. Box 156
Niagara Falls, NY 14302

Normand D. Corbin
Norton Company, Advanced Ceramics
Goddard Road
Northboro, MA 01532-1545

Douglas Corey
Allied-Signal Aerospace Company
2525 West 190th Street
MS:T52
Torrance, CA 90504-6099

Keith P. Costello
Chand/Kare Technical Ceramics
2 Coppage Drive
Worcester, MA 01603-1252

Ed L. Courtright
Pacific Northwest Laboratory
MS:K3-59
Richland, WA 99352

Anna Cox
Mitchell Market Reports
P.O. Box 23
Monmouth Gwent NP5 4YG
UNITED KINGDOM AIR MAIL

J. Wesley Cox
BIRL
1801 Maple Avenue
Evanston, IL 60201-3135

Art Cozens
Instron Corporation
3414 Snowden Avenue
Long Beach, CA 90808

Robert C. Craft
American Ceramic Society, Inc.
757 Brooksedge Plaza Drive
Westerville, OH 43081

Mark Crawford
New Technology Week
4604 Monterey Drive
Annandale, VA 22003

Richard A. Cree
Markets & Products, Inc.
P.O. Box 14328
Columbus, OH 43214-0328

Les Crittenden
Vesuvius McDanel
Box 560
Beaver Falls, PA 15010

William J. Croft
U.S. Army Materials
Technology Laboratory
405 Arsenal Street
Watertown, MA 02172

M. J. Cronin
Mechanical Technology, Inc.
968 Albany-Shaker Road
Latham, NY 12110

Gary M. Crosbie
Ford Motor Company
1430 Culver Avenue
S-2079, SRL Building
Dearborn, MI 48121-4036

Floyd W. Crouse, Jr.
U.S. Department of Energy
Morgantown Energy
Technology Center
Collins Ferry Road
P.O. Box 880
Morgantown, WV 26505

John Cuccio
Allied-Signal Aerospace Company
Garrett Auxiliary Power Division
P.O. Box 5227, MS:1302-2Q
Phoenix, AZ 85010

Raymond Cutler
Ceramatec, Inc.
2425 South 900 West
Salt Lake City, UT 84119

Charles D'Angelo
GTE Laboratories, Inc.
40 Sylvan Road
Waltham, MA 02154

Stephen C. Danforth
Rutgers University
Ceramic Engineering Department
P.O. Box 909
Piscataway, NJ 08855-0909

Sankar Das Gupta
Electrofuel Manufacturing Co., Ltd.
9 Hanna Avenue
Toronto Ontario MGK-1W8
CANADA AIR MAIL

Charles Davis
Sverdrup Technology, Inc., MSFC
620 Discovery Drive
Huntsville, AL 35806

Frank Davis
Allied Signal Aerospace Co.
7550 Lucerne Dr., # 203
Middleburg Heights, OH 44130

Robert F. Davis
North Carolina State University
Materials Engineering Department
229 Riddick Laboratory
P.O. Box 7907
Raleigh, NC 27695

Thomas DeAngelis
Carborundum Company
Niagara Falls R&D Center
P.O. Box 832
Niagara Falls, NY 14302

George DeBell
Ford Motor Company
Material Systems Reliability Department
20000 Rotunda Drive
P.O. Box 2053, Room S-2023
Dearborn, MI 48121-2053

Michael DeLuca
AMP-AKZO
West Lane
Aquebogue, NY 11931

Gerald L. DePoorter
Colorado School of Mines
Metallurgical and Materials
Engineering Department
Golden, CO 80401

J. F. DeRidder
Omni Electro Motive, Inc.,
12 Seely Hill Road
Newfield, NY 14867

Nick C. Dellow
Materials Technology Publications
40 Sotheron Road
Watford Herts WD1 2QA
UNITED KINGDOM AIR MAIL

L. R. Dharani
University of Missouri-Rolla
224 M.E.
Rolla, MO 65401

Douglas A. Dickerson
Union Carbide Specialty Powders
1555 Main Street
Indianapolis, IN 46224

John Dodsworth
Vesuvius Research & Development
Technical Ceramics Group
Box 560
Beaver Falls, PA 15010

B. Dogan
Institut fur Werkstofforschung
GKSS-Forschungszentrum
Geesthacht GmbH
Max-Planck-Strasse
D-2054 Geesthacht
GERMANY AIR MAIL

Jean-Marie Drapier
FN Moteurs S.A.
Material and Processing
B-4041 Milmort (Herstal)
BELGIUM AIR MAIL

Kenneth C. Dreitlein
United Technologies
Research Center
Silver Lane
East Hartford, CT 06108

Robin A.L. Drew
McGill University
Department of Mining and
Metallurgical Engineering
3450 University Street
Montreal Quebec H3A 2A7
CANADA AIR MAIL

Winston H. Duckworth
BCL
Columbus Division
505 King Avenue
Columbus, OH 43201-2693

Bill Durako
Sundstrand Aviation Operations
Department 789-6
4747 Harrison Avenue
P.O. Box 7002
Rockford, IL 61125-7002

Ernest J. Duwell
212 Elm Street
Hudson, WI 54016

Chuck J. Dziedzic
Coors Ceramics Company
Structural Products Group
17750 West 32nd Avenue
Golden, CO 80401

Robert J. Eagan
Sandia National Laboratories
Engineered Materials & Processes Center
Org 1700
P.O. Box 5800
Albuquerque, NM 87185-5800

Jeffrey Eagleson
Lanxide Corporation
1001 Connecticut Avenue, N.W.
Washington, DC 20036

Harry E. Eaton
United Technologies Corporation
Research Center
Silver Lane
East Hartford, CT 06108

Harvill C. Eaton
Louisiana State University
Office of Research and Economic
Development
240 Thomas Boyd Hall
Baton Rouge, LA 70803

Christopher A. Ebel
Carborundum Company
Technology Division
P.O. Box 337
Niagara Falls, NY 14302

J. J. Eberhardt
U.S. Department of Energy
Office of Transportation Materials
CE-34
Washington, DC 20585

Jim Edler
Eaton Corporation
26201 Northwestern Highway
P.O. Box 766
Southfield, MI 48037

William A. Ellingson
Argonne National Laboratory
Materials Science & Technology Division
9700 South Cass Avenue
Argonne, IL 60439

William S. Ellis
Machined Ceramics
629 N. Graham St.
N. Industrial Park
Bowling Green, KY 42101

Glen B. Engle
Nuclear & Aerospace Materials
Corporation
16716 Martincoit Road
Poway, CA 92064

Jeff Epstein
Ceramic Technologies, Inc.
2107 Jamara Lane
Houston, TX 77077

Kenneth A. Epstein
Dow Chemical U.S.A.
Ceramics and Advanced Materials
800 Building
Midland, MI 48667

Art Erdemir
Argonne National Laboratory
Materials and Components
Technology Division
9700 South Cass Avenue
Argonne, IL 60439

E. M. Erwin
Lubrizol Corporation
1819 East 225th Street
Euclid, OH 44117

Kenji Esaki
Toyota Technical Center
U.S.A., Inc.
2000 Town Center, Suite 500
Southfield, MI 48075

John N. Eustis
U.S. Department of Energy
Industrial Energy Efficiency Division
CE-221
Washington, DC 20585

Robert C. Evans
NASA Lewis Research Center
Terrestrial Propulsion Office
21000 Brookpark Road, MS:86-6
Cleveland, OH 44135

W. L. Everitt
Kyocera International, Inc.
8611 Balboa Avenue
San Diego, CA 92123

Gordon Q. Evison
332 South Michigan Avenue
Suite 1730
Chicago, IL 60604

John W. Fairbanks
U.S. Department of Energy
Advanced Propulsion Division
CE-322
Washington, DC 20585

Tim Fawcett
Dow Chemical Company
Central Research, Advanced
Ceramics Laboratory
1776 Building
Midland, MI 48674

Robert W. Fawley
Sundstrand Power Systems
Division of Sundstrand Corporation
4400 Ruffin Road
P.O. Box 85757
San Diego, CA 92186-5757

John J. Fedorchak
GTE Products Corporation
Hawes Street
Towanda, PA 18848-0504

Jeff T. Fenton
Vista Chemical Company
900 Threadneedle
Houston, TX 77079

Larry Ferrell
Babcock & Wilcox
Old Forest Road
Lynchburg, VA 24505

Raymond R. Fessler
BIRL
Industrial Research Lab
1801 Maple Avenue
Evanston, IL 60201

Ross F. Firestone
Ross Firestone Company
188 Mary Street
Winnetka, IL 60093-1520

Sharon L. Fletcher
Arthur D. Little, Inc.
15 Acorn Park
Cambridge, MA 02140-2390

Thomas F. Foltz
Textron Specialty Materials
2 Industrial Avenue
Lowell, MA 01851

Renee G. Ford
Materials and Processing Report
P.O. Box 72
Harrison, NY 10528

John Formica
Supermaterials
2020 Lakeside Avenue
Cleveland, OH 44114

Edwin Frame
Southwest Research Institute
Division 2
P.O. Drawer 28510
San Antonio, TX 78284

Armanet Francois
French Scientific Mission
4101 Reservoir Road, N.W.
Washington DC 20007-2176

R. G. Frank
Technology Assessment Group
10793 Bentley Pass Lane
Loveland, OH 45140

David J. Franus
Forecast International
22 Commerce Road
Newtown, CT 06470

Marc R. Freedman
NASA Lewis Research Center
21000 Brookpark Road
MS:49-3
Cleveland, OH 44135

Douglas Freitag
LTV Missiles Division
P.O. Box 650003
MS:WT-21
Dallas, TX 75265

Brian R.T. Frost
Argonne National Laboratory
9700 South Cass Avenue
Building 900
Argonne, IL 60439

Lawrence R. Frost
Instron Corporation
100 Royall Street
Canton, MA 02021

George A. Fryburg
Norton/TRW Ceramics
7A-4 Raymond Avenue
Salem, NH 03079

Xiren Fu
Shanghai Institute of Ceramics
Chinese Academy of Sciences
1295 Ding-xi Road
Shanghai 200050
CHINA AIR MAIL

John Gahimer
P.O. Box 1302
Dublin, OH 43017

J. P. Gallagher
University of Dayton Research
Institute
300 College Park, JPC-250
Dayton, OH 45469-0120

Tom Garritano
University of Tennessee
Science Alliance
101 South College
Knoxville, TN 37996-1328

Joy A. Garwood
Norton Company
Advanced Ceramics
Goddard Road
Northboro, MA 01532-1545

H. Maury Gatewood
Reynolds Metals Company
Corporate R&D
Fourth and Canal Streets
P.O. Box 27003
Richmond, VA 23261

L. J. Gauckler
ETH-Zurich
Sonneggstrasse 5
CH-8092 Zurich 8092
SWITZERLAND AIR MAIL

Peter A. Gaydos
Battelle Columbus Laboratories
505 King Avenue
Columbus, OH 43201

George E. Gazza
U.S. Army Materials
Technology Laboratory
Ceramics Research Division
405 Arsenal Street
Watertown, MA 02172-0001

D. Gerster
CEA-DCOM
33 Rue De La Federation
Paris 75015
FRANCE AIR MAIL

John Ghinazzi
Coors Technical Ceramics Company
1100 Commerce Park Drive
Oak Ridge, TN 37830

Robert Giddings
General Electric Company
Research Laboratory
P.O. Box 8
Schenectady, NY 12301

A. M. Glaeser
University of California
Materials Science and Mineral Engineering
Lawrence Berkeley Laboratory
Hearst Mining Building
Berkeley, CA 94720

Joseph W. Glatz
Naval Air Propulsion Center
Systems Engineering Division
P.O. Box 7176, PE24
Trenton, NJ 08628

W. M. Goldberger
Superior Graphite Company
R&D
2175 East Broad Street
Columbus, OH 43209

Allan E. Goldman
U.S. Graphite, Inc.
907 West Outer Drive
Oak Ridge, TN 37830

Stephen T. Gonczy
Allied Signal Research
P.O. Box 5016
Des Plaines, IL 60017

Jeffrey M. Gonzales
GTE Products Corporation
Hawes Street
Towanda, PA 18848-0504

Robert J. Gottschall
U.S. Department of Energy
ER-131, MS:G-236
Washington, DC 20545

Earl Graham
Cleveland State University
Department of Chemical Engineering
Euclid Avenue at East 24th Street
Cleveland, OH 44115

William A. Graham
Lanxide Corporation
P.O. Box 6077
Newark, DE 19714-6077

Robert E. Green, Jr.
Johns Hopkins University
Materials Science and Engineering
Department
Baltimore, MD 21218

Lance Groseclose
General Motors Corporation
Allison Gas Turbine Division
P.O. Box 420, MS:W-5
Indianapolis, IN 46206

Mark F. Gruninger
Union Carbide Corporation
Specialty Powder Business
1555 Main Street
Indianapolis, IN 46224

Ernst Gugel
Cremer Forschungsinstitut
GmbH&Co.KG
Oeslauer Strasse 35
D-8633 Roedental 8633
GERMANY AIR MAIL

Donald L. Guile
Corning Glass Works
SP-DV-1-9
Corning, NY 14831

Bimleshwar P. Gupta
Solar Energy Research Institute
Mechanical and Industrial
Technology Division
1617 Cole Boulevard
Golden, CO 80401

John P. Gyekenyesi
NASA Lewis Research Center
21000 Brookpark Road, MS:6-1
Cleveland, OH 44135

Nabil S. Hakim
Detroit Diesel Corporation
13400 West Outer Drive
Detroit, MI 48239

Philip J. Haley
General Motors Corporation
Vehicular Engineering
P.O. Box 420, MS:T12A
Indianapolis, IN 46236

Judith Hall
Fiber Materials, Inc.
Biddeford Industrial Park
5 Morin Street
Biddeford, ME 04005

Y Hamano
Kyocera Corporation
5-22 Kitainoue-Cho, Higashino
Yamashina-Ku Kyoto 607
Japan AIR MAIL

Y. Harada
IIT Research Institute
Nometallic Materials and Composites
10 West 35th Street
Chicago, IL 60616

R. A. Harmon
25 Schalren Drive
Latham, NY 12110

Norman H. Harris
Hughes Aircraft Company
P.O. Box 800520
Saugus, CA 91380-0520

Alan M. Hart
Dow Chemical Company
Advanced Ceramics Laboratory
1776 Building
Midland, MI 48674

Pat E. Hart
Battelle Pacific Northwest Laboratories
Ceramics and Polymers
Development Section
P.O. Box 999
Richland, WA 99352

Stephen D. Hartline
Norton Company
Advanced Ceramics
Goddard Road
Northboro, MA 01532-1545

Michael H. Haselkorn
Caterpillar, Inc.
Engineering Research Materials
Technical Center, Building E
P.O. Box 1875
Peoria, IL 61656-1875

N. B. Havewala
Corning, Inc.
SP-PR-11
Corning, NY 14831

John Haygarth
Teledyne WAA Chang Albany
P.O. Box 460
Albany, OR 97321

Norman L. Hecht
University of Dayton Research Institute
300 College Park
Dayton, OH 45469-0172

Peter W. Heitman
General Motors Corporation
Allison Gas Turbine Division
P.O. Box 420, MS:W-5
Indianapolis, IN 46206-0420

Robert W. Hendricks
Virginia Polytechnic Institute
and State University
Materials Engineering Department
210 Holden Hall
Blacksburg, VA 24061-0237

Wynne Henley
Hertel Cutting Technologies, Inc.
1000 Clearview Court
Oak Ridge, TN 37830

Thomas L. Henson
GTE Products Corporation
Chemical & Metallurgical Division
Hawes Street
Towanda, PA 18848

Thomas P. Herbell
NASA Lewis Research Center
21000 Brookpark Road
MS:49-3
Cleveland, OH 44135

Marlene Heroux
Rolls-Royce, Inc.
2849 Paces Ferry Road
Suite 450
Atlanta, GA 30339-3769

Robert L. Hershey
Science Management Corporation
1255 New Hampshire Ave., N.W.
Suite 1033
Washington, DC 20036

Hendrik Heystek
Bureau of Mines
Tuscaloosa Research Center
P.O. Box L
University, AL 35486

Wallace C. Higgins
Norwal Unlimited
P.O. Box 1258
Alfred, NY 14802

Robert V. Hillery
GE Aircraft Engines
One Neumann Way, M.D. H85
Cincinnati, OH 45215

Arthur Hindman
Instron Corporation
100 Royall Street
Canton, MA 02021

Jon Hines
American Ceramic Society, Inc.
757 Brooksedge Plaza Drive
Westerville, OH 43081-6136

Hans Erich Hintermann
CSEM
Materials and Micromechanics
Division
Rue Breguet 2
Neuchatel 2000
SWITZERLAND AIR MAIL

Shinichi Hirano
Mazda R&D of North America, Inc.
1203 Woodridge Avenue
Ann Arbor, MI 48105

Tommy Hiraoka
NGK Locke, Inc.
1000 Town Center
Southfield, MI 48075

John M. Hobday
U.S. Department of Energy
Morgantown Energy Technology Center
Collins Ferry Road
P.O. Box 880
Morgantown, WV 26507

Clarence Hoenig
Lawrence Livermore National Laboratory
P.O. Box 808, Mail Code L-369
Livermore, CA 94550

Thomas Hollstein
Fraunhofer-Institut fur
Werkstoffmechanik IWM
Wohlerstrabe 11
D-7800 Freiburg
GERMANY AIR MAIL

Richard Holt
National Research Council of Canada
Structures and Materials Laboratory
Ottawa Ontario K1A 0R6
CANADA AIR MAIL

A. T. Hopper
Battelle Columbus Laboratories
Metals and Ceramics Department
505 King Avenue
Columbus, OH 43201-2693

Michael Horgan
Materials Engineering Magazine
1100 Superior Avenue
Cleveland, OH 44114

Woodie Howe
Coors Technical Ceramics Company
1100 Commerce Park Drive
Oak Ridge, TN 37830

Stephen M. Hsu
National Institute of Standards
and Technology
Gaithersburg, MD 20899

Hann S. Huang
Argonne National Laboratory
9700 South Cass Avenue
Argonne, IL 60439-4815

Gene Huber
Precision Ferrites & Ceramics
5576 Corporate Drive
Cypress, CA 90630

M. L. Huckabee
GTE Laboratories, Inc.
40 Sylvan Road
Waltham, MA 02254

Harold A. Huckins
Princeton Advanced Technology, Inc.
56 Finley Road
Princeton, NJ 08540

Fred R. Huettic
Advanced Magnetics, Inc.
45 Corey Lane
Mendham, NJ 07945

Brian K. Humphrey
Lubrizol Petroleum Chemicals Co.
3000 Town Center, Suite 1340
Southfield, MI 48075-1201

Robert M. Humrick
Dylon Ceramic Technologies
3100 Edgehill Road
Cleveland Heights, OH 44118

Lorretta Inglehart
National Science Foundation
Division of Materials Research
1800 "G" Street, N.W.,
Room 408
Washington, DC 20550

Michael S. Inoue
Kyocera International, Inc.
KII Library, 8611 Balboa Avenue
San Diego, CA 92123-1580

Osama Jadaan
University of Wisconsin-Platteville
General Engineering Division
1 University Plaza
Platteville, WI 53818

Curtis A. Johnson
General Electric Company
Corporate R&D
Room MB-187
P.O. Box 8
Schenectady, NY 12301

Sylvia Johnson
SRI International
333 Ravenswood Avenue
Menlo Park, CA 94025

Thomas A. Johnson
Lanxide Corporation
1300 Marrows Road
P.O. Box 6077
Newark, DE 19714-6077

W. S. Johnson
Indiana University
One City Centre, Suite 200
Bloomington, IN 47405

Walter F. Jones
Air Force Office of Scientific Research
AFOSR/NA
Bolling Air Force Base
Washington, DC 20332-6448

Jill E. Jonkouski
U.S. Department of Energy
9800 South Cass Avenue
Argonne, IL 60439-4899

L. A. Joo
Great Lakes Research Corporation
P.O. Box 1031
Elizabethton, TN 37643

A. David Joseph
SPX Corporation
700 Terrace Point
Muskegon, MI 49443

Adam Jostsons
Australian Nuclear Science &
Technology Organization
Lucas Heights Research Laboratories
New Illawarra Road
Lucas Heights New South Wales
AUSTRALIA AIR MAIL

Matthew K. Juneau
Ethyl Corporation
451 Florida Street
Baton Rouge, LA 70801

Hartmut Kainer
Didier-Werke AG
Anlagentechnik Wiesbaden
Abraham-Lincoln-Str. 16
D-62 Wiesbaden
GERMANY AIR MAIL

Tom Kalamasz
Norton/TRW Ceramics
7A-4 Raymond Avenue
Salem, NH 03079

Lyle R. Kallenbach
Phillips Petroleum Company
R&D
Mail Drop:123AL
Bartlesville, OK 74004

Nick Kamiya
Kyocera Industrial Ceramics Corporation
2700 River Road
Des Plaines, IL 60018

Roy Kamo
Adiabatics, Inc.
3385 Commerce Park Drive
Columbus, IN 47201

Chih-Chun Kao
Industrial Technology Research Institute
Materials Research Laboratories
195 Chung-Hsing Road, Sec. 4
Chutung Hsinchu 31015 R.O.C.
TAIWAN AIR MAIL

Keith R. Karasek
Allied-Signal, Inc.
Engineered Materials Research Center
50 East Algonquin Road
P.O. Box 5016
Des Plaines, IL 60017-5016

Martha R. Kass
U.S. Department of Energy
Oak Ridge Operations
Building 4500N
P.O. Box 2008, MS:6269
Oak Ridge, TN 37831-6269

Robert E. Kassel
Ceradyne, Inc.
3169 Redhill Avenue
Costa Mesa, CA 92626

Allan Katz
Wright Laboratory
Metals and Ceramics Division
WL/MLLM
Wright-Patterson AFB, OH 45433

R. Nathan Katz
Worcester Polytechnic Institute
Dept. of Mechanical Engineering
100 Institute Road
Worcester, MA 01609

Ted Kawaguchi
Tokai Carbon America, Inc.
375 Park Avenue, Suite 3802
New York, NY 10152

Noritsugu Kawashima
TOSHIBA Corporation
Mechanical Engineering Laboratory
4-1 Ukishima-Cho
Kawasaki-Ku Kawasaki 210
JAPAN AIR MAIL

Lisa Kempfer
Penton Publishing
Materials Engineering
1100 Superior Avenue
Cleveland, OH 44114-2543

Frederick L. Kennard, III
General Motors Corporation
AC Rochester
Department 32-24, EB
1300 North Dort Highway
Flint, MI 48556

David O. Kennedy
Lester B. Knight Cast
Metals Inc.
549 West Randolph Street
Chicago, IL 60661

George Keros
Photon Physics
3175 Penobscot Building
Detroit, MI 48226

Pramod K. Khandelwal
General Motors Corporation
Allison Gas Turbine Division
P.O. Box 420, MS:W05
Indianapolis, IN 46206

Jim R. Kidwell
Allied-Signal Aerospace Company
Garrett Auxiliary Power Division
P.O. Box 5227
Phoenix, AZ 85010

Han J. Kim
GTE Laboratories, Inc.
40 Sylvan Road
Waltham, MA 02254

Shin Kim
Korea Institute of Machinery & Metals
66 Sangnam-dong, Changwon
Kyungnam 641-010
KOREA AIR MAIL

W. C. King
Mack Truck, Z-41
1999 Pennsylvania Avenue
Hagerstown, MD 21740

Carol Kirkpatrick
MSE, Inc.
CDIF Technical Library
P.O. Box 3767
Butte, MT 59702

Tony Kirn
Caterpillar, Inc.
Defense Products Department, JB7
Peoria, IL 61629

James D. Kiser
NASA Lewis Research Center
21000 Brookpark Road, MS:49-3
Cleveland, OH 44135

Max Klein
Gas Research Institute
Thermodynamics
8600 West Bryn Mawr Avenue
Chicago, IL 60631

Richard N. Kleiner
Coors Ceramics Company
4545 McIntyre Street
Golden, CO 80403

Stanley J. Klima
NASA Lewis Research Center
21000 Brookpark Road
MS:6-1
Cleveland, OH 44135

Chris E. Knapp
Norton Advanced Ceramics
of Canada Ltd.
8001 Daly Street
Niagara Falls, Ontario L2G 6S2
CANADA AIR MAIL

Albert S. Kobayashi
University of Washington
Mechanical Engineering Department
MS:FU10
Seattle, WA 98195

Shigeki Kobayashi
Toyota Central Research Labs, Inc.
Nagakute Aichi 480-11
JAPAN AIR MAIL

Richard A. Kole
Z-Tech Corporation
8 Dow Road
Bow, NH 03304

E. Kostiner
University of Connecticut
Chemistry Department, U-60
Storrs, CT 06269-3060

Kenneth A. Kovaly
Technical Insights, Inc.
P.O. Box 1304
Fort Lee, NJ 07024-9967

Ralph G. Kraft
Spraying Systems Company
North Avenue at Schmale Road
Wheaton, IL 60189-7900

Saunders B. Kramer
U.S. Department of Energy
Advanced Propulsion Division
CE-322, Forrestal Building
Washington, DC 20585

Arthur Kranish
Trends Publishing, Inc.
1079 National Press Building
Washington, DC 20045

A. S. Krieger
Radiation Science, Inc.
P.O. Box 293
Belmont, MA 02178

Pieter Krijgsman
Ceramic Design International
Holding B.V.
P.O. Box 68
Hattem 8050-AB
THE NETHERLANDS AIR MAIL

Waltraud M. Kriven
University of Illinois
Materials Science and
Engineering Department
105 South Goodwin Avenue
Urbana, IL 61801

Edward J. Kubel, Jr.
ASM International Advanced
Materials & Processes
Materials Park, OH 44073

Dave Kupperman
Argonne National Laboratory
9700 South Cass Avenue
Argonne, IL 60439

Oh-Hun Kwon
Norton Company
Advanced Ceramics
Goddard Road
Northboro, MA 01532-1545

W. J. Lackey
Georgia Institute of Technology
Materials Science and Technology
Atlanta, GA 30332

Jai Lala
Tenmat Ltd., 40 Somers Road
Rugby Warwickshire CV22 7DH
ENGLAND AIR MAIL

Hari S. Lamba
General Motors Corporation
Electro-Motive Division
9301 West 55th Street
LaGrange, IL 60525

Richard L. Landingham
Lawrence Livermore National
Laboratory
Ceramics, Corrosion, and
Thermochemistry
P.O. Box 808, L-369
Livermore, CA 94550

Charles J. Landry
Chand Kare Technical Ceramics
712 Flat Hill Road
Lumenburg, MA 01462

Manfred W. Langer
Volkswagen AG
Material Technology
3180 Wolfsburg 1
GERMANY AIR MAIL

James Lankford
Southwest Research Institute
Department of Materials Sciences
6220 Culebra Road
San Antonio, TX 78228-0510

Stanley B. Lasday
Business News Publishing Co.
Manor Oak One
1910 Cochran Road, Suite 630
Pittsburgh, PA 15220

Mark S. Laser
Solar Turbines, Inc.
2211 Erie Street
San Diego, CA 92110

S. K. Lau
Carborundum Company
Technology Division
P.O. Box 832, B-100
Niagara Falls, NY 14302

Edward A. Lauder
Advanced Composite Materials
Corporation
1525 South Buncombe Road
Greer, SC 29651-9208

J. Lawrence Lauderdale
Babcock & Wilcox
Contract Research Division
1850 "K" Street, Suite 950
Washington, DC 20006

Harry A. Lawler
Carborundum Company
Technology Division
P.O. Box 832
Niagara Falls, NY 14302

Jean F. LeCostaouec
Textron Speciality Materials
2 Industrial Avenue
Lowell, MA 01851

Benson P. Lee
Interscience, Inc.
9718 Lake Shore Boulevard
Cleveland, OH 44108

Burtrand I. Lee
Clemson University
Department of Ceramic
Engineering
Olin Hall
Clemson, SC 29634-0907

June-Gunn Lee
KIST
Structural Ceramic Lab
P.O. Box 131, Cheong-Ryang
Seoul 130-650
KOREA AIR MAIL

Ran-Rong Lee
Ceramics Process Systems Corporation
155 Fortune Boulevard
Milford, MA 01757

Stan Levine
NASA Lewis Research Center
21000 Brookpark Road
MS:49-3
Cleveland, OH 44135

Alan V. Levy
Lawrence Berkeley Laboratory
One Cyclotron Road, MS:62-203
Berkeley, CA 94720

Ai-Kang Li
Materials Research Laboratories, ITRI
195-5 Chung-Hsing Road, Sec. 4
Chutung Hsinchu 31015 R.O.C.
TAIWAN AIR MAIL

Winston W. Liang
Hong Kong Industrial
Technology Centre Co. Ltd.
78 Tat Chee Avenue
4/F, HKPC Building
Howloon
HONG KONG AIR MAIL

Robert Licht
Norton Company
Advanced Ceramics
Goddard Road
Northboro, MA 01532-1545

E. Lilley
Norton Company
Advanced Ceramics
Goddard Road
Northboro, MA 01532-1545

Laura J. Lindberg
Allied-Signal Aerospace Company
Garrett Fluid Systems Division
1300 West Warner
MS: 93-901-1207-4TT
P.O. Box 22200
Tempe, AZ 85284-2200

Leonard C. Lindgren
General Motors Corporation
Allison Gas Turbine Division
P.O. Box 420, Speed Code:T-20A
Indianapolis, IN 46206-0420

Hans A. Lindner
Cremer Forschungsinstitut
GmbH&Co.KG
Oeslauer Strasse 35
D-8633 Rodental 8866
GERMANY AIR MAIL

Ronald E. Loehman
Sandia National Laboratories
Chemistry & Ceramics
Department 1840
P.O. Box 5800
Albuquerque, NM 87185

Jeffrey C. Logas
Winona State University
Composite Materials Engineering
115 Pasteur Hall
Winona, MN 55987

Bill Long
Babcock & Wilcox
P.O. Box 11165
Lynchburg, VA 24506

William D. Long
Wacker Chemicals (USA), Inc.
ESK Engineered Ceramics
50 Locust Avenue
New Canaan, CT 06840

L. A. Lott
EG&G Idaho, Inc.
Idaho National Engineering Laboratory
P.O. Box 1625
Idaho Falls, ID 83415-2209

Raouf O. Loutfy
MER Corporation
7960 South Kolb Road
Tucson, AZ 85706

Gordon R. Love
Aluminum Company of America
Alcoa Technical Center
Alcoa Center, PA 15069

Lydia Luckevich
Ortech International
2395 Speakman Drive
Mississauga Ontario L5K 1B3
CANADA AIR MAIL

James W. MacBeth
Carborundum Company
Structural Ceramics Division
P.O. Box 1054
Niagara Falls, NY 14302

H. MacLaren
General Electric Company
Thomson Laboratory, Materials
Engineering 36807
1000 Western Avenue
Lynn, MA 01910

George Maczura
Aluminum Company of America
Industrial Chemicals Division
670 One Allegheny Square
Pittsburgh, PA 15212

David Maginnis
Tinker AFB
OC-ALC/LIIRE
Tinker AFB OK 73145-5989

Frank Maginnis
Aspen Research, Inc.
220 Industrial Boulevard
Moore, OK 73160

Tai-il Mah
Universal Energy Systems, Inc.
Ceramics and Composites
Research
4401 Dayton-Xenia Road
Dayton, OH 45432

Kenneth M. Maillar
Barbour Stockwell Company
83 Linskey Way
Cambridge, MA 02142

Lorenzo Majno
Instron Corporation
100 Royall Street
Canton, MA 02021

S. G. Malghan
National Institute of Standards
and Technology
I-270 & Clopper Road
Gaithersburg, MD 20899

Lars Malmrup
United Turbine AB
Box 13027
Malmo S-200 44
SWEDEN AIR MAIL

John Mangels
Ceradyne, Inc.
3169 Redhill Avenue
Costa Mesa, CA 92626

Russell V. Mann
Matec Applied Sciences, Inc.
75 South Street
Hopkinton, MA 01748

William R. Manning
Champion Aviation Products Division
Old Norris Road
P.O. Box 686
Liberty, SC 29657

Ken Marnoch
Amercom, Inc.
8928 Fullbright Avenue
Chatsworth, CA 91311

Robert A. Marra
Aluminum Company of America
Alcoa Technical Center
Advanced Ceramics Center - E
Alcoa Center, PA 15069

Chauncey L. Martin
3M Company
3M Center, Building 60-1N-01
St. Paul, MN 55144

Steven C. Martin
Advanced Refractory
Technologies, Inc.
699 Hertel Avenue
Buffalo, NY 14207

Kelly J. Mather
Williams International Corporation
2280 West Maple Road
P.O. Box 200
Walled Lake, MI 48088

James P. Mathers
3M Company
3M Center
Building 201-3N-06
St. Paul, MN 55144

Ron Mayville
Arthur D. Little, Inc.
15-163 Acorn Park
Cambridge, MA 02140

F. N. Mazadarany
General Electric Company
Research Laboratory
Building K-1, Room MB-159
P.O. Box 8
Schenectady, NY 12301

James W. McCauley
Alfred University
NYS College of Ceramics
Binns-Merrill Hall
Alfred, NY 14802

Louis R. McCreight
2763 San Ramon Drive
Rancho Palos Verdes, CA 90274

Colin F. McDonald
McDonald Thermal Engineering
1730 Castellana Road
La Jolla, CA 92037

B. J. McEntire
Norton Company, TRW Ceramics
Goddard Road
Northboro, MA 01532-1545

Chuck McFadden
Coors Ceramics Company
600 9th Street
Golden, CO 80401

Henry McFadden
Magnetic Bearings, Inc.
Engineering Library
609 Rock Road
Radford, VA 24141

Thomas D. McGee
Iowa State University
Materials Science and
Engineering Department
110 Engineering Annex
Ames, IA 50011

Carol McGill
Corning Inc.
Sullivan Park, FR-02-08
Corning, NY 14831

T. C. McLaren
Cameron Forged Products
Company
P.O. Box 1212
Houston, TX 77251-1212

James McLaughlin
Sundstrand Power Systems
4400 Ruffin Road
P.O. Box 85757
San Diego, CA 92186-5757

Matt McMonigle
U.S. Department of Energy
Improved Energy Productivity
Division
CE-231
Washington, DC 20585

Dennis McMurtry
EG&G Idaho, Inc.
Idaho National Engineering
Laboratory
P.O. Box 1625
Idaho Falls, ID 83415

J. C. McVickers
Allied-Signal Aerospace Company
Garrett Auxiliary Power Division
Bldg. 1303-206
P.O. Box 5227, MS:9317-2
Phoenix, AZ 85010

D. B. Meadowcroft
National Power Technology
and Environmental Centre
Kelvin Avenue
Leatherhead Surrey
KT22 7SE
ENGLAND AIR MAIL

Jo Meglen
11004 Birdfoot Court
Reston, VA 22091

Joseph J. Meindl
Reynolds International, Inc.
6603 West Broad Street
P.O. Box 27002
Richmond, VA 23261-7003

Michael D. Meiser
Allied-Signal Aerospace Company
Garrett Ceramic Components Division
2525 West 190th Street
P.O. Box 2960, MS:T21
Torrance, CA 90509-2960

George Messenger
National Research Council of
Canada
Engine Laboratory
Building M-7
Ottawa Ontario K1A OR6
CANADA AIR MAIL

D. Messier
U.S. Army Materials Technology
Laboratory
SLCMT-EMC
405 Arsenal Street
Watertown, MA 02172-0001

Arthur G. Metcalfe
Arthur G. Metcalfe and
Associates, Inc.
2108 East 24th Street
National City, CA 91950

R. Metselaar
Eindhoven University
Centre for Technical Ceramics
P.O. Box 513
Eindhoven 5600 MB
THE NETHERLANDS AIR MAIL

David J. Michael
Harbison-Walker Refractories Company
P.O. Box 98037
Pittsburgh, PA 15227

Ken Michaels
Chrysler Motors Corporation
Ceramics Development
Metallurgical Processes
P.O. Box 1118, CIMS:418-17-09
Detroit, MI 48288

Bernd Michel
Institute of Mechanics
Fracture and Micromechanics
Department
P.O. Box 408
D-9010 Chemnitz
GERMANY AIR MAIL

David E. Miles
Commission of the European
Communities
rue de la Loi, 200
B-1049 Brussels
BELGIUM AIR MAIL

Carl E. Miller
AC Rochester
1300 North Dort Highway,
MS:32-31
Engineering Building B
Flint, MI 48556

Charles W. Miller, Jr.
Centorr Furnaces/Vacuum Industries
542 Amherst Street
Nashua, NH 03063

R. Mininni
Enichem America
2000 Cornwall Road
Monmouth Junction, NJ 08852

Michele V. Mitchell
Allied-Signal Aerospace
Company
Garrett Ceramic Components
Division
2525 West 190th Street
P. O. Box 2960, MS:T21
Torrance, CA 90501-2960

Howard Mizuhara
WESGO
477 Harbor Boulevard
Belmont, CA 94002

Helen Moeller
Babcock & Wilcox
P.O. Box 11165
Lynchburg, VA 24506-1165

Francois R. Mollard
Concurrent Technologies Corporation
1450 Scalp Avenue
Johnstown, PA 15904-3374

Phil Mooney
Panametrics
NDE Division
221 Crescent Street
Waltham, MA 02254

Geoffrey P. Morris
3M Company
3M Traffic Control Materials
Division
Bldg. 209-BW-10, 3M Center
St. Paul, MN 55144-1000

Jay A. Morrison
Rolls-Royce, Inc.
Engineering and Information
Center, Overlook 1
2849 Paces Ferry Road,
Suite 450
Atlanta, GA 30339-3769

Joel P. Moskowitz
Ceradyne, Inc.
3169 Redhill Avenue
Costa Mesa, CA 92626

Brij Moudgil
University of Florida
Material Science and
Engineering
Gainesville, FL 32611

Christoph J. Mueller
Sprechsaal Publishing
Group
P.O. Box 2962, Mauer 2
D-8630 Coburg
GERMANY AIR MAIL

Thomas W. Mullan
Vapor Technologies Inc.
345 Route 17 South
Upper Saddle River, NJ 07458

M. K. Murthy
MKM Consultants International
10 Avoca Avenue, Unit 1906
Toronto Ontario M4T 2B7
CANADA AIR MAIL

David L. Mustoe
Custom Technical Ceramics
8041 West I-70 Service Road,
Unit 6
Arvada, CO 80002

Curtis V. Nakaishi
U.S. Department of Energy
Morgantown Energy Technology
Center
Collins Ferry Road
P.O. Box 880
Morgantown, WV 26507-0880

Yoshio Nakamura
Faicera Research Institute
2-5-8 Hiyakunin-cho Shinjuku-Ko
Tokyo
JAPAN AIR MAIL

K. S. Narasimhan
Hoeganaes Corporation
River Road
Riverton, NJ 08077

Samuel Natansohn
GTE Laboratories, Inc.
40 Sylvan Road
Waltham, MA 02254

Robert Naum
Applied Resources, Inc.
P.O. Box 241
Pittsford, NY 14534

Malcolm Naylor
Cummins Engine Company, Inc.
P.O. Box 3005, Mail Code 50183
Columbus, IN 47202-3005

Jeffrey Neil
GTE Laboratories, Inc.
40 Sylvan Road
Waltham, MA 02254

Fred A. Nichols
Argonne National Laboratory
9700 South Cass Avenue
MCT - Building 212
Argonne, IL 60439

H. Nickel
Furschungszentrum Jüelich (KFA)
P.O. Box 1913
Jüelich 1-5170 BRD NRW
GERMANY AIR MAIL

Dale E. Niesz
Rutgers University
Center for Ceramic Research
P.O. Box 909
Piscataway, NJ 08855-0909

David M. Nissley
United Technologies Corporation
Pratt & Whitney Aircraft
400 Main Street, MS:163-10
East Hartford, CT 06108

Bruce E. Novich
Ceramics Process Systems Corporation
155 Fortune Boulevard
Milford, MA 01757

Daniel Oblas
GTE Laboratories, Inc.
40 Sylvan Road
Waltham, MA 02254

Don Ohanehi
Magnetic Bearings, Inc.
1908 Sussex Road
Blacksburg, VA 24060

D. O'Neil
GTE Laboratories, Inc.
40 Sylvan Road
Waltham, MA 02254

Robert Orenstein
General Electric Company
55-112, River Road
Schenectady, NY 12345

Norb Osborn
Aerodyne Dallas
151 Regal Row,
Suite 120
Dallas, TX 75247

Richard Palicka
Cercom, Inc.
1960 Watson Way
Vista, CA 92083

Muktesh Paliwal
GTE Products Corporation
Hawes Street
Towanda, PA 18848

Joseph E. Palko
General Electric Company
55-113, River Road
Schenectady, NY 12345

Joseph E. Palko
General Electric Company
55-113, River Road
Schenectady, NY 12345

Joseph N. Panzarino
Norton Company
Advanced Ceramics
Goddard Road
Northboro, MA 01532-1545

Pellegrino Papa
Corning Inc.
MP-WX-02-1
Corning, NY 14831

E. Beth Pardue
MPC
8297 Williams Ferry Road
Lenoir City, TN 37771

Soon C. Park
3M Company
3M Center
Building 142-4N-02
P.O. Box 2963
St. Paul, MN 55144

Hartmut Paschke
Schott Glaswerke
Christoph-Dorner-Strasse 29
D-8300 Landshut
GERMANY AIR MAIL

Marina R. Pascucci
GTE Laboratories, Inc.
40 Sylvan Road
Waltham, MA 02254

James W. Patten
Cummins Engine Company, Inc.
Materials Engineering
P.O. Box 3005, Mail
Code 50183
Columbus, IN 47202-3005

Robert A. Penty
Eastman Kodak Company
KAD/D73 - 35612
901 Elmgrove Road
Rochester, NY 14653

Robert W. Pepper
Textron Specialty Materials
2 Industrial Avenue
Lowell, MA 01851

Peter Perdue
Detroit Diesel Corporation
Research Advanced Development
Group
13400 Outer Drive West
Speed Code L-04
Detroit, MI 48239-4001

Bruce Peters
Dow Chemical Company
Building 52
Midland, MI 48667

John J. Petrovic
Los Alamos National Laboratory
Group MST-4, MS:G771
Los Alamos, NM 87545

Frederick S. Pettit
University of Pittsburgh
Pittsburgh, PA 15261

Ben A. Phillips
Phillips Engineering Company
721 Pleasant Street
St. Joseph, MI 49085

Richard C. Phoenix
Ohmtek, Inc.
2160 Liberty Drive
Niagara Falls, NY 14302

Bruce J. Pletka
Michigan Technological
University
Metallurgical and Materials
Engineering Department
Houghton, MI 49931

John P. Pollinger
Allied-Signal Aerospace Company
Garrett Ceramic Components
Division
2525 West 190th Street
P.O. Box 2960, MS:T21
Torrance, CA 90509-2960

P. Popper
High Technology Ceramics
International Journal
22 Pembroke Drive
Westlands Newcastle-under-Lyme
Staffs ST5 2JN
ENGLAND AIR MAIL

F. Porz
Universitat Karlsruhe
Institut fur Keramik Im
Maschinendau
Postfach 6980
D-7500 Karlsruhe
GERMANY AIR MAIL

Harry L. Potma
Royal Netherlands Embassy
Science and Technology
4200 Linnean Avenue, N.W.
Washington, DC 20008

Bob R. Powell
General Motors Research
Laboratories
Metallurgy Department
30500 Mound Road
Box 9055
Warren, MI 48090-9055

Stephen C. Pred
ICD Group, Inc.
1100 Valley Brook Avenue
Lyndhurst, NJ 07071

Karl M. Prewo
United Technologies Research
Center
411 Silver Lane
MS:24
East Hartford, CT 06108

Peter E. Price
Industrial Materials
Technology, Inc.
P.O. Box 9565
Andover, MA 01810

Joseph M. Proud
GTE Laboratories, Inc.
Materials Science Laboratory
40 Sylvan Road
Waltham, MA 02254

Vimal K. Pujari
Norton Company
Advanced Ceramics
Goddard Road
Northboro, MA 01532-1545

George Quinn
National Institute of
Standards and Technology
Ceramics Division, Bldg. 223
Gaithersburg, MD 20899

Ramas V. Raman
Ceracon, Inc.
1101 North Market Boulevard,
Suite 9
Sacramento, CA 95834

Charles F. Rapp
Owens Corning Fiberglass
2790 Columbus Road
Granville, OH 43023-1200

Dennis W. Readey
Colorado School of Mines
Department of Metallurgy
and Materials Engineering
Golden, CO 80401

Wilfred J. Rebello
PAR Enterprises, Inc.
12601 Clifton Hunt Lane
Clifton, VA 22024

Harold Rechter
Chicago Fire Brick Company
R&D
7531 South Ashland Avenue
Chicago, IL 60620

Robert R. Reeber
U.S. Army Research Office
P.O. Box 12211
Research Triangle Park, NC 27709

K. L. Reifsnider
Virginia Polytechnic Institute
and State University
Department of Engineering
Science and Mechanics
Blacksburg, VA 24061

Paul E. Rempes
McDonnell Douglass
Aircraft Company
P.O. Box 516,
Mail Code:0642263
St. Louis, MO 63166-0516

Gopal S. Revankar
John Deere Company
Metals Research
3300 River Drive
Moline, IL 61265

K. T. Rhee
Rutgers University
Mechanical Engineering
P.O. Box 909
Piscataway, NJ 08854

James Rhodes
Advanced Composite Materials
Corporation
1525 South Buncombe Road
Greer, SC 29651

Roy W. Rice
W. R. Grace and Company
7379 Route 32
Columbia, MD 21044

David W. Richerson
2093 East Delmont Drive
Salt Lake City, UT 84117

Tomas Richter
J. H. France Refractories
1944 Clarence Road
Snow Shoe, PA 16874

Michel Rigaud
Ecole Polytechnique
Campus Universite De Montreal
P.O. Box 6079, Station A
Montreal, P.Q Quebec H3C 3A7
CANADA AIR MAIL

R. E. Riman
Rutgers University
Ceramics Engineering
Department
P.O. Box 909
Piscataway, NJ 08855-0909

Barry Ringstrom
Superior Graphite Company
P.O. Box 2373
Smyrna, GA 30081

John E. Ritter
University of Massachusetts
Mechanical Engineering
Department
Amherst, MA 01003

Frank L. Roberge
Allied-Signal Aerospace
Company
Garrett Auxiliary Power
Division
P.O. Box 5227
Phoenix, AZ 85010

W. Eric Roberts
Advanced Ceramic Technology, Inc.
990 "F" Enterprise Street
Orange, CA 92667

Y. G. Roman
TNO TPD Keramick
P.O. Box 595
Einhoven 5600 AN
HOLLAND AIR MAIL

Michael Rossetti
Arthur D. Little, Inc.
15 Acorn Park
Cambridge, MA 01240

Barry R. Rossing
Lanxide Corporation
1300 Marrows Road
Newark, DE 19714-6077

Steven L. Rotz
Lubrizol Corporation
29400 Lakeland Boulevard
Wickliffe, OH 44092

Bruce Rubinger
Global Competitiveness, Inc.
One Devonshire Place,
Suite 1011
Boston, MA 02109

Robert Ruh
Wright Laboratory
WL/MLLM
Wright-Patterson AFB, OH 45433

Robert J. Russell
17 Highgate Road
Framingham, MA 01701

L. William Sahley
Supermaterials Company
24400 Highland Road
Richmond Heights, OH 44143

Jon Salem
NASA Lewis Research Center
21000 Brookpark Center
Cleveland, OH 44135

W. A. Sanders
NASA Lewis Research Center
21000 Brookpark Road,
MS:49-3
Cleveland, OH 44135

J. Sankar
North Carolina A&T State
University
Department of Mechanical
Engineering
Greensboro, NC 27411

Yasushi Sato
NGK Spark Plugs (U.S.A.), Inc.
1200 Business Center Drive,
Suite 300
Mt. Prospect, IL 60056

Maxine L. Savitz
Allied-Signal Aerospace Company
Garrett Ceramic Components
Division
2525 West 190th Street
P. O. Box 2960, MS:T21
Torrance, CA 90509-2960

Ashok Saxena
GTRI
Materials Engineering
Atlanta, GA 30332-0245

David W. Scanlon
Instron Corporation
100 Royall Street
Canton, MA 02021

Charles A. Schacht
Schacht Consulting Services
12 Holland Road
Pittsburgh, PA 15235

James Schienle
Allied-Signal Aerospace
Company
Garrett Auxiliary Power
Division
2739 East Washington Street
P.O. Box 5227, MS:1302-2P
Phoenix, AZ 85010

John C. Schneider
San Juan Technologies
P.O. Box 49326
Colorado Springs, CO 80949-9326

Gary Schnittgrund
Rocketdyne, BA05
6633 Canoga Avenue
Canoga Park, CA 91303

Mark Schomp
Lonza, Inc.
Corporate Headquarters
17-17 Route 208
Fair Lann, NJ 07410

Joop Schoonman
Delft University of Technology
Laboratory for Inorganic Chemistry
P.O. Box 5045
2600 GA Delft
THE NETHERLANDS AIR MAIL

John Schuldies
Industrial Ceramic Technology, Inc.
37 Enterprise Drive
Ann Arbor, MI 48103

Robert B. Schulz
U.S. Department of Energy
Office of Transportation Materials
CE-34
Washington, DC 20585

Murray A. Schwartz
Materials Technology Consulting, Inc.
30 Orchard Way, North
Potomac, MD 20854

Peter Schwarzkopf
SRI International
333 Ravenswood Avenue
Menlo Park, CA 94025

William T. Schwessinger
Multi-Arc Scientific Coatings
1064 Chicago Road
Troy, MI 48083-4297

W. D. Scott
University of Washington
Materials Science Department
Mail Stop:FB10
Seattle, WA 98195

Nancy Scoville
Thermo Electron Technologies
74 West Street
P.O. Box 9046
Waltham, MA 02254-9046

Brian Seegmiller
Coors Ceramics Company
600 9th Street
Golden, CO 80401

T. B. Selover
AICRE/DIPPR
3575 Traver Road
Shaker Heights, OH 44122

J. H. Selverian
GTE Laboratories, Inc.
40 Sylvan Road
Waltham, MA 02254

Charles E. Semler
Semler Materials Services
4160 Mumford Court
Columbus, OH 43220

Thomas Service
Service Engineering Laboratory
324 Wells Street
Greenfield, MA 01301

Kish Seth
Ethyl Corporation
R&D Laboratories
P.O. Box 341
Baton Rouge, LA 70821

Karleen Seybold
Allied-Signal Aerospace Company
Garrett Auxiliary Power Division
P.O. Box 5227
Phoenix, AZ 85010

William J. Shack
Argonne National Laboratory
9700 South Cass Avenue
Building 212
Argonne, IL 60439

Peter T. B. Shaffer
Technical Ceramics
Laboratories, Inc.
4045 Nine/McFarland Drive
Alpharetta, GA 30201

Richard K. Shaltens
NASA Lewis Research Center
21000 Brookpark Road,
MS:301-2
Cleveland, OH 44135

Robert S. Shane
238 Hemlock Road
Wynnewood, PA 19096

Daniel Shanefield
Rutgers University
Ceramics Engineering Department
P.O. Box 909
Piscataway, NJ 08855-0909

Ravi Shankar
Chromalloy
Research and Technology
Division
Blaisdell Road
Orangeburg, NY 10962

Terence Sheehan
Alpex Wheel Company
727 Berkley Street
New Milford, NJ 07646

Dinesh K. Shetty
University of Utah
304 EMRO, Dept. of Materials
Science and Engineering
Salt Lake City, UT 84112

Masahide Shimizu
Ceramic Society of Japan
2-2-503 Takiyama 6-chome
Higashikurume-Shi Tokyo 203
JAPAN AIR MAIL

John Shipinski
Toyota Technical Center
U.S.A., Inc.
Technical Research Department
2000 Town Center, Suite 500
Southfield, MI 48075

Thomas Shreves
American Ceramic Society, Inc.
Library
757 Brooksedge Plaza Drive
Westerville, OH 43081-2821

Jack D. Sibold
Coors Ceramics Company
Contracts for Corporate
Technology
4545 McIntyre Street
Golden, CO 80403

George H. Siegel
Point North Associates, Inc.
P.O. Box 907
Madison, NJ 07940

Johann Siebels
Volkswagen AG
Werkstofftechnologie
Postfach
3180 Wolfsburg 1
GERMANY AIR MAIL

Richard Silberglitt
Technology Assessment and
Transfer, Inc.
133 Defense Highway, #212
Annapolis, MD 21401

Mary Silverberg
Norton Company
Advanced Ceramics Library
Goddard Road
Northboro, MA 01532-1545

Gurpreet Singh
Department of the Navy
Internal Combustion & Gas
Turbine Engine Division
Code 56X31
Washington, DC 20362-5101

Maurice J. Sinnott
University of Michigan
Chemical and Metallurgical
Engineering
5106 IST Building
Ann Arbor, MI 48109-2099

John Skildum
3M Company
3M Center
Building 224-2S-25
St. Paul, MN 55144

David P. Smith
Hoskins, Rees & Smith
1910 Cochran Road
Manor Oak II, Suite 658
Pittsburgh, PA 15220

Richard H. Smoak
Smoak & Associates
3554 Hollyslope Road
Altadena, CA 91001-3923

Jay R. Smyth
Allied-Signal Aerospace Company
Garrett Auxiliary Power Division
2739 East Washington Street
P.O. Box 5227
MS:93-173/1303-207
Phoenix, AZ 85010

Rafal A. Sobotowski
British Petroleum Company
Technical Center, Broadway
3092 Broadway Avenue
Cleveland, OH 44115

A. G. Solomah
SAC International Ltd.
1445 Bonhill Road, # 13
Mississauga Ontario L5T 1V3
CANADA AIR MAIL

S. Somiya
Nishi Tokyo University
3-7-19 Seijo, Setagaya
Tokyo 157
JAPAN AIR MAIL

Boyd W. Sorenson
DuPont Lanxide Composites
1300 Marrows Road
P.O. Box 6077
Neward, DE 19707

Charles A. Sorrell
U.S. Department of Energy
Advanced Industrial Concepts Division
CE-232
Washington, DC 20585

C. Spencer
EA Technology
Capenhurst Chester
CH1 6ES
UNITED KINGDOM AIR MAIL

Allen Spizzo
Hercules, Inc.
Hercules Plaza
Wilmington, DE 19894

Richard M. Spriggs
Alfred University
Center for Advanced Ceramic Technology
Alfred, NY 14802

Charles Spuckler
NASA Lewis Research Center
21000 Brookpark Road
MS: 5-11
Cleveland, OH 44135-3191

M. Srinivasan
Material Solutions
P.O. Box 663
Grand Island, NY 14702-0663

Gordon L. Starr
Cummins Engine Company, Inc.
Design & Technology
P.O. Box 3005
Mail Code 50182
Columbus, IN 47202-3005

Jim Stevenson
Windrock, Incorporated
835 Innovation Drive
Knoxville, TN 37932

Tom Stillwagon
Allied-Signal Aerospace Company
Garrett Ceramic Components Division
2525 West 190th Street
P. O. Box 2960, MS:T21
Torrance, CA 90509-2960

H. M. Stoller
TPL Inc.
3754 Hawkins, N.E.
Albuquerque, NM 87109

Harold L. Stocker
General Motors Corporation
Allison Gas Turbine Division
P.O. Box 420
Indianapolis, IN 46206

Paul D. Stone
Dow Chemical USA
1776 "Eye" Street, N.W.,
Suite 575
Washington, DC 20006

Roger S. Storm
Carborundum Company
Technology Division
P.O. Box 337
Niagara Falls, NY 14302-0337

F. W. Stringer
Aero & Industrial Technology Ltd.
P.O. Box 46, Wood Top
Burnley Lancashire BB11 4BX
UNITED KINGDOM AIR MAIL

Thomas N. Strom
NASA Lewis Research Center
21000 Brookpark Road
MS:86-6
Cleveland, OH 44135

M. F. Stroosnijder
Institute for Advanced
Materials
Joint Research Centre
21020 Ispra (VA)
ITALY AIR MAIL

Karsten Styhr
30604 Ganado Drive
Rancho Palos Verdes, CA 90274

T. S. Sudarshan
Materials Modification, Inc.
2929-P1 Eskridge Center
Fairfax, VA 22031

M. J. Sundaresan
University of Miami
Mechanical Engineering
Department
P.O. Box 248294
Coral Gables, FL 33124

Patrick L. Sutton
U.S. Department of Energy
Advanced Propulsion Division
CE-322
Washington, DC 20585

Willard H. Sutton
United Technologies Corporation
Research Center, MS:24
Silver Lane
East Hartford, CT 06108

Ron Sviben
100 Indel Avenue
Rancocas, NJ 08073

J. J. Swab
U.S. Army Materials Technology
Laboratory
Ceramics Research Division
SLCMT-EMC
405 Arsenal Street
Watertown, MA 02172

Robert E. Swanson
Metalworking Technology, Inc.
1450 Scalp Avenue
Johnstown, PA 15904

Scott L. Swartz
Battelle Columbus
Laboratories
Metals and Ceramics
505 King Avenue
Columbus, OH 43201

Steve Szaruga
Air Force Wright Aeronautical
Laboratory
Materials Directorate
WL/MLBC
Wright-Patterson
AFB, OH 45433-6533

Yo Tajima
NGK Spark Plug Company, Ltd.
NTK Technical Ceramic Division
2808 Iwasaki
Komaki-shi Aichi-ken 485
JAPAN AIR MAIL

Fred Teeter
5 Tralee Terrace
East Amherst, NY 14051

Monika O. Ten Eyck
Carborundum Company
Technology Division
P.O. Box 832
Niagara Falls, NY 14302

David F. Thompson
Corning Glass Works
SP-DV-02-1
Corning, NY 14831

Merle L. Thorpe
Hobart Tafa Technologies, Inc.
146 Pembroke Road
Concord, NH 03301

Eberhard Tiefenbacher
Daimler-Benz AG Abt. F1S
Mercedes-Strabe 136
Stuttgart 60
GERMANY AIR MAIL

T. Y. Tien
University of Michigan
Materials Science and
Engineering Department
Dow Building
Ann Arbor, MI 48103

D. M. Tracey
Norton Company
Advanced Ceramics
Goddard Road
Northboro, MA 01532-1545

Dick Trippett
General Motors Corporation
Allison Gas Turbine Division
P.O. Box 420, MS:W-16
Indianapolis, IN 46206-0420

L. J. Trostel, Jr.
Box 199
Princeton, MA 01541

W. T. Tucker
General Electric Company
Corporate R&D
Building K1-4C35
P.O. Box 8
Schenectady, NY 12301

Masanori Ueki
Nippon Steel Corporation
Central R&D Bureau
1618 Ida
Nakahara-Ku Kawasaki 211
JAPAN AIR MAIL

Filippo M. Ugolini
ATA Studio
Via Degli Scipioni, 268A
ROMA 00192
ITALY AIR MAIL

Donald L. Vaccari
General Motors Corporation
Allison Gas Turbines
P.O. Box 420
Speed Code S49
Indianapolis, IN 46206-0420

Carl F. Van Conant
Boride Products, Inc.
2879 Aero Park Drive
Traverse City, MI 49684

Marcel H. Van De Voorde
Commission of the European
Communities
Institute for Advanced
Materials
Joint Research Centre
P.O. Box 2
1755 ZG Petten
THE NETHERLANDS AIR MAIL

O. Van Der Biest
Katholieke Universiteit Leuven
Departement Metaalkunde en
Toegepaste
de Croylaan 2
B-3030 Leuven
BELGIUM AIR MAIL

Michael Vannier
Washington University,
St. Louis
Mallinckrodt Institute of
Radiology
510 South Kings Highway
St. Louis, MO 63110

Stan Venkatesan
Southern Coke & Coal
Corporation
P.O. Box 52383
Knoxville, TN 37950

V. Venkateswaran
Carborundum Company
Niagara Falls R&D Center
P.O. Box 832
Niagara Falls, NY 14302

Dennis Viechnicki
U.S. Army Materials Technology
Laboratory
405 Arsenal Street
Watertown, MA 02172-0001

Ted Vojnovich
U.S. Department of Energy
Office of Energy Research,
ER-42
Washington, DC 20585

John D. Volt
E. I. Dupont de Nemours &
Company, Inc.
P.O. Box 80262
Wilmington, DE 19880

John B. Wachtman
Rutgers University
Ceramics Department
P.O. Box 909
Piscataway, NJ 08855

Shigetaka Wada
Toyota Central Research
Labs, Inc.
Nagakute Aichi 480-11
JAPAN AIR MAIL

Janet Wade
Allied-Signal Aerospace
Company
Garrett Auxiliary Power
Division, Department 93-772
P.O. Box 5227, MS:1303-2
Phoenix, AZ 85010

Richard L. Wagner
Ceramic Technologies, Inc.
537 Turtle Creek South Drive,
Suite 24D
Indianapolis, IN 46227

J. Bruce Wagner, Jr.
Arizona State University
Center for Solid State Science
Tempe, AZ 85287-1704

Daniel J. Wahlen
Kohler, Co.
444 Highland Drive
Kohler, WI 53044

Ingrid Wahlgren
Royal Institute of Technology
Studsvik Library
S-611 82 Nykoping
SWEDEN AIR MAIL

Ron H. Walecki
Allied-Signal Aerospace Company
Garrett Ceramic Components Division
2525 West 190th Street
P.O. Box 2960, MS:T21
Torrance, CA 90509-2960

Michael S. Walsh
Vapor Technologies Inc.
2100 Central Avenue
Boulder, CO 80301

Chien-Min Wang
Industrial Technology Research Institute
Materials Research Laboratories
195 Chung-Hsing Road, Sec. 4
Chutung Hsinchu 31015 R.O.C.
TAIWAN AIR MAIL

Robert M. Washburn
ASMT
11203 Colima Road
Whittier, CA 90604

S. F. Wayne
GTE Laboratories, Inc.
40 Sylvan Rd.
Waltham, MA 02254

Gerald Q. Weaver
Carborundum Specialty Products
42 Linus Allain Avenue
Gardner, MA 01440-2478

Karen E. Weber
Detroit Diesel Corporation
Technology and Planning
13400 West Outer Drive
Detroit, MI 48239-4001

R. W. Weeks
Argonne National Laboratory
MCT-212
9700 South Cass Avenue
Argonne, IL 60439

J. K. Weddell
DuPont Fibers
Experimental Station, E302
Wilmington, DE 19880-0302

Ludwig Weiler
ASEA Brown Boveri AG
Corporate Research
Eppelheimer Str. 82
D-6900 Heidelberg
GERMANY AIR MAIL

James Wessel
Dow Corning Corporation
1800 "M" Street, N.W.,
Suite 325 South
Washington, DC 20036

Robert D. West
Therm Advanced Ceramics
P.O. Box 220
Ithaca, NY 14851

Thomas J. Whalen
Ford Motor Company
26362 Harriet
Dearborn Heights, MI 48127

Ian A. White
Hoeganaes Corporation
River Road
Riverton, NJ 08077

Alan Whitehead
General Electric Company
1 River Road, 55-111
Schenectady, NY 12345

Sheldon M. Wiederhorn
National Institute of
Standards and Technology
Building 223, Room A329
Gaithersburg, MD 20899

John F. Wight
Alfred University
McMahon Building
Alfred, NY 14802

D. S. Wilkinson
McMaster University
Materials Science and
Engineering Department
1280 Main Street, West
Hamilton Ontario L8S 4L7
CANADA AIR MAIL

James C. Williams
General Electric Company
Engineering Materials
Technology Labs
One Neumann Way
Mail Drop: H85
Cincinnati, OH 45215-6301

Janette R. Williams
Kollmorgen Corporation
PCK Technology Division
150 Motor Parkway, # 262
Hauppauge, NY 11788-5108

Steve J. Williams
RCG Hagler Bailly, Inc.
1530 Wilson Boulevard,
Suite 900
Arlington, VA 22209-2406

Craig A. Willkens
Norton Company
Advanced Ceramics
Goddard Road
Northboro, MA 01532-1545

Roger R. Wills
TRW, Inc.
Valve Division
1455 East 185th Street
Cleveland, OH 44110

David Gordon Wilson
Massachusetts Institute of
Technology
Mechanical Engineering
Department
77 Massachusetts Avenue,
Room 3-455
Cambridge, MA 02139

Matthew F. Winkler
Seaworthy Systems, Inc.
P.O. Box 965
Essex, CT 06426

Gerhard Winter
Hermann C. Starck Berlin GmbH,
Werk Goslar
P.O. Box 25 40
D-3380 Goslar 3380
GERMANY AIR MAIL

W. L. Winterbottom
Ford Motor Company
Material Systems Reliability
Department
20000 Rotunda Drive
SRL, Room E-3182
P.O. Box 2053
Dearborn, MI 48121

David G. Wirth
Coors Ceramics Company
600 9th Street
Golden, CO 80401

Thomas J. Wissing
Eaton Corporation
Engineering & Research Center
P.O. Box 766
Southfield, MI 48037

James C. Withers
MER Corporation
7960 South Kolb Road
Building F
Tucson, AZ 85706

Dale E. Wittmer
Southern Illinois University
Mechanical Engineering
Department
Carbondale, IL 62901

Warren W. Wolf
Owens Corning Fiberglass
2790 Columbus Road, Route 16
Granville, OH 43023

Egon E. Wolff
Caterpillar Inc.
Technical Center
P.O. Box 1875
Peoria, Il 61656-1875

George W. Wolter
Howmet Turbine Components
Corporation
Technical Center
699 Benston Road
Whitehall, MI 49461

James C. Wood
NASA Lewis Research Center
21000 Brookpark Road
MS:86-6
Cleveland, OH 44135

Marrill Wood
LECO Corporation
Augusta Division
P.O. Box 211688
Augusta, GA 30917-1688

Wayne L. Worrell
University of Pennsylvania
Department of Materials
Science and Engineering
3231 Walnut Street
Philadelphia, PA 19104

John F. Wosinski
Corning Inc.
ME-2 E-5 H8
Corning, NY 14830

Ian G. Wright
Battelle Columbus Laboratories
505 King Avenue
Columbus, OH 43201

Ruth Wroe
ERDC
Metals & Materials Industries
Division
Capenhurst Chester CH1 6ES
ENGLAND AIR MAIL

Bernard J. Wrona
Advanced Composite Materials
Corporation
1525 South Buncombe Road
Greer, SC 29651

Carl C. M. Wu
Naval Research Laboratory
Ceramic Branch, Code 6373
Washington, DC 20375

John C. Wurst
University of Dayton Research
Institute
300 College Park
Dayton, OH 45469-0101

Neil Wyant
ARCH Development Corp.
9700 South Cass Avenue
Building 202
Argonne, IL 60439

Roy Yamamoto
Texaco Inc.
P.O. Box 509
Beacon, NY 12508-0509

John Yamanis
Allied-Signal, Inc.
Ceramics Program
P.O. Box 1021
Morristown, NJ 07962-1021

Harry C. Yeh
Allied-Signal Aerospace
Company
Garrett Ceramic Components
Division
2525 West 190th Street
P.O. Box 2960, MS:T21
Torrance, CA 90509-2960

Hiroshi Yokoyama
Hitachi Research Lab
4026 Kuji-Cho
Hitachi-shi Ibaraki 319-12
JAPAN AIR MAIL

Thomas M. Yonushonis
Cummins Engine Company, Inc.
P.O. Box 3005
Mail Code 50183
Columbus, IN 47202-3005

Thomas J. Yost
Corning, Inc.
Technical Products Division,
Main Plant 21-1-2
Corning, NY 14831

Jong Yung
Sundstrand Aviation Operations
Department 789-6
4747 Harrison Avenue
Rockford, IL 61125

A. L. Zadoks
Caterpillar Inc.
Technical Center, Building L
P.O. Box 1875
Peoria, IL 61656-1875

Avi Zangvil
University of Illinois
Materials Research Laboratory
104 South Goodwin Avenue
Urbana, IL 61801

Charles H. Zenuk
Transtech
6569 East Calle Cavalier
Tucson, AZ 85715

Anne Marie Zerega
U.S. Department of Energy
Office of Energy Research,
ER-42
Washington, DC 20585

Carl Zweben
General Electric Company
P.O. Box 8555, VFSC/V4019
Philadelphia, PA 19101

Klaus M. Zwilsky
National Research Council
National Materials Advisory Board
2101 Constitution Avenue
Washington, DC 20418

Department of Energy
DOE Field Office, Oak Ridge
Assistant Manager for Energy
Research and Development
P.O. Box 2001
Oak Ridge, TN 37831-8501

Department of Energy (10)
Office of Scientific and
Technical Information
Office of Information Services
P.O. Box 62
Oak Ridge, TN 37831

DATE
FILMED
6/8/93